Theoretical investigation of the interplay of proximity-induced spin interactions and correlated phenomena in multilayer graphene systems

Dissertation
zur Erlangung des Doktorgrades der Naturwissenschaften
(Dr. rer. nat.)
der Fakultät für Physik
der Universität Regensburg

vorgelegt von

Iaroslav Zhumagulov

aus

Snezhinsk, Russland

im Jahr 2023

Promotionsgesuch eingereicht am: 21.06.2023
Die Arbeit wurde angeleitet von: Prof. Dr. Jaroslav Fabian

Prüfungsausschuss:

Vorsitzender:	Prof. Dr. Jascha Repp
Erstgutachter:	Prof. Dr. Jaroslav Fabian
Zweitgutachter:	Prof. Dr. Milena Grifoni
weiterer Prüfer:	Prof. Dr. Vladimir Braun

Termin Promotionskolloquium: 16.11.2023

Abstract

The interplay of proximity-induced spin interactions and correlated phenomena in multilayer graphene systems is a promising avenue for developing electronics and spintronics. Being able to manipulate and alter correlated states in these systems is of great importance in studying new physical phenomena. This thesis delves into the interplay of proximity-induced spin interactions and correlated phenomena in Bernal bilayer graphene (BBG) and rhombohedral trilayer graphene (RTG) systems in detail. We utilize *ab initio*-fitted effective models of BBG and RTG, which are encapsulated by transition metal dichalcogenides (spin-orbit proximity effect) and ferromagnetic $Cr_2Ge_2Te_6$ (exchange proximity effect) and include Coulomb interactions using the random-phase approximation to study potential correlated phases at different displacement field and doping. Our results show a wide range of spin-valley resolved Stoner and intervalley coherence instabilities induced by the spin-orbit proximity effects, such as the emergence of a *spin-valley-coherent* phase due to valley-Zeeman coupling.

Zusammenfassung

Die Wechselwirkung von durch Nähe induzierten Spin-Wechselwirkungen und korrelierten Phänomenen in mehrschichtigen Graphensystemen bietet vielversprechende Möglichkeiten für die Entwicklung von Elektronik und Spintronik. Die Fähigkeit, korrelierte Zustände in diesen Systemen zu manipulieren und zu verändern, ist von großer Bedeutung für die Erforschung neuer physikalischer Phänomene. Diese Arbeit untersucht im Detail das Zusammenspiel von durch Nähe induzierten Spin-Wechselwirkungen und korrelierten Phänomenen in Bernal Bilayer Graphene (BBG) und rhomboedrischem Trilayer Graphene (RTG). Wir verwenden *ab initio*-angepasste effektive Modelle von BBG und RTG, die von Übergangsmetall-Dichalkogeniden (Spin-Bahn-Proximity-Effekt) und ferromagnetischem $Cr_2Ge_2Te_6$ (Austausch-Proximity-Effekt) eingekapselt sind und Coulomb-Wechselwirkungen unter Verwendung der Random-Phase-Approximation einschließen, um potenziell korrelierte Phasen bei unterschiedlichen Verschiebungsfeldern und Dotierungen zu untersuchen. Unsere Ergebnisse zeigen eine breite Palette von spin-valley aufgelösten Stoner- und intervalley Kohärenzinstabilitäten, die durch die Spin-Bahn-Proximity-Effekte induziert werden, wie zum Beispiel das Auftreten einer *spin-valley-kohärenten* Phase aufgrund der Valley-Zeeman-Kopplung.

List of used acronyms:

DFT – Density Functional Theory
LDA – Local Density Approximation
GGA – Generalized Gradient Approximation
SDFT – Spin Density Functional Theory
LSDA – Local Spin Density Approximation
NCPP – Norm-Conserving Pseudopotentials
USPP – Ultrasoft Pseudopotentials
PAW – Projector-Augmented Wave
SOC – Spin-Orbit Coupling
MLWF – Maximally Localized Wannier Functions
TMDC – Transition Metal Dichalcogenides
2D – two-dimensional/two dimensions
PIA – Pseudospin Inversion Asymmetry
QSHE – Quantum Spin Hall Effect
RPA – Random Phase Approximation
BCS – Bardeen-Cooper-Schrieffer
TWBG – Twisted Bilayer Graphene
RTG – Rhombohedral Trilayer Graphene
BBG – Bernal Bilayer Graphene
SO – Spin-Orbit
EX – Exchange
CGT – $Cr_2Ge_2Te_6$
IVC – Intervalley Coherent
SVC – Spin-Valley-Coherent
FM – Ferromagnetic
AFM – Antiferromagnetic
CDW – Charge-Density-Wave
SVP – Spin-Valley-Polarized
VP – Valley-Polarized
VP – Spin-Polarized
FL – Fermi-Liquid
PDW – Pair-Density-Wave

Contents

Introduction

The field of 2D materials offers a rich platform for exploring new physics and device innovation. Since the discovery of graphene, there has been a surge in research in this area, with growing interest in other 2D materials such as insulating transition metal dichalcogenides (TMDCs), superconductors, and magnetic materials. Although many of these materials have great technological potential, graphene remains the focus of many research institutions due to its unique dispersion properties and recent advances in device manufacturing.

Meanwhile, spintronics, also known as spin electronics, is a rapidly developing field that aims to exploit electron spin properties to create information storage devices and logic devices that exploit the electron spin degrees of freedom. Spintronics mainly relies on materials with pronounced magnetic and spin-orbital properties. In particular, spin-orbit coupling is critical in various spintronics phenomena and devices, such as the spin Hall effect, spin relaxation, and spin transistors.

Despite graphene's excellent charge transport properties and status as the most common two-dimensional material, it is of little use for spintronics due to its weak magnetic and spin-orbit properties. However, graphene's potential in spintronics is still being explored as we delve deeper into 2D materials, especially van der Waals heterostructures. The electronic states of these materials can be influenced not only by their intrinsic properties but also by proximity effects, which can enhance spin interactions in graphene despite its weak spin-orbit coupling. The researchers theoretically predicted and experimentally confirmed that in graphene-based heterostructures, it is possible to induce spin-orbit and exchange interactions using the proximity effect, leading to spin splitting at the meV level, sufficient to build spintronic devices operating at the temperature of liquid helium. Thus, Chapter 1 of the thesis aims to lay a theoretical foundation for studying and evaluating proximity-induced spin interactions in graphene.

Proximitized graphene has an attractive property where its proximity-induced valley-Zeeman intrinsic spin-orbit coupling can create pseudohelical edge states. These states carry pure spin solely current along the zigzag edge of graphene. What is unique about these edge states is that they are protected by time-reversal symmetry. As long as the scatterers at the edges maintain this symmetry, particles in this state cannot scatter back. These states are non-dissipative, which could lead to a groundbreaking change in on-chip interconnects by significantly decreasing power consumption in spintronics devices. However, there is an issue with graphene systems that have valley-Zeeman intrinsic spin-orbit coupling, as pseudohelical edge states coexist with intravalley states that lack time-reversal symmetry protection. It nullifies the benefits of pseudohelical edge states. Is it possible to isolate the pseudohelical edge states and remove the unwanted intravalley states? The Chapter 2 of the text addresses this problem and provides a

solution.

The discovery of correlated phases and superconductivity in magic-angle twisted bilayer graphene, which has a planar band structure at the Fermi level, has led to extensive research both theoretically and experimentally. However, controlling the twist angle and minimizing twist disorder remains a challenge, even though twist angle is a new way to tune the electronic properties of van der Waals heterostructures. Recent results have shown that correlation phenomena are present not only in moiré structures: semi- and quarter-metallic states and superconductivity have been observed in rhombohedral trilayer graphene (RTG), and isospin magnetism and spin-polarized superconductivity in Bernal bilayer graphene (BBG) demonstrating that the rich physics of strong electronic correlations can manifest itself in more traditional graphene systems without moiré pattern. In RTG and BBG, the low-energy band structure can be efficiently tuned using a displacement field, and the correlated phases are easily accessible through gate doping. This tunability makes RTG and BBG promising platforms for studying strongly correlated physics.

Given the advancements in researching strong electronic correlations in multilayer graphene systems and the spin interactions induced by the proximity effect, it is natural to raise a question: What would happen if these phenomena were combined? What kind of effects can be achieved, and is it possible to induce new correlated states in multilayer graphene systems through the spin interactions induced by the proximity effect? Chapters 4 and 5 are devoted to attempts to answer these questions.

Before exploring proximity-induced spin interactions and correlated phenomena in multilayer graphene systems, it is crucial to establish the theoretical foundation for our study. Despite the various methods available to study strong electronic correlations, we opted for many-body perturbation theory using Green's functions, introduced in Chapter 3. This method is widely accepted and provides reliable results in this field. By utilizing the Random Phase Approximation to examine correlated instabilities in the particle-hole channel and the linearized Eliashberg equation and parquet equation to analyze correlated instabilities in the particle-particle channel, we present a comprehensive overview of correlated states in multilayer graphene systems with proximity-induced spin interactions and address any inquiries on the topic.

1. From materials to models

1.1. Introduction

In the world of quantum mechanics, various interactions and phenomena influence the behavior of materials at the atomic and molecular levels. This Chapter delves into the theoretical frameworks and approximations that help us comprehend and anticipate these behaviors. We begin with the fundamental Born-Oppenheimer approximation, simplifying the many-body problem by separating nuclear and electronic motions. Moving forward, we explore Density Functional Theory (DFT), a powerful tool that has advanced our understanding of electronic systems. In DFT, we analyze the role of spin, which leads us to the Spin Density Functional Theory (SDFT) and the challenges and solutions presented by the pseudopotential approach. As we venture further, the Chapter sheds light on the relativistic effects within DFT, introducing the Dirac equation and its implications for Spin-Orbit Coupling (SOC). This section explains how the pseudopotential approach is modified to include relativistic effects. After that, we move from the continuous to the discrete and explore tight-binding models based on DFT. Our focus then centers on the Wannier orbitals basis, explicitly highlighting the importance of Maximally Localized Wannier Functions (MLWF).

The Chapter culminates by applying these theoretical constructs to a real-world marvel - monolayer graphene. We will dissect its tight-binding model, explore the role of MLWFs in graphene, and finally, probe into the intriguing world of proximity-induced spin-orbit and exchange couplings in graphene. The provided models of proximity-induced spin-orbit and exchange couplings in graphene serve as a starting point for our modeling of topological edge states in graphene flakes/nanoribbons Chapter 2 and also of the correlated states in multilayer graphene systems in Chapters 4 and 5.

As we navigate this Chapter, readers will gain a comprehensive understanding of the theoretical underpinnings that govern the quantum behavior of materials, setting the stage for subsequent Chapters that delve into applications and advanced topics.

1.2. Born-Oppenheimer approximation

Crystals and molecules, consisting of many interacting atomic nuclei and electrons, are canonical examples of the many-body problem. Many degrees of freedom make it impossible to solve this problem exactly. However, since, in most cases, we are interested in describing the physics of specific phenomena, physical science provides for and encourages the use of approximations. Thus, one of the most common approximations of solid state physics is the Born-Oppenheimer approximation [1], which assumes that, since the

mass of atomic nuclei is much greater than the mass of electrons, atomic nuclei can be considered in most cases static when studying the electronic subsystem of solids.

The Born-Oppenheimer approximation allows us to assume that we can describe the interaction of electrons with atomic nuclei based on the Hamiltonian.

$$\hat{H} = \underbrace{\sum_a \frac{\hat{\mathbf{P}}_a^2}{2M_a} + \frac{1}{2}\sum_{a,b}^{a\neq b} \frac{Z_a Z_b}{|\hat{\mathbf{R}}_a - \hat{\mathbf{R}}_b|}}_{\hat{H}_{nuc}} \underbrace{\sum_i -\frac{\nabla_i^2}{2} + \frac{1}{2}\sum_{i,j}^{i\neq j} \frac{1}{|\hat{\mathbf{r}}_i - \hat{\mathbf{r}}_j|}}_{\hat{H}_{el}} + \underbrace{\sum_{a,i} \frac{Z_a}{|\hat{\mathbf{R}}_a - \hat{\mathbf{r}}_i|}}_{\hat{H}_{el-nuc}}, \tag{1.1}$$

with Z_a are nucleus charges, M_a are nucleus masses, and nucleus momentum operators $\hat{\mathbf{P}}_a$, by the interaction of electrons with a periodic potential $V(\hat{\mathbf{r}})$. So, we can write the electron subsystem Hamiltonian as

$$\hat{H} = \underbrace{\sum_i \left[-\frac{\nabla_i^2}{2} + V(\hat{\mathbf{r}}_i)\right]}_{\hat{H}_{kin}} + \underbrace{\frac{1}{2}\sum_{i,j}^{i\neq j} \frac{1}{|\hat{\mathbf{r}}_i - \hat{\mathbf{r}}_j|}}_{\hat{H}_{int}}, \tag{1.2}$$

This Hamiltonian is written in atomic units and does not imply relativistic and magnetic effects, which will be discussed in subsequent Chapters. As stated, the (1.2) Hamiltonian consists of two parts: $\hat{H}_{kin}$ is a one-particle component, and $\hat{H}_{int}$ is the interaction between electrons. $\hat{H}_{kin}$ describes the motion of electrons in a periodic potential and is a one-particle problem that can be solved exactly. However, the second part of the Hamiltonian (1.2), $\hat{H}_{int}$, describing the interaction between electrons, is completely many-particle and, in most cases cannot be solved exactly. As in the case of the interaction of electrons with atomic nuclei, various approximations are often used to solve the problem of the interaction of electrons, one of which is the Density Functional Theory, which will be considered in the next section.

1.3. Density Functional Theory

The DFT is one of the main approximations for solving the many-particle problem of electron interaction. First formalized by Hohenberg and Kohn in 1964 [2, 3], it provides a remarkably efficient way to calculate the ground-state properties of many-electron systems. DFT is based on the Hohenberg-Kohn theorem [2, 4], which states that the energy of the ground state of a many-particle electron system is an electron density functional, which is at a minimum with the electron density of the ground state. Although the theorem is easy to prove [5], finding the exact functional takes time and effort. The most common form of total energy density functional is [6]:

$$E[\rho] = \underbrace{E_{kin}[\rho] + E_{ion}[\rho]}_{\hat{H}_{kin}} + \underbrace{E_H[\rho] + E_{xc}[\rho]}_{\hat{H}_{int}}, \tag{1.3}$$

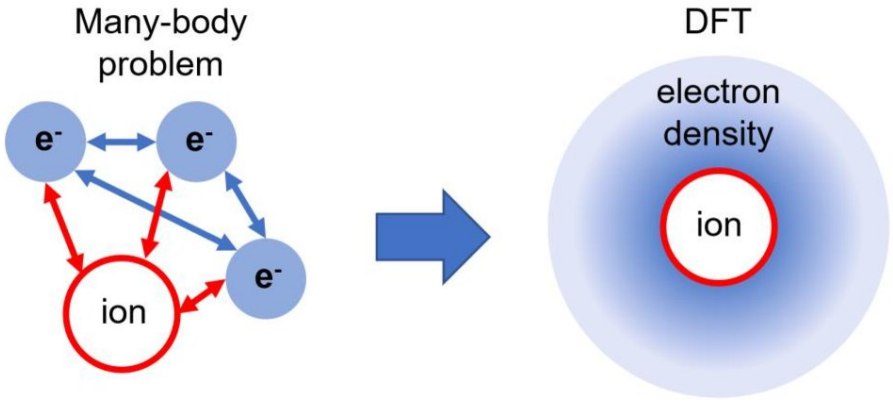

Figure 1.1: A schematic representation of the conversion from a many-electron system to its corresponding electron density via Density Functional Theory. Adapted from [7].

where $E_{kin}[\rho]$ is kinetic term, $E_{ion}[\rho]$ - ionic term, $E_H[\rho]$ - Hartree term and the last, $E_{xc}[\rho]$, is the exchange-correlation energy term. The first two terms describe the kinetic part of the (1.2) $\hat{H}_{kin}$ electron subsystem Hamiltonian. In comparison, the last two terms correspond to electron interaction Hamiltonian $\hat{H}_{int}$. As the Hohenberg-Kohn theorem states [2], to find the electron density of the ground state, one must minimize the energy of the ground state, i.e.,

$$\frac{\delta\{E[\rho] - \mu(\int d^3r\rho(\mathbf{r}) - N)\}}{\delta\rho} = 0 \tag{1.4}$$

where μ is the Lagrange multiplier (chemical potential), which fixes the system's number of electrons N [6].

The first exactly known term of the energy density functional is $E_{ion}[\rho]$, which describes the interaction of electrons with atomic nuclei. $E_{ion}[\rho]$ can be expressed as:

$$E_{ion}[\rho] = \int d^3r V_{ion}(\mathbf{r})\rho(\mathbf{r}) \tag{1.5}$$

with the ionic potential

$$V_{ion}(\mathbf{r}) = \sum_l \frac{Z_a}{|\mathbf{r} - \mathbf{R}_a|}, \tag{1.6}$$

where Z_l is the charge of the atomic nucleus, and $\mathbf{R}_l$ is its position. This component is completely classical since it describes only the electrostatic interaction between atomic nuclei and electrons without implying any quantum statistics of electrons or atomic nuclei.

At the same time, the interaction between electrons cannot be factorized as the product of two densities, just like the interaction between electrons and atomic nuclei. Therefore, the interaction between electrons is described by two components of the total energy density functional $E_{xc}[\rho]$ and $E_H[\rho]$. Hartree term $E_H[\rho]$ which can be expressed as:,

$$E_H[\rho] = \frac{1}{2}\int d^3r d^3r' \frac{\rho(\mathbf{r})\rho(\mathbf{r}')}{|\mathbf{r} - \mathbf{r}'|} \tag{1.7}$$

It describes the classical electrostatic interaction between electron densities, while the exchange-correlation component includes quantum exchange and correlation processes stemming from the fermionic statistics of electrons.

At the moment, we are facing the problem that the two remaining components, such as $E_{kin}[\rho]$ and $E_{xc}[\rho]$, do not have the exact form. To solve this problem for the kinetic energy functional, a set of auxiliary wave functions $\{\phi_i(\mathbf{r})\}$ are usually used that reproduce the electron density of the system:

$$\rho(\mathbf{r}) = \sum_{i}^{N} |\phi_i(\mathbf{r})|^2 \tag{1.8}$$

With the introduction of a set of auxiliary orthogonal wave functions, the problem of determining the kinetic energy functional becomes exactly solvable and can be expressed as:

$$E_{kin}[\rho] = -\frac{1}{2}\sum_{i}^{N}\langle\phi_i|\nabla^2|\phi_i\rangle \tag{1.9}$$

Although using a set of auxiliary functions solves the problem of calculating the kinetic functional, attempts to derive a kinetic functional depending only on the electron density continue. So, the approximate kinetic energy functionals are the basis of orbital free density functional theory. One of the simplest approximations for only density-dependent kinetic functionals is the Thomas-Fermi model:

$$E_{kin}[\rho] = E_{TF}[\rho] = \frac{3}{10}(3\pi)^{\frac{2}{3}}\int d^3r\rho(\mathbf{r})^{\frac{5}{3}}, \tag{1.10}$$

which was obtained for a homogeneous gas and is inaccurate for most systems. Using auxiliary wave functions significantly increases the accuracy of calculating the kinetic part of the ground state energy. However, it also substantially increases the computational cost.

In the next step, we transform the problem of finding the ground state by minimizing the energy concerning density ρ into the problem of finding the ground state by minimizing the energy concerning a set of auxiliary wave functions ϕ_i, with the following equation

$$\frac{\{\delta E[\rho] - \varepsilon_i(\int d^3r|\phi_i(\mathbf{r})|^2 - 1)\}}{\delta\phi_i} = 0, \tag{1.11}$$

where ε_i are the Lagrange multipliers, guarantee normalization of the auxiliary wave functions [6]. Such minimization of the ground state energy through auxiliary wave functions introduces the wide-known Kohn-Sham equation [8]:

$$\frac{\delta}{\delta\phi_i(\mathbf{r})}\left[E[\rho] - \varepsilon_i(\int d^3r'|\phi_i(\mathbf{r})|^2 - 1)\right] = \tag{1.12}$$
$$\left[-\frac{\nabla^2}{2} + V_{ion}(\mathbf{r}) + \int d^3r'\frac{\rho(\mathbf{r}')}{|\mathbf{r}-\mathbf{r}'|} + \frac{\delta E_{xc}[\rho]}{\delta\rho(\mathbf{r})}\right]\phi_i(\mathbf{r}) - \varepsilon_i\phi_i(\mathbf{r}) = 0$$

which can be solved iteratively to determine the ground state density. The problem is reduced to solving the effective single-particle problem with Kohn-Sham potential $V_{KS}(\mathbf{r})$, which has the following form:

$$V_{KS}(\mathbf{r}) = \sum_l \frac{Z_l}{|\mathbf{r} - \mathbf{R}_l|} + \int d^3r' \frac{\rho(\mathbf{r}')}{|\mathbf{r} - \mathbf{r}'|} + \frac{\delta E_{xc}[\rho]}{\delta \rho(\mathbf{r})} \tag{1.13}$$

The exchange-correlation functional is the last unknown component of the total energy density functional. The most common and the most simple form of the $E_{xc}[\rho]$ functional is the local density approximation (LDA) [4, 9, 10, 11]. In this approximation, the nonlocal exchange-correlation functional is replaced by its form for a homogeneous electron gas as a function of local density so that total exchange-correlation energy can be evaluated as the integral of the local components [9, 10, 11]:

$$E_{xc}[\rho] = \int d^3r E_{xc}^{\mathrm{LDA}}[\rho(\mathbf{r})] \tag{1.14}$$

LDA implies a weak spatial electron density variation, perfectly describing s-metals. Still, it is poorly suited for semiconductors or d-f electrons, with a robust electron density localization. Despite the limitations of LDA, it is widely used to study the band structure of electronic systems. It gives fascinatingly correct results, while the original DFT was designed to calculate the ground state energy.

To calculate the band structure using Kohn-Sham equations, the Lagrange multipliers ε_i are usually interpreted as the physical single-particle energies of the electron system, which correspond to the approximation of the interaction of electrons by the effective potential indicated in Eq.(1.13). The set of auxiliary wave functions $\{\phi_i(\mathbf{r})\}$ can also be interpreted as single-particle wave functions of the electronic system and called Kohn-Shame orbitals. Such an approach often describes the electronic structure surprisingly well, although it fails to explain the band gap in semiconductors or systems of highly correlated electrons with strong localization [12, 13, 6]. However, for most cases, LDA serves as the starting point, based on which models and ingredients are built for many-body methods that correct the above-described shortcomings of LDA.

LDA is not the only method used to describe the exchange-correlation functional, which is a critical component in DFT. Many other approximations have been developed and utilized, each with unique strengths and weaknesses. One of the most widespread approximations is the Generalized Gradient Approximation (GGA) [14, 15, 11]:

$$E_{xc}[\rho] = \int d^3r E_{xc}^{\mathrm{GGA}}[\rho(\mathbf{r}), \nabla\rho(\mathbf{r}), \nabla^2\rho(\mathbf{r})] \tag{1.15}$$

The GGA exchange-correlation functional is influenced not solely by the local density but also by the gradients of the local density. While it is a step beyond LDA in terms of complexity and accuracy, it does not necessarily provide a significant advantage when accurately describing electronic systems. It is because GGA, like LDA, is based on the electron gas model and can sometimes fail to capture the nuances of real-world systems.

The most recent significant progress in developing exchange-correlation functionals is hybrid functionals [16, 17, 13]. The fundamental concept behind these functionals is to

substitute a fraction α of the exchange energy from GGA functional with exact Fock exchange:

$$E_{xc} = E_c^{\mathrm{GGA}} + (1-\alpha)\, E_x^{\mathrm{GGA}} + \alpha E_x^{\mathrm{Fock}}, \tag{1.16}$$

where

$$E_x^{\mathrm{Fock}} = -\sum_{ij}^{N} \frac{\phi_i^*(\mathbf{r})\phi_j(\mathbf{r})\phi_j^*(\mathbf{r}')\phi_i(\mathbf{r}')}{|\mathbf{r}-\mathbf{r}'|} \tag{1.17}$$

Hybrid functionals are particularly effective in addressing issues that other approximations struggle with. For instance, they are known to provide a solution to the semiconductor band gap problem, which is a notorious challenge in computational materials science. It makes hybrid functionals a valuable tool in studying and predicting the electronic properties of semiconductors.

However, it is essential to note that hybrid functionals are not entirely based on first principles. It is because they incorporate a free parameter α, which controls the functional's " hybridity " degree. This parameter determines the mix of exchange-correlation energy derived from DFT and the Hartree-Fock theory. While this flexibility can be advantageous, it also means that the results can depend on the chosen α value, which is not derived from fundamental principles but is instead fitted to experimental data. It introduces empiricism into the calculations, which departs from the purely first-principles approach of methods like LDA or GGA.

1.3.1. Spin in Density Functional Theory

Since its inception by Hohenberg and Kohn in the 1960s [2, 3], DFT has emerged as a powerful tool in studying condensed matter systems. Its ability to approximate the behavior of a many-electron system using functionals of electron density has revolutionized our understanding of complex materials. However, incorporating spin into DFT, known as Spin Density Functional Theory (SDFT), adds another layer of complexity and potential to this already potent theoretical framework.

The most explicit approach to incorporate spin into DFT is by expressing the Kohn-Sham orbitals in a spin-resolved representation [18, 19, 4, 12]

$$\phi_i(\mathbf{r}) = \begin{pmatrix} \phi_{i\uparrow}(\mathbf{r}) \\ \phi_{i\downarrow}(\mathbf{r}) \end{pmatrix}. \tag{1.18}$$

As a consequence, the resulting density will also be decomposed in terms of spin and will exhibit the following structure:

$$\hat{\rho}(\mathbf{r}) = \rho_{\alpha\beta}(\mathbf{r}) = \sum_{i}^{N} \phi_{i\alpha}(\mathbf{r})\phi_{i\beta}^*(\mathbf{r}) \tag{1.19}$$

where α and β are the spin indices. The electron density matrix, denoted as $\rho_{\alpha\beta}$, represents the density matrix considering spin degrees of freedom. Therefore, we can

express the charge density of the system as $n(\mathbf{r}) = \frac{1}{2}\,\mathrm{Tr}\,[\hat{\rho}(\mathbf{r})\hat{\sigma}_0]$ and the magnetic density as $m(\mathbf{r}) = \frac{1}{2}\,\mathrm{Tr}\,[\hat{\rho}(\mathbf{r})\hat{\sigma}_z]$, where $\hat{\sigma}_i$ are the spin 1/2 Pauli matrices:

$$\sigma_0 = \begin{pmatrix} 1 & 0 \\ 0 & 1 \end{pmatrix} \quad \text{and} \quad \sigma_z = \begin{pmatrix} 1 & 0 \\ 0 & -1 \end{pmatrix} \tag{1.20}$$

Incorporating spin into DFT does not affect the classical components of the ground state energy, such as kinetic, Hartree, and ionic contributions, as they do not convey information about the fermionic spin statistics of electrons:

$$E_{kin}[\hat{\rho}] = -\frac{1}{2}\sum_{i\alpha}\langle\phi_{i\alpha}|\nabla^2|\phi_{i\alpha}\rangle \tag{1.21}$$

$$E_H[\hat{\rho}] = \frac{1}{2}\int d^3r d^3r' \frac{n(\mathbf{r})n(\mathbf{r}')}{|\mathbf{r}-\mathbf{r}'|} \tag{1.22}$$

$$E_{ion}[\hat{\rho}] = \int d^3r V_{ion}(\mathbf{r})n(\mathbf{r}). \tag{1.23}$$

However, the exchange-correlation functional, which integrates quantum effects, demonstrates a significant dependence not only on the electron charge density $n(\mathbf{r})$ but also on the electron magnetization $m(\mathbf{r})$ within a given system

$$E_{xc}[\hat{\rho}] = \int d^3r E_{xc}[\hat{\rho}] = \int d^3r E_{xc}^{LSDA}[n(\mathbf{r}), m(\mathbf{r})]. \tag{1.24}$$

For this, the Local Spin Density Approximation (LSDA) [18] was developed based on and similar to the LDA. LSDA considers the magnetization of the system and is accurate for systems in which the magnetization changes slowly. Despite strict assumptions, this approximation successfully describes various physical systems, from atoms and molecules to solids and surfaces. However, it is critical to recognize that LSDA has limitations and issues that encourage continuous research and improvement in this area.

Incorporating spin into the DFT turns identifying the ground state into an iterative process, considering the electron density and the system's magnetization. Consequently, the resulting effective Kohn-Sham equation for the spin-differentiated Kohn-Sham orbital adopts the following form:

$$\sum_\alpha \left[\left(-\frac{\nabla^2}{2} + V_{ion}(\mathbf{r}) + \int d^3r' \frac{n(\mathbf{r}')}{|\mathbf{r}-\mathbf{r}'|} + V_{xc}(\mathbf{r})\right)\hat{\sigma}_0 - \frac{1}{2}B_{xc}(\mathbf{r})\hat{\sigma}_z\right]_{\alpha\beta} \phi_{i\beta}(\mathbf{r}) = \varepsilon_{i\alpha}\phi_{i\alpha}(\mathbf{r}), \tag{1.25}$$

where

$$V_{xc}(\mathbf{r}) = \frac{E_{xc}[\hat{\rho}]}{\delta n(\mathbf{r})} \tag{1.26}$$

effective exchange-correlation single-particle potential similar to LDA and

$$B_{xc}(\mathbf{r}) = \frac{E_{xc}[\hat{\rho}]}{\delta m(\mathbf{r})} \tag{1.27}$$

an effective exchange-correlation magnetic field.

LSDA simplifies the complex many-body problem with magnetic effects by approximating the exchange-correlation energy as a local function of spin density. Although this approximation is not exact, it has successfully predicted various physical properties of various systems, from simple atoms to complex solids [20, 21, 22]. LSDA has succeeded in many systems but faces disadvantages in others due to its fundamental local approximation. Several enhancements have been introduced to LSDA, known as spin-dependent GGAs and hybrid functionals [23, 24, 4]. Problems and limitations are inherent in SDFT, including self-interaction errors and difficulties in accurately representing exchange-correlation functionals. Despite these challenges, including spin in DFT has opened up new possibilities for studying magnetic materials, spintronic devices, and other spin-dependent phenomena in condensed matter physics [25].

1.3.2. Pseudopotential approach

The description of the DFT method is complete with a brief introduction of the pseudopotential approach [26]. The idea of the pseudopotential method is to replace the problem for all electrons with a pseudo-problem that reduces computational complexity while maintaining high accuracy.

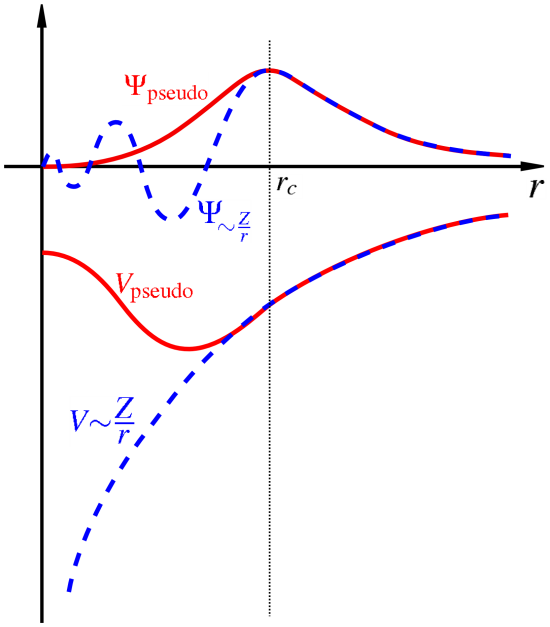

Figure 1.2: Comparison of a wavefunction in the Coulomb potential of the nucleus (blue) to the one in the pseudopotential (red). Adapted from [27].

One of the critical problems in DFT calculations is associated with rapidly oscillating wave functions of core electrons near atomic nuclei, which require substantial computational resources to process [4, 28]. Pseudopotentials are introduced to simplify this task. They replace the strongly bound core electrons and the atomic nucleus with a

smooth, effective potential, which is then used to solve the Kohn-Sham equation for valence electrons. It eliminates the need to account for fluctuations in the wave functions of core electrons with high momentum, as shown in fig.1.2.

The freedom to construct a pseudopotential also allows one to use the frozen core approximation [29]. This approximation assumes that the Kohn-Sham orbitals of the core electrons remain fixed during the complete calculation. This approximation has become extremely popular due to its well-controlled accuracy and efficiency, which is determined by one parameter - the number of frozen orbitals. It simplifies the calculation by reducing the number of electrons that must be accounted for explicitly.

The first step of constructing any pseudopotential is a self-consistent DFT calculation in an atom. In the non-relativistic case, the Kohn-Sham equation will look like this as

$$-\frac{1}{2}\frac{d^2\phi_l^{ae}(r)}{dr^2} + \left(\frac{1}{2}\frac{l(l+1)}{r^2} + V_{KS}(r) - \varepsilon_l^{ae}\right)\phi_l^{ae}(r) = 0 \tag{1.28}$$

where l is orbital momentum quantum number, $V_{KS}(r) = V_H(r) + V_{xc}(r) + V_{ion}(r)$ is Kohn-Sham potential and $\phi_l(r)$ are Konh-Sham orbitals. The subsequent steps in constructing pseudopotentials may differ depending on their type. In our work, we will consider one of the simplest and most common types of pseudopotentials, norm-conserving pseudopotentials (NCPP), introduced by Hamann, Schlüter, and Chiang in 1979 [30]. For a given reference atomic configuration, they must meet the following conditions:

1. The Kohn-Sham orbital energies from the pseudopotential solution should match those from the all-electron solution, $\varepsilon_l^{ps} = \varepsilon_l^{ae}$.

2. The pseudopotential solution Kohn-Sham orbitals (pseudo states), $\phi_l^{ps}(r)$, should be nodeless.

3. The pseudopotential solution Kohn-Sham orbitals $\phi_l^{ps}(r)$ should match the all-electron solution Kohn-Sham orbitals $\phi_l^{ae}(r)$ (atomic states) outside the core radius r_c, which roughly corresponds to the wavefunction's extreme peak.

4. Norm-conservation criteria $\int_0^{r_c} |\phi_l^{ps}(r)|^2 dr = \int_0^{r_c} |\phi_l^{ae}(r)|^2 dr$.

Fulfilling the above conditions requires us to generate the Kohn-Sham orbitals $\phi_l^{ps}(r)$. So, the next step is to invert the Kohn-Sham equation to extract the effective potential $V_l(r)$. The last step is the unscreening process: removing valence contribution to Hartree and exchange-correlation potentials:

$$V_l^{ps}(r) = V_l(r) - V_H\left[n^{ps}(r)\right] - V_{xc}\left[n^{ps}(r)\right], \tag{1.29}$$

where $n^{ps}(r) = \frac{1}{4\pi}\sum_l f_l |\phi_l^{ps}(r)|$ with f_l is the occupancy of state with orbital momentum l. The result of the procedure performed is a pseudopotential, which has the form

$$\hat{V}^{ps} = \sum_{lm} V_l^{ps}(r)|lm\rangle\langle lm| = \sum_{lm} V_l^{ps}(r)\delta(r-r')Y_{lm}(\hat{\mathbf{r}})Y_{lm}^*(\hat{\mathbf{r}}'), \tag{1.30}$$

where $Y_{lm}(\hat{\mathbf{r}})$ are spherical harmonics with l - orbital momentum quantum number and m - magnetic quantum number. Such form immediately indicates the nonlocal nature of

pseudopotential, which is a non-ideal from the side of computational efficiency. However, at the moment, the most common norm-conserving pseudopotential has a full nonlocal separable form, which improves this drawback:

$$\hat{V}^{ps} = V^{ps}_{loc}(r) + \hat{V}^{ps}_{non-loc}, \tag{1.31}$$

where $V^{ps}_{loc}(r)$ is behaving like long-range potential $-Z_v/r$ with Z_v as the pseudo-ion charge for $r > r_c$, while the second component represents short-range nonlocal ionic scattering potential for $r > r_c$. It is very convenient to recast the nonlocal part on the pseudopotential into the fully nonlocal form [31, 32]:

$$\hat{V}^{ps}_{non-loc} = \sum_{lm} \frac{|\delta V^{ps}_l \phi^{ps}_{lm}\rangle\langle\delta V^{ps}_l \phi^{ps}_{lm}|}{\langle\phi^{ps}_{lm}|\delta V^{ps}_l|\phi^{ps}_{lm}\rangle} = \sum_i v_i|\beta_i\rangle\langle\beta_i|, \tag{1.32}$$

where $\delta V_l(r) = V^{ps}_l(r) - V^{ps}_{loc}(r)$, and $|\beta_i\rangle$ is the set of scattering projectors with corresponding scattering amplitudes v_i. The form (1.31) significantly increases the computational efficiency, comparing with (1.30), which makes it possible to efficiently calculate $\hat{V}^{ps}|\psi\rangle$:

$$\hat{V}^{ps}\psi\rangle = V^{ps}_{loc}(r)|\psi\rangle + \sum_i v_i|\beta_i\rangle\langle\beta_i|\psi\rangle \tag{1.33}$$

It requires only $O(pN)$ computations for each Kohn-Sham orbital, where p represents the number of projectors $|\beta_i\rangle$ and N denotes the size of the plane waves basis or the number of mesh grid points.

Pseudopotential construction is only sometimes straightforward. Choosing the correct reference electronic configuration, defining the appropriate cutoff radius r_c, and constructing smooth pseudopotentials are all non-trivial tasks [4, 24, 28]. Furthermore, the pseudopotential depends on the exchange-correlation functional used in its construction and may not be transferable to other functionals or systems with a significantly different electronic environment.

In addition to norm-preserving pseudopotentials, there are other types, each with advantages and limitations. The next step in the evolution above norm-conserving pseudopotentials is Ultrasoft Pseudopotentials (USPP) [33], which were introduced to overcome the transferability issues in NCPPs and reduce the plane-wave cutoff energy or mesh grid spacing in total DFT calculations. General formulation of $\hat{V}_{US}$ for USPP is the same as NCPP:

$$\hat{V}_{US} = V_{loc}(r) + \sum_{lm} D_{lm}|\beta_l\rangle\langle\beta_m| \tag{1.34}$$

However, in contrast to the norm-conserving pseudopotential, charge density with USPP can "leak":

$$n(r) = \sum_i |\psi_i(\mathbf{r})|^2 + \sum_i \sum_{lm} \langle\psi_i|\beta_l\rangle Q_{lm}(r)\langle\beta_m|\psi_i\rangle \tag{1.35}$$

where the Q_{lm} are augmentation charges

$$Q_{lm}(r) = \phi^*_l(r)\phi_m(r) - \tilde{\phi}^*_l(r)\tilde{\phi}_m(r), \tag{1.36}$$

with atomic states $\phi_m(r)$ and pseudo-waves $\tilde{\phi}_l$. Violation of the norm conservation significantly enhances the transferability of the pseudopotential. However, this also increases computational complexity and challenges developing post-DFT methods.

Moreover, the current final step of the evolution of pseudopotentials for DFT calculations is Projector-Augmented Wave (PAW) pseudopotentials [34], compromising efficiency and accuracy. This method keeps the full wave function information and can reconstruct the all-electron wave function when needed. It makes PAW pseudopotentials highly accurate and applicable to various systems. PAW method introduced a linear transformation $\hat{T}$, which connects "true" orbitals $|\psi_i\rangle$ to "pseudo" orbitals $|\tilde{\psi}_i\rangle$:

$$|\psi_i\rangle = \hat{T}|\tilde{\psi}_i\rangle = |\tilde{\psi}_i\rangle + \sum_l \left(|\phi_l\rangle - |\tilde{\phi}_l\rangle\right) \langle\beta_l|\tilde{\psi}_i\rangle \tag{1.37}$$

where $|\phi_l\rangle$ are atomic states and $|\tilde{\phi}_l\rangle$ are pseudo-waves. Assuming that in the core region $|\tilde{\psi}_i\rangle = |\tilde{\phi}_l\rangle\langle\beta_l|\tilde{\psi}_i\rangle$ we can easily recover the USPP expression for the charge density $n(r)$. The PAW procedure can be used to reconstruct all-electron orbitals from pseudo-orbitals

The choice of the correct pseudopotential for DFT calculation depends on the specifics of the system under study, including the elements involved, the properties to be computed, and the computational resources available. Although pseudopotentials significantly reduce computational costs, it is essential to note that they also introduce another level of approximations, and all-electron calculations or experimental results must verify their use to ensure accurate predictions.

1.4. Relativistic effects in Density Functional Theory

Relativistic effects appear in many areas of physics, including condensed matter. They can significantly change the electronic structure and materials' physical and chemical properties. These effects are especially noticeable in heavy element compounds, in which valence electrons move at high speeds comparable to the speed of light. As a result, relativistic effects can change these materials' molecular bond characteristics, band structure, magnetism, and other properties [35].

There are two main relativistic effects in condensed matter physics:

1. The relativistic kinetic correction that arises from the increase in the effective mass of an electron as its speed approaches the speed of light

$$m = \frac{m_e}{\sqrt{1 - \frac{v^2}{c^2}}} \tag{1.38}$$

which results in a contraction of the Bohr radius of the electron orbitals:

$$a_0 = \frac{\hbar^2}{me^2} \tag{1.39}$$

This effect is known as the Lorentz contraction. It causes a shift in the energy levels of electronic states, changing the material's band structure accordingly.

2. And the spin-orbit coupling (SOC) arises due to the electron spin's interaction with the nuclei's electrostatic field gradient. This effect leads to splitting and mixing spin electronic states, significantly affecting the material's properties.

The standard DFT formulation does not take into account relativistic effects. However, the relativistic formulation of the DFT or the Dirac-Kohn-Sham method includes them [36, 37]. The Dirac-Kohn-Sham is based on the Dirac equation, which describes quantum mechanics and special relativity in a compatible manner. Dirac-Kohn-Sham calculations can consider special relativistic effects and spin-orbit coupling, making them suitable for studying materials with heavy elements. While this adds complexity, it provides a more accurate and comprehensive understanding of these materials and their properties.

1.4.1. Dirac equation: Spin-Orbit Coupling

Before we delve into the development of the Dirac-Kohn-Sham equations, it is necessary to review the Dirac equation. The report by Andrea Dal Corso significantly influenced this section, "Introduction to non-collinear magnetism and spin-orbit coupling in quantum espresso" (Cissa and Democritus, Trieste), and the doctoral degree of Tobias Frank Thesis [38].

The Dirac wave equation, developed by Paul Dirac in 1928 [39], describes elementary particles with spin $\frac{1}{2}$, such as electrons, within the framework of quantum mechanics. The Dirac equation for an electron, written in Hartree units ($c = 1/\alpha = 137.04$), can be expressed as follows [39, 40]:

$$i\frac{\partial\psi(\mathbf{r},t)}{\partial t} = \left(\hat{\boldsymbol{\alpha}}\hat{\mathbf{p}} - \hat{\beta}c^2\right)\psi(\mathbf{r},t) \tag{1.40}$$

where, $\hat{\mathbf{p}} = -i\boldsymbol{\nabla}$ is momentum operator, and

$$\hat{\boldsymbol{\alpha}} = (\sigma_x \otimes \sigma_x, \sigma_x \otimes \sigma_y, \sigma_x \otimes \sigma_z) \tag{1.41}$$

and

$$\hat{\beta} = \sigma_z \otimes \sigma_0 \tag{1.42}$$

are given in terms of the Pauli matrices:

$$\sigma_0 = \begin{pmatrix} 1 & 0 \\ 0 & 1 \end{pmatrix}, \sigma_x = \begin{pmatrix} 0 & 1 \\ 1 & 0 \end{pmatrix}, \sigma_y = \begin{pmatrix} 0 & -i \\ i & 0 \end{pmatrix}, \sigma_z = \begin{pmatrix} 1 & 0 \\ 0 & -1 \end{pmatrix} \tag{1.43}$$

A convenient transformation of the Dirac eigenfunctions is the division of the four-component spinor

$$\psi(\mathbf{r},t) = \begin{pmatrix} \psi_1(\mathbf{r},t) \\ \psi_2(\mathbf{r},t) \\ \psi_3(\mathbf{r},t) \\ \psi_4(\mathbf{r},t) \end{pmatrix} \tag{1.44}$$

into major

$$\psi_A(\mathbf{r},t) = \begin{pmatrix} \psi_1(\mathbf{r},t) \\ \psi_2(\mathbf{r},t) \end{pmatrix} \tag{1.45}$$

and minor

$$\psi_B(\mathbf{r},t) = \begin{pmatrix}\psi_3(\mathbf{r},t)\\ \psi_4(\mathbf{r},t)\end{pmatrix} \tag{1.46}$$

components. After turning on the interaction of an electron with an external electromagnetic field, with the corresponding vector $\mathbf{A}(\mathbf{r})$ and scalar $\phi(\mathbf{r})$ fields, using ansatz $\psi(\mathbf{r},t) = \exp[-iEt]\psi(\mathbf{r})$ and minimal coping $\hat{\mathbf{p}} \to \hat{\mathbf{p}} + \mathbf{A}(\mathbf{r}) = \hat{\boldsymbol{\pi}}$ and $E \to E + \phi(\mathbf{r})$, we can derive the following set of equations:

$$c\hat{\boldsymbol{\sigma}}\hat{\boldsymbol{\pi}}\psi_B(\mathbf{r}) + \left[c^2 - \phi(\mathbf{r}) - E\right]\psi_A(\mathbf{r}) = 0 \tag{1.47}$$

$$c\hat{\boldsymbol{\sigma}}\hat{\boldsymbol{\pi}}\psi_A(\mathbf{r}) - \left[c^2 + \phi(\mathbf{r}) + E\right]\psi_B(\mathbf{r}) = 0 \tag{1.48}$$

We can simplify these equations further, bringing them to the non-relativistic limit. Employing the definition of the reduced energy as $E' = E - c^2$, we can rewrite the equation (1.48) as

$$\psi_B(\mathbf{r}) = \frac{c\hat{\boldsymbol{\sigma}}\hat{\boldsymbol{\pi}}\psi_A(\mathbf{r})}{E' + 2c^2 + \phi(\mathbf{r})} \approx \frac{1}{2c}\hat{\boldsymbol{\sigma}}\hat{\boldsymbol{\pi}}\psi_A(\mathbf{r}) \tag{1.49}$$

where we expanded the denominator in a Taylor series of $[E' + \phi(\mathbf{r})]/2m$, ignoring term of order $1/c^2$. Inserting expression (1.49) in the equation (1.47), we obtain the Pauli equation

$$\left[\frac{1}{2}\left(\hat{\boldsymbol{\sigma}}\hat{\boldsymbol{\pi}}\right)\left(\hat{\boldsymbol{\sigma}}\hat{\boldsymbol{\pi}}\right) - \phi(\mathbf{r}) - E'\right]\psi_A(\mathbf{r}) = 0 \tag{1.50}$$

Using the relationship:

$$\left(\hat{\boldsymbol{\sigma}}\hat{\boldsymbol{\pi}}\right)\left(\hat{\boldsymbol{\sigma}}\hat{\boldsymbol{\pi}}\right) = \hat{\boldsymbol{\pi}}^2 + \hat{\boldsymbol{\sigma}}\cdot\nabla\times\mathbf{A}(\mathbf{r}) \tag{1.51}$$

we can rewrite Pauli's equations as follows:

$$\left[\hat{H}_{Pauli} - E'\right]\psi_A(\mathbf{r}) = \left[\frac{\hat{\boldsymbol{\pi}}^2}{2} + \frac{1}{2}\hat{\boldsymbol{\sigma}}\times\mathbf{B}(\mathbf{r}) - \phi(\mathbf{r}) - E'\right]\psi_A(\mathbf{r}) = 0 \tag{1.52}$$

This equation illustrates that the electron's magnetic moment is attributed to its orbital motion and spin-orbital momentum. By keeping terms up to the order of $1/c^2$ in the Taylor series, we derive the equation $\hat{H}\psi = E'\psi$ applicable for a two-component spinor, representing the Hamiltonian as [40]

$$\hat{H} = \hat{H}_{Pauli} - \frac{\hat{\mathbf{p}}^4}{8c^2} - \frac{1}{8c^2}\nabla\cdot\nabla\phi(\mathbf{r}) - \frac{1}{4c^2}\hat{\boldsymbol{\sigma}}\cdot[\nabla\phi(\mathbf{r})\times\hat{\mathbf{p}}] \tag{1.53}$$

The first two corrections to the Hamiltonian Pauli are scalar-relativistic mass velocity and Darwinian components. The function of the mass velocity component is to serve as a kinetic energy modification of the second order, which facilitates orbit contraction. Meanwhile, Darwin's part causes energy shifts in s-like states.

The spin-orbit coupling (SOC) is the third correction of the equation referenced as (1.53). The energy changes caused by the scalar-relativistic mass velocity and Darwin's components are generally near 0.01 meV. On the other hand, the spin-orbit interaction

predominantly ranges from 1 to 100 meV for valence electrons [40]. Due to their negligible energy scale, the first two corrections - scalar-relativistic mass velocity and Darwin's components - can typically be disregarded.

The most important correction to Pauli Hamiltonian is spin-orbit coupling, which can be rewritten in the case of a spherical potential as [40]

$$\hat{H}_{\mathrm{SOC}} = \frac{1}{4c^2}\hat{\boldsymbol{\sigma}} \cdot [\nabla\phi(\mathbf{r}) \times \hat{\mathbf{p}}] = \frac{1}{4c^2}\frac{\partial\phi(r)}{r\partial r}\hat{\boldsymbol{\sigma}} \cdot (\hat{\mathbf{r}} \times \hat{\mathbf{p}}) = \frac{1}{2c^2}\frac{\partial\phi(r)}{r\partial r}\hat{\mathbf{S}} \cdot \hat{\mathbf{L}} \tag{1.54}$$

where $\hat{\mathbf{L}} = \hat{\mathbf{r}} \times \hat{\mathbf{p}}$ is orbital momentum and $\hat{\mathbf{L}} = \hat{\boldsymbol{\sigma}}/2$ is spin orbital momentum.

Spin-orbit coupling removes degeneracy from $2(2l+1)$ levels $|nlm_lm_s\rangle$. Each level is characterized by shell number n, orbital momentum quantum number l, magnetic quantum number m_l, and spin quantum number m_s. It splits states into two groups: one with degeneracy $2l+2$, in which spin and orbital momentum are parallel ($j = l + \frac{1}{2}$), and another with degeneracy $2l$, where spin and orbital momentum are antiparallel ($j = l - \frac{1}{2}$). Spin-orbit coupling eigenstates are usually denoted as $|nljm_j\rangle$, where j and m_j are the quantum numbers of the total orbital momentum $\hat{J} = \hat{L} + \hat{S}$ and its projection on the selected axis.

The splitting of energy levels of the hydrogen-like atom under the influence of the spin-orbit coupling can be represented as

$$\Delta E_{\mathrm{SOC}} = \frac{1}{2}\frac{Z^4\alpha}{n^3}\frac{l}{l(l+1)} \tag{1.55}$$

where $\alpha = 1/c$ is the fine structure constant approximately, Z is the nuclear charge, l is the quantum number of the orbital momentum. Thus, spin-orbit coupling is expected to be especially pronounced in systems with heavy elements.

1.4.2. Pseudopotential approach: Spin-Orbit Coupling

In this subsection, we describe a minimal implementation of the spin-orbit coupling in the DFT framework. To achieve this, we will be utilizing the norm-conserving pseudopotential methodology, which has been explained in detail in previous sections of this discussion.

It would be helpful to express the radial Dirac-Kohn-Sham equations, shown in Equation (1.48), using Hartree atomic units. The equations are presented below:

$$c\left(\frac{d}{dr} - \frac{\kappa}{r}\right)\psi_B(r) + [\varepsilon - V_{KS}(r)]\,\psi_A(r) = 0, \tag{1.56}$$

$$c\left(\frac{d}{dr} + \frac{\kappa}{r}\right)\psi_A(r) - \left[2c^2 + \varepsilon - V_{KS}(r)\right]\psi_B(r) = 0. \tag{1.57}$$

Here, ε is defined as $E - c^2$ and the radial Kohn-Sham potential, $V_{KS}(r)$, is a summation of the ionic potential $V_{ion}(r)$, Hartree potential $V_H(r)$, and exchange-correlation potential $V_{xc}(r)$.

Next, for valence electrons outside the core region, we propose a $\psi_B(r)$ in Equation (1.57), which is:

$$\psi_B(r) = \frac{1}{2c}\left(\frac{d}{dr} + \frac{\kappa}{r}\right)\psi_A(r) \tag{1.58}$$

This substitution is valid under the assumption that ε and $V_{KS}(r)$ for $r > r_c$ are negligible in magnitude. The outcome of this simplification leads to the ensuing Dirac-Kohn-Sham equation:

$$\frac{1}{2}\left(\frac{d^2}{dr^2} + \frac{\kappa(\kappa+1)}{r^2}\right)\psi_A(r) + [V_{KS}(r) - \varepsilon]\,\psi_A(r) = 0 \tag{1.59}$$

The equation implies that the radial wave function for positive energy is $\psi_A(r)/r$. Similarly, the wave function for negative energy is $\psi_B(r)/r$, which mixes significantly with $\psi_A(r)$ in heavy atoms, mainly within the nucleus area.

The quantum number κ represents the relativistic quantum number, which is equal to the orbital momentum quantum number l when $j = l - \frac{1}{2}$, and to $-(l+1)$ when $j = l + \frac{1}{2}$. The orbital wave function associated with $\psi_A(r)$ has a specific structure. For $j = l + \frac{1}{2}$ and $m_j = m + \frac{1}{2}$, the following is valid:

$$|\Phi^{l,j}_{m_j}\rangle = \left(\frac{l+m+1}{2l+1}\right)^{\frac{1}{2}} |Y^m_l\rangle|\uparrow\rangle + \left(\frac{l-m}{2l+1}\right)^{\frac{1}{2}} |Y^{m+1}_l\rangle|\downarrow\rangle. \tag{1.60}$$

However, for $j = l - \frac{1}{2}$ and $m_j = m - \frac{1}{2}$, the orbital wave function form is different:

$$|\Phi^{l,j}_{m_j}\rangle = \left(\frac{l-m+1}{2l+1}\right)^{\frac{1}{2}} |Y^{m-1}_l\rangle|\uparrow\rangle + \left(\frac{l+m}{2l+1}\right)^{\frac{1}{2}} |Y^m_l\rangle|\downarrow\rangle. \tag{1.61}$$

$|\uparrow\rangle$ and $|\downarrow\rangle$ are represent the eigenfunctions of the z-component of the Pauli spin operator.

The following steps are much like those used to construct the norm-conserving pseudopotential described earlier. The outcome will be $\hat{V}^{ps}$ in the form presented below:

$$\hat{V}^{ps}(r) = \sum_{l,m_j} |\Phi^{l,j}_{m_j}\rangle V^{ps}_{l,j}(r)\langle\Phi^{l,j}_{m_j}| \tag{1.62}$$

$$= \sum_{l,m_j} |\Phi^{l,j}_{m_j}\rangle V^{ps}_{l+1/2}(r)\langle\Phi^{l,j}_{m_j}| + |\Phi^{l,j'}_{m'_j}\rangle V^{ps}_{l-1/2}(r)\langle\Phi^{l,j'}_{m'_j}| \tag{1.63}$$

where $j = l + \frac{1}{2}$, $m_j = m + \frac{1}{2}$, $j' = l - \frac{1}{2}$ and $m'_j = m - \frac{1}{2}$. It may be rewritten as

$$\hat{V}^{ps}(r) = \sum_l |l\rangle[V^{ion}_l(r) + V^{so}_l(r)\hat{\mathbf{L}}\cdot\hat{\mathbf{S}}]\langle l| \tag{1.64}$$

where

$$V^{ion}_l(r) = \frac{1}{2l+1}[lV^{ps}_{l,l-1/2}(r) + (l+1)V^{ps}_{l,l+1/2}(r)] \tag{1.65}$$

and

$$V^{so}_l(r) = \frac{2}{2l+1}[V^{ps}_{l,l+1/2}(r) - V^{ps}_{l,l-1/2}(r)] \tag{1.66}$$

By using a pseudopotential like the one in Eq.(1.64), it becomes possible to utilize the Pauli equation (Eq.(1.51)) instead of the entire relativistic four-component Dirac equation when considering spin-orbit coupling in DFT. This method is called the scalar relativistic approach and can accurately account for all relativistic effects up to order $1/c^2$ [41].

It should be noted that a fully relativistic pseudopotential approach and a full-electron fully relativistic approach with a four-component Dirac equation give higher accuracy than the scalar-relativistic pseudopotential approach. However, the choice of the correct approximation always depends on the required accuracy, and often, a less accurate but more extensive calculation can give much more reliable theoretical predictions.

1.5. Tight-binding models from DFT

The tight-binding method is a quantum mechanical approach to studying the electronic structure of molecules and solids [42, 43, 44, 45]. One of its main advantages is that it requires less computer time than other electronic structure calculations while still producing accurate results. The tight-coupling method is a popular and almost indispensable tool in electron transport [46, 47] or strong electron correlations [48, 49].

For non-interacting systems, tight-binding calculations are explicit, and analytic results can often be obtained by studying electrons in molecules and solids [44, 45]. In this section, we offer a basic overview of the construction process of the tight-binding models based on the DFT/Kohn-Sham equation results, explaining how to obtain the Hamiltonian matrix by selecting a basis of Wannier functions.

1.5.1. Wannier orbitals basis

The tight-binding model is commonly used in solid-state physics to describe the behavior of electrons in a crystal. This model approximates where the wave function of an electron located at each lattice site in a crystal can be represented as a superposition of atomic orbitals. When periodic boundary conditions are applied, Kohn-Sham's potential or any other single-particle potential will show periodicity for any given lattice vector $\mathbf{R}$. It can be expressed mathematically as:

$$V(\mathbf{r}) = V(\mathbf{r} + \mathbf{R}) \tag{1.67}$$

By utilizing Bloch's theorem, the Kohn-Sham orbitals (represented as ψ) can be defined in the following form:

$$\psi_{\mathbf{k}n}(\mathbf{r}) = e^{i\mathbf{k}\mathbf{r}} u_{\mathbf{k}n}(\mathbf{r}) \tag{1.68}$$

The equation uses $\mathbf{k}$ to represent a crystal momentum wavevector within the first Brillouin zone, while n stands for a band index. It is necessary to define the Wannier orbitals [42, 50], labeled as w_n, and represent localized wave functions. These orbitals can be described using a Fourier series of Bloch waves, as demonstrated below:

$$w_n(\mathbf{r} + \mathbf{R}) = \frac{V}{(2\pi)^3} \int_{BZ} d^3k e^{i\mathbf{k}\mathbf{R}} \psi_{\mathbf{k}n}(\mathbf{r}) \tag{1.69}$$

Electrons in Wannier orbitals are tightly bound to lattice sites and move by hopping from one site to another [42, 50]. The corresponding energy of this hopping process can be calculated as

$$t_{ij}^{nm} = \int d^3r w_n^*(\mathbf{r}+\mathbf{R}_i)\left[-\frac{\nabla^2}{2}+V(\mathbf{r})\right]w_m(\mathbf{r}+\mathbf{R}_j) \tag{1.70}$$

As a result, we have hopping amplitude t_{ij}^{nm} from lattice site i and Wannier orbital n to lattice site j and Wannier orbital m. The next step is to rewrite the Kohn-Sham equation using the second quantization language

$$\hat{H} = \sum_\sigma \int d^3r \hat{\psi}_\sigma^\dagger(\mathbf{r})\left[-\frac{\nabla^2}{2}+V_{KS}(\mathbf{r})\right]\hat{\psi}_\sigma(\mathbf{r}) \tag{1.71}$$

where $V_{KS}(\mathbf{r})$ is Kohn-Sham potential, μ is the chemical potential, and $\hat{\psi}_\sigma^\dagger(\hat{\psi}_\sigma)$ is creation (annihilation) operators for an electron of spin σ at position $\mathbf{r}$. Redefining field operator $\hat{\psi}_\sigma^\dagger$ as

$$\hat{\psi}_\sigma^\dagger = \sum_{in} w_n^*(\mathbf{r}+\mathbf{R}_i)\hat{c}_{in\sigma}^\dagger \tag{1.72}$$

where $\hat{c}_{in\sigma}^\dagger(\hat{c}_{in\sigma})$ is the creation (annihilation) operator for an electron of spin σ at Wannier orbital n at lattice site i. As a result, we can define the general tight-binding form of Hamiltonian (1.71):

$$\hat{H} = \sum_\sigma \sum_{ij,nm} t_{ij}^{nm}\hat{c}_{in\sigma}^\dagger\hat{c}_{jm\sigma} \tag{1.73}$$

Thus, we encoded all information from the Kohn-Sham equations into the compact form of the matrix t_{ij}^{nm} without losing generality.

In the Wannier function basis, the Hamiltonian is a tight-binding model that proves very practical [47, 48, 46]. Wannier basis helps obtain a minimal model with only a few essential orbitals while retaining the fundamental physics. It is crucial when dealing with complex materials since the electronic structure problem could comprise thousands of degrees of freedom on a plane-wave or real-space basis. In contrast, on a Wannier basis, the whole problem could fit into a few/lesser number degrees of freedom [52].

1.5.2. Maximally Localized Wannier Functions

When working with the construction tight-binding model from DFT, mentioning Maximally Localized Wannier Functions (MLWF) is crucial [53, 51]. Wannier functions can have different centers and spreads, which means they are not unique without specific details. The Maximally Localization approach is commonly used to construct the Wannier orbital basis. The process involves solving an optimization problem that seeks the set of unitary transformations of the Bloch wavefunctions that minimize the spread of the Wannier functions. The MLWFs are highly localized in real space; each function is only non-zero in a small crystal region. This characteristic makes the MLWFs an excellent

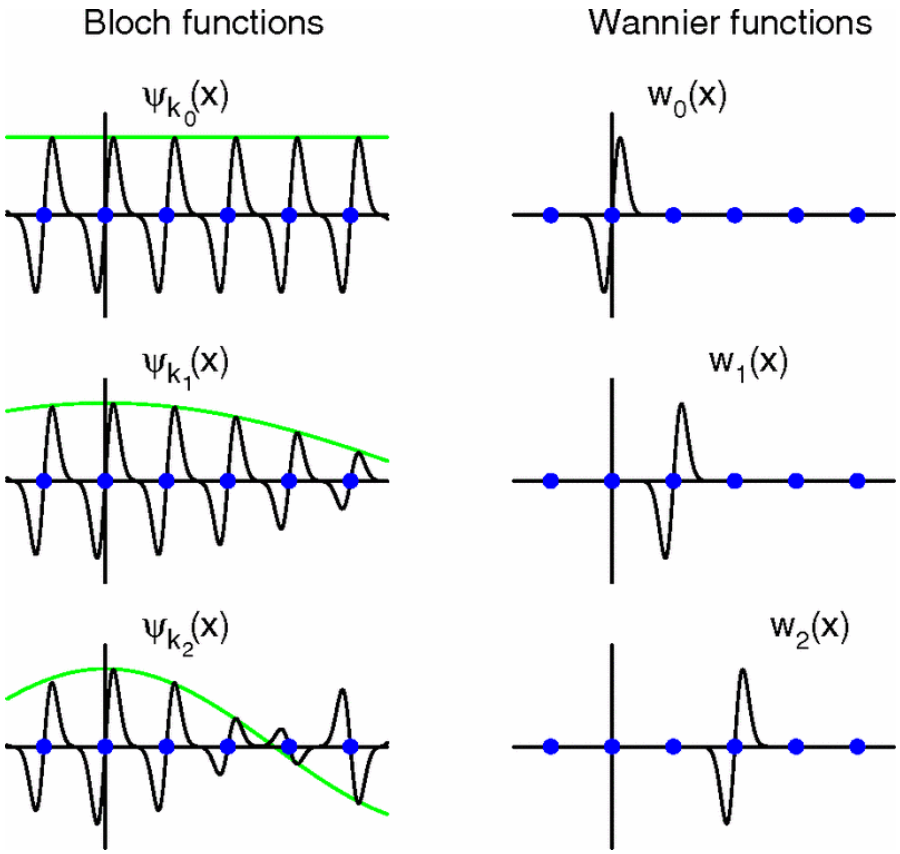

Figure 1.3: This illustration shows how Bloch functions can be converted into Wannier functions. The left side of the image displays a real-space representation of three Bloch functions, denoted as $e^{ikx}\psi_{kn}(x)$, which belong to a single band in 1D. Each Bloch function has a different value of the wave vector k, and filled circles represent the lattice vectors. The thin lines depict each Bloch function's e^{ikx} envelopes. The Wannier functions associated with the same band are shown on the right side of the image. These functions create periodic replicas that are identical to one another. The two sets of Bloch functions at every k value within the Brillouin zone and Wannier functions at each lattice vector encompass the same Hilbert space. Adapted from [51].

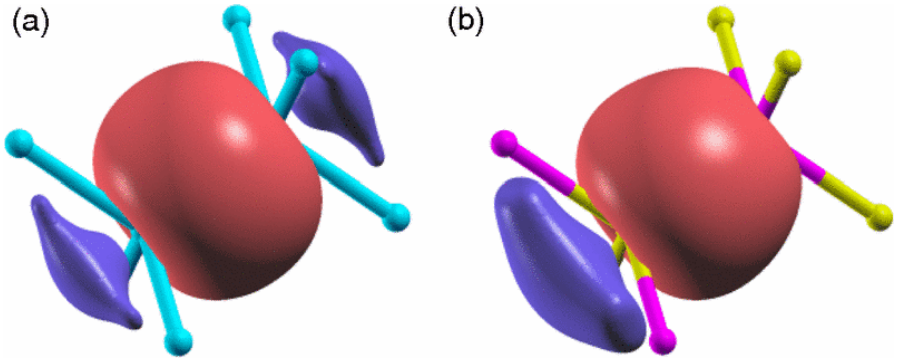

Figure 1.4: Examples of the Maximally Localized Wannier Functions produced from the DFT results for Si (a) and GaAs (b). These MLWFs illustrate the σ-bonded combinations of sp^3 hybrids. The red and blue colors in the isosurfaces represent opposite amplitude values for the real-valued MLWFs. Adapted from [51].

basis for real-space calculations and a valuable tool for interpreting chemical bonding or electronic structure.

The Wannier function with band index n at cell $\mathbf{R}$ is commonly defined as follows:

$$|w_{n\mathbf{R}}\rangle = \frac{V}{(2\pi)^4}\int d^3k e^{-i\mathbf{kR}}|\psi^w_{\mathbf{k}n}\rangle \tag{1.74}$$

The Bloch function, denoted as $|\psi^w_{\mathbf{k}n}\rangle$, can be expressed as a linear combination of the Kohn-Sham wavefunctions

$$|\psi^w_{\mathbf{k}n}\rangle = \sum_m U_{nm}(\mathbf{k})|\psi_{\mathbf{k}m}\rangle \tag{1.75}$$

The Wannier function scheme aims to localize the coefficients $U_{mn}(\mathbf{k})$ to ensure the wavefunctions have a minimal quadratic extent.

$$\Omega = \sum_n \langle w_{n0}|\mathbf{r}^2|w_{n0}\rangle - |\langle w_{n0}|\mathbf{r}|w_{n0}\rangle|^2 \tag{1.76}$$

When the bands are energy-separated, the Wannier orbitals are well-defined and occupy the same Hilbert space as the separated bands. However, when bands are present in the same energy range, an *frozen* energy window is introduced, and $U_{mn}(\mathbf{k})$ is optimized with bounded states within the window. As the frozen energy window increases, the Wannier function becomes more localized as the optimization is performed in a larger Hilbert space. If the band structure is entangled outside the window, an additional entangling procedure can be introduced using the operator $\mathbf{U}^{dis}(\mathbf{k})$

$$|\psi^w_{\mathbf{k}n}\rangle = \sum_m U_{nm}(\mathbf{k})\sum_l U^{dis}_{ml}(\mathbf{k})|\psi_{\mathbf{k}l}\rangle \tag{1.77}$$

which, by rotating the wavefunctions, removes entanglement between the Bloch wavefunctions outside the frozen energy window for bands fixed in the window. A more detailed description of this procedure is presented in the review article.

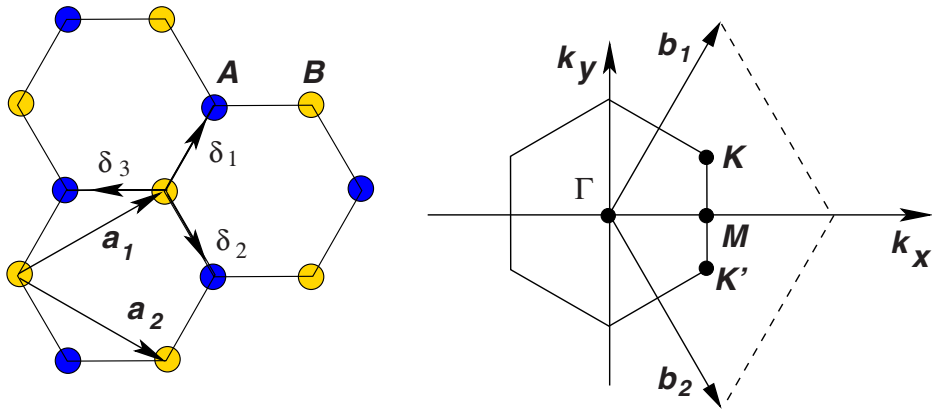

Figure 1.5: Honeycomb lattice and its Brillouin zone. Left: The lattice structure of graphene, made out of two interpenetrating triangular lattices ($\mathbf{a}_1$ and $\mathbf{a}_2$ are the lattice unit vectors, and δ_i, $i = 1, 2, 3$ are the nearest-neighbor vectors). Right: corresponding Brillouin zone. The Dirac cones are at the K and K' points. Adapted from [55].

1.6. Proximity-induced spin-interactions in graphene

In this section, we discuss examples of the applicability of the theory described in previous Chapters. This section describes the properties of graphene, including its band structure and underlying tight-binding Hamiltonian. The tight-binding Hamiltonians are based on the effective p_z orbitals of graphene, which can be influenced by proximity materials such as monolayer transition metal dichalcogenides (TMDCs) or ferromagnets causing modification of the Dirac bands. These modifications can be quantified using a set of parameters that consider spin-orbit and exchange effects. Finally, we briefly overview the predicted proximity-induced spin-orbit and exchange interactions in single- and multilayer graphene with realistic model parameters from density functional theory examples.

1.6.1. Tight-binding model of monolayer graphene

Graphene, a single layer of carbon atoms arranged in a hexagonal lattice, has extraordinary electronic properties and potential applications in nanoelectronics [54, 55, 56, 57, 58, 59, 60]. The tight-binding model offers a computationally efficient approach to understanding and predicting the electronic properties of graphene. However, accurately determining the hopping parameters from first-principles calculations, particularly DFT, is crucial for the model's fidelity. This section discusses the parametrization of the graphene tight-binding model using DFT, ensuring a strong foundation for subsequent investigations and applications.

The band structure and orbital-specific density of states of graphene are shown in Fig. 1.6, calculated using the LDA approach in spinless DFT, obtained using *Quantum Espresso* code [61, 62], applying norm-conserving pseudopotentials and the LDA exchange-

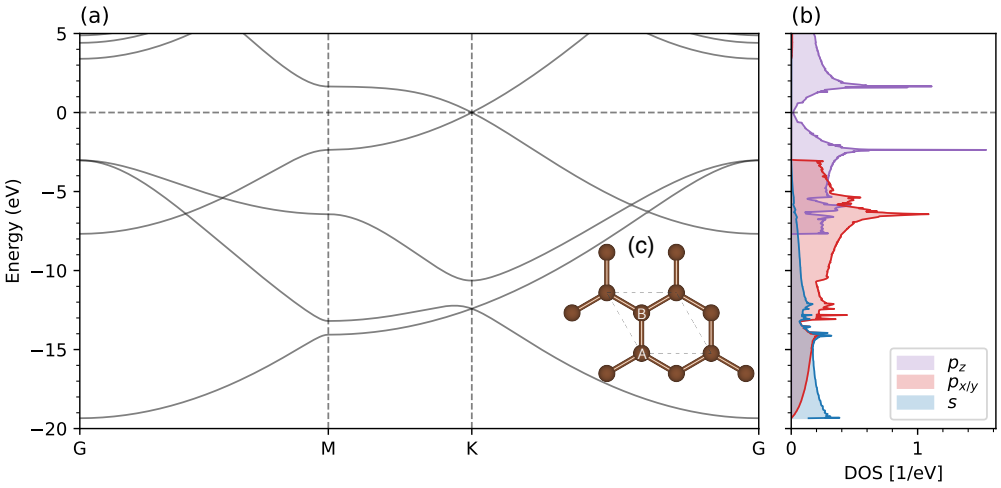

Figure 1.6: Graphene's band structure (a) and orbital-resolved density of states (b) are calculated, along with a top view of its unit cell (c). Zero energy corresponds to the Fermi level.

correlation functional. The s, p_x, and p_y orbitals merge to form sp_2 hybridized covalent σ-bonds in the graphene plane, which endow it with exceptional mechanical resilience. The remaining p_z orbitals, extending from the graphene plane, form π-bands near the Fermi energy and influence graphene electronic and spin transport properties.

At the $\pm K$ points in the Brillouin zone, forming valence and conduction bands intersect at Dirac points. Here, charge carriers behave like massless Dirac fermions with a Fermi velocity of approximately $10^6 m/s$. The simplest tight-binding Hamiltonian, which reproduces Dirac bands near $\pm K$ points in the Brillouin zone, considers only nearest-neighbor hopping and can be written as:

$$\begin{aligned}\hat{H} &= -\gamma_0 \sum_{s,\langle ij\rangle} \left(\hat{c}^{\dagger}_{As}(\mathbf{R}_i)\hat{c}_{Bs}(\mathbf{R}_j) + \hat{c}^{\dagger}_{Bs}(\mathbf{R}_j)\hat{c}_{As}(\mathbf{R}_i)\right) \\ &= -\gamma_0 \sum_{s,i\boldsymbol{\delta}} \left(\hat{c}^{\dagger}_{As}(\mathbf{R}_i)\hat{c}_{Bs}(\mathbf{R}_i+\boldsymbol{\delta}) + \hat{c}^{\dagger}_{Bs}(\mathbf{R}_i+\boldsymbol{\delta})\hat{c}_{is}(\mathbf{R}_i)\right)\end{aligned} \tag{1.78}$$

where $\hat{c}^{\dagger}_{(A/B)s}(\mathbf{R}_i)$ $\left(\hat{c}_{(A/B)s}(\mathbf{R}_i)\right)$ is the creation (annihilation) operator for an electron at sublattice A/B, shown in Fig. 1.5 (c), of spin s, and at unit cell i, γ_0 is the nearest-neighbor hopping amplitude, and $\boldsymbol{\delta}$ is carbon-carbon translation vectors in graphene, represented in Fig.1.5. Sum over $\boldsymbol{\delta}$ is carried out over the nearest-neighbor vectors. We diagonalize the Hamiltonian (1.78). Since graphene has a translation symmetry, we

perform a Fourier transformation:

$$\begin{aligned}\hat{H} =& -\gamma_0 \sum_{s,i\boldsymbol{\delta}} \left(\hat{c}^\dagger_{As}(\mathbf{R}_i)\hat{c}_{Bs}(\mathbf{R}_i+\boldsymbol{\delta}) + \hat{c}^\dagger_{Bs}(\mathbf{R}_i+\boldsymbol{\delta})\hat{c}_{is}(\mathbf{R}_i)\right) \\ =& -\frac{\gamma_0}{N}\sum_{s,i\boldsymbol{\delta}} e^{i\mathbf{k}\boldsymbol{\delta}}\left(\hat{c}^\dagger_{As}(\mathbf{k})\hat{c}_{Bs}(\mathbf{k}) + \hat{c}^\dagger_{Bs}(\mathbf{k})\hat{c}_{As}(\mathbf{k})\right) \end{aligned} \tag{1.79}$$

where $\hat{c}^\dagger_{(A/B)s}(\mathbf{k})\left(\hat{c}_{(A/B)s}(\mathbf{k})\right)$ is the creation (annihilation) operator for an electron at sublattice A/B, with spin s and momentum $\mathbf{k}$. So, if we define

$$\psi_{\mathbf{k}} = (\hat{c}_{A\uparrow}(\mathbf{k})\hat{c}_{A\downarrow}(\mathbf{k})\hat{c}_{B\uparrow}(\mathbf{k})\hat{c}_{B\downarrow}(\mathbf{k}))^T \tag{1.80}$$

we can rewrite Hamiltonian (1.79) as

$$\hat{H} = \sum_{\mathbf{k}} \psi^\dagger_{\mathbf{k}} h(\mathbf{k})\psi_{\mathbf{k}} \tag{1.81}$$

where matrix $h(\mathbf{k})$, also called the Bloch Hamiltonian, takes the form

$$h(\mathbf{k}) = \begin{pmatrix} 0 & \gamma_0 f(\mathbf{k}) \\ \gamma_0 f^*(\mathbf{k}) & 0 \end{pmatrix} \otimes s_0. \tag{1.82}$$

Pauli matrix s_0 is defined in spin basis and equal to identity since we have SU(2) symmetry in Eq.(1.78). For the further derivation, we define the structural function

$$f(\mathbf{k}) = -\sum_{\boldsymbol{\delta}} e^{i\mathbf{k}\boldsymbol{\delta}}. \tag{1.83}$$

Expanding in the Taylor series the structural factor from Eq.(1.83) near $\pm K$ points in the Brillouin zone, we can obtain

$$f(+K+\mathbf{q}) = -\frac{\sqrt{3}a}{2}(q_x + iq_y) \tag{1.84}$$

$$f(-K+\mathbf{q}) = -\frac{\sqrt{3}a}{2}(-q_x + iq_y) \tag{1.85}$$

It is necessary to say that the phase of $f(\mathbf{k})$ carries no physical significance. Near K and K' points in the Brillouin zone, the Hamiltonian (1.82) can be approximated as

$$h(+K+\mathbf{q}) = -\frac{\sqrt{3}a}{2}\gamma_0 \begin{pmatrix} 0 & (-q_x - iq_y) \\ (-q_x + iq_y) & 0 \end{pmatrix} \otimes s_0 \tag{1.86}$$

$$h(-K+\mathbf{q}) = -\frac{\sqrt{3}a}{2}\gamma_0 \begin{pmatrix} 0 & (+q_x - iq_y) \\ (+q_x + iq_y) & 0 \end{pmatrix} \otimes s_0 \tag{1.87}$$

So, we can effectively rewrite Hamiltonians (1.87) as

$$h(\tau K+\mathbf{k}) = v_F\left(\tau k_x\sigma_x - k_y\sigma_y\right) \otimes s_0 \tag{1.88}$$

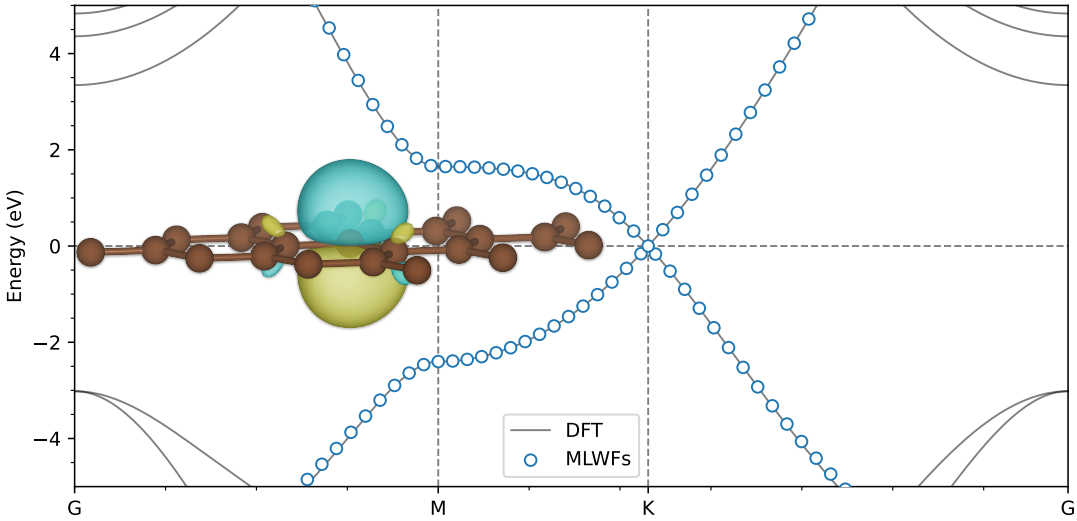

Figure 1.7: MLWF produced from the DFT results for graphene and band structure obtained from DFT and MLWF tight-binding model. This MLWF illustrates the p_z-orbitals. The blue and yellow colors in the isosurfaces represent opposite amplitude values for the real-valued MLWFs. Zero energy corresponds to Fermi level.

where $v_F = \frac{\sqrt{3}a}{2}\gamma_0$ is Fermi velocity, σ_x/y are Pauli matrices defined in sublattice A/B basis and $\tau = \pm 1$ is valley quantum number, which defines the proximity of $\mathbf{q}$ to $+K$ or $-K$ in the Brillouin zone. Eq.(1.88) is 2D massless Dirac Hamiltonian (1.40), where we have v_F instead of c. Thus, we have obtained the famous Dirac Hamiltonian for a graphene monolayer. Diagonalizing Hamiltonian (1.88), we obtain a linear dispersion

$$E(\mathbf{q}) = \pm v_F q \tag{1.89}$$

The Fermi velocity parameter can be estimated by fitting the band structure of graphene from DFT in Fig.1.6 near $\pm K$ points in the Brillouin zone using Eq.(1.89). From DFT calculations, the value of γ_0 usually falls in the range of 2.5 to 3.1 eV [55]. However, this can vary based on the specific DFT functional used and the degree of convergence achieved in the calculations. For the particular graphene's band structure, depicted in Fig.1.6 (a), $\gamma_0 = 2.574$ eV.

1.6.2. Maximally Localized Wannier Functions in Graphene

In this subsection, we will briefly describe the construction procedure on Maximally Localized Wannier Functions in graphene to describe the bandstructure of graphene near the Fermi level. As we have discussed before, the construction of MLWFs involves transforming the Bloch functions, which are delocalized over the entire crystal, into a set of localized functions that span the same subspace. The goal is to obtain a set of Wannier functions that are as localized as possible within the unit cell or a chosen localization region.

Recall, that the Wannier function $w_n(\mathbf{r})$ corresponding to band n can be expressed as [51]:

$$w_n(\mathbf{r}) = \frac{1}{\sqrt{N}} \sum_{\mathbf{k}} e^{-i\mathbf{k}\cdot\mathbf{r}} u_{n\mathbf{k}}(\mathbf{r}) \tag{1.90}$$

where $u_{n\mathbf{k}}(\mathbf{r})$ is the periodic part of the Bloch function obtained by DFT using *Quantum Espresso* package [61, 62], using norm-conserving pseudopotentials and the LDA exchange-correlation functional.

The construction starts with an initial guess for the Wannier functions. For graphene, a natural choice is the atomic orbitals of carbon, specifically the s, p_x, and p_y orbitals that form the sp_2 hybridization and the p_z orbital responsible for π bonding. As shown in Fig.1.6, graphene's band structure near the Fermi level is mainly formed by p_z orbitals. So, a natural choice for the initial guess for MLWFs in graphene to describe band structure near the Fermi level is p_z carbon orbitals [55].

The Bloch functions of graphene are projected onto the trial orbitals, which we choose as p_z carbon orbitals, to obtain the initial Wannier functions. This projection ensures that the Wannier functions are close to the desired atomic-like character.

$$|w_n^{(0)}\rangle = \sum_m |u_{m\mathbf{k}}\rangle\langle\phi_n|u_{m\mathbf{k}}\rangle \tag{1.91}$$

where $|\phi_n\rangle$ represents the trial MLWFs as p_z carbon orbitals. Using the iterative localization procedure, implemented in *Wannier90* package [52, 63], the key step in constructing MLWFs, by minimization of a Wannier function spread Ω defined as

$$\Omega = \langle w_n|\mathbf{r}^2|w_n\rangle - \langle w_n|\mathbf{r}|w_n\rangle^2, \tag{1.92}$$

we obtain the MLWF corresponding to the p_z orbital, localized around each carbon atom but oriented perpendicular to the plane, representing the π bond. Our result for MLWF is presented in Fig.1.7. Based on obtained MLWFs, we obtain all hopping parameters for the Bloch Hamiltonian for graphene

$$t_{ij}^{nm} = \int d^3r w_n^*(\mathbf{r}+\mathbf{R}_i) \left[-\frac{\nabla^2}{2} + V_{KS}(\mathbf{r})\right] w_m(\mathbf{r}+\mathbf{R}_j) \tag{1.93}$$

using Kohn-Sham potential $V_{KS}(\mathbf{r})$, obtained from DFT.

After a Fourier transform of the (1.93) hopping parameters and diagonalization of the resulting Bloch Hamiltonian, we can obtain a band structure based on MLWFs. An example of such a band structure for graphene is presented in Fig.1.7, where we can see that the band structure based on MLWFs describes the results of DFT near the Fermi level. We should note that hopping parameters (1.93) take into account not only the hopping to the nearest neighbors but also the neighbors of the following order, inducing particle-hole asymmetry beyond Fermi level, represented in Fig.1.6. A direct comparison of nearest-neighbor hopping amplitude estimated from MLWFs hopping amplitude obtained from a fitting procedure described in the previous subsection must be corrected.

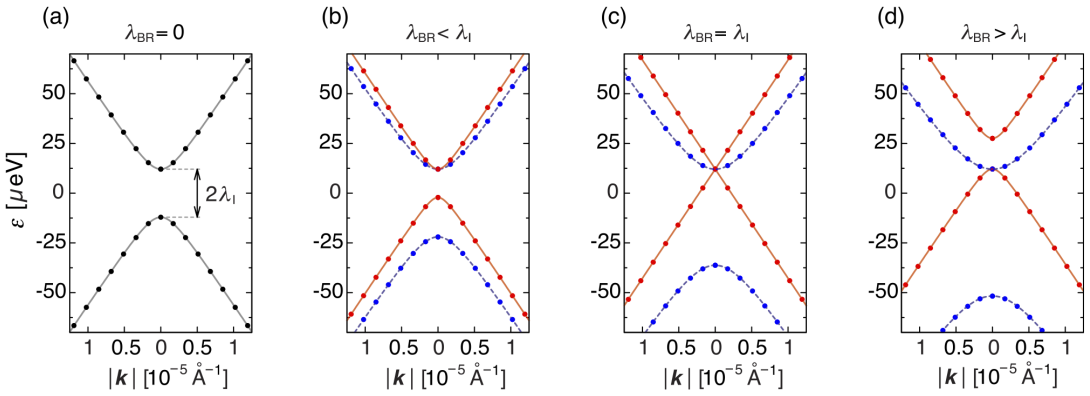

Figure 1.8: Pristine graphene band structure with different electric fields. (a) Without an electric field. (b) Electric field at E=1.0 V/nm. (c) E=2.44 V/nm. (d) E=4.0 V/nm. Circles indicate the first principle's results (with the Fermi level set at zero). Colorcode denotes spin-polarization: red - up, blue - down, while black is an unpolarized case. Adapted from [64].

1.6.3. Proximity-induced spin-orbit and exchange couplings

Graphene, characterized by a two-dimensional honeycomb arrangement of carbon atoms, has excellent electronic, thermal, and mechanical properties. Its unique electron dispersion reflects the behavior of Dirac particles, making it a platform for observing relativistic quantum mechanics in solid-state media [54, 55, 56, 57, 58, 59, 60]. However, its spin-orbit coupling is particularly weak, limiting its usefulness in spintronics [64, 65, 66, 67]. Recent research has deepened the understanding of the proximity effect to enhance the SOC in graphene when it comes into contact with different materials [68, 69, 70, 71, 72, 73, 74, 75, 76, 77].

Every carbon atom inherently possesses SOC, represented by the parameter λ_I^{atom}. In its pristine graphene, SOC only slightly affects the dispersion around the Dirac points $\pm K$, with the following form of intrinsic SOC Hamiltonian [78, 79, 71, 68, 80, 70, 81, 82, 83, 84],

$$h_I = \lambda_I \tau \sigma_z s_z \tag{1.94}$$

The parameter λ_I, consistent across all graphene atoms and approximately 12 μeV [64], leading to a negligible gap of 24 μeV in its spectrum, even though the spin-orbit splitting for pure atomic p states is about 8.74 meV [64]. For pristine graphene, the parameter λ_I is mainly determined by the atomic spin-orbit coupling of carbon p orbitals through hybridization with d orbitals [64], which have significant SOC splitting due to the large orbital number $l = 2$.

Introducing a transverse electric field to the graphene plane slightly breaks the mirror symmetry, inducing Rashba extrinsic SOC, with the following Hamiltonian

$$h_R = \lambda_R \left(\tau \sigma_x s_y - \sigma_y s_x\right) \tag{1.95}$$

characterized by the electric field-dependent parameter $\lambda_R = \kappa V$, where V is amplitude of the electric field and $\kappa = 10\mu$eV nm/V. As a result, pristine graphene band topology can be tuned via an electric field, as shown in Fig.1.8. In the intrinsic case, without an external field, the Dirac cones at $\pm K$ points are split into two cones with a gap of 24 eV(0.28 K). Bands have double degeneracy due to the simultaneous presence of time-reversal and mirror symmetries. However, applying a transverse electric field breaks the spatial inversion symmetry, leading to $2\lambda_{\mathrm{R}}$ spin splitting of energy levels. This type of extrinsic splitting is analogous to the Rashba spin-orbit interaction observed in semiconductor heterostructures.

The problem is to amplify this interaction without undermining graphene's standout features [56]. When graphene is in contact with a material known for its potent SOC, its interface can lead to the hybridization of quantum states of both materials, facilitating the transfer of specific attributes. Transition Metal Dichalcogenides, renowned for their robust intrinsic SOC, emerge as ideal candidates to initiate SOC in graphene through proximity [68, 69]. For instance, graphene on WS_2 displays signs of increased SOC, as evidenced by weak anti-localization in magnetotransport measurements [85]. Likewise, $MoSe_2$ and WSe_2 substrates have yielded encouraging outcomes. DFT simulations suggest that the SOC introduced in graphene layered on TMDs arises from combining graphene's π states with the TMDs' d-orbitals. The nature and strength of the SOC are influenced by the specific TMD chosen and the alignment of their structures [86].

Numerous investigations into the spin-orbit and exchange proximity effects in graphene have the introduction of a Hamiltonian rooted in effective p_z orbitals [78, 79, 71, 68, 80, 70, 84]. This Hamiltonian mirrors that of (1.88), symbolized as $\sigma \otimes s$. Here, σ represents the sublattice domain (A, B), and s signifies the spin domain ($\uparrow$,$\downarrow$), leading to the four foundational states $|\mathrm{A}\uparrow\rangle$, $|\mathrm{A}\downarrow\rangle$, $|\mathrm{B}\uparrow\rangle$, and $|\mathrm{B}\downarrow\rangle$. As established in preceding sections, the low-energy band structure of graphene around the $\pm K$ points in its Brillouin zone can be depicted by the massless Dirac Hamiltonian:

$$h(\mathbf{k}) = v_F \left(\tau k_x \sigma_x - k_y \sigma_y\right) \otimes s_0 \tag{1.96}$$

In this equation, v_F denotes the Fermi velocity, and $\mathbf{k}$ is gauged from $\pm K$, with the associated valley quantum number being $\tau = \pm 1$.

The primary effect of proximity on the massless Dirac Hamiltonian is the distinct effective potentials for sublattices A and B. The Hamiltonian can be represented as:

$$h_\Delta = \Delta \sigma_z \otimes s_0 \tag{1.97}$$

Here, Δ signifies the variance between the sublattice potentials. This component effectively characterizes the mass term from the Dirac Hamiltonian as seen in (1.40). It disrupts the sublattice symmetry and introduces a bandgap in the Dirac cone dispersion. When mass is introduced, graphene has the potential to shift into a topological insulator phase under specific scenarios, showcasing edge states that remain stable despite defects.

When graphene is positioned on a substrate, disrupting its sublattice symmetry, an added spin-orbit coupling can emerge due to the proximity effect. It leads to distinct spin-orbit coupling parameters for each sublattice, denoted as λ_I^A and λ_I^B. The Hamiltonian

can describe this phenomenon:

$$h_I = \tau \left(\lambda_I^A \sigma_+ + \lambda_I^B \sigma_- \right) \otimes s_z \tag{1.98}$$

Here, $\sigma_\pm$ is defined as $\frac{1}{2}(\sigma_z \pm \sigma_0)$. The two most prominent configurations arise from Eq. (1.98): one where $\lambda_I^A \approx \lambda_I^B$ and another where $\lambda_I^A \approx -\lambda_I^B$. The first leads to the Kane-Mele spin-orbit coupling [87], transforming graphene into a phase with quantum spin Hall insulator properties and producing helical edge states resistant to backscattering. The second configuration is termed valley-Zeeman spin-orbit coupling [68, 69]. With this, graphene can support valley-polarized currents, offering a foundation for potential valleytronic devices. This valley-Zeeman effect emerges from the disruption of inversion symmetry and functions differently across the two valleys.

When a substrate is introduced, it can disrupt mirror symmetry, resulting in extra SOC components. It is represented by:

$$h_R = -\lambda_R \left(\tau \sigma_x \otimes s_y + \sigma_y \otimes s_x \right) \tag{1.99}$$

This equation is termed the Rashba SOC Hamiltonian, characterized by the Rashba SOC parameter, λ_R. Disrupting mirror symmetry can also be achieved by applying a gate voltage to a graphene layer. However, this impact is minimal when compared to the proximity effect.

The interaction between Rashba SOC and the unique behavior of electrons in graphene offers a vast potential for spintronics [56, 88, 89, 90, 91, 92]. The Rashba SOC causes an energy zone separation and eliminates spin degeneracy in the band structure. By harnessing and adjusting Rashba SOCs, upcoming devices could utilize both charge and spin, paving the way for quantum computing and data processing advancements.

In situations where mirror symmetry is disrupted, an additional Hamiltonian can be added to the Rashba SOC in graphene:

$$h_{\mathrm{PIA}} = a \left(\lambda_{\mathrm{PIA}}^A \sigma_+ - \lambda_{\mathrm{PIA}}^B \sigma_- \right) \otimes (k_x s_y - k_y s_x) \tag{1.100}$$

It is known as the sublattice-resolved pseudospin inversion asymmetry (PIA) SOC Hamiltonian. It's defined by parameters λ_{PIA}^A and λ_{PIA}^B, which gauge the intensity of the mirror plane asymmery [68, 69]. Nonetheless, the PIA's presence near the valley's center is typically negligible, as its magnitude is tied to $\mathbf{k}$. As a result, this proximity-induced SOC component is frequently excluded from theoretical discussions.

Finally, when graphene is placed on a magnetic insulator, electrons from the Dirac cone experience the magnetic order from the insulator. It breaks time-reversal symmetry, which effectively leads to the following Hamiltonian:

$$h_{ex} = \left(-\lambda_{ex}^A \sigma_+ + \lambda_{ex}^B \sigma_- \right) \otimes s_z \tag{1.101}$$

where λ_{ex}^A and λ_{ex}^B being sublattice-resolved exchange parameters. Several experiments have confirmed the presence of proximity-induced magnetic order in graphene. This

Substrate	γ_0 [eV]	Δ [meV]	λ_R [meV]	λ_I^A [meV]	λ_I^B [meV]
MoS_2	2.668	0.52	0.13	–0.23	0.28
$MoSe_2$	2.526	0.44	0.26	–0.19	0.16
WS_2	2.657	1.31	0.36	–1.02	1.21
WSe_2	2.507	0.54	0.56	–1.22	1.16

Table 1.1: Calculated tight-binding model orbital and spin-orbital parameters for graphene/TMD heterostructures. Adapted from [69].

order can be detected through the non-zero anomalous Hall effect and spatially resolved magnetization maps from spin-polarized scanning tunneling microscopy [93, 72, 73].

Proximity-induced exchange coupling in graphene has garnered significant attention due to its potential in spintronic applications. One of the primary methods to induce this phenomenon is placing graphene close to a magnetic substrate. Ferromagnetic insulators, such as yttrium iron garnet [94], are popular as they induce strong exchange coupling without introducing additional charge carriers. Another promising substrate is chromium triiodide (CrI3) [73, 95], which, when layered with graphene, can lead to the observation of spin-filtered tunneling. Additionally, hexagonal boron nitride (h-BN) layers, when sandwiched between graphene and a magnetic insulator, can enhance the coupling strength [70]. Overall, the choice of substrate plays a pivotal role in determining the strength and nature of the proximity-induced exchange coupling in graphene.

As previously highlighted, TMDs are an excellent substrate for promoting spin-orbit splitting in the Dirac cone. Through applying DFT, norm-conserving pseudopotentials, and the PBE exchange-correlation functional, this study estimated the parameters for proximity-induced spin-orbit coupling in the graphene Dirac cone within graphene/TMD combinations [68, 69]. These findings are tabulated in Table 1.1. The research primarily delves into how proximity effects influence the Dirac cone band structure. A comprehensive analysis of four distinct graphene/TMD heterostructures is depicted in Fig. 1.9. Three main observations emerge [69]:

1. An orbital gap resulting from the effective staggered potential Δ.
2. Band anticrossing due to spin-orbit couplings λ_I^A and λ_I^B.
3. Band spin splittings stemming from spin-orbit interactions and the disruption of inversion symmetry.

Notably, the identified gap and spin-orbit coupling surpass those in pristine graphene. The Rashba SOC effect remains negligible, attributed to the low Rashba SOC parameter amplitude. In conclusion, the research suggests that when graphene is layered on WSe_2, it can manifest half-topological states safeguarded against backscattering on a single edge, along with helical edge states. It implies the potential for graphene on WSe_2 to display the quantum spin Hall effect.

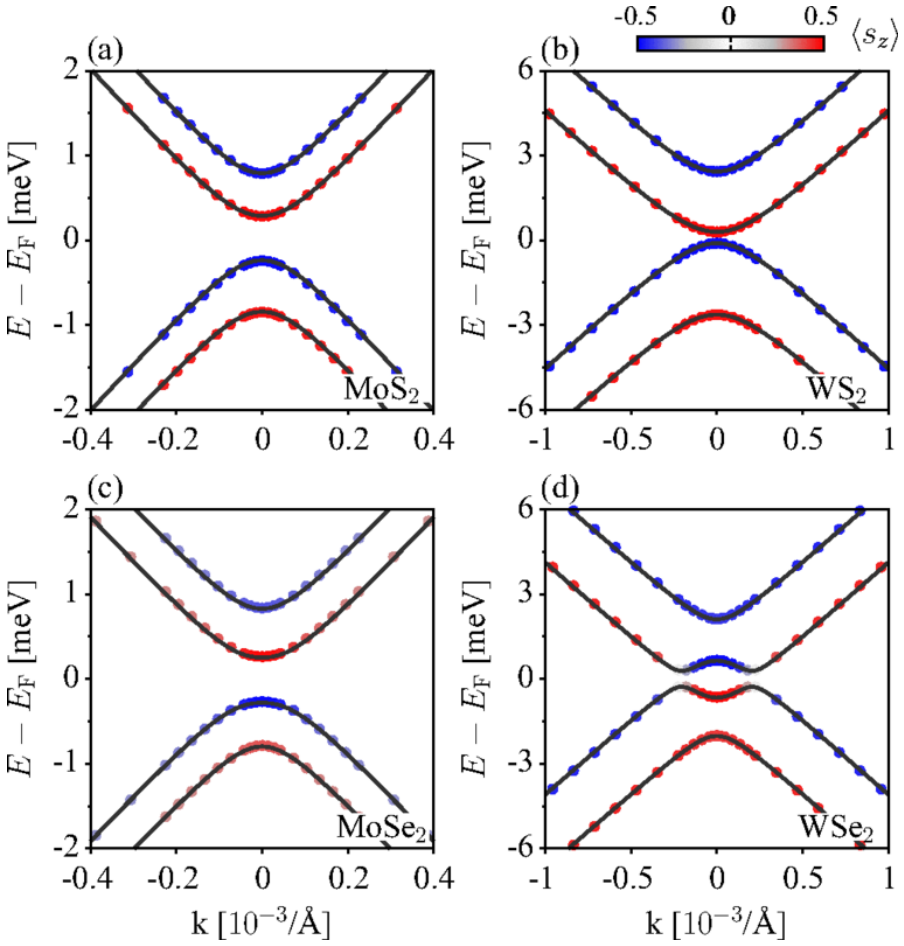

Figure 1.9: Calculated electronic band structures for graphene/TMDC heterostructures near the Dirac point are shown for (a) MoS_2, (b) WS_2, (c) $MoSe_2$, and (d) WSe_2. The solid lines represent model fits, while the circles correspond to first-principles data. The colors indicate the z component of the spin expectation value. Adapted from [69].

2. Edge states in proximitized graphene ribbons and flakes in a perpendicular magnetic field: the emergence of lone pseudohelical pairs and pure spin-current states

2.1. Introduction

Before we delve into the complex study of correlation effects in multilayer graphene systems, it was necessary first to provide insight into the phenomenon of proximity-induced spin-orbit coupling in graphene. To do this, we studied the edge states of graphene ribbons and flakes under a perpendicular magnetic field. Although our original intention was to make this project primarily "educational", its development has exceeded our expectations. The study grew into a full-fledged publication. In this Chapter, we will discuss in detail the methodology we used and the findings of this study.

The manipulation and external control of the electronic structure in two-dimensional materials through the proximity effect have garnered considerable attention in both experimental and technological domains. It is particularly relevant for engineering systems with unique magnetic and spin properties [56, 96, 97]. A case in point is the incorporation of spin interactions into graphene, a material whose Dirac electrons are characterized by weak spin-orbit coupling. One promising approach to achieve this is by bringing graphene into close contact with transition metal dichalcogenides, which leads to spin-orbit couplings at the meV scale [68, 98, 69, 99]. Furthermore, this coupling can be fine-tuned by twisting the materials [100, 101, 102, 103].

The proximity-induced spin-orbit coupling generally depends on the sublattice [80, 78]. However, TMDC substrates introduce valley-Zeeman and Rashba couplings, which result in uniform pseudospin spin-orbit fields that are opposite at the K and K' points [68, 98, 104], which was described in previous Chapter 1. Similar effects have been predicted for graphene when it is placed on Bi_2Se_3-family topological insulators [105, 106], and also for bilayer Jacutingaite [107]. A substantial body of experimental work has already confirmed the existence of valley-Zeeman coupling in graphene subjected to proximity effects [108, 109, 110, 111, 74, 91, 112, 90, 113, 114, 115, 116, 117].

Graphene exhibits two main types of edge states when spin-orbit coupling is present: quantum spin Hall helical edge states and pseudohelical edge states. The discovery of quantum spin Hall effect by Kane-Mele [87] was a consequence of the intrinsic SOC,

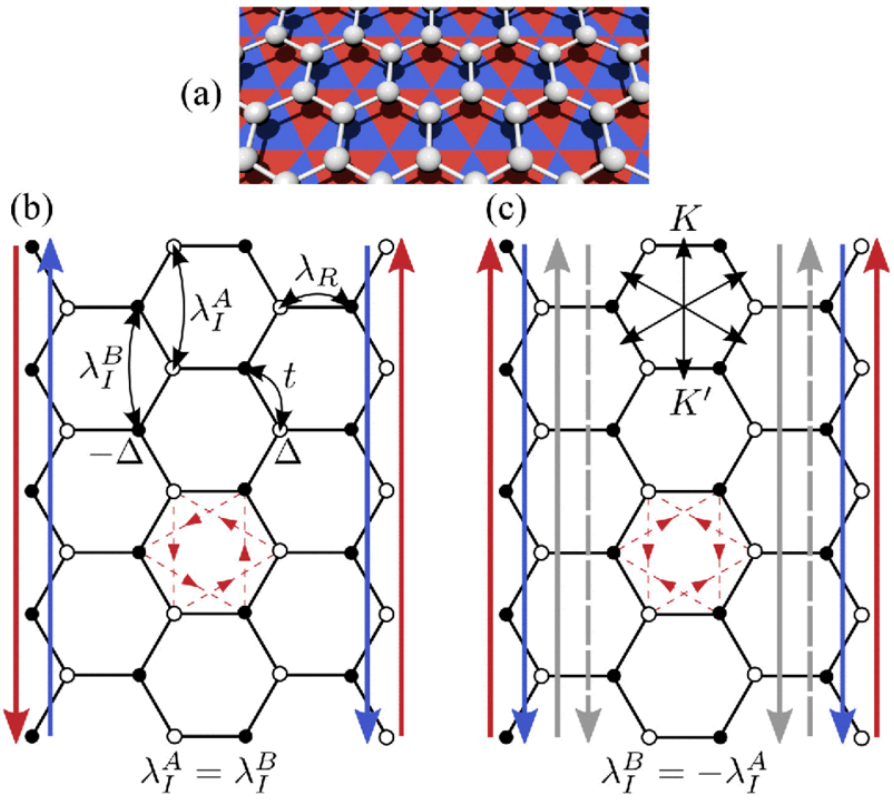

Figure 2.1: Diagram illustrating proximity-induced properties in graphene. (a) Graphene is positioned over a symmetry-breaking substrate. (b) The hopping parameters in the study. Empty dots represent sublattice A, while filled dots denote sublattice B. Spin-up characteristics are shown in red, and spin-down in blue. Dashed red lines highlight spin-up intrinsic SOC hoppings (directions marked by arrows) for a consistent $\lambda_I^A = \lambda_I^B$ within a hexagon. Extended arrows mark helical states and their movement directions. (c) The reciprocal K and K' directions relative to the lattice are displayed. Intrinsic SOC hoppings for staggered intrinsic SOC, $\lambda_I^A = -\lambda_I^B$, are marked by red dashed lines. Solid (dashed) gray arrows point to valley edge states in the $\tau = 1$ (-1) valley. Red and blue arrows depict pseudohelical states with a measurable spin current along the ribbon. Adapted from [118].

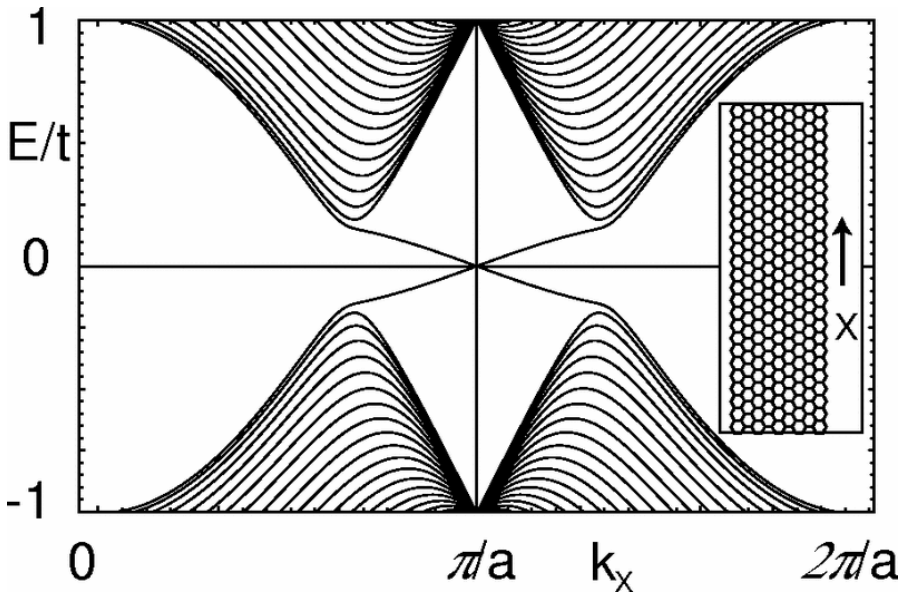

Figure 2.2: Band structure of a one-dimensional graphene nanoribbon in QSHE regime. Adapted from [87].

provided that each sublattice has equivalent intrinsic SOC values (i.e., $\lambda_I^A = \lambda_I^B$). The bulk band structure is gapped in the quantum spin Hall effect (QSHE) regime, while gapless helical states carry spin and charge transport. Figure 2.2 shows the band structure of a one-dimensional graphene nanoribbon in the QSHE regime, and helical states are depicted in Figure 2.1(b). However, their existence has yet to be experimentally confirmed in graphene due to the inherent weakness of the intrinsic coupling [64].

In graphene proximitized to exhibit valley-Zeeman coupling, two edge states emerge within the spin-orbit gap: pseudohelical (intervelley), which are depicted in Figure 2.1(c), and intravalley states [119]. For nanoscale ribbons with widths less than one micron, the intravalley states are eliminated due to confinement-induced hybridization, leaving only a single pseudohelical pair at each edge. These states are fully protected against backscattering by time-reversal defects, much like the helical states observed in the spin quantum Hall effect [87]. Interestingly, robust helical surface states can also be generated through a mechanism very similar to that of pseudohelical states in graphene, as demonstrated in the anisotropic Bernewig-Hughes-Zhang model [120].

The question arises: Can the lone pseudohelical pair be preserved in larger ribbons and flakes where intravalley states are typically present? Our work demonstrates that this can be achieved by applying a perpendicular magnetic field to proximitized graphene. Magnetic effects usually manifest in Zeeman-like effects that create spin imbalance and orbital effects that lead to Landau quantization. Previous studies have explored Zeeman effects in proximitized graphene, revealing phenomena such as the quantum anomalous Hall effect [121] and chiral Majorana modes [122]. The orbital response of helical edge states to magnetic fields has also been investigated [123, 124, 125, 126, 127, 128, 129, 99].

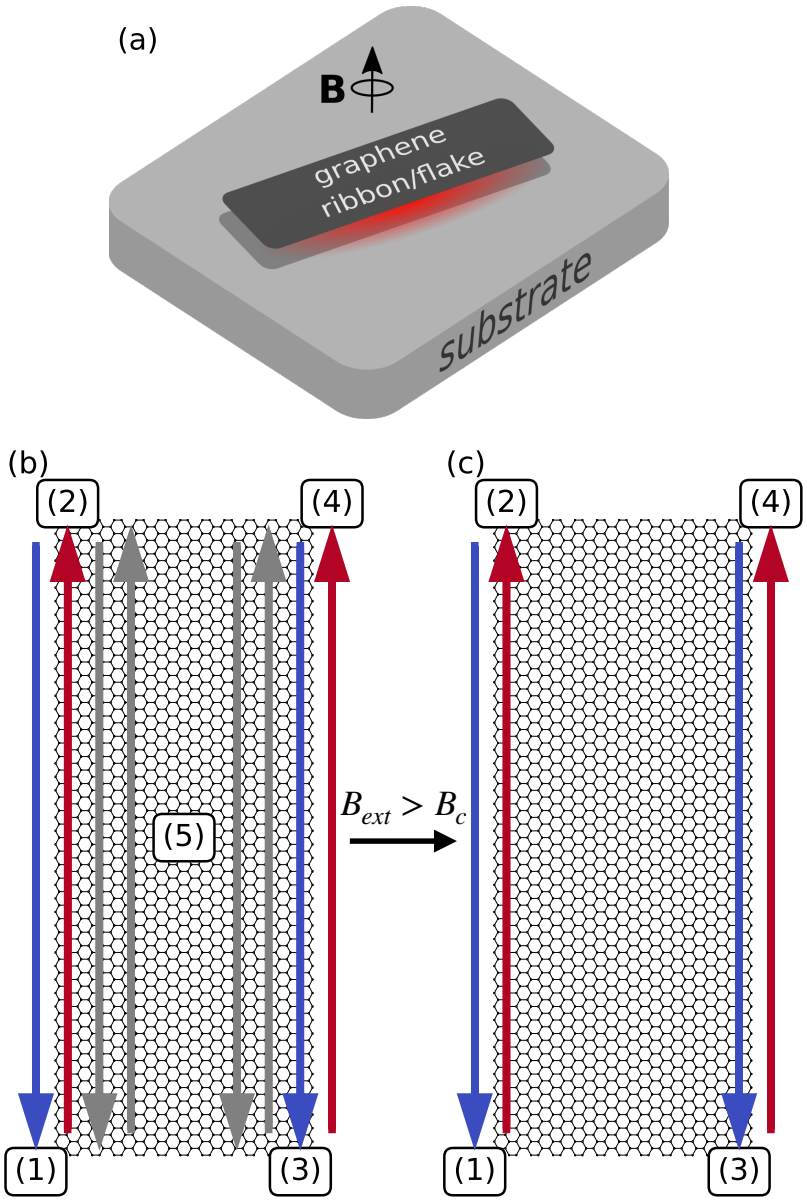

Figure 2.3: (a) Illustration of a graphene strip or fragment positioned on a substrate like a TMDC, generating valley-Zeeman spin-orbit and Rashba coupling effects. A vertical magnetic field influences the orbital conditions of the Dirac electrons. (b) Two categories of edge states proximate to the Fermi level in graphene influenced by valley-Zeeman spin-orbit interactions: (1-4) states with spin polarization and pseudohelical characteristics between valleys, and (5) states within the same valley. (c) Isolated pairs of pseudohelical states that appear beyond the threshold magnetic field.

Surprisingly, the quantum spin Hall edge states, generated by uniform intrinsic (Kane-Mele) spin-orbit coupling, are not necessarily eradicated by the cyclotron effect [130, 131]. However, a crossover between topological and trivial regimes can occur when a perpendicular magnetic field is applied [132, 133].

Our work focuses on the theoretical response of pseudohelical and intravalley edge states in proximitized graphene, specifically using realistic parameters for a graphene/WSe_2 heterostructure to an external perpendicular magnetic field. Using a tight-binding model, supplemented with Peierl's substitution, explores the electronic structure of graphene zigzag nanoribbons and finite flakes. The Landau levels calculated through this approach are in excellent agreement with bulk predictions [124]. The pairs of pseudohelical edge states are preserved even when the magnetic field breaks time-reversal symmetry, similar to the quantum spin Hall effect [130]. However, the intravalley states, originating from Rashba spin-orbit coupling [119], vanish when the magnetic field exceeds a specific critical value B_c. Beyond this point, intravalley edge states merge with the conduction and valence bands, opening an intravalley gap. A lone pair of pseudohelical states is found within this gap at each zigzag edge. Effectively, the magnetic field eliminates the weakly localized intravalley states, mimicking the effects of finite-size confinement [119].

2.2. Model and Methods

Our study focuses on Dirac electrons in graphene that proximity effects with transition metal dichalcogenides or topological insulators have influenced. These proximity effects induce significant spin-orbit interactions on the meV scale, specifically of the valley-Zeeman and Rashba types. We are particularly interested in investigating finite systems such as zigzag ribbons and flakes of graphene.

We employ a tight-binding Hamiltonian to model these systems as described in previous works [69, 78, 134]. The Hamiltonian is given by:

$$\begin{aligned}\hat{\mathcal{H}} = &\sum_{\langle i,j\rangle} t c_{is}^{\dagger} c_{js} + \sum_{i} \xi_i \Delta c_{is}^{\dagger} c_{is} \\ &+ \frac{2i}{3} \sum_{\langle i,j\rangle} \lambda_R c_{is}^{\dagger} c_{js'} \left[(\hat{\mathbf{s}} \times \mathbf{d}_{ij})_z\right]_{ss'} \\ &+ \frac{i}{3} \sum_{\langle\langle i,j\rangle\rangle} \frac{\lambda_I^i}{\sqrt{3}} c_{is}^{\dagger} c_{js} \left[\nu_{ij} \hat{\mathbf{s}}_z\right] \ , \end{aligned} \tag{2.1}$$

In this Hamiltonian, $c_{is}^{\dagger}$ and c_{is} are the creation and annihilation operators for an electron at site i with spin s. The notation $\langle i,j\rangle$ refers to nearest neighbors, while $\langle\langle i,j\rangle\rangle$ refers to next-nearest neighbors.

The Hamiltonian consists of four terms:

1. The first term represents the nearest-neighbor hopping with amplitude t between sites i and j, while preserving the spin.

2. The second term accounts for the staggered potential Δ induced by the proximity effects. The signs ξ_i are $+1$ or -1 for the A and B sublattices, respectively.

3. The third term describes the Rashba spin-orbit coupling with amplitude λ_R [135, 136]. This term breaks the horizontal reflection symmetry and mixes states of opposite spins and sublattices. The symbols $\mathbf{d}_{ij}$ and $\hat{\mathbf{s}}$ denote the unit vector from site j to site i and the vector of spin Pauli matrices, respectively.

4. The fourth term models the valley-Zeeman spin-orbit coupling [68, 98, 125]. This term preserves the spin but varies the intra-sublattice hopping depending on whether the path along a hexagonal ring from the site j to i is clockwise ($\nu_{ij} = -1$) or counterclockwise ($\nu_{ij} = +1$). The intrinsic spin-orbit coupling λ_I^i is generalized for different strengths at the A and B sublattices.

The above-mentioned hoppings are depicted in Fig. 2.1(c).

Additionally, we model the orbital effects of a perpendicular magnetic field using Peierl's substitution [137, 138], which is mathematically represented as:

$$c_j^\dagger \to c_j^\dagger \exp\left(-i\frac{e}{\hbar c}\Lambda(\mathbf{r}_j)\right), \tag{2.2}$$

Here, $\Lambda(\mathbf{r})$ serves as the function that generates the gauge transformation of the vector potential $\mathbf{A}(\mathbf{r})$, such that $\mathbf{A}(\mathbf{r}) \to \mathbf{A}(\mathbf{r}) + \nabla\Lambda(\mathbf{r})$. Upon undergoing a gauge transformation, this term evolves into:

$$\begin{aligned}\hat{\mathcal{H}} &= \sum_{ij} t_{ij} \exp\left(-i\frac{e}{\hbar c}(\Lambda(\mathbf{r}_j) - \Lambda(\mathbf{r}_l))\right) c_i^\dagger c_j + \text{h.c.} \\ &= \sum_{ij} t_{ij} \exp\left(-i\frac{e}{\hbar c}(\int_{\mathbf{r}_i}^{\mathbf{r}_i} d\mathbf{r}' \cdot \mathbf{A}(\mathbf{r}')\right) c_i^\dagger c_j + \text{h.c.}\end{aligned} \tag{2.3}$$

This equation is commonly referred to as the Peierls substitution in lattice models. We do not consider the Zeeman effects of the magnetic field as they are negligible for the fields we are interested in, which are on the militesla scale.

The subsequent sections present numerical results that rely on parameters obtained from first-principles calculations specific to the graphene/WSe_2 system. These parameters are taken from the work of Gmitra et al. [69]. They include the nearest-neighbor hopping parameter $t = -2.507$ eV, the staggered potential $\Delta = 0.56$ meV, the Rashba spin-orbit coupling parameter $\lambda_R = 0.54$ meV, and the intrinsic SOC parameters $\lambda_I^A = 1.22$ meV and $\lambda_I^B = -1.16$ meV.

For the computational implementation, we utilize the Python-based numerical package KWANT to calculate the band structure of zigzag nanoribbons and the electronic states of a graphene flake with proximity-induced spin-orbit interaction [46].

2.2.1. Scalling technique

Our study focuses on micron-sized systems where magnetic orbital effects remain significant and intravalley edge states are not eliminated. The spin-orbit parameters are in the meV range, so the systems under consideration must be large enough to resolve these energy scales in their subband structures. We use a scaling technique described by Liu et al. [139] to overcome the computational challenges associated with large structures. This approach allows us to investigate smaller systems with appropriately rescaled parameters.

The finite-size level spacings in graphene ribbons are approximately given by $\Delta E \approx \pi\hbar v_F/w$, as indicated in [140]. It can be reduced by modifying the Fermi velocity v_F through rescaling the nearest-neighbor hopping parameter

$$\tilde{t} = t/s_f, \tag{2.4}$$

where s_f is the scaling factor. Such rescaling also necessitates a corresponding adjustment in the lattice constant a, mapped to

$$\tilde{a} = s_f a, \tag{2.5}$$

to maintain an invariant energy spectrum. Significantly, this scaling trick does not affect the Rashba and Zeeman spin-orbit terms, as these terms are independent of the lattice constant a or Fermi velocity v_F in the $k \cdot p$ theory near K/K' valleys [118]. Utilizing the Fourier transform methodology along with the linearization of the Hamiltonian, as described in Eq. (2.1), we can derive an effective $k \cdot p$ Hamiltonian in the vicinity of the K and K' points [119]. The Hamiltonian can be expressed as a sum of four components:

$$\hat{\mathcal{H}} = \hat{\mathcal{H}}_k + \hat{\mathcal{H}}_\Delta + \hat{\mathcal{H}}_R + \hat{\mathcal{H}}_I, \tag{2.6}$$

$$\hat{\mathcal{H}}_k = \frac{3}{2} ta \left(\tau k_x \hat{\sigma}_x - k_y \hat{\sigma}_y\right) \hat{s}_0, \tag{2.7}$$

$$\hat{\mathcal{H}}_\Delta = \Delta \hat{\sigma}_z \hat{s}_0, \tag{2.8}$$

$$\hat{\mathcal{H}}_R = \lambda_R \left(-\tau \hat{\sigma}_x \hat{s}_y + \hat{\sigma}_y \hat{s}_x\right), \tag{2.9}$$

$$\hat{\mathcal{H}}_I = \frac{1}{2}\left[\lambda_I^A \left(\hat{\sigma}_z + \hat{\sigma}_0\right) + \lambda_I^B \left(\hat{\sigma}_z - \hat{\sigma}_0\right)\right] \tau \hat{s}_z, \tag{2.10}$$

where $\tau = \pm 1$ denotes the valley index and a represents the lattice site spacing. The Pauli matrices $\hat{\sigma}$ describe the sublattice degrees of freedom. Scaling affects only the $\hat{\mathcal{H}}_k$ term in Eq.Z(2.7), while leaving it invariant:

$$\begin{aligned} \hat{\mathcal{H}}_k =& \frac{3}{2} \tilde{t}\tilde{a} \left(\kappa k_x \hat{\sigma}_x - k_y \hat{\sigma}_y\right) \hat{s}_0 \\ =& \frac{3}{2} ta \left(\tau k_x \hat{\sigma}_x - k_y \hat{\sigma}_y\right) \hat{s}_0 \end{aligned} \tag{2.11}$$

Scaling does not affect the remaining components of the Hamiltonian, as described in Eq. (2.6).

Our calculations reveal that the intravalley states remain unchanged for s_f up to 600. It suggests that the criterion $s_f \ll 3t\pi/E_{\max}$ from Ref. [139] may be too lenient when the

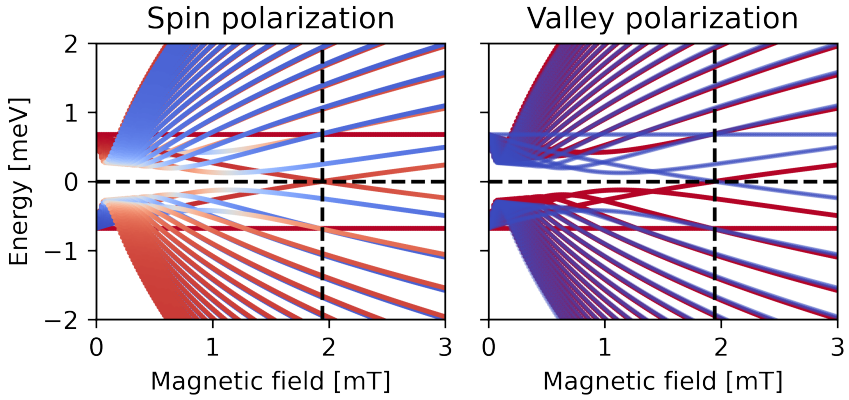

Figure 2.4: Calculated evolution of the bulk Landau levels in graphene/WSe_2 with increasing the external magnetic field. The crossover magnetic field is indicated as a dashed line. The color code corresponds to the s_z expectation value in the left column and the τ_z (valley) expectation value in the right column.

spin-orbit coupling is considered. Additionally, we observe that the Dirac cone broadens as s_f increases. It is because the momentum is expressed in units of $\pi/\tilde{a}$, which varies with s_f. Notably, the finite-size quantization in the subband structure is consistent across different scaling factors, and the intravalley states maintain the same velocities. The intervalley states are also well-preserved, although their velocities change linearly with s_f.

The cyclotron energy in graphene is expressed as $\hbar\omega_c = \sqrt{2e\hbar B}v_F$. We also rescale the external perpendicular magnetic field B to $B \to Bs_f^2$ to preserve this energy scale. This rescaling remains physically meaningful if we focus on low-energy states where the linear dispersion is applicable [139]. The scaling technique enables us to maintain the cyclotron energy scale near the SOC parameters while substantially reducing the computational resources needed for simulating large systems. The primary criterion for selecting the scaling factor s_f is $s_f \ll 3t\pi/E_{\max}$, where $E_{\max}$ is the maximum energy of interest [139]. Our study aims to resolve energies up to $E_{\max} = 2$ meV, which adequately covers the spin-orbit gap region where edge states form. Accordingly, we choose $s_f = 400$, which minimizes the finite-size effects to 0.05 meV for a system width comprising 400 unit cells. The magnetic field strength corresponding to this energy scale is approximately 10^{-5} T.

2.3. Results

2.3.1. Bulk results

The initial step in understanding the behavior of edge states in proximitized graphene subjected to an external magnetic field oriented perpendicularly to the plane involves investigating the Landau levels in the bulk of the material. It is a crucial aspect, as

the Landau levels provide insights into the electronic structure of the system in the presence of a magnetic field. A comprehensive derivation of the Hamiltonian governing these Landau levels in bulk proximitized graphene has been thoroughly discussed in the literature, specifically in Ref. [124]. It is worth noting that graphene with spin-orbit coupling in magnetic fields has also been explored from various angles by multiple research groups [141, 127]. To visualize the behavior of Landau levels, we construct what is known as a Landau fan diagram, as depicted in Fig. 2.4. When we compare this with the Kane-Mele model for graphene [87, 130], we find that a staggered intrinsic SOC fails to maintain a gap when an external magnetic field is applied. In the bulk of proximitized graphene, the band gap predominantly forms between the nonzero Landau levels originating from the K and K' valleys. Interestingly, this gap can be modulated by varying the strength of the magnetic field. In contrast, the Kane-Mele model's bulk band gap is stable and forms between the zero Landau levels even when an external magnetic field is present.

For systems that incorporate valley-Zeeman spin-orbit coupling, the bulk band gap undergoes a transition: it closes and subsequently reopens when the external magnetic field reaches a specific crossover value, as given by the equation [124]

$$B_c = \frac{\left[\lambda_I^A - \lambda_I^B - 2\Delta\right]\left[\left(\Delta + \lambda_I^A\right)\left(\Delta - \lambda_I^B\right) + 4\lambda_R^2\right]}{2e\hbar v_F^2\left[2\Delta + \lambda_I^A - \lambda_I^B\right]}. \tag{2.12}$$

Utilizing the parameter set outlined in Ref. [68, 119] for our Hamiltonian, denoted by Eq. (2.1), we find that the crossover magnetic field value for the graphene/WSe_2 heterostructure is precisely 1.942 mT. This crossover point serves as a demarcation between two distinct regimes. Below this field strength, the bulk band gap is formed by differing nonzero Landau levels. Above this field, however, the first Landau levels define the bulk band gap.

2.3.2. Zigzag ribbon results

The electronic band structure of zigzag graphene ribbons is systematically analyzed under varying magnitudes of an externally applied magnetic field that is oriented perpendicular to the ribbon plane. Specifically, we focus on ribbons with a width of 4.1 μm. Utilizing scaling factor $s_f = 400$, the computational domain of the ribbon is effectively reduced to encompass 72 carbon-carbon bonds, thereby making the simulation computationally tractable. Figure 2.5 presents the computed band structure for three distinct magnetic field strengths: 0 mT, 1.5 mT, and 3.0 mT. At a null magnetic field, the zigzag ribbon exhibits two categories of edge states: the spin-unpolarized intravalley states and the pseudohelical intervalley states that show strong spin polarization [119, 69]. Notably, the intravalley edge states are more spatially extended into the bulk than the intervalley states, a phenomenon attributed to their spectral closeness to the bulk states.

For comparative analysis with the bulk graphene properties [124], the Landau levels at the K and K' valleys are also plotted. At low magnetic field strengths, specifically 1.5 mT, the formation of Landau levels becomes evident, and the bands at the K and K'

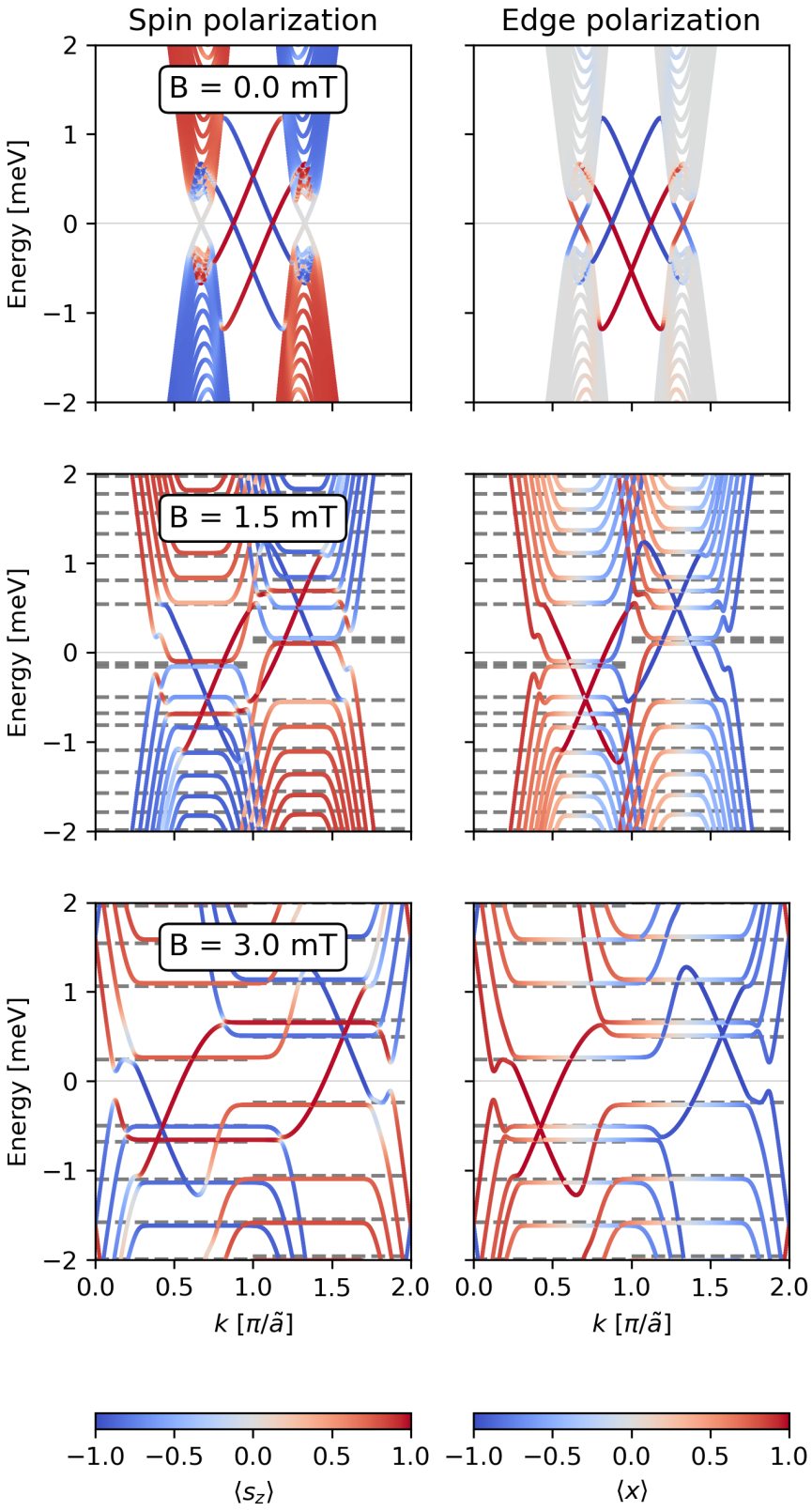

Figure 2.5: Calculated band structures for a zigzag ribbon with a perpendicular magnetic field at $B = 0$ mT (a), $B = 1.5$ mT (b), and $B = 3$ mT (c). The color scheme represents spin polarization on the left and edge polarization on the right. Dashed lines mark the bulk Landau levels.

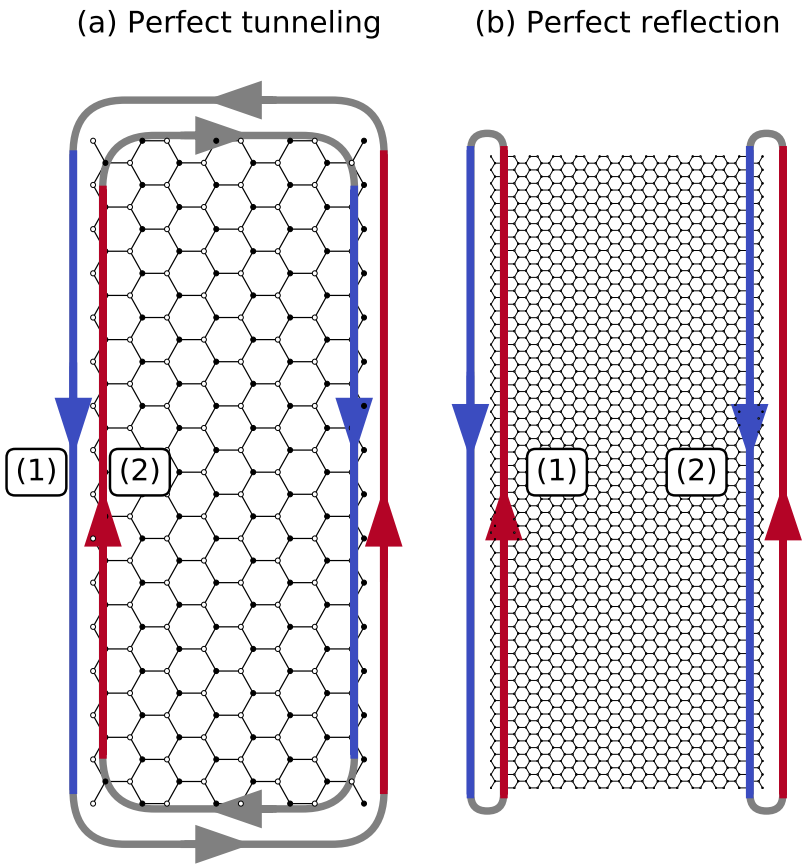

Figure 2.6: (a) Diagram illustrating pseudohelical states in a graphene flake enhanced by proximity effects. These states originate at zigzag edges and move toward the armchair edges, where they experience tunneling and spin inversion due to Rashba coupling. The colors indicate the spin orientation orthogonal to the graphene layer. Tunneling is flawless along the armchair edges when the magnetic field is zero. (b) In larger flakes where $B > B_c$, the opposing pseudohelical edge states are fully reflected at the armchair edges, forming a stationary, non-moving wave. This wave carries a net spin current but lacks a charge current, resulting in a spin-unpolarized state. Refer to Fig. 2.3(c) for additional details.

valleys exhibit a loss of dispersion. These Landau levels exhibit predominantly bulk-like characteristics, as evidenced by the lack of edge polarization. This observation agrees with analytical predictions [124], thereby validating the scaling approach employed in our simulations. At the extremities of the bulk energy continuum, edge states begin to emerge, which are instrumental in the manifestation of the quantum Hall effect in graphene. As the external magnetic field's magnitude increases, the intervalley edge states shift in k-space. Specifically, states with identical spin polarization shift coherently in one direction, while states with opposite spin polarization shift in the opposite direction. In general, the intervalley edge states remain relatively unaffected by the variations in the perpendicular magnetic field.

Conversely, the intravalley states undergo significant modifications, eventually merging with the bulk bands at magnetic fields below 1.5 mT. This behavior is analogous to the predictions for 2D topological insulators subjected to a magnetic field [133]. A bulk energy gap opens at a crossover magnetic field value of $B_c \approx 1.942\,\mathrm{mT}$. Consequently, the intravalley edge states vanish, leaving only the pseudohelical edge states, with one pair at each zigzag edge of the ribbon.

2.3.3. Flake results

To investigate the properties of edge states, we conducted computational analyses on low-energy states of graphene flakes with different sizes. In a zero magnetic field scenario, pseudohelical states appear at the zigzag edges and reflect into intravalley states. This reflection leads to the formation of standing waves that are distributed throughout the flake. For nanoribbons with dimensions smaller than a micron, the intravalley states become energetically gapped, allowing the pseudohelical states to tunnel through the armchair edges and propagate freely along the edges of the flake.

We extended our study to consider the behavior of these states under a magnetic field more significant than a critical value $B > B_c$. In such conditions, the intravalley states in wide ribbons are also gapped. One may question whether the pseudohelical states exhibit similar behavior to those in nanoribbons under these circumstances. Our results indicate that this is not the case. Unlike the zero magnetic field condition, where pseudohelical states are prohibited from reflecting at the armchair edges due to time-reversal symmetry (as the pseudohelical pair is composed of time-reversal partners), introducing a magnetic field enables such reflection. Remarkably, this reflection is perfect, resulting in the localization of the pseudohelical pair at the zigzag edges and the emergence of standing waves that exclusively carry spin currents. The fundamental distinction between propagating pseudohelical edge states and non-propagating states carrying pure spin current is illustrated in Figure 2.6.

In our research, we adopt the following definition for current J:

$$J_{ab} = i\left(\psi_b^\dagger H_{ab}^\dagger \hat{M} \psi_a - \psi_a^\dagger \hat{M} H_{ab} \psi_b\right), \tag{2.13}$$

where ψ denotes the wavefunction, H_{ab} is the hopping matrix facilitating the transition from site b to site a, and $\hat{M}$ is the density operator. Specifically, $\hat{M}$ is equal to $\hat{s}_0$ for charge current and $\hat{s}_z$ for spin current.

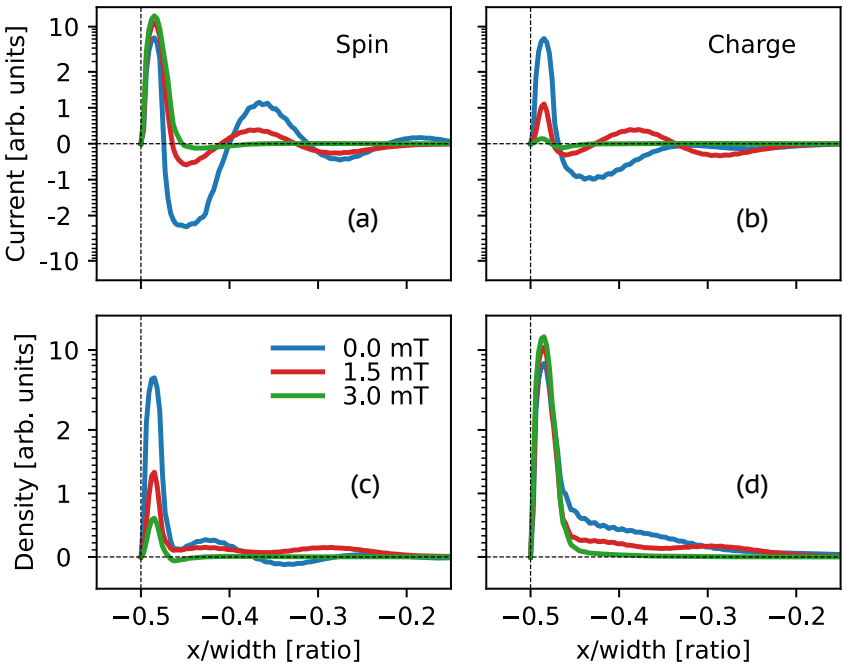

Figure 2.7: Calculated spin (a) and charge (b) currents of the highest occupied flake states (see text for flake parameters) through the cut in the middle of the flake and the presence of a perpendicular magnetic field. Spin (c) and charge (d) densities of the highest occupied state at the cut in the middle of the flake and in the presence of a magnetic field.

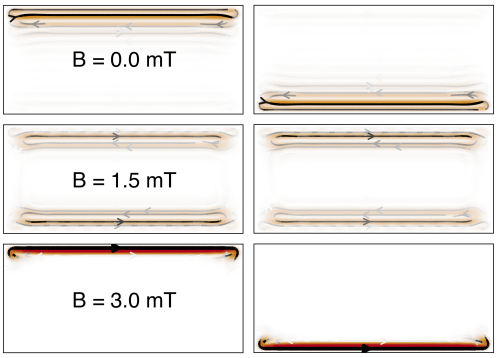

(a) Evolution of the spin current of the highest occupied flake state in the left column and of the lowest unoccupied flake state in the right column. The color bar corresponds to the value of the spin current and is normalized to the maximum value of the spin current.

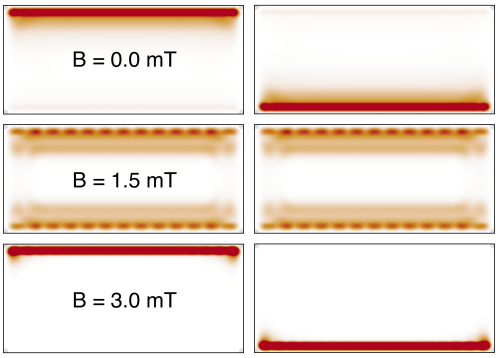

(b) Evolution of the charge density of the highest occupied flake state in the left column and the lowest unoccupied flake state in the right column. The color bar corresponds to the charge density value and is normalized to the maximum charge density value.

Figure 2.8: Magnetic field evolution of pure spin current edge states.

The formation mechanisms for graphene flakes' pseudohelical and pure spin current states are fundamentally different yet intriguing. Pseudohelical states arise due to the perfect tunneling of intervalley states across the armchair edge of the graphene flake. In contrast, pure spin current states are formed through an ideal reflection mechanism of the armchair edge. This distinction in the formation mechanisms is attributed to the exponential decay in the probability of tunneling between zigzag edges as the distance between them increases [119]. It is important to note that transitioning continuously from pseudohelical states to pure spin current states is not feasible due to the periodic opening and closing of the subband gap. Nevertheless, pseudohelical states are more prevalent in narrow graphene flakes, while pure spin current states dominate in wider flakes. These represent two distinct physical regimes.

To quantify the transition between these states, we introduce the typical spin-flip length l_R for the Rashba spin-orbit interaction, given by

$$l_R \approx 3a\frac{t}{\lambda_R}. \tag{2.14}$$

For the specific case of graphene coupled with WSe_2, we find l_R to be approximately 3.4 μm, smaller than the flake width considered in our study. Both pseudohelical and pure spin current states are constructed from combinations of intervalley states. Specifically, they consist of states (1) and (2) at the left edge and states (3) and (4) at the right edge, as illustrated in Fig. 2.3(c). The critical difference lies in the mechanism by which these states are combined. We researched the behavior of pure spin current states in a graphene flake with dimensions of 16.3584 $\mu m \times 4.0896$ μm, scaled by a factor of $r = 400$, which corresponds to an auxiliary flake with 288×72 carbon-carbon bonds. The perfect

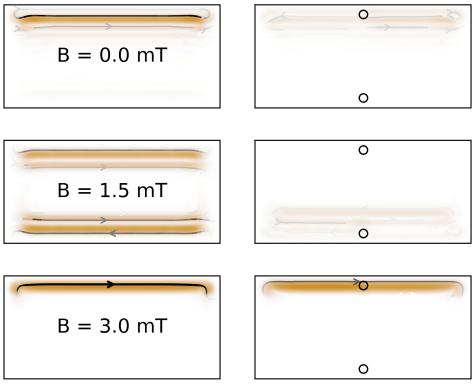

(a) Evolution of the spin current of the highest occupied flake state without defects in the left column and with two defects on zigzag edges in the right column. Spin current in the pure spin current regime is stable under the influence of the internal scatters.

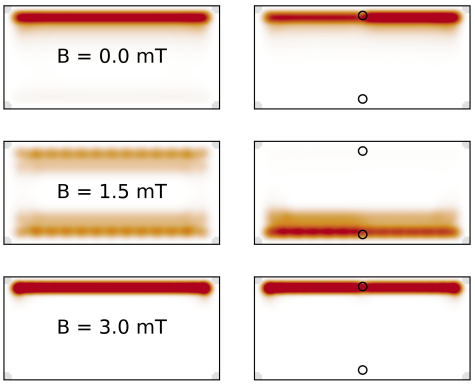

(b) Evolution of the charge density of the highest occupied flake state without defects on the left column and with two defects on zigzag edges on the right column. Charge density in the pure spin current regime is stable under the influence of the internal scatters.

Figure 2.9: Resilience of pure spin current edge states to internal scatterers. Edge defects are represented as circles.

reflection mechanism is the dominant factor in this scenario, given that the flake width exceeds the Rashba spin-flip length. We also analyzed the spin and charge currents and densities in the center of the flake, perpendicular to the zigzag direction, as shown in Fig. 2.7. Our findings suggest that charge current and spin densities disappear as the external magnetic field increases, resulting in complete edge localization. Additionally, the highest occupied states switch to pure spin current states with minimal spin density. The same trend is observed for the lowest unoccupied states.

Fig. 2.8a illustrates the evolution of spin currents for these states. The highest occupied and lowest unoccupied states exhibit similar spin current behaviors but are on opposite zigzag edges. Pure spin currents emerge when the external magnetic field exceeds a crossover value of B_c. Below this value, the states closest to the Fermi level are a complex mixture of strongly localized intervalley states and weakly localized intravalley states. These form a standing wave at the zigzag boundary, as tunneling through the armchair edge is prohibited, supported by gapped ribbon armchair band structures [119]. Our analysis indicates that when exposed to a magnetic field exceeding a specific threshold, identified as B_c, distinct states emerge, characterized by a significant pure spin current. These states mainly localize along a single edge of the graphene structure. Upon inspecting the band structure of a zigzag ribbon configuration, it becomes apparent that these pure spin current states are formed by combining intervalley edge states that reside on the same edge of the ribbon. Remarkably, the stability of these states persists even when a magnetic field is applied. This behavior is comparable to pseudohelical states, known for

their resilience against scattering due to defects. Specifically, in the case of pure spin current states, they demonstrate resistance against scattering events that could happen at the zigzag edge of the graphene flake.

We evaluate the spin current and charge density to demonstrate the resilience of pure spin current states when subjected to internal scatterers, considering two defects on the zigzag edges of a proximitized graphene flake. The results are depicted in Figures 2.9a and 2.9b. When the magnetic field exceeds the crossover value B_c, the spin current and charge density remain stable, even after introducing internal defects by removing a lattice site.

2.4. Conclusion

In our study, we explored the complex behavior of the electronic structure in graphene ribbons and flakes when exposed to a perpendicular magnetic field. We focused on graphene/WSe_2 heterostructures, predicted to exhibit pseudohelical states [118]. Our observations indicate that the magnetic field uniquely impacts these states. Specifically, the pseudohelical edge states are preserved, while the intravalley edge states disappear when the magnetic field reaches a critical value, denoted as $B_c \approx 1.9$ mT. This critical value is noteworthy as it signifies where the gap between the bulk Landau levels closes and reopens. We further extended our analysis to finite flakes of graphene with micron dimensions. Our findings reveal an intriguing phenomenon: rather than the pseudohelical states perfectly tunneling through the armchair edges at zero magnetic fields, and they reflect their counterpropagating partners when $B > B_c$. This reflection leads to the formation of non-propagating, spin-unpolarized pure spin current states. Remarkably, these states exhibit strong Resilience against scattering from zigzag edge defects. Our research implies that these pure spin currents should be observable in wide graphene flakes with dimensions of at least a few microns, particularly in graphene/TMDC heterostructures. These states can be detected even under relatively weak magnetic fields, on the order of a few milliteslas. Additionally, lone pseudohelical pairs can be observed in wide ribbons when $B > B_c$ or nanosized flakes where perfect tunneling through armchair edges is feasible and intravalley states are gapped even without a magnetic field.

3. Many-body pertrubation theory

3.1. Introduction

Our primary objective was to examine the behavior of many-body physics in multilayer graphene systems, focusing on their interplay with spin interactions due to the proximity effect. Although we have previously explored spin Hamiltonians resulting from the proximity effect, our exploration of many-body theory has been limited, mainly through DFT. While DFT is practical, it needs improvement in exploring the impact of strong correlations. To gain a comprehensive understanding, we must expand our theoretical horizons to include methods that can accurately explain strong electronic correlations. Many-body perturbation theory using Green's functions becomes a reliable and widespread method in this context.

The upcoming Chapter will examine the one-particle and two-particle Green's functions, highlighting their primary characteristics. These mathematical foundations are necessary for interpreting the many physical properties present in any system, including the spectral, mechanical, and thermodynamic domains.

For example, the single-particle Green's function is crucial in examining the spectral function, which can supply information about photoemission spectroscopy. It encompasses the excitation spectrum of individual particles within a system. It provides insight into phenomena such as renormalization and its impact on attributes such as the effective mass of electrons. A thorough understanding of the single-particle Green's function is vital in accurately predicting single-particle observables in a system, including aspects such as density, spin, and more.

Additionally, the importance of two-particle Green's functions must be considered. They play a crucial role in determining the linear response of the system to external disturbances caused by electric and magnetic fields or even pressure changes. A detailed understanding of two-particle Green's functions allows us to predict the system's response to these subtle external stimuli.

In summary, one- and two-particle Green's functions are essential in understanding and predicting many physical properties within a system. Their research is academically relevant for physical experiments and observations. This Chapter will provide readers with essential theoretical tools, including one-particle and two-particle perturbation theories, and provide a theoretical foundation for the following Chapters 4 and 5. These tools will enable a more profound analysis of interplay correlated phenomena with spin interactions, especially in the context of proximity effects in multilayer graphene systems.

3.2. Single-particle Green's function

Let us delve into many-body perturbation theory by examining Green's functions, characteristics, and practical uses. All discussions in this section are based on various resources and textbooks[142, 143, 144, 145]. Robert Eder's talk "Green's functions and self-energy functionals" [146] has substantially influenced this section.

We will consider a model of interacting electrons in a complete set of single electron states ϕ_a, where a represents the full single-particle quantum numbers such as unit cell, orbital number, and z-component of spin. By introducing creation $\hat{c}_{\bar{a}}^{\dagger}$ and annihilation $\hat{c}_a$ operators for electron states ϕ_a, we can rewrite the Hamiltonian of the interacting electron system.

$$\hat{H} = \hat{H}_{kin} + \hat{H}_{int} \tag{3.1}$$

where

$$\hat{H}_{kin} = \sum_{a\bar{b}} t_{\bar{a}b} \hat{c}_{\bar{a}}^{\dagger} \hat{c}_{\bar{b}} \tag{3.2}$$

and

$$\hat{H}_{int} = \frac{1}{2} \sum_{\bar{a}\bar{b}cd} V_{\bar{a}\bar{b}cd} \hat{c}_{\bar{a}}^{\dagger} \hat{c}_{\bar{b}}^{\dagger} \hat{c}_c \hat{c}_d \tag{3.3}$$

The matrix elements in this Hamiltonian were discussed in Chapter 1 and defined as

$$t_{\bar{a}b} = \int dx \phi_{\bar{a}}^*(x) \left[-\frac{\nabla^2}{2} + V(x) \right] \phi_b(x) \tag{3.4}$$

and

$$V_{\bar{a}\bar{b}cd} = \int dx \int dx' \phi_{\bar{a}}^*(r) \phi_d(r) V(r - r') \phi_{\bar{b}}^*(r') \phi_c(r') \tag{3.5}$$

The thermal average of any operator $\hat{O}$ defined as

$$\langle \hat{O} \rangle = \frac{1}{Z} \mathrm{Tr} \left(e^{-\beta(\hat{H} - \mu\hat{N})} \hat{O} \right) \tag{3.6}$$

where $\beta = 1/k_B T$ is inverse temperature, μ is a chemical potential and $\hat{N}$ is the operator for the number of electrons. The grand partition function is defined as

$$Z = \mathrm{Tr} \left(e^{-\beta(\hat{H} - \mu\hat{N})} \right) \tag{3.7}$$

We continue our discussion by introducing Green's functions [143, 142, 145], which are used to model hypothetical scenarios where a system is initially in thermal equilibrium. At a specified time t, an operator called $\hat{A}$ intervenes in the system by creating or destroying an electron, inverting a spin, or performing a similar operation. After some time, the modification is canceled using another operator, $\hat{B}$, which is often the complex conjugate of $\hat{A}$. We then calculate the overlap with the state if the system had evolved unperturbed. Green's function essentially characterizes how the disturbance created by $\hat{A}$ moves from time t to t' before $\hat{B}$ is eliminated.

To better understand this concept, we discuss Green's functions in imaginary time ($\tau = it$) [147, 143, 142, 145]. Specifically, we will focus on the single-particle Green's function, where the disturbance involves either the removal or addition of a particle represented by $\hat{A} = \hat{c}_a$ and $\hat{B} = \hat{c}_{\bar{b}}^\dagger$, or the inverse. The Heisenberg operator in imaginary time ($\tau = it$) for any given operator $\hat{O}$ is defined as $\hat{O}(\tau) = e^{\tau \hat{K}} \hat{O} e^{-\tau \hat{K}}$, where $\hat{K} = \hat{H} - \mu \hat{N}$. The Green's function in imaginary time is defined similarly.

$$
\begin{aligned}
G_{a\bar{b}}(\tau_a, \tau_{\bar{b}}) &= -\langle T[\hat{c}_a(\tau_a)\hat{c}_{\bar{b}}^\dagger(\tau_{\bar{b}})]\rangle \\
&= -\Theta(\tau_a - \tau_{\bar{b}})\langle \hat{c}_a(\tau_a)\hat{c}_{\bar{b}}^\dagger(\tau_{\bar{b}})\rangle + \Theta(\tau_{\bar{b}} - \tau_a)\langle \hat{c}_{\bar{b}}^\dagger(\tau_{\bar{b}})\hat{c}_a(\tau_a)\rangle \qquad (3.8) \\
&= \frac{1}{Z}\Bigg(-\Theta(\tau_a - \tau_{\bar{b}}) \sum_{ij} e^{-\beta K_i} e^{(\tau_a - \tau_{\bar{b}})(K_i - K_j)} \langle i|\hat{c}_a|j\rangle\langle j|\hat{c}_{\bar{b}}^\dagger|i\rangle \qquad (3.9) \\
&\qquad + \Theta(\tau_{\bar{b}} - \tau_a) \sum_{ij} e^{-\beta K_i} e^{(\tau_a - \tau_{\bar{b}})(K_j - K_i)} \langle i|\hat{c}_{\bar{b}}^\dagger|j\rangle\langle j|\hat{c}_a|i\rangle \Bigg)
\end{aligned}
$$

In this equation, T represents the time ordering operator [142, 143, 145], which rearranges the Heisenberg operators to ensure they decrease the time from left to right and multiplies by -1 for each exchange of two fermionic operators. The symbols $|i\rangle$ and $|j\rangle$ refer to the exact eigenstates (please do not confuse with single-particle states) of the many-body Hamiltonian $\hat{H}$ with corresponding eigenvalues E_i and number of electrons N_i, which yield $K_i = E_i - \mu N_i$. From Eq. (3.9), we can observe that $G_{a\bar{b}}(\tau_a, \tau_{\bar{b}})$ solely depends on $\tau - \tau_{\bar{b}}$, hence $G_{a\bar{b}}(\tau_a, \tau_{\bar{b}}) = G_{a\bar{b}}(\tau_a - \tau_{\bar{b}})$, and we can simplify further by assuming $\tau_{\bar{b}} = 0$. So, we will obtain the following form of the Green's function:

$$
\begin{aligned}
G_{a\bar{b}}(\tau) = \frac{1}{Z}\Bigg(&-\Theta(\tau) \sum_{ij} e^{-(\beta - \tau)K_i} e^{-\tau K_j} \langle i|\hat{c}_a|j\rangle\langle j|\hat{c}_{\bar{b}}^\dagger|i\rangle \qquad (3.10) \\
&+ \Theta(-\tau) \sum_{ij} e^{-(\beta + \tau)K_i} e^{\tau K_j} \langle i|\hat{c}_{\bar{b}}^\dagger|j\rangle\langle j|\hat{c}_a|i\rangle \Bigg)
\end{aligned}
$$

The τ dependence for both terms in Eq. (3.10) is $e^{-(\beta - |\tau|)K_i}$ and $e^{-|\tau|K_j}$. The infinite sum over all eigengenstate $|i\rangle$ and $|j\rangle$ will converge only if

$$\beta - |\tau| > 0 \qquad (3.11)$$

So, it is easy to see, that Green's function $\mathbf{G}(\tau)$ is well-defined only for $\tau \in [-\beta, +\beta]$ [148]. Therefore, we can express it as a Fourier series with frequencies $n\pi/\beta$, and it is evident from Eq. (3.10) that $\mathbf{G}(\tau + \beta) = -\mathbf{G}(\tau)$. Hence, only odd n values contribute to the Fourier series, and we can define the Fourier expansion of Green's function $G(\tau)$.

$$G_{a\bar{b}}(\tau) = \frac{1}{\beta} \sum_{n=-\infty}^{\infty} e^{-i\nu_n \tau} G_{a\bar{b}}(i\nu_n), \qquad (3.12)$$

$$G_{a\bar{b}}(i\nu_n) = \int_0^\beta d\tau e^{i\nu_n \tau} G_{a\bar{b}}(\tau), \qquad (3.13)$$

where $\nu_n = (2n+1)\pi/\beta$ are fermionic Matsubara frequencies [147]. Using Fourier expansion, we can rewrite $G_{a\bar{b}}(\tau)$ as

$$G_{a\bar{b}}(i\nu_n) = \frac{1}{Z}\sum_{ij}\frac{e^{-\beta K_i}+e^{-\beta K_j}}{i\nu_n-(K_j-K_i)}\langle i|\hat{c}_a|j\rangle\langle j|\hat{c}_{\bar{b}}^\dagger|j\rangle \tag{3.14}$$

This so-called Lehmann representation of the Green's function [143, 142, 145] is useful for practical computation using the exact diagonalization technique [149].

Defining the real-time Heisenberg operator $\hat{O}(t) = e^{itK}\hat{O}e^{-itK}$, we can now write retarded real-time Green's function

$$G_{a\bar{b}}^R(t-t') = -i\Theta(t-t')\left(\langle\hat{c}_a(t)\hat{c}_{\bar{b}}^\dagger(t')\rangle + \langle\hat{c}_{\bar{b}}^\dagger(t')\hat{c}_a(t)\rangle\right) \tag{3.15}$$

$$= -i\Theta(t-t')\frac{1}{Z}\left(\sum_{ij}e^{-\beta K_i}e^{(t-t')(K_i-K_j)}\langle i|\hat{c}_a|j\rangle\langle j|\hat{c}_{\bar{b}}^\dagger|i\rangle\right. \tag{3.16}$$

$$\left. -\sum_{ij}e^{-\beta K_i}e^{(t-t')(K_j-K_i)}\langle i|\hat{c}_{\bar{b}}^\dagger|j\rangle\langle j|\hat{c}_a|i\rangle\right) \tag{3.17}$$

and using the formula

$$-i\Theta(t-t')e^{-iEt} = \lim_{\eta\to 0}\frac{1}{2\pi}\int_{-\infty}^{\infty}d\omega\frac{e^{-i\omega t}}{\omega-E+i\eta} \tag{3.18}$$

we can define retarded Green's function for real frequencies

$$G_{a\bar{b}}^R(\omega) = \frac{1}{Z}\lim_{\eta\to 0}\sum_{ij}\frac{e^{-\beta K_i}+e^{-\beta K_j}}{\omega+i\eta-(K_j-K_i)}\langle i|\hat{c}_a|j\rangle\langle j|\hat{c}_{\bar{b}}^\dagger|i\rangle \tag{3.19}$$

It is easy to notice that we can obtain Eq. (3.19) from (3.14) by replacing $i\nu_n \to \omega + i\eta$. So, there is only one function $G_{a\bar{b}}(z)$ of the complex variable z, which gives $G_{a\bar{b}}(i\nu_n)$ when it is evaluated for the Matsubara frequencies and $G_{a\bar{b}}^R(\omega)$ when it evaluated on a line infinitesimally above the real axis.

Introducing the imaginary-time Green's function is to provide a function that can be computed with a powerful decomposition method on Feynman diagrams [150, 143, 142]. Although the real-time Green's functions are interesting because they contain valuable information about the system's photoemission and inverse photoemission spectrum, they are often difficult to evaluate using Feynman diagrams [143, 142]. The standard approach is to approximate $\mathbf{G}(i\nu_n)$ by expanding it in Feynman diagrams and only get the real-time Green's functions. The real-time Green's function can be obtained by analytic continuation of the Green's function represented in Matsubara frequencies $\mathbf{G}(i\nu_n)$ to the real frequency axis, thereby obtaining the Green's functions $\mathbf{G}(\omega)$ for real frequencies. Many methods exist for a given analytic continuation procedure, such as the Padé approximation [151] and maximum entropy method [152].

To complete this section, we derive the Green's function of a system of electrons without interaction with Hamiltonian $\hat{H}_0 = \sum_{a\bar{b}} t_{\bar{a}b}\hat{c}^\dagger_{\bar{a}}\hat{c}_{\bar{b}}$ at zero temperature $\beta \to \infty$. The Green's function $\mathbf{G}(z)$ will have the following form:

$$G_{a\bar{b}}(z) = \sum_i \left(\frac{\langle 0|\hat{c}_a|i\rangle\langle i|\hat{c}^\dagger_{\bar{b}}|0\rangle}{z-(K_i-K_0)} + \frac{\langle 0|\hat{c}^\dagger_{\bar{b}}|i\rangle\langle i|\hat{c}_a|0\rangle}{z+(K_i-K_0)} \right) \tag{3.20}$$

where $|0\rangle$ is a many-body ground state. By diagonalizing the Hamiltonian

$$\hat{H}_0 = \sum_{a\bar{b}} t_{\bar{a}b}\hat{c}^\dagger_{\bar{a}}\hat{c}_b = \sum_s \varepsilon_s \hat{c}^\dagger_{\bar{s}}\hat{c}_s \tag{3.21}$$

we will obtain

$$\sum_{a\bar{b}} (\phi^s)^*_{\bar{a}}\, t_{\bar{a}b}\phi^s_b = \varepsilon_s \quad \text{with} \quad \hat{c}^\dagger_{\bar{s}} = \sum_a \phi^s_{\bar{a}}\hat{c}^\dagger_{\bar{a}} \quad \text{and} \quad \hat{c}_s = \sum_a (\phi^s_a)^*\,\hat{c}_a \tag{3.22}$$

The many-body ground state $|0\rangle$ can be represented as

$$|0\rangle = \sum_{\varepsilon_s<\mu} \hat{c}^\dagger_{\bar{s}}|\text{vac}\rangle = \sum_{\varepsilon_s<\mu} |s\rangle, \tag{3.23}$$

where $|s\rangle$ are single-particle states. Therefore, with identity $\sum_i |i\rangle\langle i| = 1$, we can calculate

$$\begin{aligned} \langle 0|\hat{c}^\dagger_{\bar{b}}|i\rangle\langle i|\hat{c}_a|0\rangle &= \langle 0|\hat{c}^\dagger_{\bar{b}}\hat{c}_a|0\rangle = \rho_{a\bar{b}} \\ \langle 0|\hat{c}_a|i\rangle\langle i|\hat{c}^\dagger_{\bar{b}}|0\rangle &= \langle 0|\hat{c}_a\hat{c}^\dagger_{\bar{b}}|0\rangle = 1-\rho_{a\bar{b}} \end{aligned} \tag{3.24}$$

where $\rho_{a\bar{b}}$ is density matrix of the ground state. For the single-particle case, the density matrix will look like

$$\rho_{a\bar{b}} = \sum_{\varepsilon_s<\mu} \phi^s_a(\phi^s_{\bar{b}})^* \quad \text{and} \quad 1-\rho_{a\bar{b}} = \sum_{\varepsilon_s>\mu} \phi^s_a(\phi^s_{\bar{b}})^* \tag{3.25}$$

There is no interaction in this Hamiltonian. Based on Eq.(3.20), we can conclude that the difference between K_i and K_0 should be equal to $\varepsilon_s - \mu$ for the first component, and $K_i - K_0$ should be equal to $-\varepsilon_s + \mu$ for the second component. It is because the only difference between $|i\rangle$ and $|0\rangle$ is one electron, which gives a non-zero component. Finally, we arrive at the following result:

$$\begin{aligned} G_{a\bar{b}}(z) &= \sum_{\varepsilon_s<\mu} \frac{\phi^s_a(\phi^s_{\bar{b}})^*}{z-(\varepsilon_s-\mu)} + \sum_{\varepsilon_s>\mu} \frac{\phi^s_a(\phi^s_{\bar{b}})^*}{z-(\varepsilon_s-\mu)} \\ &= \sum_s \frac{\phi^s_a(\phi^s_{\bar{b}})^*}{z-(\varepsilon_s-\mu)} \end{aligned} \tag{3.26}$$

which can be represented as an inverse operator to the bilinear form of the Hamiltonian $\hat{H}_0 = \hat{H}_{kin} - \mu\hat{N}$

$$\mathbf{G}(z) = \frac{1}{z - \hat{H}_0} = \sum_s \frac{|s\rangle\langle s|}{z - \varepsilon_s + \mu} \tag{3.27}$$

This form of Green's function $\mathbf{G}(z)$ is quite common and is used in many theories and approximations. Also, this notation allows one to extract the effective single-particle frequency-dependent Hamiltonian $\hat{H}(z)$ by inverting the Green's function obtained from a many-particle calculation, which, for example, is very useful when calculating topological numbers.

In conclusion, we demonstrate that when there is no many-particle interaction, any operator that commutes with the Hamiltonian $\left[\hat{U}, \hat{H}_0\right] = 0$ will also commute with the single-particle Green's function $\left[\hat{U}, \mathbf{G}(z)\right] = 0$. So we can present the following:

$$\hat{H}_0 = \sum_s (\varepsilon_s - \mu) |s\rangle\langle s|. \tag{3.28}$$

So we can write

$$\left[\hat{U}, \hat{H}_0\right] = \sum_s (\varepsilon_s - \mu) \left(\hat{U}|s\rangle\langle s| - |s\rangle\langle s|\hat{U}\right) = 0 \tag{3.29}$$

A non-trivial solution for this equation will yields

$$\hat{U}|s\rangle\langle s| - |s\rangle\langle s|\hat{U} = 0 \tag{3.30}$$

Using this condition, we can prove that

$$\left[\hat{U}, \mathbf{G}(z)\right] = \sum_s \frac{\hat{U}|s\rangle\langle s| - |s\rangle\langle s|\hat{U}}{z - \varepsilon_s + \mu} = 0 \tag{3.31}$$

For a system without interaction, the single-particle Green's function preserves all the symmetries inherent in the Hamiltonian of the system.

3.2.1. Dyson equation

The Dyson equation has vast applications in many-body quantum physics. It relates the "full" Green's function, which considers the effects of the interaction of particles, with the non-interacting Green's function. Although the equation is conceptually simple, its applications have far-reaching implications and contribute to a better understanding of interacting systems. The equation was developed to explain how particles such as electrons behave under the influence of the collective effects of many other particles. Instead of giving exact solutions for these complex systems, the Dyson equation allows iterative approximation of the system's behavior, taking into account interaction effects step by step.

To derive the Dyson equation, suppose we have a system that can be described by the single-particle Hamiltonian $\hat{H}_0$. We will add a single-particle perturbation through the external potential $\hat{V}$. The Lippmann-Schwinger equation gives us the relation between

the unperturbed state $|\phi_0\rangle$ with energy ω and the eigenstate $|\phi\rangle$ of the full Hamiltonian $\hat{H} = \hat{H}_0 + \hat{V}$ as

$$|\phi\rangle = \left(1 - G_0\hat{V}\right)^{-1} |\phi_0\rangle \tag{3.32}$$

where

$$G_0 = \left(\omega + i\eta - \hat{H}_0\right)^{-1}_{|_{\eta\to 0^+}} \tag{3.33}$$

It should be noted that the Green's function G_0 depends only on $\hat{H}_0$. Hence, we can continue the discussion and show that the equation (3.32) is equivalent to $|\phi\rangle = GG_0^{-1}|\phi_0\rangle$, where $G = (1 - G_0\hat{V})^{-1}G_0$ is the "full" Green's function, which expresses the Dyson equation:

$$G = G_0 + G_0\hat{V}G \tag{3.34}$$

In general terms $a = \{a, \tau_a\}$, where a is full single-particle quantum numbers and τ_a - imaginary time, the Dyson equation can be written as

$$G_{a\bar{b}} = G^0_{a\bar{b}} + \sum_{\bar{c}d} G^0_{a\bar{c}}\hat{V}_{\bar{c}d}G_{d\bar{b}} \tag{3.35}$$

where all repeated indexes are integrated. Green's functions G and G_0 can be completely non-local in space, spin, and time. Similar criteria can be applied to an external potential perturbation $\hat{V}$. The Dyson equation is the sum of a geometric progression, where the zero element is the Green's function of the unperturbed system G_0, and the denominator of the progression is $G_0\hat{V}$. Despite its simplicity, the Dyson equation is the most common in quantum many-body physics due to the introduction of the self-energy concept, which we will consider in the next section.

3.2.2. Self-energy

To continue our discussion, we introduce the concept of the self-energy component. To do this, we return to the definition of the Heisenberg evolution of the operator $\hat{O}(\tau)$ in the imaginary time τ. We can write the equation of motion for a given operator as

$$-\partial_\tau\hat{O}(\tau) = \left[\hat{O}(\tau), \hat{H}\right] \tag{3.36}$$

and $\hat{H}$ the fully many-body Hamiltonian, represented in general terms as

$$\hat{H} = \underbrace{\sum_{\bar{a}b} t_{\bar{a}b}\hat{c}^\dagger_{\bar{a}}\hat{c}_{\bar{b}}}_{\hat{H}_{kin}} + \underbrace{\frac{1}{2}\sum_{\bar{a}\bar{b}cd} V_{\bar{a}\bar{b}cd}\hat{c}^\dagger_{\bar{a}}\hat{c}^\dagger_{\bar{b}}\hat{c}_c\hat{c}_d}_{\hat{H}_{int}} \tag{3.37}$$

And by employing relation $[\hat{A}, \hat{B}\hat{C}] = \hat{B}[\hat{A}, \hat{C}] + [\hat{A}, \hat{B}]\hat{C}$ and $\hat{c}^\dagger_{\bar{a}}\hat{c}_a + \hat{c}_a\hat{c}^\dagger_{\bar{a}} = 0$ we can write that Heisenberg equation of motion for the single-particle Green's function as

$$-\partial_\tau G_{a\bar{b}}(\tau) = \delta(\tau) + \sum_c t_{\bar{a}c}G_{c\bar{b}}(\tau) + F_{\bar{a}\bar{b}}(\tau) \tag{3.38}$$

The last term F on the right-hand side of Eq. (3.38) carries information about many-body interaction in the system and has the following form

$$F_{\bar{a}\bar{b}}(\tau) = -\sum_{\bar{c}de} V_{\bar{a}\bar{c}de}\langle T[(\hat{c}^\dagger_{\bar{c}}\hat{c}_d\hat{c}_e)(\tau)\hat{c}^\dagger_{\bar{b}}(0)]\rangle. \tag{3.39}$$

So, now we can define self-energy $\Sigma_{\bar{a}c}(\tau)$ using equation

$$F_{\bar{a}\bar{b}}(\tau) = \int_0^\beta d\tau' \Sigma_{\bar{a}c}(\tau-\tau')G_{c\bar{b}}(\tau') \tag{3.40}$$

. And, by performing Fourier transform, we can solve the equation (3.38) as

$$(-\partial_\tau - t_{\bar{a}c})\, G_{c\bar{b}}(\tau) - \int_0^\beta d\tau' \Sigma_{\bar{a}c}(\tau-\tau')G_{c\bar{b}}(\tau') = \delta(\tau) \tag{3.41}$$

$$(i\omega_v - t_{\bar{a}c} - \Sigma_{\bar{a}c}(i\omega_v))\, G_{c\bar{b}}(\tau) = 1 \tag{3.42}$$

Moreover, as a result, we can restore the famous Dyson equation:

$$G_{a\bar{b}}(i\omega_v) = G^0_{a\bar{b}}(i\omega_v) + G^0_{a\bar{c}}(i\omega_v)\Sigma_{\bar{c}d}(i\omega_v)G_{d\bar{b}}(i\omega_v) \tag{3.43}$$

where $G^0_{a\bar{b}}$ correspond to a solution of Eq.(3.42) in a non-interacting case $\Sigma = 0$:

$$(i\omega_v - t_{\bar{a}c})\, G^0_{c\bar{b}}(\tau) = 1 \tag{3.44}$$

So, we define the self-energy component as a bilinear correction $\Sigma_{\bar{a}b}$ to $t_{\bar{a}b}$ that accurately describes the influence of many-electron interactions on the single-particle Green's function. Exact calculation of the (3.39) is often impossible; therefore, self-energy component approximation techniques are prevalent. One such technique is the Hartree-Fock approximation. Using Wick's theorem, described in details in Appendix A with neglecting two-particle correlations ($\hat{H}_{int} \approx 0$ in Eq.(3.37)), we can decompose

$$\begin{aligned}\langle T[(\hat{c}^\dagger_{\bar{c}}\hat{c}_d\hat{c}_e)(\tau)\hat{c}^\dagger_{\bar{b}}(0)]\rangle =& \langle T[\hat{c}^\dagger_{\bar{c}}(\tau)\hat{c}_e(\tau)]\rangle\langle T[\hat{c}^\dagger_{\bar{b}}(0)\hat{c}_d(\tau)]\rangle - \langle T[\hat{c}^\dagger_{\bar{c}}(\tau)\hat{c}_d(\tau)]\rangle\langle T[\hat{c}^\dagger_{\bar{b}}(0)\hat{c}_e(\tau)]\rangle \\ =& \rho_{e\bar{c}}G_{d\bar{b}}(\tau) - \rho_{d\bar{c}}G_{e\bar{b}}(\tau)\end{aligned} \tag{3.45}$$

and get the following expression

$$\begin{aligned}F_{\bar{a}\bar{b}}(\tau) =& -\sum_{\bar{c}de} V_{\bar{a}\bar{c}de}\langle T[(\hat{c}^\dagger_{\bar{c}}\hat{c}_d\hat{c}_e)(\tau)\hat{c}^\dagger_{\bar{b}}(0)]\rangle \\ =& \sum_{\bar{c}de}\left(V_{\bar{a}\bar{c}ed} - V_{\bar{a}\bar{c}de}\right)\rho_{e\bar{c}}G_{d\bar{b}}(\tau)\end{aligned} \tag{3.46}$$

So, we can obtain the equations for the self-energy component in the Hartree-Fock approximation as

$$\Sigma^{HF}_{\bar{a}\bar{b}} = \sum_{\bar{c}d}(\underbrace{V_{\bar{a}\bar{c}d\bar{b}}}_{\text{Hartree}} - \underbrace{V_{\bar{a}\bar{c}\bar{b}d}}_{\text{Fock}})\rho_{d\bar{c}} \tag{3.47}$$

We can use the Hartree-Fock approximation under the conditions of applicability of the Wick theorem (See Appendix A), that is, under the conditions of the absence of two-particle correlations in the system, which corresponds to the original derivation of the Hartree-Fock method for a many-particle function in the form of the Slater determinant [153].

3.2.3. Quartic symmetrized interaction tensor

In further Chapters and sections, to simplify the story, we will use the quartic symmetrized interaction tensor, which can be obtained from the interaction tensor V, defined through the interaction Hamiltonian as

$$\hat{H}_{int} = \frac{1}{2} \sum_{\bar{a}\bar{b}cd} V_{\bar{a}\bar{b}cd} \hat{c}^{\dagger}_{\bar{a}} \hat{c}^{\dagger}_{\bar{b}} \hat{c}_c \hat{c}_d \tag{3.48}$$

Now, we carry out symmetrization over all pair-wise fermionic permutations as

$$V_{\bar{a}\bar{b}cd} = \frac{1}{2} \left(V_{\bar{a}\bar{b}cd} - V_{\bar{b}\bar{a}cd} \right) \tag{3.49}$$

$$V_{\bar{a}\bar{b}cd} = \frac{1}{2} \left(V_{\bar{a}\bar{b}cd} - V_{\bar{a}\bar{b}dc} \right) \tag{3.50}$$

and as a second step, we perform reindexing as

$$V_{\bar{a}\bar{b}cd} \Rightarrow V_{c\bar{a}d\bar{b}}. \tag{3.51}$$

Therefore, the Hamiltonian (3.48) can be rewritten as

$$\hat{H}_{int} = \frac{1}{2} \sum_{\bar{a}\bar{b}cd} V_{c\bar{a}d\bar{b}} \hat{c}^{\dagger}_{\bar{a}} \hat{c}^{\dagger}_{\bar{b}} \hat{c}_c \hat{c}_d \tag{3.52}$$

For further future derivations simplification, we will multiply the tensor V by 2, so

$$\hat{H}_{int} = \frac{1}{2} \sum_{\bar{a}\bar{b}cd} V_{c\bar{a}d\bar{b}} \hat{c}^{\dagger}_{\bar{a}} \hat{c}^{\dagger}_{\bar{b}} \hat{c}_c \hat{c}_d \Rightarrow \frac{1}{4} \sum_{\bar{a}\bar{b}cd} V_{c\bar{a}d\bar{b}} \hat{c}^{\dagger}_{\bar{a}} \hat{c}^{\dagger}_{\bar{b}} \hat{c}_c \hat{c}_d \tag{3.53}$$

One example of the resulting simplification is the formula for Hartree-Fock self-energy from Eq. (3.47):

$$\Sigma^{HF}_{\bar{b}a} = \sum_{c\bar{d}} V_{a\bar{b}c\bar{d}} \rho_{c\bar{d}} \tag{3.54}$$

When further mentioning interaction tensor V, we will mean quartic symmetrized interaction tensor.

3.2.4. Single-particle Green's function perturbation theory

When dealing with non-interacting systems, calculating the single-particle Green's function is simple. However, adding interactions to the system makes the process more

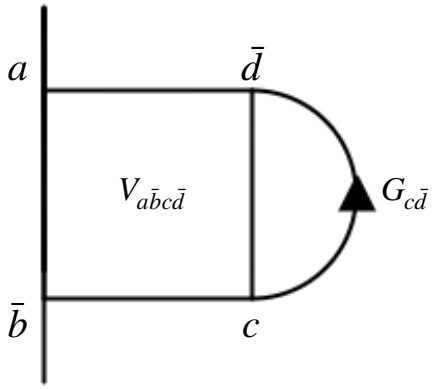

Figure 3.1: First-order Feynman diagram for the single-particle Green's function.

complex, and direct numerical solutions become impossible due to the exponential growth of the Hilbert space with the number of degrees of freedom. To overcome this problem, perturbation theory is commonly used, starting from the non-interaction limit and using the relation between interaction and kinetic parts of the Hamiltonian as the perturbation parameter.

The use of Feynman diagrams is to represent perturbations and the complexity of interaction problems visually. These diagrams are translated into mathematical expressions through specific rules to obtain all terms of the perturbation series. The Green's function, which includes interaction effects, can be represented as a perturbation series [143, 154]. The Feynman diagram technique is a systematic way of building all terms in a given series order. First and second-order Feynman diagrams are depicted in Fig.3.1 and Fig.3.2, respectively. However, constructing an infinite sum of Feynman diagrams is impossible, so the series must be truncated in a particular order.

Upon examining the diagrams of second order (Fig. 3.2), we notice that some are repeats of first-order diagrams connected with a non-interacting Green's function. These are called single-particle reducible diagrams. They can be split into two diagrams by cutting one non-interacting Green's function $G_{f\bar{e}}$ (Fig. 3.2 (a)). In contrast, diagrams that cannot be split by cutting one Green's function are called single-particle irreducible (Fig. 3.2 (b)), including first- and second-order diagrams. To create all Feynman diagrams systematically, we start with single-particle irreducible ones and remove the incoming and outgoing Green's functions from these diagrams. We refer to the sum of these irreducible diagrams as the self-energy $\Sigma_{\bar{b}a}$, shown diagrammatically in Fig.3.3, representing the

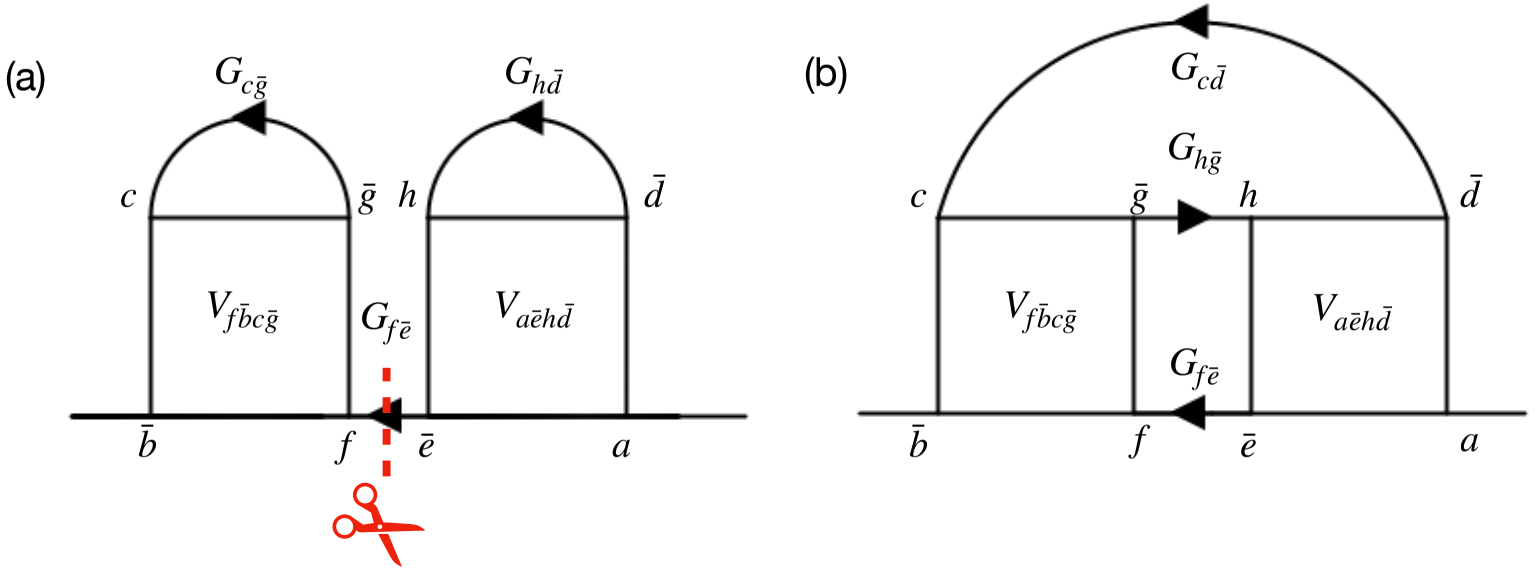

Figure 3.2: Second-order Feynman diagrams for the single-particle Green's function, including reducible diagram (a) and irreducible diagram (b).

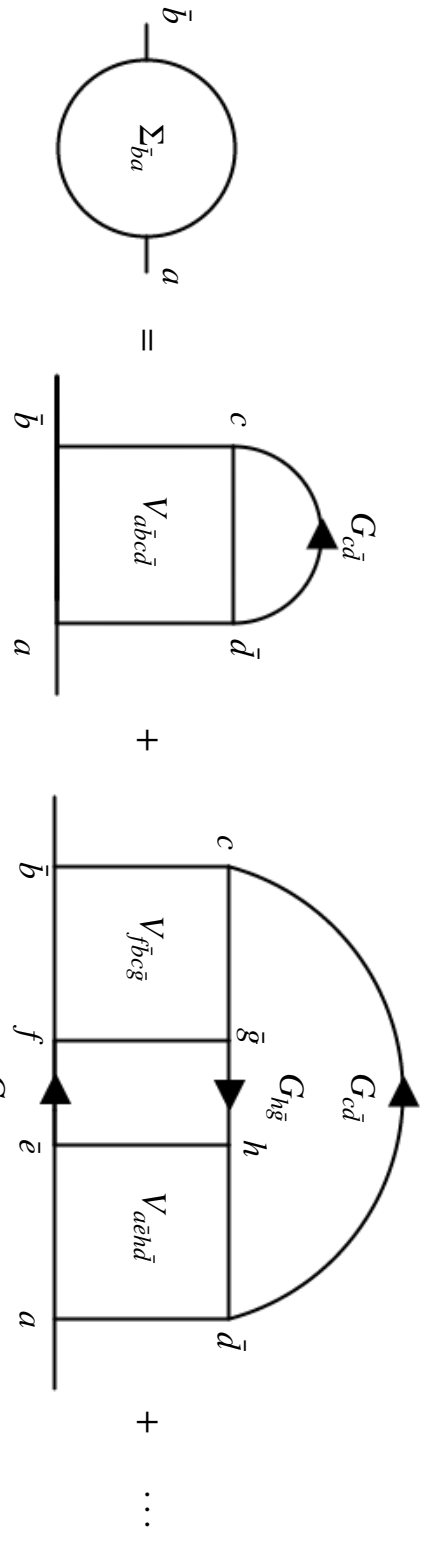

Figure 3.3: Diagrammatic representation of the self-energy Σ - sum of all irreducible diagramms.

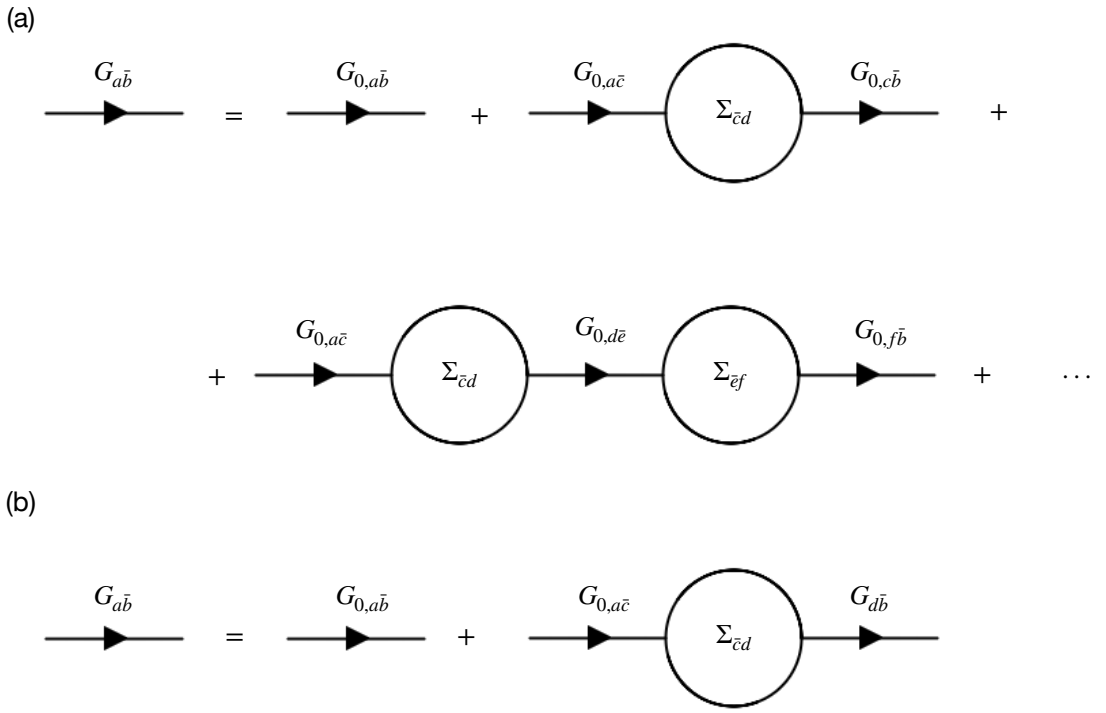

Figure 3.4: Dyson equation in two different representations. (a) is an infinite ladder, while the (b) is a sum of geometric progression.

following equation

$$\Sigma_{\bar{b}a} = \sum_i \Sigma^i \tag{3.55}$$

$$\Sigma^{(1)}_{\bar{b}a} = \sum_{c\bar{d}} V_{a\bar{b}c\bar{d}} G_{c\bar{d}} \tag{3.56}$$

$$\Sigma^{(2)}_{\bar{b}a} = \sum_{c\bar{d}f\bar{g}h\bar{e}} V_{f\bar{b}c\bar{g}} G_{h\bar{g}} G_{f\bar{e}} V_{a\bar{e}h\bar{d}} G_{c\bar{d}} \tag{3.57}$$

All possible perturbations for the single-particle Green's function can be reconstructed using self-energy and the famous Dyson equation, diagrammatically shown in Fig.3.4. Since the Dyson equation represents an infinite ladder, geometric progression sum with scale factor $G_0\Sigma$, all reducible diagrams will be restored by multiplying the non-interacting single-particle Green's function with self-energy.

3.3. Two-particle Green's function

Before we continue our discussion, it must be mentioned that Georg Rohringer's works [155, 156, 157] has substantially influenced this section. We continue our story by defining the two-particle Green's function's most general form [143, 156, 97, 157]:

$$G_{\bar{a}b\bar{c}d}(\tau_{\bar{a}}, \tau_b, \tau_{\bar{c}}, \tau_d) = \left\langle T\left[\hat{c}^\dagger_{\bar{a}}(\tau_a)\hat{c}_b(\tau_b)\hat{c}^\dagger_{\bar{c}}(\tau_c)\hat{c}_d(\tau_d)\right]\right\rangle \tag{3.58}$$

Assuming the time ordering $\tau_a > \tau_b > \tau_c > \tau_d$, we can rewrite the two-particle Green's function as

$$G_{\bar{a}b\bar{c}d}(\tau_{\bar{a}}, \tau_b, \tau_{\bar{c}}, \tau_d) = \frac{1}{Z}\sum_i e^{-(\beta+\tau_d-\tau_a)K_i}\langle i|\hat{c}^\dagger_a e^{(\tau_b-\tau_a)\hat{K}}\hat{c}_b e^{(\tau_c-\tau_b)\hat{K}}\hat{c}^\dagger_c e^{(\tau_d-\tau_c)\hat{K}}\hat{c}_d|i\rangle \tag{3.59}$$

So, we can state that the infinity sum over states $|i\rangle$ of equation (3.59) will converge only in case of

$$\beta + \tau_d - \tau_{\bar{a}} > 0 \tag{3.60}$$

Taking into account that the two-particle Green's function has τ_d as the smallest imaginary time and $\tau_{\bar{a}}$ as the largest, we can obtain

$$\tau_d + \beta > \tau_{\bar{a}} > \tau_b > \tau_{\bar{c}} > \tau_d \tag{3.61}$$

So, each time argument must be within β. We can further simplify the two-particle Green's functions by exploiting the cyclic property of the trace. If we assume that $\tau_{\bar{a}}$ is the largest and τ_d is the smallest argument of imaginary time, then using

$$\begin{aligned} G_{\bar{a}b\bar{c}d}(\tau_{\bar{a}}, \tau_b, \tau_{\bar{c}}, \tau_d) =& \mathrm{Tr}\left[e^{-\beta\hat{K}}e^{\tau_{\bar{a}}\hat{K}}\hat{c}^\dagger_a e^{-\tau_{\bar{a}}\hat{K}}\hat{c}_b(\tau_b)\hat{c}^\dagger_c(\tau_{\bar{c}})e^{\tau_d\hat{K}}\hat{c}_d e^{-\tau_d\hat{K}}\right] \\ =& \mathrm{Tr}\left[e^{-\beta\hat{K}}\hat{c}_b(\tau_b)\hat{c}^\dagger_c(\tau_{\bar{c}})e^{\tau_d\hat{K}}\hat{c}_d e^{-\tau_d\hat{K}}e^{(\tau_{\bar{a}}-\beta)\hat{K}}\hat{c}^\dagger_a e^{-(\tau_{\bar{a}}-\beta)\hat{K}}\right] \\ =& \mathrm{Tr}\left[e^{-\beta\hat{K}}e^{(\tau_d+\beta)\hat{K}}\hat{c}_d e^{-(\tau_d+\beta)\hat{K}}e^{\tau_{\bar{a}}\hat{K}}\hat{c}^\dagger_a e^{-\tau_a\hat{K}}\hat{c}_b(\tau_b)\hat{c}^\dagger_c(\tau_{\bar{c}})\right] \end{aligned} \tag{3.62}$$

we can write the Kubo-Martin-Schwinger boundary conditions [158, 159]:

$$G_{\bar{a}b\bar{c}d}(\tau_{\bar{a}},\tau_b,\tau_{\bar{c}},\tau_d) = -\,G_{\bar{a}b\bar{c}d}(\tau_a-\beta,\tau_b,\tau_c,\tau_d) \tag{3.63}$$

$$G_{\bar{a}b\bar{c}d}(\tau_{\bar{a}},\tau_b,\tau_{\bar{c}},\tau_d) = -\,G_{\bar{a}b\bar{c}d}(\tau_{\bar{a}},\tau_b,\tau_{\bar{c}},\tau_d+\beta) \tag{3.64}$$

Please be aware that these relationships only apply when τ_a is the largest time argument, and τ_d is the smallest time argument. If this is not the case, transforming $\tau_{\bar{a}}$ into $\tau_{\bar{a}}-\beta$ or τ_d into $\tau_d+\beta$ will result in a set of imaginary times that do not meet the necessary condition (3.61). As a result, these times will not be within the domain of definition for the two-particle Green's function.

According to Eqs. (3.64), all time imaginary arguments can be limited to the range of $[0,\beta]$. We can use Eq. (3.64) repeatedly for the largest or smallest time argument to compute the value of the two-particle Green's function for all other combinations of time arguments. Finally, we can represent the two-particle Green's function as a Fourier expansion thanks to the antiperiodicity condition in Eq. (3.64):

$$G_{\bar{a}b\bar{c}d}(\tau_{\bar{a}},\tau_b,\tau_{\bar{c}},\tau_d) = \frac{1}{\beta^4}\sum_{a,b,c,d} e^{i(\nu_{\bar{a}}\tau_{\bar{a}}-\nu_b\tau_b+\nu_{\bar{c}}\tau_{\bar{c}}-\nu_d\tau_d)}G_{\bar{a}b\bar{c}d}(\nu_{\bar{a}},\nu_b,\nu_{\bar{c}},\nu_d) \tag{3.65}$$

$$\begin{aligned} G_{\bar{a}b\bar{c}d}(\nu_{\bar{a}},\nu_b,\nu_{\bar{c}},\nu_d) = &\int_0^\beta d\tau_{\bar{a}}\int_0^\beta d\tau_b\int_0^\beta d\tau_{\bar{c}}\int_0^\beta d\tau_d \\ &e^{-i(\nu_{\bar{a}}\tau_{\bar{a}}-\nu_b\tau_b+\nu_{\bar{c}}\tau_{\bar{c}}-\nu_d\tau_d)}G_{\bar{a}b\bar{c}d}(\tau_{\bar{a}},\tau_b,\tau_{\bar{c}},\tau_d) \end{aligned} \tag{3.66}$$

where ω_i are odd (fermionic) Matsubara frequencies.

3.3.1. Symmetry properties of the two-particle Green's function

We continue our discussion with the overall approach to analyzing the symmetry properties of the two-particle Green's functions. Specifically, we will look at a transformation represented by an invertible operator called $\hat{U}$. This operator will change how the creation and annihilation operators behave.

$$\hat{c}^{\dagger\prime}_{\bar{i}} = \hat{U}^{-1}\hat{c}^\dagger_{\bar{i}}\hat{U} \quad \text{and} \quad \hat{c}^{\prime}_{i} = \hat{U}^{-1}\hat{c}_i\hat{U} \tag{3.67}$$

We can define Green's function as transformed, expressed using the transformed fermionic operators.

$$G^{\prime}_{\bar{a}b\bar{c}d}(\tau_{\bar{a}},\tau_b,\tau_{\bar{c}},\tau_d) = \left\langle T\left[\hat{c}^{\dagger\prime}_{\bar{a}}(\tau_{\bar{a}})\hat{c}^{\prime}_b(\tau_b)\hat{c}^{\dagger\prime}_{\bar{c}}(\tau_{\bar{c}})\hat{c}^{\prime}_d(\tau_d)\right]\right\rangle \tag{3.68}$$

The Green's function that has transformed can be expressed in the following manner:

$$G^{\prime}_{\bar{a}b\bar{c}d}(\tau_{\bar{a}},\tau_b,\tau_{\bar{c}},\tau_d) = \left\langle T\Big[\hat{c}^{\dagger\prime}_{\bar{a}}(\tau_{\bar{a}})e^{\tau_b\hat{K}}\hat{U}^{-1}\hat{c}_b\underbrace{\hat{U}e^{-\tau_b\hat{K}}e^{\tau_{\bar{c}}\hat{K}}\hat{U}^{-1}}_{e^{(\tau_{\bar{c}}-\tau_b)\hat{K}^\prime}}\hat{c}^\dagger_{\bar{c}}\hat{U}e^{-\tau_c\hat{K}}\hat{c}^{\prime}_d(\tau_d)\Big]\right\rangle \tag{3.69}$$

The matrix element can be interpreted differently according to the associative law.

$$G'_{\bar{a}b\bar{c}d}(\tau_{\bar{a}},\tau_b,\tau_{\bar{c}},\tau_d)=\left\langle T\left[e^{\tau_{\bar{a}}\hat{K}}\hat{U}^{-1}\hat{c}^\dagger_{\bar{a}}e^{(\tau_b-\tau_{\bar{a}})\hat{K}'}\hat{c}_b e^{(\tau_{\bar{c}}-\tau_b)\hat{K}'}\hat{c}^\dagger_{\bar{c}}e^{(\tau_d-\tau_{\bar{c}})\hat{K}'}\hat{c}_d\hat{U}e^{-\tau_{\bar{c}}\hat{K}}\right]\right\rangle \quad (3.70)$$

where $\hat{K}'$ is defined as:

$$\hat{K}'=\hat{U}\hat{K}\hat{U}^{-1} \quad (3.71)$$

Assuming time ordering with $\tau_a>\tau_b>\tau_c>\tau_d$ and considering the cyclic property of the trace, we can express it as follows:

$$\begin{aligned}G'_{\bar{a}b\bar{c}d}(\tau_{\bar{a}},\tau_b,\tau_{\bar{c}},\tau_d)&=\mathrm{Tr}\Big[e^{-\beta\hat{K}}e^{\tau_{\bar{a}}\hat{K}}\hat{U}^{-1}\hat{c}^\dagger_{\bar{a}}e^{(\tau_b-\tau_{\bar{a}})\hat{K}'}\hat{c}_b e^{(\tau_{\bar{c}}-\tau_b)\hat{K}'}\hat{c}^\dagger_{\bar{c}}e^{(\tau_d-\tau_{\bar{c}})\hat{K}'}\hat{c}_d\hat{U}e^{-\tau_d\hat{K}}\Big]\\&=\mathrm{Tr}\Big[\underbrace{\hat{U}e^{-\tau_d\hat{K}}e^{-\beta\hat{K}}e^{\tau_{\bar{a}}\hat{K}}\hat{U}^{-1}}_{e^{-\tau_d\hat{K}'}e^{-\beta\hat{K}'}e^{\tau_{\bar{a}}\hat{K}'}}\hat{c}^\dagger_{\bar{a}}e^{(\tau_b-\tau_{\bar{a}})\hat{K}'}\hat{c}_b e^{(\tau_{\bar{c}}-\tau_b)\hat{K}'}\hat{c}^\dagger_{\bar{c}}e^{(\tau_d-\tau_{\bar{c}})\hat{K}'}\hat{c}_d\Big]\\&=\mathrm{Tr}\Big[e^{-\beta\hat{K}'}e^{\tau_{\bar{a}}\hat{K}'}\hat{c}^\dagger_{\bar{a}}e^{(\tau_b-\tau_{\bar{a}})\hat{K}'}\hat{c}_b e^{(\tau_{\bar{c}}-\tau_b)\hat{K}'}\hat{c}^\dagger_{\bar{c}}e^{(\tau_d-\tau_{\bar{c}})\hat{K}'}\hat{c}_d e^{-\tau_d\hat{K}'}\Big] \quad (3.72)\end{aligned}$$

We assume the system recognizes $\hat{U}$ as a symmetry if it commutes with $\hat{K}$. It means that the transformed Hamiltonian is the same as the original one.

$$\Big[\hat{U},\hat{K}\Big]=0 \quad \rightarrow \quad \hat{K}'=\hat{K} \quad (3.73)$$

Hence, in this case, the modified Green's function will match the initial one:

$$\begin{aligned}G'_{\bar{a}b\bar{c}d}(\tau_{\bar{a}},\tau_b,\tau_{\bar{c}},\tau_d)=&\mathrm{Tr}\Big[e^{-\beta\hat{K}'}e^{\tau_{\bar{a}}\hat{K}'}\hat{c}^\dagger_{\bar{a}}e^{(\tau_b-\tau_{\bar{a}})\hat{K}'}\hat{c}_b e^{(\tau_{\bar{c}}-\tau_b)\hat{K}'}\hat{c}^\dagger_{\bar{c}}e^{(\tau_d-\tau_{\bar{c}})\hat{K}'}\hat{c}_d e^{-\tau_d\hat{K}'}\Big]\\=&\mathrm{Tr}\Big[e^{-\beta\hat{K}}e^{\tau_{\bar{a}}\hat{K}}\hat{c}^\dagger_{\bar{a}}e^{(\tau_b-\tau_{\bar{a}})\hat{K}}\hat{c}_b e^{(\tau_{\bar{c}}-\tau_b)\hat{K}}\hat{c}^\dagger_{\bar{c}}e^{(\tau_d-\tau_{\bar{c}})\hat{K}}\hat{c}_d e^{-\tau_d\hat{K}}\Big]\\=&G_{\bar{a}b\bar{c}d}(\tau_{\bar{a}},\tau_b,\tau_{\bar{c}},\tau_d) \quad (3.74)\end{aligned}$$

We can assert that the two-particle Green's function is stable over the transformation using the symmetry operator $\hat{U}$, which commutes with the Hamiltonian of the system. In the following, we will discuss the symmetry properties of Green's functions, which can be formally derived using this equation as the basis.

One of the key properties of the two-particle Green's function is time and space translation symmetry. If Hamiltonian $\hat{K}$ is time-independent, the two-particle Green's function does not explicitly depend on four imaginary-times $\tau_{\bar{a}},\tau_b,\tau_{\bar{c}}$ and τ_d, but only on three $\tau_d-\tau_{\bar{a}},\tau_b-\tau_d$, and $\tau_d-\tau_{\bar{c}}$. To prove it, we consider the time translation operator

$$\hat{T}_\tau=e^{-\tau\hat{K}} \quad (3.75)$$

which commutes with any time-independent Hamiltonian. For the specific choice $\tau=-\tau_d$ we can transform the two-particle Green's function using the time translation operator $\hat{T}_\tau=e^{-\tau_d\hat{K}}$ and we obtain that

$$G_{\bar{a}b\bar{c}d}(\tau_{\bar{a}},\tau_b,\tau_{\bar{c}},\tau_d)=G_{\bar{a}b\bar{c}d}(\tau_d-\tau_{\bar{a}},\tau_b-\tau_d,\tau_d-\tau_{\bar{c}},0) \quad (3.76)$$

Together with Kubo-Martin-Schwinger boundary conditions, the time translation invariance of the two-particle Green's function leads to a further simplification:

$$\tilde{G}_{\bar{a}b\bar{c}d}(\nu_{\bar{a}},\nu_b,\nu_{\bar{c}},\nu_d) = \int_0^\beta d\tau_{\bar{a}} \int_0^\beta d\tau_b \int_0^\beta d\tau_{\bar{c}} \int_0^\beta d\tau_d \\ e^{-i(\nu_{\bar{a}}\tau_{\bar{a}}-\nu_b\tau_b+\nu_{\bar{c}}\tau_{\bar{c}}-\nu_d\tau_d)} G_{\bar{a}b\bar{c}d}(\tau_d-\tau_{\bar{a}},\tau_b-\tau_d,\tau_d-\tau_{\bar{c}},0) \tag{3.77}$$

To introduce new time variables τ_i, where $i = a, b, c$, we use the transformation $\tau_i = \tau_i + \tau_d$. The integral over τ_i needs to be performed within the interval $[-\tau_d, \beta - \tau_d]$. However, as the two-particle Green's function is antiperiodic concerning τ_i with a period of β, integrating this function over any interval with a length of β is equivalent to integrating it from 0 to β. Finally, we can integrate the remaining time variable τ_d, which only appears in the phase factor $e^{-i(\nu_{\bar{a}}\tau_{\bar{a}}-\nu_b\tau_b+\nu_{\bar{c}}\tau_{\bar{c}}-\nu_d\tau_d)}$, to obtain the energy conservation relation:

$$\int_0^\beta d\tau_d e^{-i(\nu_{\bar{a}}\tau_{\bar{a}}-\nu_b\tau_b+\nu_{\bar{c}}\tau_{\bar{c}}-\nu_d\tau_d)} = \beta\delta(\nu_{\bar{a}}-\nu_b+\nu_{\bar{c}}-\nu_d) \tag{3.78}$$

As a result, we obtain that:

$$\begin{aligned}\tilde{G}_{\bar{a}b\bar{c}d}(\nu_{\bar{a}},\nu_b,\nu_{\bar{c}},\nu_d) =& \beta\delta(\nu_{\bar{a}}-\nu_b+\nu_{\bar{c}}-\nu_d) \int_0^\beta d\tau_{\bar{a}} \int_0^\beta d\tau_b \int_0^\beta d\tau_{\bar{c}} \\ & e^{-i(\nu_{\bar{a}}\tau_{\bar{a}}-\nu_b\tau_b+\nu_{\bar{c}}\tau_{\bar{c}})} G_{\bar{a}b\bar{c}d}(\tau_{\bar{a}},\tau_b,\tau_{\bar{c}},\tau_d) \\ =& \beta\delta(\nu_{\bar{a}}-\nu_b+\nu_{\bar{c}}-\nu_d) G_{\bar{a}b\bar{c}d}(\nu_{\bar{a}},\nu_b,\nu_{\bar{c}})\end{aligned} \tag{3.79}$$

The preceding discussion reveals that analyzing the two-particle Green's function in Fourier space is only necessary, which relies on three frequencies instead of four. It is because of the system's time-translational invariance, which results in energy conservation.

We will also consider translational symmetry, which implies that the system remains invariant when shifted by the lattice vector $\mathbf{R}$. We denote the operator associated with this shift as $\hat{U} = \hat{T}_{\mathbf{R}}$. Similar to our previous discussion of time translation symmetry, where we chose $\mathbf{R} = \mathbf{R}_d$, we can easily derive a relation similar to the equation (3.76), but this time taking into account lattice vectors $\mathbf{R}_i$ instead of time intervals τ_i.

$$G_{\bar{a}b\bar{c}d}(\mathbf{R}_{\bar{a}},\mathbf{R}_b,\mathbf{R}_{\bar{c}},\mathbf{R}_d) = G_{\bar{a}b\bar{c}d}(\mathbf{R}_{\bar{a}}-\mathbf{R}_d,\mathbf{R}_b-\mathbf{R}_d,\mathbf{R}_{\bar{c}}-\mathbf{R}_d,\mathbf{R}_0) \tag{3.80}$$

where $\mathbf{R}_0$ represent the origin of the coordinate system. Performing the Fourier transform with respect to the $\mathbf{R}_i$ we obtain:

$$\begin{aligned}\tilde{G}_{\bar{a}b\bar{c}d}(\mathbf{k}_{\bar{a}},\mathbf{k}_b,\mathbf{k}_{\bar{c}},\mathbf{k}_d) =& \sum_{\mathbf{R}_{\bar{a}},\mathbf{R}_b,\mathbf{R}_{\bar{c}},\mathbf{R}_d} e^{i(\mathbf{k}_{\bar{a}}\mathbf{R}_{\bar{a}}+\mathbf{k}_b\mathbf{R}_b+\mathbf{k}_{\bar{c}}\mathbf{R}_{\bar{c}}+\mathbf{k}_d\mathbf{R}_d)} G_{\bar{a}b\bar{c}d}(\mathbf{R}_{\bar{a}},\mathbf{R}_b,\mathbf{R}_{\bar{c}},\mathbf{R}_d) \\ =& \frac{(2\pi)^d}{V}\delta(\mathbf{k}_{\bar{a}}-\mathbf{k}_b+\mathbf{k}_{\bar{c}}-\mathbf{k}_d) G_{\bar{a}b\bar{c}d}(\mathbf{k}_{\bar{a}},\mathbf{k}_b,\mathbf{k}_{\bar{c}}).\end{aligned} \tag{3.81}$$

The symbol $\mathbf{k}_0$ refers to zero momentum, V represents the volume of the unit cell, and d is the system's dimensionality. Therefore, examining the two-particle Green's function is only required to study a system with translation symmetry, which depends on three momentums $\mathbf{k}_i$ instead of four.

3.3.2. SU(2) spin symmetry

A system exhibits SU(2) spin symmetry when its Hamiltonian commutes with each generator of this group, particularly with the spin operators in all three spatial dimensions.

$$[\hat{K}, \hat{s}_i] = 0 \quad i = x, y, z \tag{3.82}$$

where $\hat{s}_i$ are spin operators, which reads:

$$\hat{s}_i = \frac{1}{2} \sum_{\bar{s}s} \hat{c}^\dagger_{\bar{s}} s^i_{\bar{s}s} \hat{c}_s \tag{3.83}$$

with sum over j - lattice sites and $s^i_{\bar{s}s}$ denotes Pauli matrices

$$s_x = \begin{pmatrix} 0 & 1 \\ 1 & 0 \end{pmatrix}, s_y = \begin{pmatrix} 0 & -i \\ i & 0 \end{pmatrix}, s_z = \begin{pmatrix} 1 & 0 \\ 0 & -1 \end{pmatrix} \tag{3.84}$$

A consequence of the SU(2) spin symmetry is spin conservation of the n-particle Green's function, specifically for the z-component of the spin. It can be expressed as:

$$\underbrace{s_{\bar{a}} + s_{\bar{c}}}_{s_z \text{ of the outgoing particles}} = \underbrace{s_c + s_d}_{s_z \text{ of the ingoing particles}} \tag{3.85}$$

For incoming particles, their total spin in the z-direction must match that of the outgoing particles. This statement can be proven by dividing the Hilbert space into orthogonal subspaces based on corresponding eigenvalues of the hermitian operator $\hat{s}_z$. The two-particle Green's function can then be represented accordingly.

$$G_{s_{\bar{a}} s_b s_{\bar{c}} s_d}(\tau_{\bar{a}}, \tau_b, \tau_{\bar{c}}, \tau_d) = \frac{1}{Z} \sum_i \sum_{s_z} e^{-\beta K_{i,s_z}} \langle i, s_z | \hat{c}^\dagger_{s_{\bar{a}}}(\tau_{\bar{a}}) \hat{c}_{s_b}(\tau_b) \hat{c}^\dagger_{s_{\bar{c}}}(\tau_{\bar{c}}) \hat{c}_{s_d}(\tau_d) | i, s_z \rangle \tag{3.86}$$

assuming time-ordering $\tau_{\bar{a}} > \tau_b > \tau_{\bar{c}} > \tau_d$. Since the operators $\hat{s}_i$ commute with the Hamiltonian, we can state that for any operator of the form $e^{\gamma \hat{K}}$:

$$e^{\gamma \hat{K}} |i, s_z\rangle = |i, s_z\rangle \tag{3.87}$$

Commutation relations between the creation and annihilation operators, respectively, and $\hat{s}_z$ read:

$$[\hat{s}_z, \hat{c}^\dagger_s] = s \hat{c}^\dagger_s \quad [\hat{s}_z, \hat{c}_s] = -s \hat{c}_s, \tag{3.88}$$

where $s = \pm \frac{1}{2}$ corresponds to spin-up and spin-down states, respectively. So, it immediately follows that

$$\hat{c}^\dagger_s |i, s_z\rangle = |j, s_z + s\rangle \quad \hat{c}_s |i, s_z\rangle = |j, s_z - s\rangle \tag{3.89}$$

So, now, we can calculate

$$\begin{aligned}\langle i, s_z|\hat{c}^\dagger_{s_{\bar{a}}}(\tau_{\bar{a}})\hat{c}_{s_b}(\tau_b)\hat{c}^\dagger_{s_{\bar{c}}}(\tau_{\bar{c}})\hat{c}_{s_d}(\tau_d)|i, s_z\rangle = \\ = \langle i, s_z|j, s_z + s_{\bar{a}} - s_b + s_{\bar{c}} - s_d\rangle \propto \delta(s_{\bar{a}} - s_b + s_{\bar{c}} - s_d)\end{aligned} \tag{3.90}$$

This equation represents the principle of spin conservation, provided that states with different s_z values are orthogonal. Spin conservation leads to a significant simplification of the two-particle Green's functions. Only six spin combinations remain under SU(2) spin symmetry out of $2^4 = 16$ combinations for a two-particle Green's function.

$$s_{\bar{a}} = s_b = s_{\bar{c}} = s_d, \quad (s_{\bar{a}} = s_b) \neq (s_{\bar{c}} = s_d), \quad (s_{\bar{a}} = s_d) \neq (s_b = s_{\bar{c}}) \tag{3.91}$$

Due to Eqs. (3.85) and (3.90), the two-particle Green's functions vanish for all other spin combinations.

3.3.3. Crossing symmetry

The Fermi-Dirac statistics and Pauli principle are demonstrated by crossing symmetry. The "symmetry" designation is misleading since it is unrelated to Hamiltonian invariance. It originates from the time-ordering of fermionic operators in equation (3.58). The order of fermionic operators chosen to define the Green's function does not play a role other than the sign. The replacement of two creation or annihilation operators in equation (3.58) does not change the two-particle Green's function, except for an additional minus sign:

$$G_{\bar{a}b\bar{c}d}(\tau_{\bar{a}}, \tau_b, \tau_{\bar{c}}, \tau_d) = -G_{\bar{a}c\bar{b}d}(\tau_{\bar{a}}, \tau_c, \tau_{\bar{b}}, \tau_d) \tag{3.92}$$

Please keep in mind that the intersection numbers need to be either even or odd, indicating the corresponding statements' placement in the trace. Suppose the parity of the intersection numbers varies. In that case, this leads to a series of creation and annihilation operators that need to be covered in the definition of the two-particle Green's function mentioned in Eq. (3.58). As a result, such permutations are not appropriate for demonstrating cross symmetry. It is worth noting that there is no cross relation for the single-particle Green's function. However, there is a specific relationship applicable to the two-particle version:

$$\begin{aligned}G_{\bar{a}b\bar{c}d}(\tau_{\bar{a}}, \tau_b, \tau_{\bar{c}}, \tau_d) =& - G_{\bar{c}b\bar{a}d}(\tau_{\bar{c}}, \tau_b, \tau_{\bar{a}}, \tau_d) \\ =& - G_{\bar{a}d\bar{c}b}(\tau_{\bar{a}}, \tau_d, \tau_{\bar{c}}, \tau_b) \\ =& G_{\bar{c}d\bar{a}b}(\tau_{\bar{c}}, \tau_d, \tau_{\bar{a}}, \tau_b)\end{aligned} \tag{3.93}$$

Working with two-particle Green's functions becomes more accessible by considering crossing-symmetry, as it allows for significant simplifications.

3.3.4. Generalized susceptibiliy

Studying how systems respond to external perturbations is crucial in condensed matter physics. One mathematical representation that captures this response is the generalized

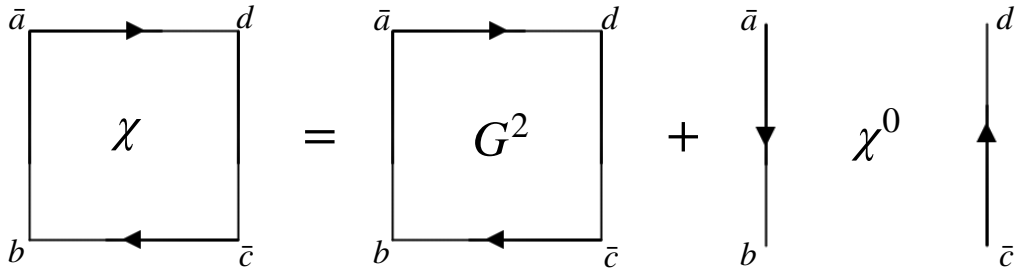

Figure 3.5: Diagrammatic representation of Eq.(3.96)

susceptibility. In this section, we explore its intricacies and implications. The generalized susceptibility has the following form

$$\chi_{\bar{a}b\bar{c}d}(\tau_{\bar{a}},\tau_b,\tau_{\bar{c}},\tau_d) = G^2_{\bar{a}b\bar{c}d}(\tau_{\bar{a}},\tau_b,\tau_{\bar{c}},\tau_d) - G^1_{b\bar{a}}(\tau_b-\tau_{\bar{a}})G^1_{d\bar{c}}(\tau_d-\tau_{\bar{c}}) \tag{3.94}$$

where G^2 is the two-particle Green's function and G^1 is the single-particle Green's function. Using Wick's theorem, we can express the generalized susceptibility in non-interacting scenarios in terms of single-particle Green's function as

$$\begin{aligned}\chi^0_{\bar{a}b\bar{c}d}(\tau_{\bar{a}},\tau_b,\tau_{\bar{c}},\tau_d) =& G^2_{\bar{a}b\bar{c}d}(\tau_{\bar{a}},\tau_b,\tau_{\bar{c}},\tau_d) - G^1_{b\bar{a}}(\tau_b-\tau_{\bar{a}})G^1_{d\bar{c}}(\tau_d-\tau_{\bar{c}})\\ =& G^1_{b\bar{a}}(\tau_b-\tau_{\bar{a}})G^1_{d\bar{c}}(\tau_d-\tau_{\bar{c}}) - G^1_{d\bar{a}}(\tau_d-\tau_{\bar{a}})G^1_{b\bar{c}}(\tau_b-\tau_{\bar{c}})\\ &- G^1_{b\bar{a}}(\tau_b-\tau_{\bar{a}})G^1_{d\bar{c}}(\tau_d-\tau_{\bar{c}})\\ =& - G^1_{d\bar{a}}(\tau_d-\tau_{\bar{a}})G^1_{b\bar{c}}(\tau_b-\tau_{\bar{c}})\end{aligned} \tag{3.95}$$

Therefore, we can write the (3.94) equation as

$$\chi_{\bar{a}b\bar{c}d}(\tau_{\bar{a}},\tau_b,\tau_{\bar{c}},\tau_d) = G^2_{\bar{a}b\bar{c}d}(\tau_{\bar{a}},\tau_b,\tau_{\bar{c}},\tau_d) - \chi^0_{\bar{a}d\bar{c}b}(\tau_{\bar{a}},\tau_d,\tau_{\bar{c}},\tau_b), \tag{3.96}$$

which diagrammatic representation is shown in Figure 3.5.

The system's time translation invariance allows the expression of the generalized susceptibility through three distinct time variables: τ_1, τ_2, and τ_3. Hence, the generalized susceptibility will have the form:

$$\chi_{\bar{a}b\bar{c}d}(\tau_{\bar{a}},\tau_b,\tau_{\bar{c}},\tau_d) = \chi_{\bar{a}b\bar{c}d}(\tau_{\bar{a}}-\tau_d,\tau_b-\tau_d,\tau_{\bar{c}}-\tau_d,\tau_d-\tau_d) = \chi_{\bar{a}b\bar{c}d}(\tau_1,\tau_2,\tau_3) \tag{3.97}$$

After the Fourier transformation, the generalized susceptibility will depend only on three fermionic Matsubara frequencies due to energy conservation $\nu_d = \nu_{\bar{a}} - \nu_b + \nu_{\bar{c}}$. We introduce two frequency notations to simplify the representation: particle-hole (particle-hole) and particle-particle (particle-particle).

$$ph: \quad \nu_{\bar{a}} = \nu, \quad \nu_b = \omega+\nu, \quad \nu_{\bar{c}} = \omega+\nu', \quad \nu_d = \nu' \tag{3.98}$$

$$pp: \quad \nu_{\bar{a}} = \nu, \quad \nu_b = \omega-\nu, \quad \nu_{\bar{c}} = \omega-\nu', \quad \nu_d = \nu' \tag{3.99}$$

where $\nu = \frac{\pi}{\beta}(2n+1)$ and $\nu = \frac{\pi}{\beta}(2n'+1)$ are fermionic Matsubara frequencies and $\omega = \frac{\pi}{\beta}2m$ is a bosonic Matsubara frequency. Considering that the creation and annihilation operators correspond to outgoing and incoming electrons and incoming and outgoing holes, the frequency convention has a physical basis in both scenarios:

1. In the particle-hole case, an electron with energy $\nu + \omega$ scatters off a hole with energy $-\nu$ (minus sign due to particle-hole transformation), transferring energy ω.

2. In the particle-particle-case, two electrons with energies ν' and $\omega - \nu'$ scatter, transferring energy ω.

Therefore, based on the previously mentioned frequency conventions, we define the Fourier transform of the three-time generalized susceptibility in two ways. For particle-hole-case:

$$\chi^{ph}_{\bar{a}b\bar{c}d}(\nu,\nu',\omega) = \int_0^\beta d\tau_1 \int_0^\beta d\tau_2 \int_0^\beta d\tau_3 \chi_{\bar{a}b\bar{c}d}(\tau_1,\tau_2,\tau_3) e^{-i\nu\tau_1} e^{i(\omega+\nu)\tau_2} e^{-i(\omega+\nu')\tau_3} \quad (3.100)$$

and for particle-particle-case:

$$\chi^{pp}_{\bar{a}b\bar{c}d}(\nu,\nu',\omega) = \int_0^\beta d\tau_1 \int_0^\beta d\tau_2 \int_0^\beta d\tau_3 \chi_{\bar{a}b\bar{c}d}(\tau_1,\tau_2,\tau_3) e^{-i\nu\tau_1} e^{i(\omega-\nu')\tau_2} e^{-i(\omega-\nu)\tau_3} \quad (3.101)$$

Since the full two-particle Green's function includes particle-hole and particle-particle scattering, χ^{ph} can be expressed in terms of χ^{pp} and vice versa. After performing a Fourier transform, the corresponding susceptibilities $\chi^{0,ph}$ and $\chi^{0,pp}$ will have the following forms:

$$\chi^{0,ph}_{\bar{a}b\bar{c}d}(\nu,\nu',\omega) = -\beta G^1_{d\bar{a}}(\nu) G^1_{b\bar{c}}(\omega+\nu)\delta_{\nu\nu'} \qquad \chi^{0,pp}_{\bar{a}b\bar{c}d}(\nu,\nu',\omega) = -\beta G^1_{d\bar{a}}(\nu) G^1_{b\bar{c}}(\omega-\nu)\delta_{\nu\nu'} \quad (3.102)$$

For systems with translational symmetry, to further simplify the representation of the generalized susceptibility in momentum space, taking into account symmetry relations (3.80) and (3.81), we also introduce momentum notations, by analogy with frequency representation $\omega \to \mathbf{q}$, $\nu \to \mathbf{k}$ and $\nu' \to \mathbf{k}'$ for particle-hole (particle-hole) and particle-particle (particle-particle) channels:

$$ph: \quad \mathbf{k}_{\bar{a}} = \mathbf{k}, \quad \mathbf{k}_b = \mathbf{q} + \mathbf{k}, \quad \mathbf{k}_{\bar{c}} = \mathbf{q} + \mathbf{k}', \quad \mathbf{k}_d = \mathbf{k}' \quad (3.103)$$

$$pp: \quad \mathbf{k}_{\bar{a}} = \mathbf{k}, \quad \mathbf{k}_b = \mathbf{q} - \mathbf{k}, \quad \mathbf{k}_{\bar{c}} = \mathbf{q} - \mathbf{k}', \quad \mathbf{k}_d = \mathbf{k}' \quad (3.104)$$

The momentum convention is physically motivated:

1. In the particle-hole-case, an electron with momentum $\mathbf{k} + \mathbf{q}$ scatters off a hole with momentum $-\mathbf{k}$ (minus sign due to particle-hole transformation), transferring momentum $\mathbf{q}$.

2. In the particle-particle-case, two electrons with energies $\mathbf{k}'$ and $\mathbf{q} - \mathbf{k}'$ scatter, transferring momentum $\mathbf{k}$.

We define the Fourier transform of the generalized susceptibility (Eq.(3.80)) using the momentum frequency conventions mentioned earlier, for particle-hole-case:

$$\chi^{ph}_{\bar{a}b\bar{c}d}(\mathbf{k},\mathbf{k}',\mathbf{q}) = \sum_{\mathbf{R}_1,\mathbf{R}_2,\mathbf{R}_3} \chi_{\bar{a}b\bar{c}d}(\mathbf{R}_1,\mathbf{R}_2,\mathbf{R}_3,\mathbf{R}_0) e^{-i\mathbf{k}\mathbf{R}_1} e^{i(\mathbf{q}+\mathbf{k})\mathbf{R}_2} e^{-i(\mathbf{q}+\mathbf{k}')\mathbf{R}_3} \quad (3.105)$$

and for particle-particle-case:

$$\chi^{pp}_{\bar{a}b\bar{c}d}(\mathbf{k},\mathbf{k}',\mathbf{q}) = \sum_{\mathbf{R}_1,\mathbf{R}_2,\mathbf{R}_3} \chi_{\bar{a}b\bar{c}d}(\mathbf{R}_1,\mathbf{R}_2,\mathbf{R}_3) e^{-i\mathbf{k}\mathbf{R}_1} e^{i(\mathbf{q}-\mathbf{k}')\mathbf{R}_2} e^{-i(\mathbf{q}-\mathbf{k})\mathbf{R}_3} \tag{3.106}$$

the corresponding susceptibilities $\chi^{0,ph}$ and $\chi^{0,pp}$ will have the following forms:

$$\chi^{0,ph}_{\bar{a}b\bar{c}d}(\mathbf{k},\mathbf{k}',\mathbf{q}) = -G^1_{d\bar{a}}(\mathbf{k}) G^1_{b\bar{c}}(\mathbf{q}+\mathbf{k}) \delta_{\mathbf{k}\mathbf{k}'} \tag{3.107}$$

$$\chi^{0,pp}_{\bar{a}b\bar{c}d}(\mathbf{k},\mathbf{k}',\mathbf{q}) = -G^1_{d\bar{a}}(\mathbf{k}) G^1_{b\bar{c}}(\mathbf{q}-\mathbf{k}) \delta_{\mathbf{k}\mathbf{k}'} \tag{3.108}$$

Furthermore, for further narration, in systems with translational symmetry, we will use the following notation:

$$\nu \to (\nu,\mathbf{k}) \quad \nu' \to (\nu',\mathbf{k}) \quad \omega \to (\omega,\mathbf{q}) \tag{3.109}$$

3.3.5. Physical susceptibility from generalized susceptibility

Finally, let us show that generalized susceptibility is incredibly convenient because we can calculate any physical susceptibility observed experimentally from it. To prove this statement, we introduce a generalized representation of the bilinear operators $\hat{A}$ and $\hat{B}$:

$$\hat{A}(\tau) = e^{\tau\hat{K}} \sum_{ab} \left(A_{\bar{a}b} \hat{c}^\dagger_{\bar{a}} \hat{c}_b \right) e^{-\tau\hat{K}} \tag{3.110}$$

where $\hat{K} = \hat{H} - \mu\hat{N}$, for a physical susceptibility in particle-hole-channel (according to energy conservation convention):

$$\begin{aligned}
\chi_{\hat{A}\hat{B}}(\omega) &= \int_0^\beta d\tau e^{i\omega\tau} \chi_{\hat{A}\hat{B}}(\tau) \\
&= \int_0^\beta d\tau e^{i\omega\tau} \left(\langle \hat{A}(\tau) - \langle \hat{A} \rangle \rangle \right) \left(\langle \hat{B}(0) - \langle \hat{B} \rangle \rangle \right) \\
&= \int_0^\beta d\tau e^{i\omega\tau} \langle \hat{A}(\tau)\hat{B}(0) \rangle - \beta\delta_{0\omega} \langle \hat{A} \rangle \langle \hat{B} \rangle
\end{aligned} \tag{3.111}$$

Using the (3.110) definition, we can rewrite the physical susceptibility formula as

$$\begin{aligned}
\chi_{\hat{A}\hat{B}}(\omega) &= \sum_{\bar{a}b\bar{c}d} A_{\bar{a}b} B_{\bar{c}d} \left(\int_0^\beta d\tau e^{i\omega\tau} \langle (\hat{c}^\dagger_{\bar{a}}\hat{c}_b)(\tau)(\hat{c}^\dagger_{\bar{c}}\hat{c}_d)(0) \rangle - \beta\delta_{0\omega} \langle \hat{c}^\dagger_{\bar{a}}\hat{c}_b \rangle \langle \hat{c}^\dagger_{\bar{c}}\hat{c}_d \rangle \right) \\
&= \sum_{\bar{a}b\bar{c}d} A_{\bar{a}b} B_{\bar{c}d} \frac{1}{\beta^2} \sum_{\nu\nu'} \chi^{ph}_{\bar{a}b\bar{c}d}(\nu,\nu',\omega)
\end{aligned} \tag{3.112}$$

Eq. (3.112) applies to any Hamiltonians, both with and without interaction, and is instrumental in solving theoretical problems because physical susceptibility shows clear signatures of phase transitions, such as magnetic or superconducting phase transitions.

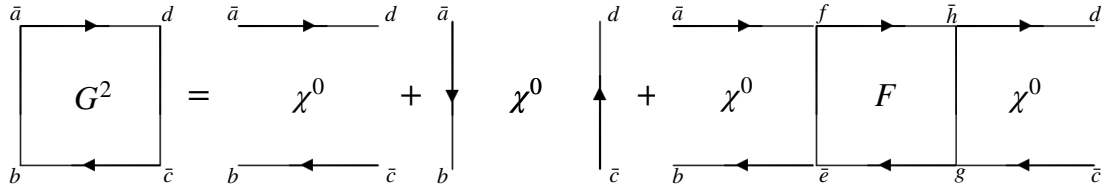

Figure 3.6: Diagrammatic representation of Eq.(3.116)

3.3.6. Full vertex function

From the previous section, we know that in the non-interacting limit, according to Wick's theorem, we can write two-particle Green's function G^2 as

$$G^2_{\bar{a}b\bar{c}d}(\tau_{\bar{a}},\tau_b,\tau_{\bar{c}},\tau_d) = G^1_{b\bar{a}}(\tau_b-\tau_{\bar{a}})G^1_{d\bar{c}}(\tau_d-\tau_{\bar{c}}) - G^1_{d\bar{a}}(\tau_d-\tau_{\bar{a}})G^1_{b\bar{c}}(\tau_b-\tau_{\bar{c}}) \tag{3.113}$$

However, in the presence of interaction, in Eq.(3.113) will be another term G^{corr}, which takes into account interaction corrections

$$\begin{aligned} G^2_{\bar{a}b\bar{c}d}(\tau_{\bar{a}},\tau_b,\tau_{\bar{c}},\tau_d) =& G^1_{b\bar{a}}(\tau_b-\tau_{\bar{a}})G^1_{d\bar{c}}(\tau_d-\tau_{\bar{c}}) - G^1_{d\bar{a}}(\tau_d-\tau_{\bar{a}})G^1_{b\bar{c}}(\tau_b-\tau_{\bar{c}}) \\ &+ G^{corr}_{\bar{a}b\bar{c}d}(\tau_{\bar{a}},\tau_b,\tau_{\bar{c}},\tau_d) \end{aligned} \tag{3.114}$$

where

$$\begin{aligned} &G^{corr}_{\bar{a}b\bar{c}d}(\tau_{\bar{a}},\tau_b,\tau_{\bar{c}},\tau_d) = \\ &\quad\sum_{f\bar{e}g\bar{h}} G^1_{f\bar{a}}(\tau_f-\tau_{\bar{a}})G^1_{b\bar{c}}(\tau_b-\tau_{\bar{c}})F_{f\bar{e}g\bar{h}}(\tau_f,\tau_{\bar{e}},\tau_g,\tau_{\bar{h}})G^1_{g\bar{c}}(\tau_g-\tau_{\bar{c}})G^1_{d\bar{h}}(\tau_d-\tau_{\bar{h}}) \end{aligned} \tag{3.115}$$

Here, we introduce the concept of the full vertex function F, which represents all scattering processes between two quasi-particles. Using the full vertex function F and the definition of the bare susceptibility χ^0, we can rewrite the expression (3.114) as

$$\begin{aligned} G^2_{\bar{a}b\bar{c}d}(\tau_{\bar{a}},\tau_b,\tau_{\bar{c}},\tau_d) =& G^1_{b\bar{a}}(\tau_b-\tau_{\bar{a}})G^1_{d\bar{c}}(\tau_d-\tau_{\bar{c}}) - G^1_{d\bar{a}}(\tau_d-\tau_{\bar{a}})G^1_{b\bar{c}}(\tau_d-\tau_{\bar{c}}) \\ &+ \sum_{f\bar{e}g\bar{h}} G^1_{f\bar{a}}(\tau_f-\tau_{\bar{a}})G^1_{b\bar{e}}(\tau_b-\tau_{\bar{e}})F_{f\bar{e}g\bar{h}}(\tau_f,\tau_{\bar{e}},\tau_g,\tau_{\bar{h}})G^1_{g\bar{c}}(\tau_g-\tau_{\bar{c}})G^1_{d\bar{h}}(\tau_d-\tau_{\bar{h}}) \\ =&\chi^0_{\bar{a}d\bar{c}b}(\tau_{\bar{a}},\tau_d,\tau_{\bar{c}},\tau_b) + \chi^0_{\bar{a}b\bar{c}d}(\tau_{\bar{a}},\tau_b,\tau_{\bar{c}},\tau_d) \\ &+ \sum_{f\bar{e}g\bar{h}} G^1_{f\bar{a}}(\tau_f-\tau_{\bar{a}})G^1_{b\bar{e}}(\tau_b-\tau_{\bar{e}})F_{f\bar{e}g\bar{h}}(\tau_f,\tau_{\bar{e}},\tau_g,\tau_{\bar{h}})G^1_{d\bar{h}}(\tau_d-\tau_{\bar{h}})G^1_{g\bar{c}}(\tau_g-\tau_{\bar{c}}) \\ =&\chi^0_{\bar{a}d\bar{c}b}(\tau_{\bar{a}},\tau_d,\tau_{\bar{c}},\tau_b) + \chi^0_{\bar{a}b\bar{c}d}(\tau_{\bar{a}},\tau_b,\tau_{\bar{c}},\tau_d) \\ &+ \sum_{f\bar{e}g\bar{h}} \chi^0_{\bar{a}b\bar{e}f}(\tau_{\bar{a}},\tau_b,\tau_{\bar{e}},\tau_f)F_{f\bar{e}g\bar{h}}(\tau_f,\tau_{\bar{e}},\tau_g,\tau_{\bar{h}})\chi^0_{\bar{h}g\bar{c}d}(\tau_{\bar{h}},\tau_g,\tau_{\bar{c}},\tau_d) \end{aligned} \tag{3.116}$$

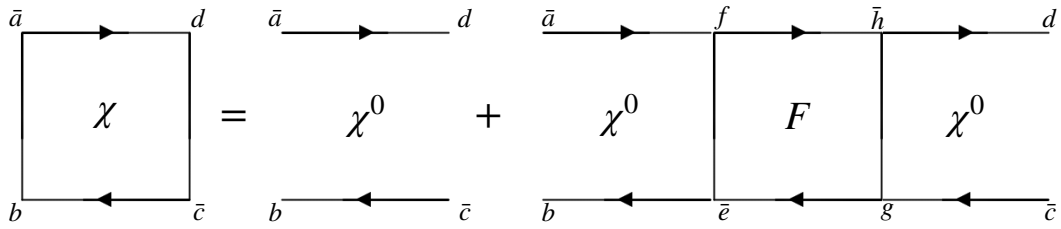

Figure 3.7: Diagrammatic representation of Eq.(3.117)

Also, we can express the full generalized susceptibility as

$$\begin{aligned}\chi_{\bar{a}b\bar{c}d}(\tau_{\bar{a}},\tau_b,\tau_{\bar{c}},\tau_d) =& \chi^0_{\bar{a}b\bar{c}d}(\tau_{\bar{a}},\tau_b,\tau_{\bar{c}},\tau_d) \\ &+ \sum_{f\bar{e}g\bar{h}} \chi^0_{\bar{a}b\bar{e}f}(\tau_{\bar{a}},\tau_b,\tau_{\bar{e}},\tau_f) F_{f\bar{e}g\bar{h}}(\tau_f,\tau_{\bar{e}},\tau_g,\tau_{\bar{h}}) \chi^0_{\bar{h}g\bar{c}d}(\tau_{\bar{h}},\tau_g,\tau_{\bar{c}},\tau_d)\end{aligned} \tag{3.117}$$

Despite the cumbersomeness of the (3.116) and (3.117) equations described above, they look quite simple in diagrammatic representation. They are shown in the Figures 3.6 and 3.7 .

3.4. Parquet equation

Before diving into the parquet equation, we must introduce the concept of reducibility for two-particle diagrams of the full vertex function F. The reducibility classification is based on how the diagrams can be separated by cutting two internal single-particle Green's function lines. Irreducible diagrams cannot be separated this way and are similar to irreducible self-energy diagrams on a single-particle level. On the other hand, reducible diagrams can be split into two parts by cutting two internal single-particle Green's function lines. The reducibility always refers to a specific channel that determines how two of the four outer legs can be separated from the other two. It is worth noting that there are different ways to cut lines in a diagram.

In Figure 3.8, we have labeled the four legs of vertex functions as a, $\bar{b}$, c, and $\bar{d}$. Among these, a and c represent outgoing particles, while $\bar{b}$ and $\bar{d}$ refer to incoming particles. Based on this labeling, we can distinguish between three possibilities in Figure 3.8:

- (a) Diagrams in which (a, $\bar{b}$) can be separated from (c, $\bar{d}$) are referred to as particle-hole longitudinal (particle-hole) reducible diagrams.
- (b) In diagrams where (a, c) can be separated from ($\bar{b}$,$\bar{d}$), we call them particle-particle (particle-particle) reducible.
- (c) Finally, (a, $\bar{d}$) from ($\bar{b}$,c) are referred to as particle-hole transversal ($p\bar{h}$) reducible diagrams.

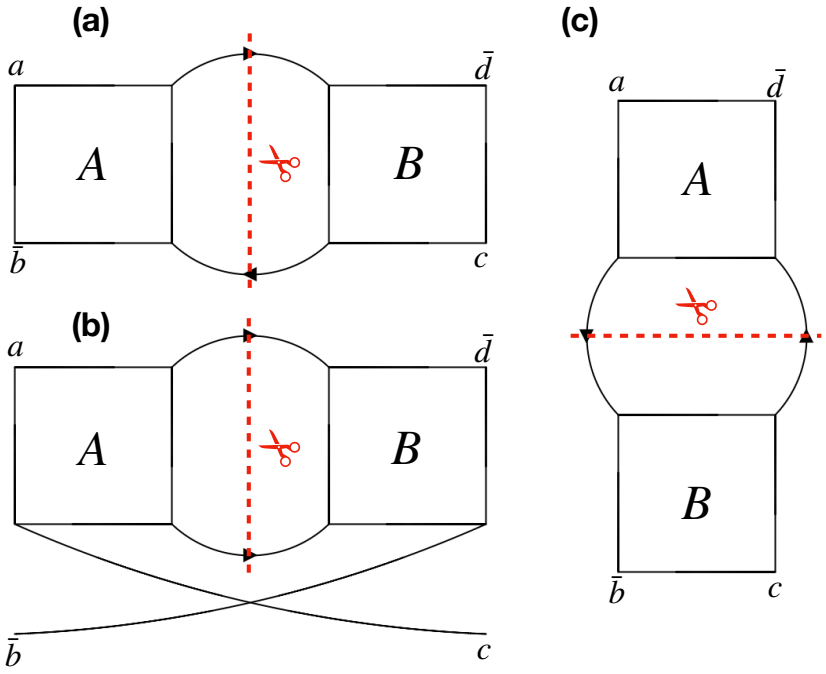

Figure 3.8: Schematic representation of a generic (a) particle-hole longitudinal reducible diagram (particle-hole), (b) particle-particle reducible diagram (particle-particle), and (c) particle-hole transversal reducible diagram ($p\bar{h}$), contributing to the full scattering amplitude F. Figure reproduced from [155].

Each diagram is fully irreducible or reducible in one channel only. For example, Fig. 3.8(a) shows the diagram in the longitudinal particle-hole channel (particle-hole). Subdiagrams A and B can be separated by cutting the Green's function lines a and $\bar{b}$. If the diagram is reducible in the transverse particle-hole channel ($p\bar{h}$), it can be divided into two parts, one of which contains the outer legs a and $\bar{d}$, and the other $\bar{b}$ and c by cutting two internal lines. However, it is impossible to divide subdiagrams A and B into two parts by cutting only one inner line because it would lead to subdiagrams with three outer branches, violating particle conservation. Hence, every diagram is either fully irreducible or reducible in at most one channel. It means that the full vertex function F can be decomposed into four parts: a completely two-particle irreducible (Λ) and a two-particle reducible contribution (Φ_r) in three different channels:

$$F = \Lambda + \Phi_{ph} + \Phi_{p\bar{h}} + \Phi_{pp} \tag{3.118}$$

This equation is the two-particle analog of the classification of single-particle diagrams as reducible and irreducible, defining self-energy.

3.4.1. Bethe-Salpeter equation

Although it is easy to calculate the full vertex function F from the generalized susceptibility χ using the (3.117) equation, to work with the parquet equation, additional relations are needed between F and the reducible vertices Φ_r. It can be achieved by defining new quantities Γ_r:

$$F = \Phi_r + \Gamma_r \quad r = pp, ph, p\bar{h} \tag{3.119}$$

Since F contains all diagrams and Φ_r contains all diagrams reducible in channel r, Γ_r is the set of all irreducible diagrams in the respective channel. Moreover, since each diagram is either fully irreducible or reducible in a given channel, we have that

$$\Gamma_r = \Lambda + \Phi_i + \Phi_j \quad i, j \neq r \tag{3.120}$$

In this case, the diagram in Fig. 3.8(a) belongs to both $\Gamma_{p\bar{h}}$ and Γ_{pp} because it is reducible in the longitudinal particle-hole (particle-hole) channel.

The Bethe-Salpeter equation [160, 143] allows to calculate the Γ_r vertices from F through an integral equation:

$$F = \Gamma_r + \Gamma_r \chi_r^0 F \quad \Phi_r = \Gamma_r \chi_r^0 F \tag{3.121}$$

As expressed in Equation (3.121), F encompasses both irreducible diagrams in channel r (denoted as Γ_r) and reducible ones (denoted as Φ_r). The reducible diagrams can be depicted using the irreducible diagrams and the complete set of diagrams, F. When these components are linked with the bare susceptibility, it produces reducible diagrams for channel r. It is worth noting that while any given reducible diagram can be divided into two subdiagrams in multiple manners, the Bethe-Salpeter stipulation ensures that the left subdiagram is always associated with the irreducible vertex Γ_r, ensuring a unique split.

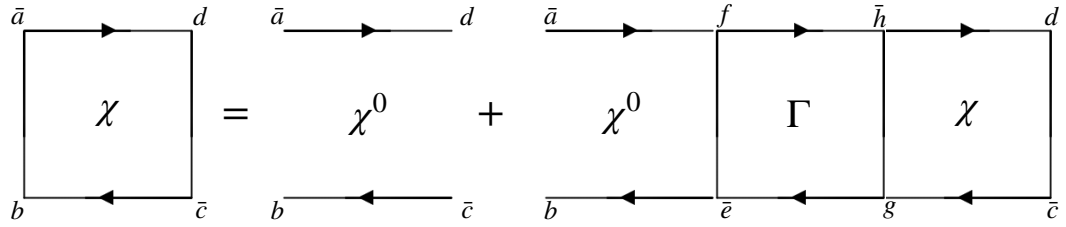

Figure 3.9: Diagrammatic representation of Bethe-Salpeter equation (3.122).

Making one of the components irreducible eliminates the potential for double counting any diagrams.

Finally, the Bethe-Salpeter equation (3.121) states another useful equation, which connects susceptibility χ_r and irreducible diagrams Γ_r in channel r.

$$\begin{aligned}\chi_r =&\chi_r^0 + \chi_r^0 F \chi_r^0 \\ =&\chi_r^0 + \chi_r^0 \left[\Gamma_r + \Gamma_r \chi_r^0 F\right] \chi_r^0 \\ =&\chi_r^0 + \chi_r^0 \Gamma_r \chi_r^0 + \chi_r^0 \Gamma_r \chi_r^0 F \chi_r^0 \\ =&\chi_r^0 + \chi_r^0 \Gamma_r \left[\chi_r^0 + \chi_r^0 F \chi_r^0\right] \\ =&\chi_r^0 + \chi_r^0 \Gamma_r \chi_r \end{aligned} \tag{3.122}$$

We can write the (3.122) equation using the sum formula for geometric progression as:

$$\chi_r = \left[1 - \chi_r^0 \Gamma_r\right]^{-1} \chi_r^0 \tag{3.123}$$

Hence, we can find a criterion for the divergence χ_r of dressed susceptibility for any channel r:

$$1 \stackrel{!}{=} \chi_r^0 \Gamma_r, \tag{3.124}$$

which we can express as an eigenvalue equation

$$\lambda \Psi_r = \chi_r^0 \Gamma_r \Psi_r \tag{3.125}$$

Here, Ψ_r represents a particle channel of χ_r, where divergence occurs. Resulting criteria (3.124) can be expressed as:

$$1 \stackrel{!}{=} \lambda \tag{3.126}$$

The above equations are convenient tools for finding phase transition points where the susceptibility tends to infinity.

Despite the original formulation (3.121), this equation is often called the Bethe-Salpeter equation. It resembles the Dyson equation but uses the bare susceptibility χ_r^0 and irreducible vertex in r channel Γ_r, rather than the bare single-particle Green's function and self-energy, respectively. As a result, we obtain the dressed susceptibility χ_r instead of the dressed single-particle Green's function.

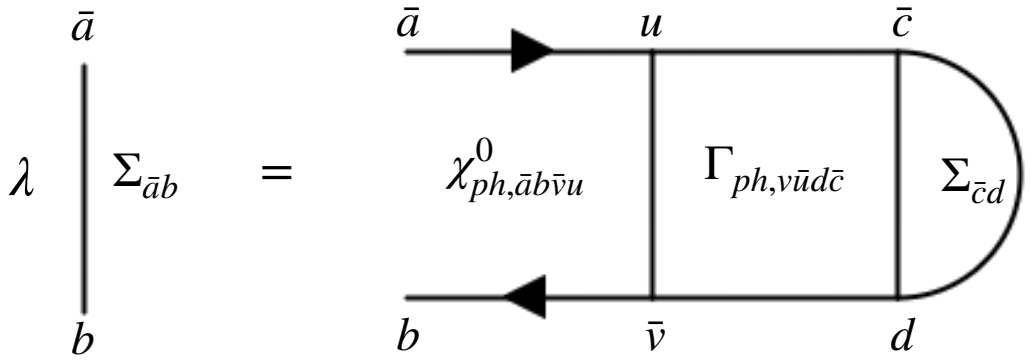

Figure 3.10: Diagrammatic representation of linearized RPA equation (3.131).

3.4.2. Random phase approximation

Bohm and Pines first proposed the random phase approximation (RPA) in 1950 [161, 162, 163]. They distinguished two types of electron response to perturbations: one that remains constant regardless of the electron's position and another that averages zero due to the unpredictable location of the electrons. RPA only considers sequential response. More recent research has shown that determining the response function using RPA is similar to endlessly adding the most significant terms of perturbation theory, resulting in a series of Feynman bubble diagrams. While RPA's straightforwardness facilitates a preliminary understanding of specific scenarios, its perturbation theory basis is most accurate when applied to non-interacting systems.

It is recognized that RPA can sometimes overestimate system response and critical phase shift temperatures. Notably, RPA does not adhere to the Mermin-Wagner theorem, which assumes magnetic states above absolute zero for 2D systems, and also violates the Pauli principle in specific sum rules. However, its value lies in its ability to simplify the study of nesting effects at the Fermi surface and because it captures the general characteristics of systems.

The RPA method is often used for superconductors, especially when spin and charge fluctuations promote Cooper pairing. This method uses the RPA susceptibility to form the core of the irreducible vertex Γ_{pp}, simplifying the calculation of critical temperature and superconducting symmetry [164, 165, 166, 167]. It has been used effectively for various materials and, in particular, has predicted d-wave pairing in cuprate models, consistent with experimental results [166, 165, 167].

The RPA approach approximate the irreducible Γ_{ph} vertex as

$$\Gamma^{\mathrm{RPA}}_{ph,a\bar{b}c\bar{d}} = V_{a\bar{b}c\bar{d}} \tag{3.127}$$

So, $\Gamma^{\mathrm{RPA}}_{ph}$ represents all possible scattering paths with amplitudes, provided via interaction

Hamiltonian $\hat{H}_{int}$:

$$\hat{H}_{int} = \frac{1}{4}\sum_{\bar{a}\bar{b}cd} \Gamma^{\mathrm{RPA}}_{ph,c\bar{a}d\bar{b}} \hat{c}^{\dagger}_{\bar{a}}\hat{c}^{\dagger}_{\bar{b}}\hat{c}_{c}\hat{c}_{d} \tag{3.128}$$

In most cases, $\Gamma^{\mathrm{RPA}}_{ph}$ is frequency independent, since $\hat{H}_{int}$ is usually frequency independent. However, in the general case, $\Gamma^{\mathrm{RPA}}_{ph}$ can be frequency dependent. The physical susceptibility in the particle-hole channel, taking into account the frequency-independent interaction, in the RPA approximation will have the form:

$$\chi^{\mathrm{RPA}}_{ph,\bar{a}b\bar{c}d}(\omega) = \chi^{0}_{ph,\bar{a}b\bar{c}d}(\omega) + \sum_{f\bar{e}g\bar{h}} \chi^{0}_{ph,\bar{a}b\bar{e}f}(\omega)\Gamma^{\mathrm{RPA}}_{ph,f\bar{e}g\bar{h}}\chi^{\mathrm{RPA}}_{ph,\bar{h}g\bar{c}d}(\omega), \tag{3.129}$$

where

$$\chi^{0}_{ph,\bar{a}b\bar{e}f}(\omega) = \frac{1}{\beta^2}\sum_{\nu\nu'} \chi^{0}_{ph,\bar{a}b\bar{c}d}(\nu,\nu',\omega). \tag{3.130}$$

Using the (3.125) equation, we can derive criteria for emerging a static ($\omega = 0$) particle-hole-instability with an infinite lifetime

$$\lambda\Sigma_{\bar{a}b} = \sum_{\bar{v}u\bar{c}d} \chi^{0}_{ph,\bar{a}b\bar{v}u}(\omega = 0)\Gamma_{ph,u\bar{v}d\bar{c}}\Sigma_{\bar{c}d} \tag{3.131}$$

where

$$\chi^{0,ph}_{\bar{a}b\bar{c}d}(\omega = 0) = -\frac{1}{\beta}\sum_{\nu} G^{1}_{d\bar{a}}(\nu)G^{1}_{b\bar{c}}(\nu) \tag{3.132}$$

Here, $\Sigma_{\bar{a}b}$ is the order parameter of possible instability in the particle-hole channel. A diagrammatic representation of Eq.(3.131) is shown in Fig.3.10. Hence, RPA is sensitive to phase symmetry breaking, so it makes RPA valuable for studying collective excitations in many-body quantum physics. By accounting interactions on the mean field level, RPA can effectively detect symmetry-breaking phases.

3.4.3. Linearized Eliashberg equation

The last topic in this Chapter is the linearized Eliashberg equation [168, 169, 170, 171]. The superconducting state occurs when the particle-particle susceptibility χ_{pp} diverges at zero frequency ($\omega = 0$). So, taking into account Eq.(3.124), we can write

$$1 \stackrel{!}{=} \chi^{0}_{pp}\Gamma_{pp} \tag{3.133}$$

Furthermore, reformulate this equation as an eigenvalue problem.

$$\begin{aligned}
\lambda\Delta_{\bar{a}\bar{b}}(\nu) =& \frac{1}{\beta^2}\sum_{\nu'\nu''}\sum_{vu\bar{c}\bar{d}} \chi^{0}_{pp,\bar{a}v\bar{b}u}(\nu,\nu')\Gamma_{pp,u\bar{d}v\bar{c}}(\nu',\nu'')\Delta_{\bar{c}\bar{d}}(\nu'') \\
=& \left\{\chi^{0,pp}_{\bar{a}b\bar{c}d}(\nu,\nu') = -\beta G^{1}_{d\bar{a}}(\nu)G^{1}_{b\bar{c}}(-\nu)\delta_{\nu\nu'}\right\} = \\
=& -\frac{1}{\beta}\sum_{\nu'}\sum_{vu\bar{c}\bar{d}} G^{1}_{v\bar{a}}(\nu)G^{1}_{u\bar{b}}(-\nu)\Gamma_{pp,u\bar{d}v\bar{c}}(\nu,\nu')\Delta_{\bar{c}\bar{d}}(\nu')
\end{aligned} \tag{3.134}$$

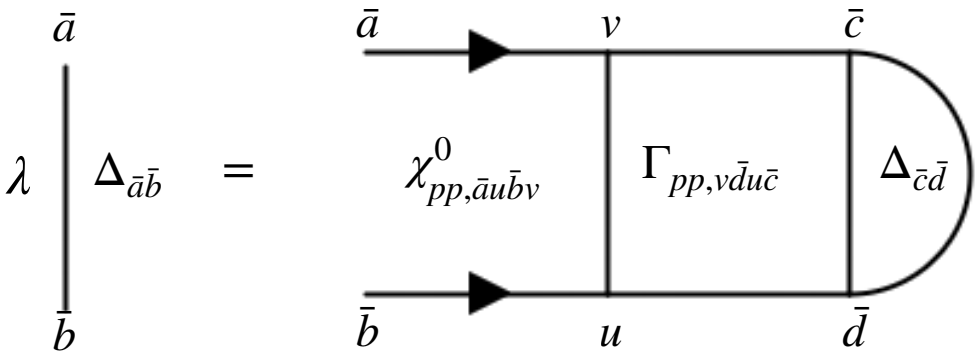

Figure 3.11: Diagrammatic representation of Linearized Eliashberg Equation (3.134).

Here, the eigenvectors $\Delta_{\bar{a}\bar{c}}(\nu)$ correspond to the particular channel in which $\chi_{pp}(\omega = 0)$ diverges. A diagrammatic representation of Eq.(3.134) is shown in Fig.3.11. This divergence corresponds to the superconducting order parameter and superconducting gap functions. One can use the linearized Eliashberg equation to find the superconducting order parameter, its symmetry, and the critical temperature of the superconducting transition T_c.

In the Bardeen-Cooper-Schrieffer (BCS) theory [172], a foundational superconductivity theory, the interaction responsible for pairing electrons is assumed to be constant within a specific frequency range. However, the linearized Eliashberg equation offers a more generalized perspective than the BCS theory. It extends the concepts of the linearized BCS gap equation to account for gaps and pairing interactions that vary with frequency. Instead of assuming a constant interaction as in BCS, the Eliashberg equation allows for interactions that can change depending on the frequency. When considering the scenario where the frequency dependence is taken to its limit, essentially making it frequency-independent, we can draw a connection between the Eliashberg equation and the BCS theory. In this scenario, the mathematical summation over fermionic Matsubara frequencies, which involves two one-particle Green's functions in the linearized Eliashberg equation, can be computed analytically. For a system characterized by a single energy band and a Green's function that does not interact with other entities and which has a specific dispersion relation, the equation becomes:

$$\Delta(\mathbf{k}) = -\frac{1}{2N_{\mathbf{k}}} \sum_{\mathbf{k}'} \frac{\tanh(\varepsilon(\mathbf{k}'))}{2\varepsilon(\mathbf{k}')} \Gamma(\mathbf{q} = 0, \mathbf{k}', \mathbf{k}) \Delta(\mathbf{k}') \tag{3.135}$$

This equation is essentially the linearized BCS gap equation. It describes the energy gap as a function of the wave vector, $\mathbf{k}$. It highlights the relationship between the Eliashberg equation and the BCS theory in the case of frequency-independent interactions.

However, the effective particle-particle coupling Γ_{pp} is still undefined. To resolve this problem, we can apply the parquet equations described in the previous sections and

RPA. The irreducible particle-particle vertex Γ_{pp} can be constructed from from fully irreducible vertex Λ, and reducible vertexes in particle-hole and $p\bar{h}$ channels Φ_{ph} and $\Phi_{p\bar{h}}$, respectively:

$$\Gamma_{pp} = \Lambda + \Phi_{ph} + \Phi_{p\bar{h}} \tag{3.136}$$

As a first approximation, we can assume that

$$\hat{H}_{int} = \frac{1}{4}\sum_{abcd} \Lambda_{a\bar{b}c\bar{d}} \hat{c}^{\dagger}_{\bar{b}} \hat{c}^{\dagger}_{\bar{d}} \hat{c}_a \hat{c}_c \tag{3.137}$$

So, we consider all first-order two-particle diagrams in fully irreducible vertex Λ. Our next step, will be constructing Φ_{ph} and $\Phi_{p\bar{h}}$ using RPA. As we know

$$\Phi_r = \Gamma_r \chi^0_r F = \Gamma_r \chi_r \Gamma_r \tag{3.138}$$

and RPA assume that $\Gamma^{\mathrm{RPA}}_{ph} = \Lambda$. Hence, we can define that

$$\Phi_{ph}(\omega) = \Lambda \chi^{\mathrm{RPA}}_{ph}(\omega) \Lambda \tag{3.139}$$

where $\chi^{\mathrm{RPA}}_{ph} = \left[1 - \chi^0_{ph}\Lambda\right]^{-1} \chi^0_{ph}$ Corresponding $\Phi^{\mathrm{RPA}}_{p\bar{h}}$ in $p\bar{h}$ channel, can be calulated from Φ^{RPA}_{ph} using crossing symmetry. To sum up, we can write the irreducible particle-particle vertex Γ_{pp} as

$$\Gamma_{pp,a\bar{b}c\bar{d}}(\omega = \nu - \nu') = \Lambda_{a\bar{b}c\bar{d}} + \Phi_{ph,a\bar{b}c\bar{d}}(\omega) \underbrace{-\Phi_{ph,a\bar{d}c\bar{b}}(\omega)}_{\text{crossing symmetry}} \tag{3.140}$$

We obtained the irreducible vertex Γ_{pp} using the parquet equation and RPA, which considers spin and charge fluctuations leading to Cooper instability. Equations (3.134) and (3.140) provide a comprehensive framework for studying superconductivity, including repulsive interaction-induced superconductivity.

4. Emergent correlated phases in rhombohedral trilayer graphene induced by proximity spin-orbit and exchange coupling

4.1. Introduction

We began to study the interaction of many-particle effects with spin interactions caused by the proximity effect from not a minimal multilayer graphene system, like Bernal bilayer graphene (BBG), but from a more complicated rhombohedral trilayer graphene (RTG) system. The groundbreaking discovery of correlated electronic phases and superconductivity in magic-angle twisted bilayer graphene (TWBG) has garnered significant attention [173, 174, 175, 176] in the condensed matter community. This system is characterized by a highly flat electronic band structure at the Fermi level, and this feature is extensively studied [177, 178, 179, 180, 181, 182, 183, 184, 185, 186, 187], in both theoretical [188, 189, 190, 191, 192, 193, 194, 195, 196, 197, 198] and experimental research [199, 200, 201, 202, 203, 204, 205, 206, 207, 208, 209, 210, 211, 212, 213]. However, controlling the stacking and twist angles in van der Waals heterostructures remains a formidable challenge [214, 215, 216, 217, 218, 219, 220, 221].

Interestingly, electronic correlations in multilayer graphene systems are not confined to moiré patterns. Recent observations have shown the emergence of half and quarter metallic states as well as superconductivity in RTG [222, 223, 224, 225, 226, 227] and BBG [228, 229, 230, 231, 232, 233, 234, 235, 236, 237, 238]. Both systems exhibit strong electronic correlations, similar to magic-angle TWBG. The common feature among all systems mentioned above is the presence of well-pronounced van Hove singularities near the charge neutrality point [177, 178, 239]. In RTG, the low energy of these singularities allows for the tuning of symmetry-breaking phases through doping [222], and its multilayer structure enables efficient control of these phases via a displacement field [239, 222]. Figure 4.1 shows the experimental results, adapted from [222], the inverse compressibility $\frac{\partial \mu}{\partial n_e}$ of the Fermi liquid in RTG as a function of displacement field and carrier density, where we can observe negative values, which are direct evidence of the presence of strong electron correlations in this system [240]. However, the nature of the correlated phases and the measurement of local magnetic structure, spin and charge transport still need to be uncovered due to insufficient experimental data.

Furthermore, van der Waals engineering offers another venue for tuning electronic band structures. Specifically, proximity-induced spin interactions, such as spin-orbit (SO)

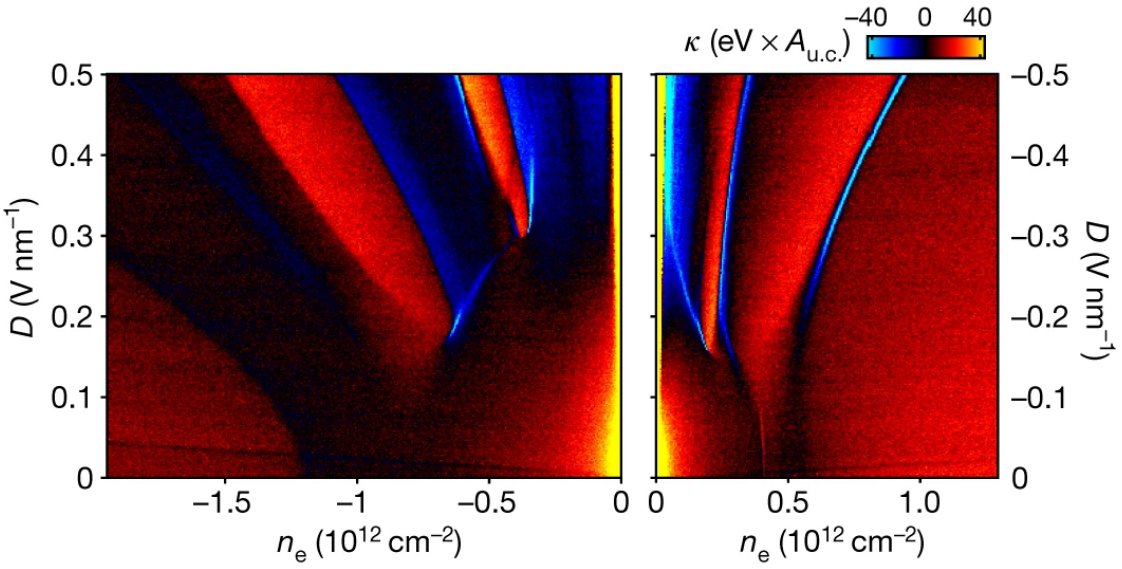

Figure 4.1: The false-color plot of the experimental inverse compressibility of RTG as a function of displacement field D and carrier density n_e for hole and electron doping regimes. Adapted from [222].

and exchange (EX) couplings, can endow graphene with inherently lacking properties, like SO or EX fields. From theoretical predictions [241, 86, 68, 69, 242, 243, 134, 244, 245, 246, 78, 242, 243, 244, 247] and experimental observations [108, 109, 111, 74, 91, 112, 90, 113, 114, 117, 248, 110] it was confirmed the appearance of various types of SO coupling as well as (anti)ferromagnetic EX couplings on the meV scale [247, 245, 246, 249, 242, 243, 244, 248, 110, 247]. Moreover, it has been suggested that these SO and EX couplings can be interchanged via a displacement field [242, 243].

One intriguing question that naturally arises is the interplay between correlated electronic physics and proximity-induced spin interactions. In the context of RTG, two key observations set the stage for this research: (i) The van Hove singularity is primarily formed by the bands that include the p_z orbitals of the top and bottom layers [239], and (ii) the scale of spin proximity effects is on the order of meV, which is also the expected scale for the correlated band gaps. These observations lead us to hypothesize that spin proximity effects could impact the symmetry-broken phases in RTG.

In the present work, we provide compelling evidence that proximity-induced SO and EX interactions give rise to and govern new strongly correlated phases. We focus our study on $MoSe_2$/RTG/WSe_2 heterostructures to investigate the SO proximity effects and on CGT/RTG/CGT heterostructures with parallel and antiparallel magnetizations of CGT ($Cr_2Ge_2Te_6$), depicted in Fig. 4.2, to explore the EX proximity effects [244]. It needs to be mentioned that $Cr_2Ge_2Te_6$ is a ferromagnetic material with layers, known for its potential use in spintronics and magnetic storage [250, 251, 252, 253, 254]. Via utilizing the random-phase approximation methodology [161, 162, 163, 255, 256, 257],

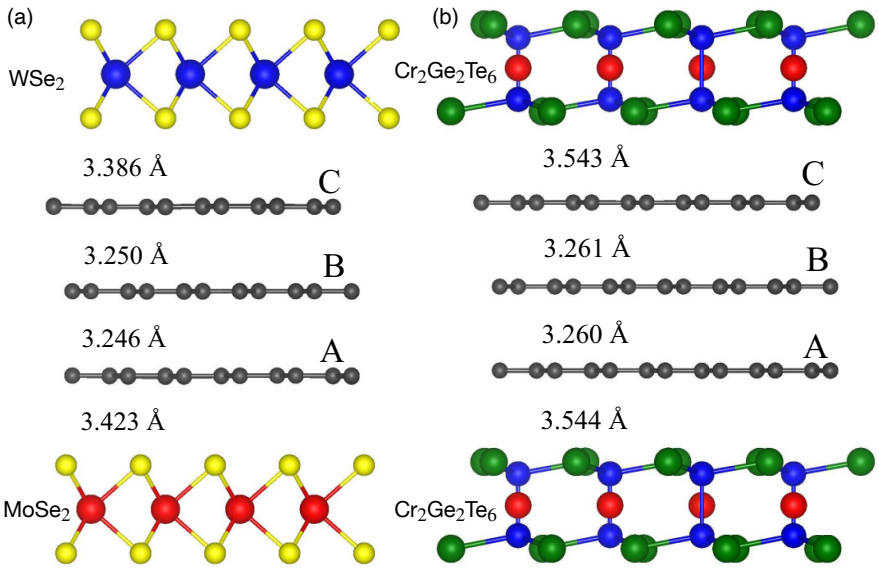

Figure 4.2: Encapsulated RTG heterostructure geometries. On the left: RTG encapsulated by TMDC ($MoSe_2$ and WSe_2). On the right: RTG encapsulated by CGT. Reproduced from [244].

we initially compute the correlated phase diagram for pristine RTG. The results reveal an intervalley coherent (IVC) state [258] and a Stoner instability, consistent with prior predictions [259, 260].

Remarkably, introducing spin interactions disrupts the degeneracies associated with the IVC and Stoner phases, thereby inducing spin anisotropy and spin bias. It leads to the emergence of novel phases, such as a *spin-valley-coherent* (SVC) state. The SVC phase is primarily driven by proximity-induced valley-Zeeman coupling, while Rashba coupling plays a secondary role. The emergence of the SVC phase opens up exciting new avenues for spintronics applications [25], as the Coulomb interactions give rise to unique spin-valley couplings. Moreover, we find that the magnetic heterostructures exhibit a pronounced magneto-correlation effect; the induced phases are highly sensitive to the relative orientation of the CGT magnetizations.

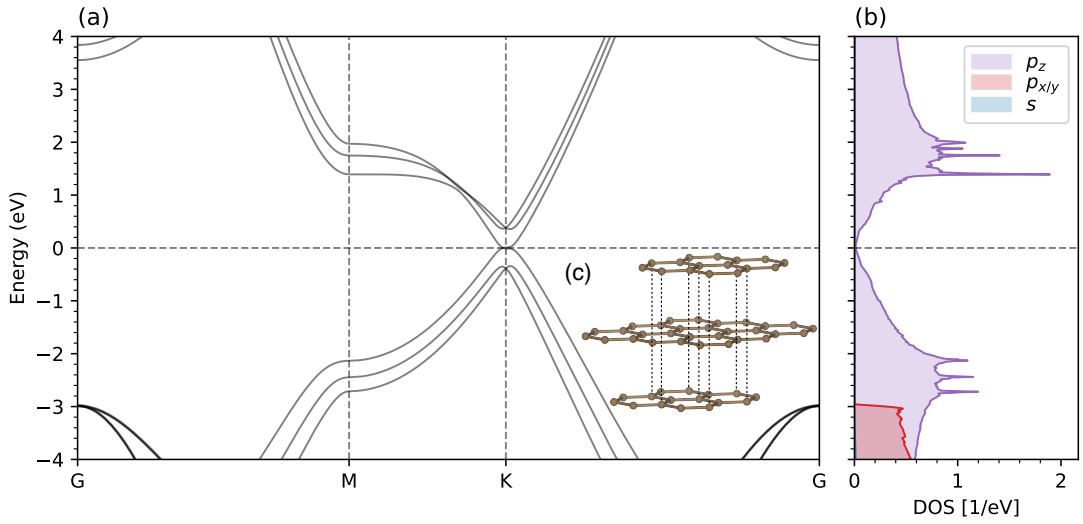

Figure 4.3: ABC-stacked Graphene's band structure (a) and orbital-resolved density of states (b) are calculated, along with its crystal structure (c).

4.2. Pristine RTG tight-binding model

To realistically model the orbital physics of RTG, we utilize the Bloch Hamiltonian from [239, 244, 261, 262, 263]:

$$\hat{h}_0(\mathbf{k},\tau) = \begin{pmatrix} \Delta+V & \gamma_0 f & \gamma_4 f^* & \gamma_1 & 0 & 0 \\ \gamma_0 f^* & \eta+V & \gamma_3 f & \gamma_4 f^* & \gamma_6 & 0 \\ \gamma_4 f & \gamma_3 f^* & \Delta+u_m & \gamma_0 f & \gamma_4 f^* & \gamma_1 \\ \gamma_1 & \gamma_4 f & \gamma_0 f^* & \Delta+u_m & \gamma_3 f & \gamma_4 f^* \\ 0 & \gamma_6 & \gamma_4 f & \gamma_3 f^* & \eta-V & \gamma_0 f \\ 0 & 0 & \gamma_1 & \gamma_4 f & \gamma_0 f^* & \Delta-V \end{pmatrix} \tag{4.1}$$

that acts on single-particle, p_z-orbital Bloch states. These states have momenta $\mathbf{k} = (k_x, k_y)$ measured from K and K' valleys. The linearized nearest-neighbor structural factor is given by $f = -\left(\sqrt{3}a/2\right)(\tau k_x - i k_y)$, where a is graphene's lattice constant and $\tau_{K/K'} = \pm 1$ is the valley index. For a visualization interpretation of the orbital hopping parameters, refer to Fig. 4.4 (a). We use an orbital basis ordered according to $(A_1, B_1, A_2, B_2, A_3, B_3)$, representing the layer-resolved sublattices $l = 1, 2, 3$. The unit cell of RTG is shown in Fig. 4.4 (a). The on-site energies V and u_m are incorporated into the Hamiltonian to account for the electrostatic potentials on different layers. The parameter u_m represents the potential energy difference between the central layer and the average potential of the outer layers. At the same time, V corresponds to the potential energy difference between the external layers, describing an effect of the displacement field. Additionally, η and Δ are on-site potentials whose asymmetry arises due to the vertical hoppings γ_1 and γ_6, see Fig. 4.4(a).

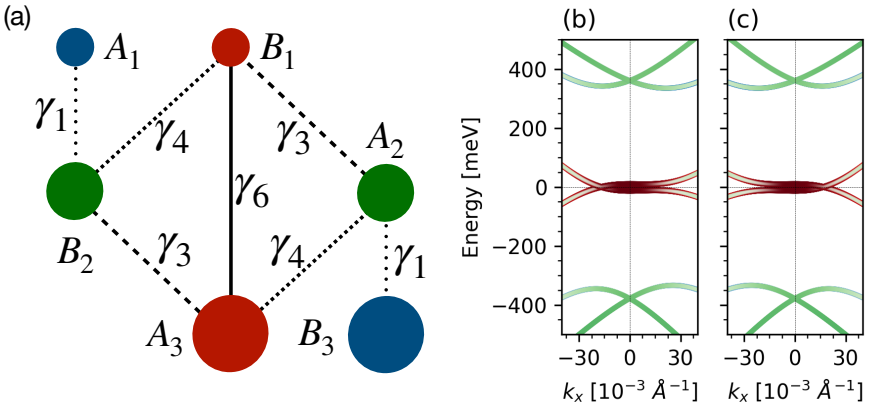

Figure 4.4: (a) The RTG unit cell displays interlayer orbital hoppings and calculated single-particle electronic dispersions at K' (b) and K (c) without displacement fields for pristine RTG. Panels (b) and (c) are color-coded to denote atomic projections, as in panel (a). The Fermi level corresponds to a zero energy value.

Our analysis began with calculating the band structure of pristine RTG. Figure 4.4 displays a single-particle electronic band structure of RTG near K' (b) and K (c) without a displacement field. The band structure is color-coded based on atomic projections defined in panel (a), and we observe that the low-energy bands are mainly localized on B_1/A_3 lattice sites. Using this information, we downfolded Hamiltonian (4.1) into a effective two-orbital Hamiltonian $\tilde{h}_0(\mathbf{k},\tau)$ in the orbital basis B_1/A_3 (See Appendix C):

$$\tilde{h}_0(\mathbf{k},\tau) = (v_f k)^3/\gamma_1^2\left[\hat{\sigma}_x\cos(3\phi) + \hat{\sigma}_y\sin(3\phi)\right] + \gamma_6\hat{\sigma}_x + V\left(1 - \frac{(v_f k)^2}{\gamma_1}\right)\sigma_z, \qquad (4.2)$$

The Fermi velocity of the Dirac electron is denoted as $v_F = (\sqrt{3}a/2)\gamma_0$, and Pauli matrices $\hat{\sigma}_i$ are defined based on B_1/A_3 sites basis while $\tan\phi = k_y/k_x$. The Hamiltonian (4.2) only considers γ_0, γ_1, and γ_6 hopping and neglects γ_3 and γ_4 for simplicity. Hopping γ_3 and γ_4 contribute minor effects on RTG band structure [239]. The downfolding procedure is described in the Appendix C.

Figure 4.5 displays the low-energy electronic band structure at K' (a) and K (b) for pristine RTG without displacement fields $V = 0$ using Hamiltonian (4.1). There is a strong trigonal effect in the low-energy band structure of pristine RTG. Reviewing Hamiltonian (4.2), we can conclude that the γ_6 hopping from the second component of Eq. (4.2) causes the trigonal warping effect in the low-energy band structure of pristine RTG, while the first component produces the Dirac cone. At the same time, the last component Eq.(4.2), which describes the influence of the displacement field, exhibits the "Mexican Hat" effect [264].

The bandgap of pristine RTG can be opened via the displacement field V, which is demonstrated in Fig. 4.6. The band structure becomes flatter, and the density of states near the van Hove singularity increases with increasing displacement field, as

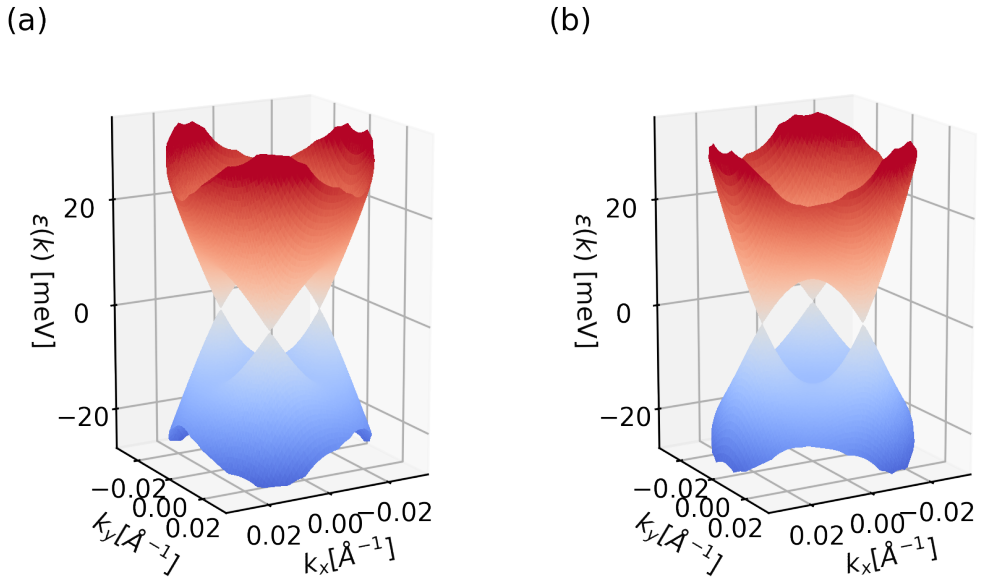

Figure 4.5: Low-energy electronic band structure of RTG at K' (a) and K (b) calculated from $\hat{h}(\mathbf{k}, \tau)$ without displacement fields for pristine RTG. Color code denote band energy.

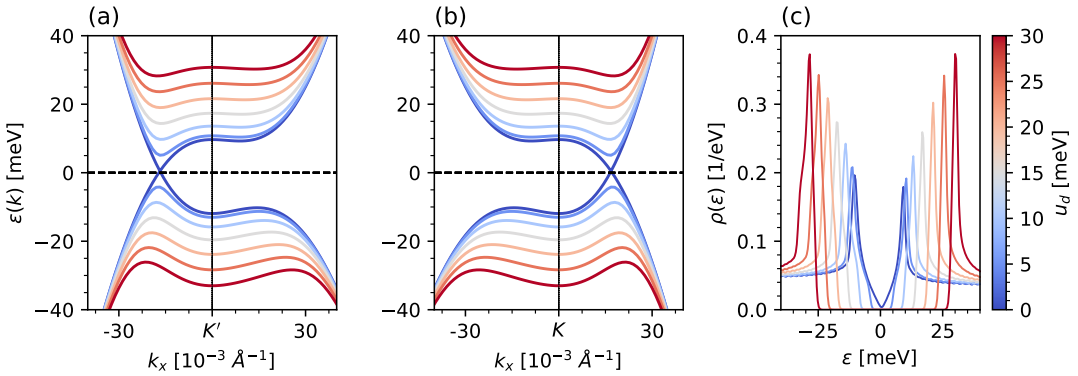

Figure 4.6: Calculated low-energy electronic dispersions at K' (a) and K (b) using $\hat{h}(\mathbf{k}, \tau)$ and the low-energy density of states (c) with and without displacement fields for pristine RTG. The amplitude of the displacement field is color-coded.

shown in Fig. 4.6 (c) with consideration of finite temperature broadening ($T = 4.2$ K). Due to trigonal warping and effective bandgap control, RTG is a promising material for correlated physics.

4.3. Proximity-induced spin interactions

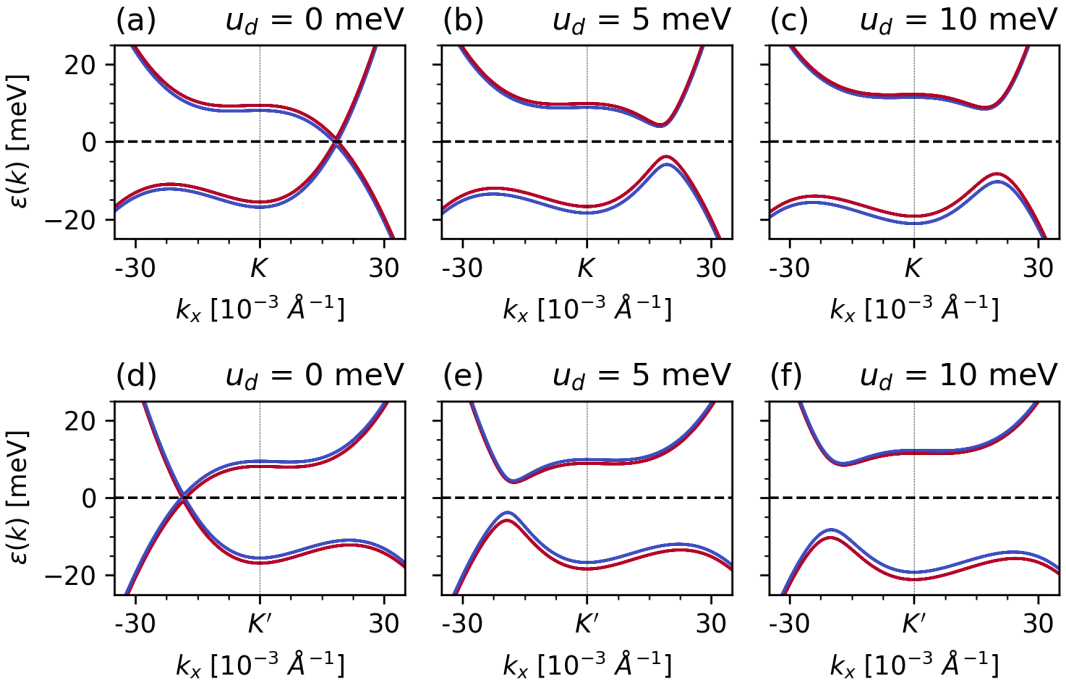

Figure 4.7: Calculated low-energy electronic dispersions at K' (a),(b), and (c) and K (d), (e) and (f) using $\hat{h}(\mathbf{k}, \tau) + \hat{h}_{prox}(\tau)$ with and without displacement fields for $MoSe_2$-/RTG/WSe_2 heterostructure. Colorcode denotes band structure spin-polarization.

Pristine RTG has weak SO coupling at K and K' valleys, around 10 μeV scale [261, 263]. To induce larger spin splittings, RTG should be encapsulated by strong SO or magnetic materials such as $MoSe_2$ and WSe_2, and ferromagnetic CGT, respectively. The corresponding Hamiltonian for proximity-induced SO and EX couplings in RTG electrons is given by $\hat{h}_{\text{prox}}(\tau) = \sum_l \hat{h}^l_R(\tau) + \hat{h}^l_I(\tau) + \hat{h}^l_{\text{ex}}(\tau)$, which includes the Rashba and intrinsic SO, and EX terms for the l-th layer [244, 69, 78, 134], parameterized by sublattice-resolved couplings λ^l_R, $\lambda_I^{A_l/B_l}$, and $\lambda_{\text{ex}}^{A_l/B_l}$, respectively.

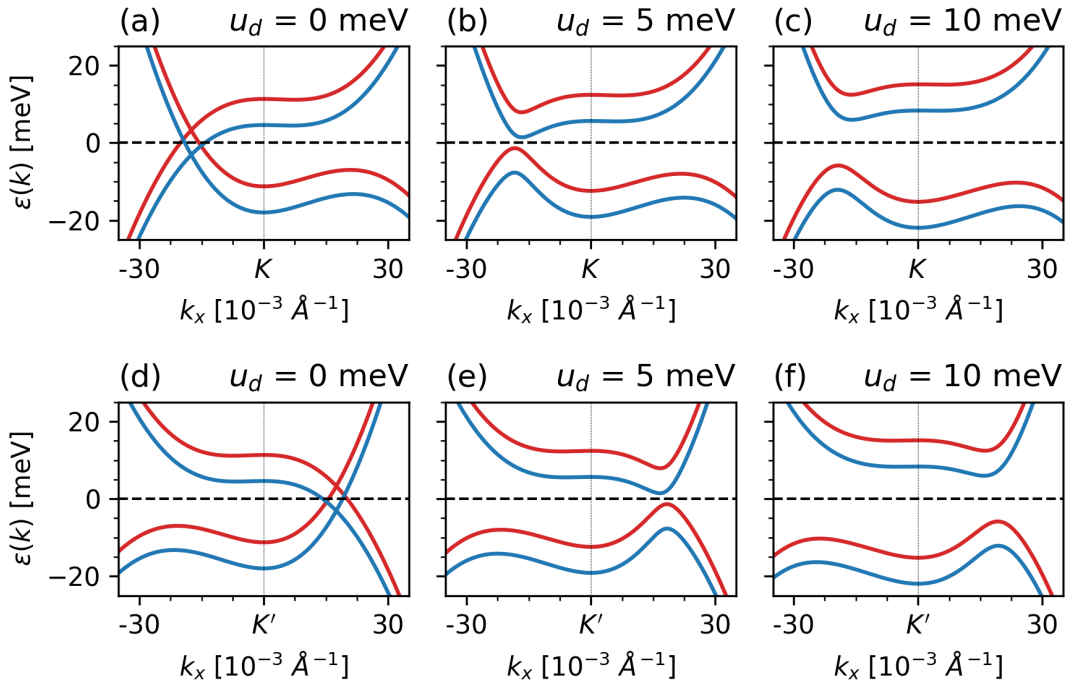

Figure 4.8: Calculated low-energy electronic dispersions at K' (a),(b), and (c) and K (d), (e) and (f) using $\hat{h}(\mathbf{k},\tau)+\hat{h}_{prox}(\tau)$ with and without displacement fields for CGT-/RTG/CGT heterostructure with ferromagnetic CGT alignments. Colorcode denotes band structure spin-polarization.

$$\hat{h}^l_R(\tau) = \begin{pmatrix} 0 & 2i\lambda^l_R\, s^\tau_- \\ -2i\lambda^l_R\, s^\tau_+ & 0 \end{pmatrix}, \tag{4.3}$$

$$\hat{h}^l_I(\tau) = \begin{pmatrix} \tau\,\lambda^{A_l}_I\, s_z & 0 \\ 0 & -\tau\,\lambda^{B_l}_I\, s_z \end{pmatrix}, \tag{4.4}$$

$$\hat{h}^l_{\mathrm{ex}}(\tau) = \begin{pmatrix} -\lambda^{A_l}_{\mathrm{ex}}\, s_z & 0 \\ 0 & -\lambda^{B_l}_{\mathrm{ex}}\, s_z \end{pmatrix}. \tag{4.5}$$

In this equation, $s_{x,y,z}$ represents the Pauli matrices, while $s^\tau_\pm$ represents valley-resolved spin-flip operators. The latter can be expressed as

$$s^\tau_\pm = \frac{1}{2}(s_x \pm i\tau s_y)$$

Each matrix $\hat{h}^l$ is a 4×4 matrix that is defined on a spin-sublattice resolved basis, consisting of four components: $A_{l\uparrow}, A_{l\downarrow}, B_{l\uparrow}, B_{l\downarrow}$. Here, A and B refer to different sublattices, while $\uparrow$ and $\downarrow$ denote the spin-up and spin-down states, respectively.

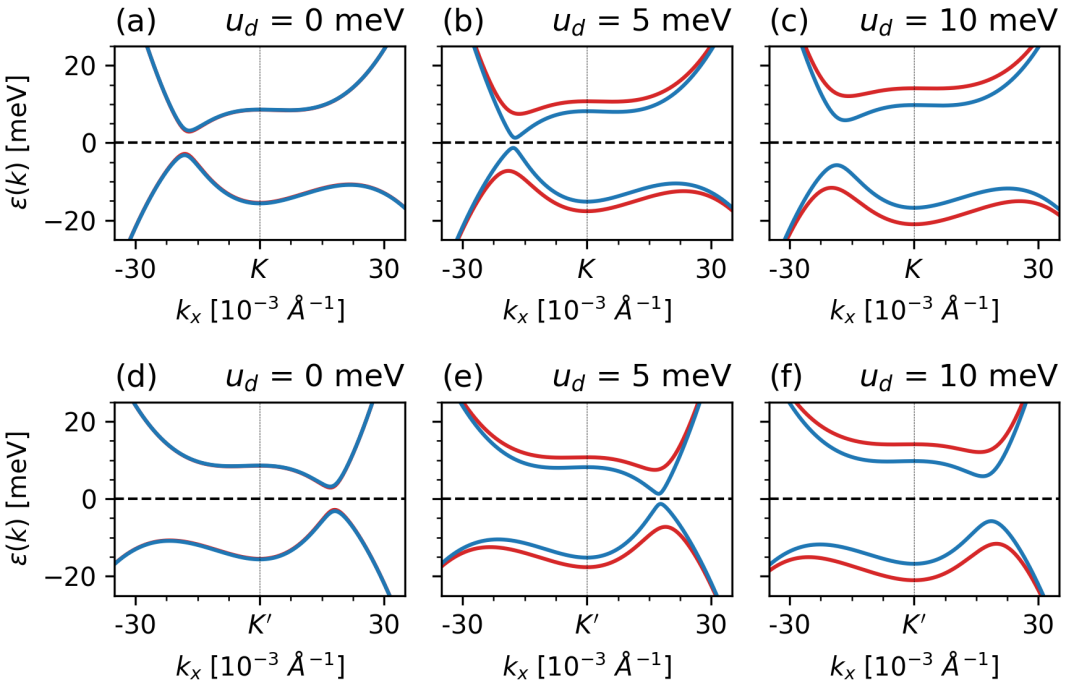

Figure 4.9: Calculated low-energy electronic dispersions at K' (a),(b), and (c) and K (d), (e) and (f) using $\hat{h}(\mathbf{k},\tau)+\hat{h}_{prox}(\tau)$ with and without displacement fields for CGT/RTG-/CGT heterostructure with antiferromagnetic CGT alignments. Colorcode denotes band structure spin-polarization.

Due to the short-range proximity effects in the system, the spin Hamiltonian only considers the two outermost layers of the material. It is a significant simplification, as the inner layers' effects are negligible or not considered in this context. Additionally, when TMDCs induce it, the SO coupling in graphene exhibits a specific characteristic known as the valley-Zeeman type. The reference [68] was discussed in detail. A notable feature of this type of SO coupling is that the values of $\lambda_I^{A_l}$ and $\lambda_I^{B_l}$ are approximately opposite in sign, which means that if one has a positive value, the other will have a negative value of the same magnitude, and vice versa.

As we wrote earlier, in our work, we considered only three types of heterostructures: $MoSe_2$/RTG/WSe_2, CGT/RTG/CGT heterostructure with ferromagnetic and antiferromagnetic CGT alignments, with the proximity-induced Hamiltonian parameters, which tabulated in Tab.4.1. The band structures and their dependence on the displacement field are shown in Fig. 4.7, Fig. 4.8, and Fig. 4.9, respectively. The $MoSe_2$/RTG/WSe_2 heterostructure is characterized by the spin order corresponding to the valley-Zeeman SO coupling, and the time-reversal symmetry is preserved. In contrast, the time-reversal symmetry is broken for the CGT/RTG/CGT heterostructures. One interesting observation is the appearance of spin splitting for a CGT/RTG/CGT heterostructure with

	$MoSe_2$/RTG/WSe_2	CGT/RTG/CGT FM	CGT/RTG/CGT AFM
λ_R^1	0.233	0	0
λ_I^{A1}	0.209	0	0
λ_I^{B1}	-0.204	0	0
λ_R^3	-0.475	0	0
λ_I^{A3}	1.125	0	0
λ_I^{B3}	-0.983	0	0
λ_{ex}^{A1}	0	-3.393	-3.393
λ_{ex}^{B1}	0	-3.393	-3.393
λ_{ex}^{A3}	0	-3.349	3.349
λ_{ex}^{B3}	0	-3.349	3.349

Table 4.1: Transposed parameters of the proximity-induced Hamiltonian for heterostructures: $MoSe_2$/RTG/WSe_2, CGT/RTG/CGT heterostructure with ferromagnetic (FM) and antiferromagnetic (AFM) CGT alignments. All parameters in meV.

antiferromagnetic CGT alignments at a finite displacement field. This effect occurs due to mirror-symmetry violation since the displacement field makes the top and bottom RTG layers inequivalent, while mirror-symmetry is preserved for the zero displacement field. Hence, we get spin splitting of van Hove singularities.

Suppose we apply a similar downfold procedure to the Hamiltonian (4.1) in the previous section for the proximity-induced Hamiltonian. In that case, we can obtain the following proximity Hamiltonians, which are extremely useful for subsequent analysis:

$$\begin{aligned}\hat{h}_R(\tau) =& \sum_l \hat{h}_R^l(\tau) \\ =&(\lambda_R^1 + \lambda_R^3)\frac{(v_F k)^2}{t_1^2}[\cos(2\phi)\,(\tau\hat{\sigma}_x\hat{s}_y - \hat{\sigma}_y\hat{s}_x) - \sin(2\phi)\,(\tau\hat{\sigma}_x\hat{s}_x - \hat{\sigma}_y\hat{s}_y)]\end{aligned} \tag{4.6}$$

$$\hat{h}_I(\tau) = \sum_l \hat{h}_I^l(\tau) = \begin{pmatrix} \tau\,\lambda_I^{A_3}\,s_z & 0 \\ 0 & -\tau\,\lambda_I^{B_1}\,s_z \end{pmatrix} \tag{4.7}$$

$$\hat{h}_{\text{ex}}(\tau) = \sum_l \hat{h}_{\text{ex}}^l(\tau) = \begin{pmatrix} -\lambda_{\text{ex}}^{A_3}\,s_z & 0 \\ 0 & -\lambda_{\text{ex}}^{B_1}\,s_z \end{pmatrix} \tag{4.8}$$

The equations (4.7) and (4.8) were obtained as the first non-zero component of the Taylor expansion near $k \to 0$.

4.4. Correlated phenomena via random phase approximation

Our research aims to explore the correlation effects within RTG. These effects are represented by the Hamiltonian, which is referred to as

$$\hat{H} = \hat{H}_{\text{kin}} + \hat{H}_{\text{int}} - \mu\hat{N}, \tag{4.9}$$

where μ denotes chemical potential and $\hat{N}$ - the operator for the number of electrons. Hamiltonian (4.9) is primarily composed of two components: the kinetic term $\hat{H}_{\text{kin}}$ and the interaction term $\hat{H}_{\text{int}}$:

$$\hat{H}_{\text{kin}} = \sum_{\mathbf{k}\tau,si,s'j} \left[\hat{h}(\mathbf{k},\tau)\right]_{si,s'j} \hat{c}^{\dagger}_{s\tau i}(\mathbf{k})\hat{c}_{s'\tau j}(\mathbf{k}), \tag{4.10}$$

$$\hat{H}_{\text{int}} = U_0 \left(n_{\uparrow K}\, n_{\downarrow K} + n_{\uparrow K'}\, n_{\downarrow K'}\right) + U_1 n_K\, n_{K'}, \tag{4.11}$$

The symbol μ represents the chemical potential. The operator $\hat{c}^{(\dagger)}_{s\tau i}(\mathbf{k})/\hat{c}_{s\tau i}(\mathbf{k})$ creation/annihilation operator Bloch electron, characterized by a spin, denoted by s, which can be either $\uparrow$ (up) or $\downarrow$ (down). Additionally, the electron is associated with a valley, symbolized by τ, which can be either K or K', RTG sublattice, represented by i, and a valley-momentum given by $\mathbf{k}$.

Our study explores the minimal interaction model, which includes intra- and interval-density interactions. Repulsive couplings characterize these interactions. Specifically, the intravalley interactions are represented by U_0, while the intervalley interactions are symbolized by U_1. Both these couplings are positive, indicating their repulsive nature. In addition to the minimal interaction model, the long-range Coulomb potential is also often used for this type of system [259, 260]

$$V(\mathbf{q}) = \frac{2\pi \tanh(qD)}{\varepsilon q} \tag{4.12}$$

which is called dual-screened potential. At this potential, D is sample-gate distance, and ε is environmental dielectric constant. Although using a dual gate-screened potential is closer to reality, we decided to use a minimal model to reduce the number of free parameters and simplify the calculations in order to extract the maximum amount of interpretable information.

The term $n_{s\tau}$ denotes the spin-valley number operator for the $s\tau$-channel, which is restricted by a momentum cut-off, Λ:

$$n_{s\tau} = \sum_{|\mathbf{k}|<\Lambda} \sum_{i} \hat{c}^{\dagger}_{s\tau i}(\mathbf{k})\hat{c}_{s\tau i}(\mathbf{k}) \tag{4.13}$$

The formula gives the valley-resolved number operator:

$$n_{\tau} = n_{\uparrow\tau} + n_{\downarrow\tau}$$

For our analysis, we emphasize the SU(4)-symmetric interactions. We assign values of 19 eV to both U_0 and U_1 [265, 259], with momentum cutoff Λ equal to 0.06 Å^{-1}. The cutoff role is minimal, and it should be sufficient to reach the criteria $\Lambda v_F \gg U_0 n_e/A$, where v_f is Fermi velocity, n_e is electron doping and A is unit cell area, which proves that kinetic energy of the system is much large than the energy of interaction, demonstrating the applicability of the many-body perturbation methods. Adopting these interaction parameters, we derive a pristine RTG phase diagram consistent with experimental findings, as in the studies [222, 266]. In the following sections, we will analyze the influence of

the Hamiltonian interaction parameters in more detail. However, it is important to clarify that we assume that these interaction parameters remain consistent when we extend our analysis to encapsulated cases, such as $MoSe_2$/RTG/WSe_2 heterostructure and CGT/RTG/CGT heterostructure with ferromagnetic and antiferromagnetic CGT alignments.

To understand the correlated phase diagram associated with our model of proximitized RTG, we utilize the Random Phase Approximation. Our initial step involves calculating the static irreducible susceptibility, denoted as χ^0_{ph}, in the context of spin-valley indices. We calculated $\chi^0_{ph}(\omega, \mathbf{q})$ as generalized Lindhard's susceptibility [255, 256, 257]:

$$\begin{aligned}
\chi^0_{ph,\bar{a}b\bar{c}d}(\omega,\mathbf{q}) =& -\frac{1}{N_{\mathbf{k}}\beta}\sum_{\nu\mathbf{k}} G_{d\bar{a}}(\nu,\mathbf{k})G_{b\bar{c}}(\omega+\nu,\mathbf{k}+\mathbf{q}) \\
=& -\frac{1}{N_{\mathbf{k}}\beta}\sum_{\nu\mathbf{k}} \underbrace{\left(\sum_i \frac{u_{nd}(\mathbf{k})u^*_{n\bar{a}}(\mathbf{k})}{i\nu-\varepsilon_n(\mathbf{k})}\right)}_{G_{d\bar{a}}(\nu,\mathbf{k})} \underbrace{\left(\sum_j \frac{u_{mb}(\mathbf{k}+\mathbf{q})u^*_{m\bar{c}}(\mathbf{k}+\mathbf{q})}{i\nu+i\omega-\varepsilon_m(\mathbf{k}+\mathbf{q})}\right)}_{G_{b\bar{c}}(\omega+\nu,\mathbf{k}+\mathbf{q})} \\
=& \frac{1}{N_{\mathbf{k}}}\sum_{\mathbf{k}}\sum_{ij} u^*_{n\bar{a}}(\mathbf{k})u_{mb}(\mathbf{k}+\mathbf{q})u^*_{m\bar{c}}(\mathbf{k}+\mathbf{q})u_{nd}(\mathbf{k})\frac{f(\varepsilon_n(\mathbf{k}))-f(\varepsilon_m(\mathbf{k}+\mathbf{q}))}{i\omega+\varepsilon_m(\mathbf{k}+\mathbf{q})-\varepsilon_n(\mathbf{k})}
\end{aligned} \tag{4.14}$$

where $u_{na}(\mathbf{k})$ and $\varepsilon_n(\mathbf{k})$ are eigenvectors and eigenvalues obtained from diagonalization bilinear form of $\hat{H}_{kin} - \mu\hat{N}$, i.e.:

$$\left[\hat{h}(\mathbf{k}) + \hat{h}_{prox}\right]_{ab} u_{nb}(\mathbf{k}) = \left[\varepsilon_n(\mathbf{k}) + \mu\right] u_{na}(\mathbf{k}) \tag{4.15}$$

Here, indexes a/b encode the combination of spin s, valley τ quantum number, and sublattice index, while n represents the band index. Temperature dependence is taken into account via Fermi-Dirac occupations:

$$f(\varepsilon) = \frac{1}{e^{\beta\varepsilon}+1} \tag{4.16}$$

In what follows, we point out that all calculations in this Chapter are done at a temperature equal to $T = 1/(k_B\beta) = 4.2$ K. Also, we constrain chemical potential by fixing electron doping:

$$n_e = \int_{|\mathbf{k}|<\Lambda} \frac{\mathrm{d}^2\mathbf{k}}{(2\pi)^2} \sum_n \left(f(\varepsilon_n(\mathbf{k})) - \frac{1}{2}\right), \tag{4.17}$$

The additional offset $-1/2$ in Eq. (4.17) is to set the chemical potential to zero at charge neutrality.

In static $\omega = 0$ and local $\mathbf{q} = 0$ limit, Eq.(4.14) can be rewritten as:

$$\chi^0_{ph,\bar{a}b\bar{c}d} = \frac{1}{N_{\mathbf{k}}}\sum_{\mathbf{k}}\sum_{ij} u^*_{n\bar{a}}(\mathbf{k})u_{mb}(\mathbf{k})u^*_{m\bar{c}}(\mathbf{k})u_{nd}(\mathbf{k})\frac{f(\varepsilon_n(\mathbf{k}))-f(\varepsilon_m(\mathbf{k}))}{\varepsilon_m(\mathbf{k})-\varepsilon_n(\mathbf{k})} \tag{4.18}$$

In our calculation, we have omitted the dependence of the generalized susceptibility on the sublattice index since the interaction Hamiltonian (4.11) does not take sublattice degrees of freedom into account. Therefore, we can trace out sublattice degrees of freedom from the generalized susceptibility (4.18):

$$\tilde{\chi}^0_{ph,\bar{a}b\bar{c}d} = \sum_{ij} \chi^0_{ph,(\bar{a}i)(bi)(\bar{c}j)(dj)} \tag{4.19}$$

Here, indexes $\bar{a}, b, \bar{c}$ and d encode only the combination of spin s and valley τ quantum number, while i and j represent sublattice indexes. Hence, $\tilde{\chi}^0_{ph}$ carries information only about spin-valley degrees of freedom. In follows, we will use the notation χ^0_{ph} for $\tilde{\chi}^0_{ph}$.

Our next step was calculating the generalized susceptibility corrected using RPA and χ^0_{ph}. RPA-corrected susceptibility, considered in Chapter 3, can be calculated as

$$\chi^{\mathrm{RPA}}_{ph,\bar{a}b\bar{c}d} = \chi^0_{ph,\bar{a}b\bar{c}d} + \sum_{\bar{e}f\bar{g}h} \chi^0_{ph,\bar{a}b\bar{e}f} \Gamma^{\mathrm{RPA}}_{ph,f\bar{e}h\bar{g}} \chi^{\mathrm{RPA}}_{ph,\bar{g}h\bar{c}d} \tag{4.20}$$

Here, $\Gamma^{\mathrm{RPA}}_{ph}$ stands for the fully-irreducible vertex in ph channel, obtained using RPA, which state that:

$$\hat{H}_{int} = \frac{1}{4} \sum_{a\bar{b}c\bar{d}} \Gamma^{\mathrm{RPA}}_{ph,c\bar{a}d\bar{b}} \hat{c}^\dagger_{\bar{a}} \hat{c}^\dagger_{\bar{b}} \hat{c}_c \hat{c}_d \tag{4.21}$$

For interaction Hamiltonian (4.11) $\Gamma^{\mathrm{RPA}}_{ph}$ has the following form:

$$\Gamma_{0220} = \Gamma_{1331} = +U_0 \tag{4.22}$$

$$\Gamma_{0022} = \Gamma_{1133} = -U_0 \tag{4.23}$$

$$\Gamma_{0110} = \Gamma_{0330} = \Gamma_{1221} = \Gamma_{2332} = +U_1 \tag{4.24}$$

$$\Gamma_{0011} = \Gamma_{0033} = \Gamma_{1122} = \Gamma_{2233} = -U_1 \tag{4.25}$$

where spin-valley indexes degrees of freedom parametrized by:

$$0 = (\uparrow \times K)\,, \quad 1 = (\uparrow \times K')\,, \quad 2 = (\downarrow \times K)\,, \quad 3 = (\downarrow \times K')\,. \tag{4.26}$$

All unmentioned components of the Γ tensor can be obtained by the relation $\Gamma_{abcd} = \Gamma_{dcba}$.

According to the linearized RPA equation, the correlated phase emerges when the largest eigenvalue, λ_c, of the product $\chi^0_{ph}\Gamma^{\mathrm{RPA}}_{ph}$ reaches or surpasses the unity. When this occurs, χ^{RPA}_{ph} experiences a divergence, leading to instability. To determine the channel of instability, we solve the linearized RPA equation:

$$\lambda_c \Sigma_{\bar{a}b} = \sum_{\bar{e}f\bar{g}h} \chi^0_{ph,\bar{a}b\bar{e}f} \Gamma^{\mathrm{RPA}}_{ph,f\bar{e}h\bar{g}} \Sigma_{\bar{g}h}, \tag{4.27}$$

where

$$\hat{\Sigma} = \sum_{\bar{a}b} \Sigma_{\bar{a}b} \hat{c}^\dagger_{\bar{a}} \hat{c}_b \tag{4.28}$$

correspond to the order parameter of emerged instability. To identify all potential correlated phases in RTG, denoted as $\hat{\Sigma}$, we diagonalize of $\chi^0_{ph}\Gamma^{\mathrm{RPA}}_{ph}$ at zero displacement field $V = 0$ and charge-neutrality point $\mu = 0$. This assumption is based on the results that the eigenvalues of tensor $\chi^0_{ph}\Gamma^{\mathrm{RPA}}_{ph}$ remain relatively constant despite changes in displacement field and doping.

4.5. Pristine RTG phase diagram

We start our study from correlated phases in pristine RTG, where we observe only two symmetry-breaking instabilities: local instability and non-local instability with spatial modulation with form-factor equal to $e^{i(K-K')r}$. Such non-local instability effectively enlarges the RTG unit cell into a "magnetic" $\sqrt{3}\times\sqrt{3}$-unit cell due to possessed spatial modulations governed by wave vector $\mathbf{q}=\frac{2\pi}{3a}(1,\sqrt{3})$. Both phases are spin-degenerate due to SU(2) spin symmetry in pristine RTG. However, local instability is characterized by Pauli matrices τ_0/τ_z in valley K/K' basis, while non-local, in τ_x/τ_y. Hence, local and non-local physical susceptibility can be obtained as:

$$\chi_{\text{non-loc}}=\sum_{\bar{a}b\bar{c}d}\left[s\otimes\tau_{x/y}\right]_{\bar{a}b}\chi^0_{ph,\bar{a}b\bar{c}d}\left[s\otimes\tau_{x/y}\right]_{\bar{c}d}, \tag{4.29}$$

$$\chi_{\text{loc}}=\sum_{\bar{a}b\bar{c}d}\left[s\otimes\tau_{0/z}\right]_{\bar{a}b}\chi^0_{ph,\bar{a}b\bar{c}d}\left[s\otimes\tau_{0/z}\right]_{\bar{c}d}, \tag{4.30}$$

where s represents any Hermitian operator in spin subspace, we can show that local physical susceptibility is equal to the density of states at the Fermi level:

$$\begin{aligned}\chi_{\text{loc}}&=\frac{1}{N_{\mathbf{k}}}\sum_{\mathbf{k}}\sum_{nm}\frac{f(\varepsilon_n(\mathbf{k}))-f(\varepsilon_m(\mathbf{k}))}{\varepsilon_m(\mathbf{k})-\varepsilon_n(\mathbf{k})}\\&\qquad\sum_{ij}\sum_{\bar{a}b\bar{c}d}\left[s\otimes\tau_{0/z}\right]_{\bar{a}b}u^*_{n(\bar{a}i)}(\mathbf{k})u_{m(bi)}(\mathbf{k})u^*_{m(\bar{c}j)}(\mathbf{k})u_{m(di)}(\mathbf{k})\left[s\otimes\tau_{0/z}\right]_{\bar{c}d}\\&=\frac{1}{N_{\mathbf{k}}}\sum_{\mathbf{k}}\sum_{ij}\frac{f(\varepsilon_n(\mathbf{k}))-f(\varepsilon_m(\mathbf{k}))}{\varepsilon_m(\mathbf{k})-\varepsilon_n(\mathbf{k})}\\&\qquad\sum_{nm}\sum_{\bar{a}b\bar{c}d}\delta_{\bar{a}b}\delta_{\bar{c}d}u^*_{n(\bar{a}i)}(\mathbf{k})u_{m(bi)}(\mathbf{k})u^*_{m(\bar{c}j)}(\mathbf{k})u_{m(di)}(\mathbf{k})\\&=\frac{1}{N_{\mathbf{k}}}\sum_{\mathbf{k}}\sum_{ij}\delta_{ij}\frac{f(\varepsilon_n(\mathbf{k}))-f(\varepsilon_m(\mathbf{k}))}{\varepsilon_m(\mathbf{k})-\varepsilon_n(\mathbf{k})}\\&=-\frac{1}{N_{\mathbf{k}}}\sum_{\mathbf{k}}\sum_{i}\frac{\partial f}{\partial\varepsilon}\Big|_{\varepsilon_{i\mathbf{k}}}=\rho(\varepsilon_F)\end{aligned} \tag{4.31}$$

Thus, the linearized RPA equation for local instability will be effectively equivalent to the Stoner criterion, which is:

$$g\rho(\varepsilon_F)\geq 1, \tag{4.32}$$

where g is effective local coupling. In follows, we will refer to the local instability as the Stoner one. Therefore, any correlated phase having the order parameter as:

$$\hat{\Sigma}_{\text{Stoner}}=\sum_{\bar{a}b}\left[s\otimes\tau_{0/z}\right]_{\bar{a}b}\hat{c}^\dagger_{\bar{a}}\hat{c}_b \tag{4.33}$$

we will call the Stoner correlated phase. In turn, we will call the non-local instability inter-valley-coherent state since the order parameter for this correlated phase has the form

$$\hat{\Sigma}_{\text{IVC}}=\sum_{\bar{a}b}\left[s\otimes\tau_{x/y}\right]_{\bar{a}b}\hat{c}^\dagger_{\bar{a}}\hat{c}_b \tag{4.34}$$

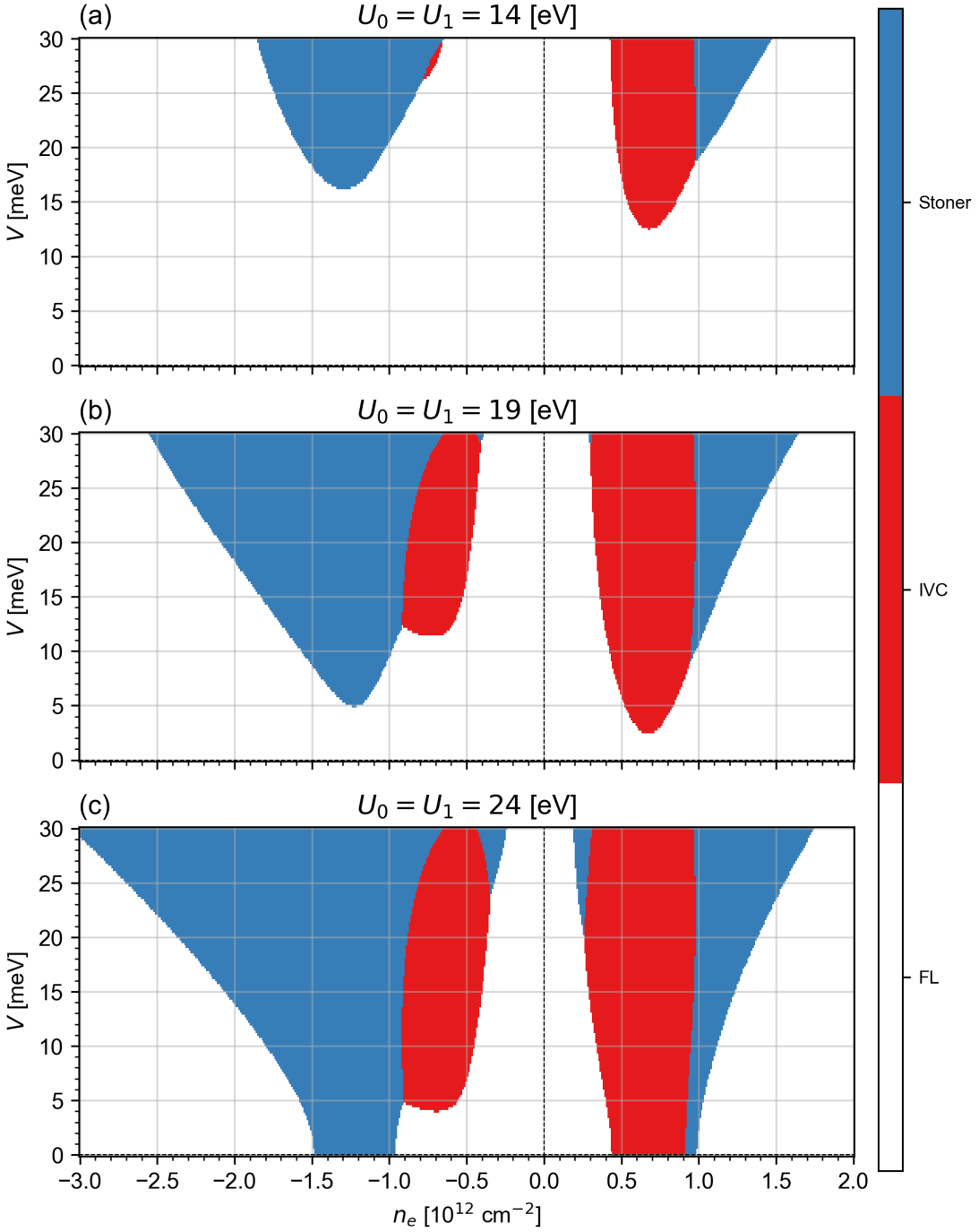

Figure 4.10: Phase diagram of pristine RTG for different n_e and V. There are two main phases: intervalley coherent (IVC) and Stoner instability. The white background represents stable Fermi liquid (FL). Based on the experimental data presented in Figure 4.1, we believe that the interaction parameters U_0 and U_1, set at 19 eV each, are the closest to the actual values. This is because the boundaries of the correlated phases, determined by these parameters, closely match the phase boundaries (indicated by negative values of inverse compressibility) in the experimental phase diagram, depicted in Fig. 4.1.

and there is an inter-valley hopping that can induce an inter-valley-coherent state.

Having found out the possible correlated phases in pristine RTG at zero doping level in the charge neutrality point, we calculated the phase diagram of pristine RTG in the axis of the level of electron doping n_e and displacement field V. To do this, we calculated the generalized susceptibility $\chi^0_{ph,\bar{a}b\bar{c}d}(n_e, V)$ for different levels of electron doping n_e by adjusting the chemical potential μ, and displacement field V. Our next step was to calculate the critical parameter λ_c for each instability, Stoner and IVC, using the following formula:

$$\begin{aligned}\lambda_c^{\Sigma}(n_e, V) =& \frac{1}{\|\Sigma\|^2}\langle\Sigma|\chi^0_{ph}(n_e, V)\Gamma^{\mathrm{RPA}}_{ph}|\Sigma\rangle \\ =& \frac{1}{\sum_{\bar{a}b}\Sigma^*_{b\bar{a}}\Sigma_{\bar{a}b}}\sum_{\bar{a}b\bar{u}v\bar{c}d}\Sigma^*_{b\bar{a}}\chi^0_{ph,\bar{a}b\bar{u}v}(n_e, V)\Gamma^{\mathrm{RPA}}_{ph,v\bar{u}d\bar{c}}\Sigma_{\bar{c}d}\end{aligned} \tag{4.35}$$

Here, prefactor $\frac{1}{\|\Sigma\|^2}$ is important in order to normalize the projection vector Σ of the tensor $\chi^0_{ph}\Gamma^{\mathrm{RPA}}_{ph}$, otherwise Eq.(4.35) will give incorrect values of λ_c. Because λ_c increases monotonically with increased interaction amplitude, the instability with a larger value of λ_c is more favorable. Figure 4.10 shows our pristine RTG phase diagrams. We define the regions of the phase diagram where none of the instabilities emerge as the Fermi-liquid (FL) regime. Stoner and IVC instabilities are observed in both hole and electron doping regimes at various levels of the displacement field. Although in Figure 4.10 we have presented phase diagrams for various SU(4) interaction parameters, we believe that the value $U_0 = U_1 = 19$ eV is the closest to the experimental phase diagram [222].

Due to the vast number of free parameters, it is difficult to establish any analytical criterion unambiguously determining the IVC or Stoner phase. However, both phases emerge near van Hove singularities and correspond to different channel nesting, IVC, at a finite momentum equivalent to the intervalley moment. In contrast, the Stoner phase corresponds to nesting at zero moment, that is, the density of states at the Fermi level. Due to SU(2)-symmetry, Stoner and IVC instabilities are strongly degenerate in the spin channel, so it is not possible to construct a band structure of correlated phases in pristine RTG.

4.6. $MoSe_2$/RTG/WSe_2 phase diagram: SO coupling

Our next step was to calculate the phase diagram of the $MoSe_2$/RTG/WSe_2 heterostructure. To identify all potential correlated phases in $MoSe_2$/RTG/WSe_2 heterosture, we diagonalize of $\chi^0_{ph}\Gamma^{\mathrm{RPA}}_{ph}$ at zero displacement field $V = 0$ and charge-neutrality point $\mu = 0$. For this heterostructure, due to the lack of SU(2)-symmetry, we obtained spin-resolved instabilities, such as:

1. Charge-Density-Wave (CDW) instability is characterized by spatial charge modulation with wave vector $\mathbf{q} = \frac{2\pi}{3a}(1, \sqrt{3})$ and is the IVC instability derivative of the charge channel instability. Therefore, the order parameter for CDW instability is:

$$\hat{\Sigma}_{\mathrm{CDW}} = \sum_{\bar{a}b}\left[s_0 \otimes \tau_{x/y}\right]_{\bar{a}b}\hat{c}^{\dagger}_{\bar{a}}\hat{c}_b \tag{4.36}$$

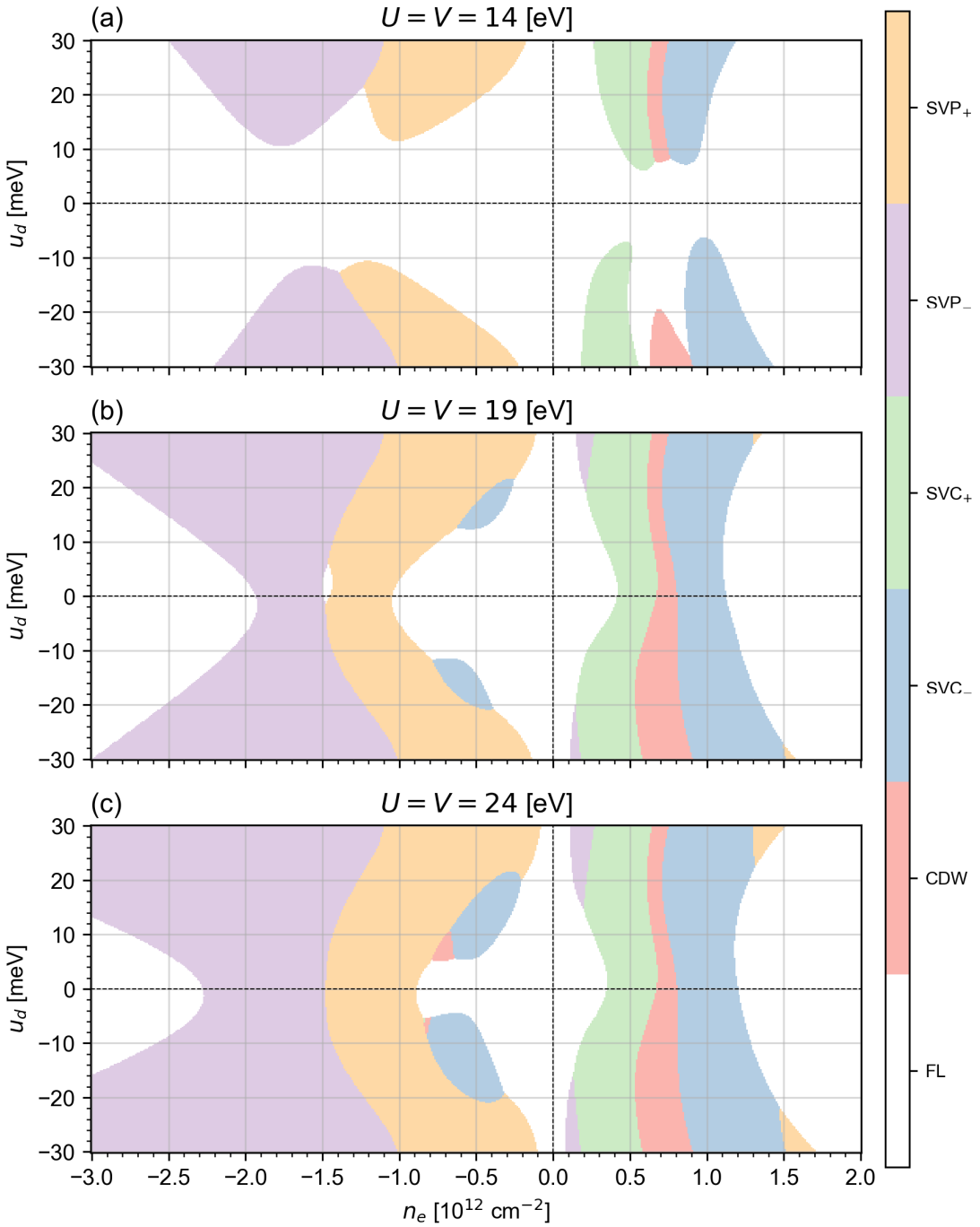

Figure 4.11: Phase diagram of the MoSe2/RTG/WSe2 heterostructure model as a function of the displacement field V and the doping density n_e for three different interaction configuration: (a) $U_0 = U_1 = 14$ eV, (b) $U_0 = U_1 = 19$ eV, and (c) $U_0 = U_1 = 24$ eV. The diagram predicts six different phases, with symmetry breaking: CDW$\pm$ (charge density wave), SVC$\pm$ (spin-valley coherence), and SVP$_\pm$ (spin-valley polarized state). These phases are color-coded to indicate potential instability in the Fermi liquid state (shown in white).

2. Spin-Valley-Coherent (SVC) instability also characterized by spatial modulation with wave vector $\mathbf{q} = \frac{2\pi}{3a}(1, \sqrt{3})$ and is the IVC instability derivative. However, in addition to spatial modulation, SVC is characterized by spin-valley-flip hopping. As a result, we have the following form of the order parameter for $\mathrm{SVC}_\pm$ instability:

$$\hat{\Sigma}_{\mathrm{SVC}_\pm} = \sum_{\bar{a}b} \left[s_x\tau_x \pm s_y\tau_y\right]_{\bar{a}b} \hat{c}^\dagger_{\bar{a}}\hat{c}_b, \tag{4.37}$$

which indicates that correlated $\mathrm{SVC}_\pm$ phases induce inter-valley spin-flip-hopping.

3. Finally, Spin-Valley-Polarized (SVP) instability is local, so is a Stoner instability derivative. $\mathrm{SVP}_\pm$ instabilities have order parameters as:

$$\hat{\Sigma}_{\mathrm{SVP}_\pm} = \sum_{\bar{a}b} \left[s_z\tau_0 \pm s_0\tau_z\right]_{\bar{a}b} \hat{c}^\dagger_{\bar{a}}\hat{c}_b, \tag{4.38}$$

and it is characterized by spin-valley polarization. So, $\mathrm{SVP}_\pm$ correlated phase induces gap opening between spin-valley flavors with an identical product of spin-valley quantum number $s_z\tau$.

Figure 4.11 displays the resulting phase diagram, which exhibits noticeable differences compared to the phase diagram of the pristine RTG, as shown in Figure 4.10. Specifically, the phase diagram now depends on the sign of the displacement field due to the non-equivalence of proximitized substrates. The Stoner phase is split into two $\mathrm{SVP}_\pm$ states. Both states exhibit spin-valley polarization in the z direction and are consistent with the behavior observed in the single-particle valley-Zeeman coupling, as discussed in [68].

In the IVC phase, the previously observed spin degeneracy has been removed. It leads to four unique states, with two being spin-valley coherent states ($\mathrm{SVC}_\pm$) and the other two indicating a charge density wave ($\mathrm{CDW}_\pm$). The $\mathrm{CDW}_\pm$ phases are almost degenerate, and their separation does not strongly depend on model parameters due to the insignificant difference in the critical parameter λ_c^Σ. The $\mathrm{SVC}_\pm$ phases appear at electron doping near van Hove singularity split by RTG fields, which can be explained by spin-valley correlations triggered by the valley-Zeeman RTG coupling [68]. We will try to delve into the nature of each phase, and also, below, we will construct a band structure for each correlated phase predicted in the MoSe2/RTG/WSe2 heterostructure.

4.6.1. Hartree-Fock correlated band structure

In the ensuing stage of our research, we shifted our focus towards elucidating the band structure for states preliminarily categorized as being correlated. We adopt the Hartree-Fock approximation as our computational methodology to meet this end. This approximation is instrumental in calculating the self-energy component while considering the influence of symmetry-breaking events. Subsequently, we tackle the solution of the modified Schrödinger equation to derive the band structure of interest. The equation is articulated as follows:

$$\sum_{bj} \left[\hat{h}_{(ai)(bj)}(\mathbf{k}) + \Sigma^{HF}_{ab}\delta_{ij}\right] \tilde{u}_{n(bj)}(\mathbf{k}) = \left[\tilde{\varepsilon}_n(\mathbf{k}) + \mu\right] \tilde{u}_{n(ai)}(\mathbf{k}), \tag{4.39}$$

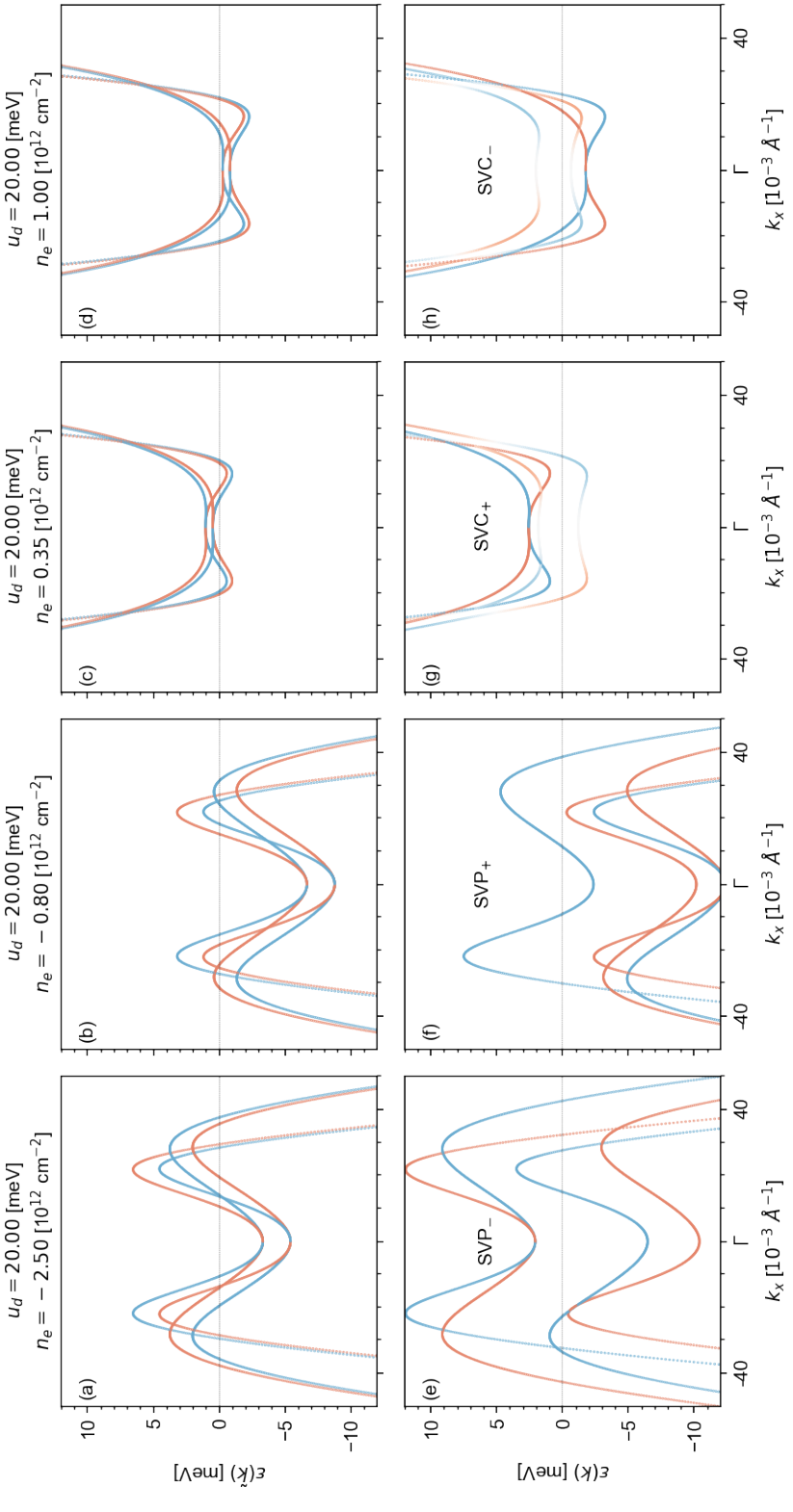

Figure 4.12: Folded to crystallographic Γ point band structure of a MoSe2/RTG/WSe2 heterostructure at displacement field equal to $V = 20$ meV and finite doping levels, with and without interaction corrections. The top row (a-d) shows Hartree-Fock band structures for SVP$_+$, SVP$_-$, SVC$_-$, and SVC$_+$ instabilities, respectively. The bottom row (e-j) shows band structures without interaction corrections. Spin polarization is indicated in red (spin up) and blue (spin down).

The term Σ^{HF}_{ab} denotes the Hartree-Fock self-energy in this mathematical expression. It is pivotal to highlight that this self-energy is explicitly defined for the degrees of freedom a and b, which pertain to spin and valley, respectively, as explicated in Equation (4.26). The remaining component of the Hamiltonian termed the "bare kinetic energy," is described as:

$$\hat{h}_{(ai)(bj)}(\mathbf{k}) = \left[\hat{h}(\mathbf{k}) + \hat{h}_{prox}\right]_{(ai)(bj)}, \tag{4.40}$$

Herein, a, b signifies the spin-valley indices and i, j represents the sublattice indices. This framework enables us to determine the single-particle wave functions $\tilde{u}_{n(ai)}(\mathbf{k})$ and the associated single-particle energies $\tilde{\varepsilon}_n(\mathbf{k})$ that incorporate interaction corrections.

We calculate the Hartree-Fock self-energy, denoted as $\Sigma^{HF}_{\bar{b}a}(\nu)$, by employing the subsequent formula:

$$\begin{aligned}
\Sigma^{HF}_{\bar{b}a}(\nu) &= -\sum_{c\bar{d}} \frac{1}{\beta^2} \sum_{\omega} \sum_{\nu'} \Gamma^{\mathrm{RPA}}_{ph,a\bar{b}c\bar{d}}(\omega, \nu, \nu') G_{c\bar{d}}(\nu') \\
&\quad \text{this term represents the general expression for Hartree-Fock self-energy} \\
&= -\sum_{c\bar{d}} \frac{1}{\beta^2} \sum_{\nu'} \left[\beta\delta(\omega = \nu - \nu') \Gamma^{\mathrm{RPA}}_{ph,a\bar{b}c\bar{d}}(\omega = \nu - \nu')\right] G_{c\bar{d}}(\nu') \\
&\quad \text{focuses on elastic scattering events} \\
&= -\sum_{c\bar{d}} \frac{1}{\beta} \sum_{\nu'} \Gamma^{\mathrm{RPA}}_{ph,a\bar{b}c\bar{d}}(\nu - \nu') G_{c\bar{d}}(\nu') \\
&\quad \text{simplifies the expression by considering static scattering} \\
&= -\sum_{c\bar{d}} \Gamma^{\mathrm{RPA}}_{ph,a\bar{b}c\bar{d}} \left[\frac{1}{\beta} \sum_{\nu'} G_{c\bar{d}}(\nu')\right] \\
&\quad \text{introduces the density matrix} \\
&= -\sum_{c\bar{d}} \Gamma^{\mathrm{RPA}}_{ph,a\bar{b}c\bar{d}} \rho_{c\bar{d}} = \Sigma^{HF}_{\bar{b}a} \qquad (4.41) \\
&\quad \text{finalizes the expression for Hartree-Fock self-energy} \qquad (4.42)
\end{aligned}$$

Here, we assume that $\Gamma^{\mathrm{RPA}}_{ph}$ is static and involves only elastic scattering. $G_{c\bar{d}}(\nu')$ is the single-particle Green function, and $\rho_{c\bar{d}}$ is the density matrix defined in $c\bar{d}$ spin-valley degrees of freedom.

Subsequently, the density matrix $\rho_{a\bar{b}}$ can be calculated as:

$$\rho_{a\bar{b}} = \sum_{n\mathbf{k}} \sum_{i} \tilde{u}_{n(ai)}(\mathbf{k}) \tilde{u}^{*}_{n(\bar{b}i)}(\mathbf{k}) \left[f(\tilde{\varepsilon}_n(\mathbf{k})) - \frac{1}{2}\right] \tag{4.43}$$

In this equation, f is the Fermi-Dirac distribution as given by Eq.(4.16). The additional offset of $-1/2$ in Eq.(4.43) is included to set the chemical potential to zero at the charge neutrality point. This adjustment is crucial when working with a finite momentum cutoff

Λ to mitigate the momentum cutoff convergence issue. The sublattice degree of freedom is also traced in Eq.(4.43).

We are now in a position to assemble a self-consistent Hartree-Fock cycle by utilizing the equations denoted by (4.39), (4.41), and (4.43). However, one of the inherent challenges of the Hartree-Fock approach lies in determining the initial self-energy, denoted as $\Sigma_{\bar{a}b}$. The method itself cannot spontaneously break any symmetries; this symmetry-breaking must be induced externally before the Hartree-Fock calculations can proceed.

To address this issue, we employ the order parameters $\Sigma_{\bar{a}b}$ obtained through the Random Phase Approximation (RPA) method. We introduce an infinitesimal prefactor γ to serve as the initial Hartree-Fock self-energy $\Sigma^{HF}_{\bar{a}b}$, as expressed in Equation (4.41):

$$\Sigma^{HF}_{\bar{a}b} = \gamma \Sigma_{\bar{a}b} \tag{4.44}$$

By doing so, we set the stage for the subsequent calculation of the band structure of correlated phases.

However, this raises an important question: Why can the phases predicted by the RPA method be reliably detected when using the Hartree-Fock approach? To answer this, we will demonstrate that RPA can be considered a linearized approximation of the Hartree-Fock method, specifically for identifying symmetry-breaking phases.

We turn our attention to the Dyson equation, given by:

$$G_{a\bar{b}}(\nu, \mathbf{k}) = G^0_{a\bar{b}}(\nu, \mathbf{k}) + \sum_{\bar{c}d\bar{e}f} G^0_{a\bar{c}}(\nu, \mathbf{k}) \Sigma^{HF}_{\bar{c}d} G^0_{d\bar{b}}(\nu, \mathbf{k}) + \dots \tag{4.45}$$

This equation treats the self-energy as being 'purely' anomalous and conforming to Equation (4.41). Assuming that the Hartree-Fock self-energy amplitude γ is small, we can linearize the Dyson equation as follows:

$$G_{a\bar{b}}(\nu, \mathbf{k}) = G^0_{a\bar{b}}(\nu, \mathbf{k}) + \gamma \sum_{\bar{c}d\bar{e}f} G^0_{a\bar{c}}(\nu, \mathbf{k}) \Sigma_{\bar{c}d} G^0_{d\bar{b}}(\nu, \mathbf{k}) + \mathcal{O}(\gamma^2) \tag{4.46}$$

After performing an integration over the fermionic Matsubara frequencies in Equation (4.46), we arrive at a new equation, which can be expressed as:

$$\frac{1}{N_{\mathbf{k}}\beta} \sum_{\nu\mathbf{k}} G_{a\bar{b}}(\nu, \mathbf{k}) = \frac{1}{N_{\mathbf{k}}\beta} \sum_{\nu\mathbf{k}} G^0_{a\bar{b}}(\nu, \mathbf{k}) + \frac{\gamma}{N_{\mathbf{k}}\beta} \sum_{\bar{c}d\bar{e}f} \sum_{\nu\mathbf{k}} G^0_{a\bar{c}}(\nu, \mathbf{k}) \Sigma_{\bar{c}d} G^0_{d\bar{b}}(\nu, \mathbf{k}) + \mathcal{O}(\gamma^2) \tag{4.47}$$

In addition, we can utilize another equation for the non-interacting susceptibility, given by:

$$\chi^0_{ph,\bar{a}b\bar{c}d} = -\frac{1}{N_{\mathbf{k}}\beta} \sum_{\nu\mathbf{k}} G_{d\bar{a}}(\nu, \mathbf{k}) G_{b\bar{c}}(\nu, \mathbf{k}) \tag{4.48}$$

By employing this equation, we can reformulate the original Dyson equation (4.46) into a more concise form:

$$\rho_{a\bar{b}} = \rho^0_{a\bar{b}} - \gamma \underbrace{\sum_{\bar{c}d\bar{e}f} \chi^0_{ph,\bar{c}d\bar{b}a} \Sigma_{\bar{c}d}}_{\tilde{\rho}_{a\bar{b}}} + \mathcal{O}(\gamma^2) \tag{4.49}$$

Here, $\tilde{\rho}_{a\bar{b}}$ represents the anomalous density matrix, while $\rho^0_{a\bar{b}}$ denotes the density matrix of the system in the absence of interaction corrections.

After calculating the new elements of the density matrix, we can incorporate them into Equation (4.41). The resulting expression for the self-energy $\Sigma^{HF}_{\bar{b}a}$ is as follows:

$$\begin{aligned}\Sigma^{HF}_{\bar{b}a} &= -\sum_{c\bar{d}} \Gamma^{\mathrm{RPA}}_{ph,a\bar{b}c\bar{d}}\rho_{c\bar{d}} \\ &= \underbrace{-\sum_{c\bar{d}} \Gamma^{\mathrm{RPA}}_{ph,a\bar{b}c\bar{d}}\rho^0_{c\bar{d}}}_{=0} + \gamma\sum_{c\bar{d}} \Gamma^{\mathrm{RPA}}_{ph,a\bar{b}c\bar{d}}\tilde{\rho}_{c\bar{d}} + \mathcal{O}(\gamma^2)\end{aligned} \tag{4.50}$$

We treat the self-energy $\Sigma^{HF}_{\bar{b}a}$ as entirely anomalous. Consequently, the first term in Equation (4.50) is nullified, reducing to zero. This simplification allows us to rewrite the equation in its final form:

$$\begin{aligned}\Sigma^{HF}_{\bar{b}a} =& \gamma\sum_{c\bar{d}} \Gamma^{\mathrm{RPA}}_{ph,a\bar{b}c\bar{d}}\tilde{\rho}_{c\bar{d}} \\ =& \gamma\sum_{\bar{c}d\bar{e}f} \Gamma^{\mathrm{RPA}}_{ph,a\bar{b}d\bar{c}}\chi^0_{ph,\bar{e}f\bar{c}d}\Sigma_{\bar{e}f} \\ =& \gamma\sum_{\bar{c}d\bar{e}f} \underbrace{\chi^0_{ph,\bar{b}a\bar{c}d}\Gamma^{\mathrm{RPA}}_{ph,d\bar{c}e\bar{f}}}_{\text{crossing symmetry}}\Sigma_{\bar{e}f} = \gamma\Sigma_{\bar{b}a}.\end{aligned} \tag{4.51}$$

This final equation aligns with the linearized RPA equation, with a critical parameter λ_c set to one. From this, we can deduce that the RPA and the Hartree-Fock method are equivalent in identifying correlated instabilities without requiring iterative convergence methods.

We performed calculations to determine the electronic band structure of the $MoSe_2$-/RTG/WSe_2 heterostructure under specific conditions. These conditions include a finite displacement field with a $V = 20$ meV value and doping levels corresponding to the correlated phases labeled as SVP_+, SVP_-, SVC_-, and SVC_+. The phase diagram identifies and predicts these specific phases, which can be referenced in Figure 4.11. The outcomes of these calculations are visually represented in Figure 4.12. In this figure, the band structures for the correlated phases SVP_+, SVP_-, SVC_-, and SVC_+ are displayed in sub-panels (a), (b), (c), and (d), respectively. To provide a basis for comparison, we also included band structures that were not corrected for interactions. These are shown in sub-panels (e), (f), (g), and (h), and they correspond to similar doping levels as their correlated-phase counterparts. It is worth noting that sub-panels (a) and (e) represent the same doping levels and displacement field conditions. However, the critical difference is that sub-panel (a) includes the effects of interaction corrections on the band structure, while sub-panel (e) does not. We opted not to consider the Charge Density Wave (CDW) phases in our calculations. This exclusion is because these phases exhibit nearly degenerate characteristics, significantly complicating the Hartree-Fock calculation method's convergence process.

In every scenario examined, considering the interaction correction via the Hartree-Fock method introduces an extra split between specific pairs of spin-valley flavors. This

split is defined by the order parameter associated with the particular instability under consideration. To quantify this additional splitting, we can calculate the correlated energy gap, denoted as γ, using the self-energy values obtained through the Hartree-Fock method. The equation for this calculation is:

$$\gamma_\Sigma = \frac{1}{\sum_{\bar{a}b} \Sigma^*_{b\bar{a}} \Sigma_{\bar{a}b}} \sum_{\bar{a}b} \Sigma_{\bar{a}b} \Sigma^{HF}_{\bar{a}b} \tag{4.52}$$

Once we have the γ value, we can model the system at the mean-field level. It is achieved by incorporating γ into the Hamiltonian, which is expressed as:

$$\hat{H}_\Sigma = \gamma_\Sigma \sum_{\bar{a}b} \Sigma_{\bar{a}b} \hat{c}^\dagger_{\bar{a}} \hat{c}_b \tag{4.53}$$

For instance, the correlated spin-valley polarized ($SVP_\pm$) state can be characterized by its own Hamiltonian, given by:

$$\hat{H}_{SVP_\pm} = \gamma_{SVP_\pm} \sum_{\bar{a}b} \left[s_z \tau_0 \pm s_0 \tau_z \right]_{\bar{a}b} \hat{c}^\dagger_{\bar{a}} \hat{c}_b \tag{4.54}$$

Similarly, the correlated spin-valley coupled ($SVC_\pm$) state can be described by:

$$\hat{H}_{SVC_\pm} = \gamma_{SVC_\pm} \sum_{\bar{a}b} \left[s_x \tau_x \pm s_y \tau_y \right]_{\bar{a}b} \hat{c}^\dagger_{\bar{a}} \hat{c}_b \tag{4.55}$$

By following this approach, we can effectively model various states of the system, each characterized by its unique Hamiltonian that incorporates the correlated energy gap γ.

In the study, we analyzed the calculated band structures as depicted in Figure 4.12. Our findings revealed specific values for the correlated gaps associated with different instabilities. Specifically, for the panel labeled as (a), which corresponds to the SVP_+ instability, we measured a correlated gap value of $\gamma_{SVP_+} = 0.992$ meV. For the panel marked as (b) related to the SVP_- instability, the correlated gap was found to be $\gamma_{SVP_-} = 1.198$ meV. Similarly, for panel (c) associated with the SVC_- instability, the correlated gap was $\gamma_{SVC_-} = 0.997$ meV. Lastly, for panel (d) corresponding to the SVC_+ instability, the correlated gap was $\gamma_{SVC_+} = 0.847$ meV.

Notably, the magnitudes of these correlated gaps are in close agreement with the values of the RTG coupling parameters. The proximity effect induces these parameters, and they serve as a direct indicator explaining the significant alterations observed in the phase diagram of the MoSe2/RTG/WSe2 heterostructure, as shown in Figure 4.11. The modifications are substantial compared to the original RTG phase diagram in Figure 4.10.

Therefore, RTG is an exceptional platform for investigating the intricate relationship between proximity-induced spin interactions and correlated phenomena.

4.6.2. Fermi surfaces and Lifshitz transitions

Since RPA mainly reveals correlated phases, whose appearance is principally associated with nesting, we construct Fermi surfaces with a finite doping level for a zero displacement

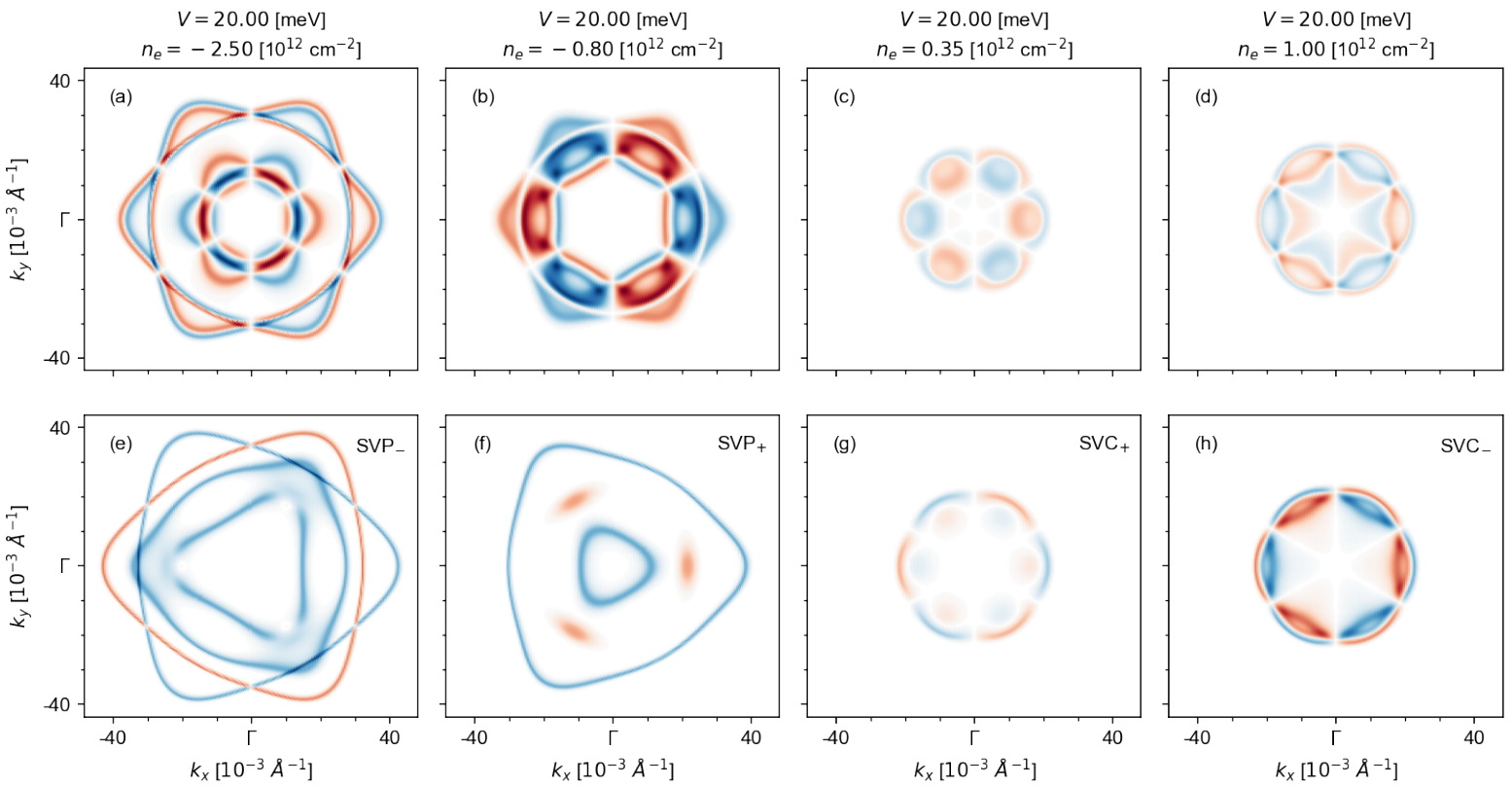

Figure 4.13: Fermi surfaces of a MoSe2/RTG/WSe2 heterostructure with a zero displacement field. Spin polarization is indicated in red for spin up and blue for spin down. The top row of panels (a),(b),(c), and (d) correspond to the K valley, and the bottom row of the panels (e),(f),(g), and (j) to the K'. The first column (a) and (e) shows the Fermi surface, which leads to SVP_+ instability, second (b) and (f) - SVP_-, third (c) and (g) - SVC_-, and last (d) and (h) - SVC_+.

field to reveal nesting. Fermi surfaces are displayed in Fig.4.13, where the top row of panels corresponds to the folded to the Γ point Fermi surfaces with correlation effects. In contrast, the bottom row of panels corresponds to the folded to the Γ point Fermi surfaces without correlation effects. Each column corresponds to a particular phase: the first column shows the Fermi surface, which leads to SVP_+ instability, second - SVC_-, third - SVC_+, and last - SVC_-. So, we can trace out which Fermi surface leads to a particular instability.

In the study illustrated by Figure 4.13, we observe that incorporating correlation effects alters the structure of the Fermi surfaces. This alteration triggers a Lifshitz transition, characterized by a shift in the number of Fermi pockets on the surface. Despite these changes, it is essential to note that the Fermi surface does not vanish entirely. It is a hallmark of the absence of the Mott transition, commonly seen in TWBG. The distinction between the correlation effects in RTG and TWBG becomes evident here. In the context of a Mott transition, the interaction parameter U is usually much larger than the bandwidth W, mathematically represented as $U/W \gg 1$. In TWBG, the bandwidth of bands near the Fermi level is constrained due to isolated bands. However, RTG presents a different scenario: it lacks such isolated bands, and its bandwidth is essentially "unlimited." In RTG, as the momentum $\mathbf{k}$ increases, the bands near the Fermi level evolve into a Dirac cone, limited only by an ultraviolet cutoff Λ. Therefore, the criterion for a Mott transition in RTG can be reformulated as $U/\Lambda \to 0$, concluding the absence of the Mott transition. Our calculations confirm that a Mott transition is unlikely to occur in RTG, underscoring the unique nature of correlation effects in different graphene-based materials.

4.6.3. Influence of Rashba coupling on the phase diagram

One of the critical differences of the $MoSe_2/RTG/WSe_2$ heterostructure, in contrast to the CGT/RTG/CGT heterostructures, is the presence of Rashba SO coupling, which in turn excludes the possibility of using the spin s_z as a good quantum number. The fractional quantum number τ_z remains a good quantum number. To determine the effect of Rashba SO coupling on the $MoSe_2/RTG/WSe_2$ heterostructure phase diagram, we performed the following numerical experiment: we turned off Rashba SO coupling and Valley-Zeeman SO coupling in turn and compared the final phase diagrams with the original complete parametrization of SO proximity-induced coupling.

The final phase diagrams are presented in Fig.4.14. Panel Fig.4.14 (a) presents the results for the full parameterization of SO proximity-induced coupling, panel (b) presents the results for pure Valley-Zeeman SO coupling, and panel (c) for pure Rashba SO coupling. As we can see, the resulting phase diagrams for complete parametrization and pure Valley-Zeeman SO coupling do not differ. In contrast, for pure Rashba SO coupling, we observe the manifestation of new correlated phases, such as:

1. Spin-Density-Wave (SDW) instability is characterized by spatial spin modulation with wave vector $\mathbf{q} = \frac{2\pi}{3a}(1, \sqrt{3})$ and is the IVC instability derivative of the spin

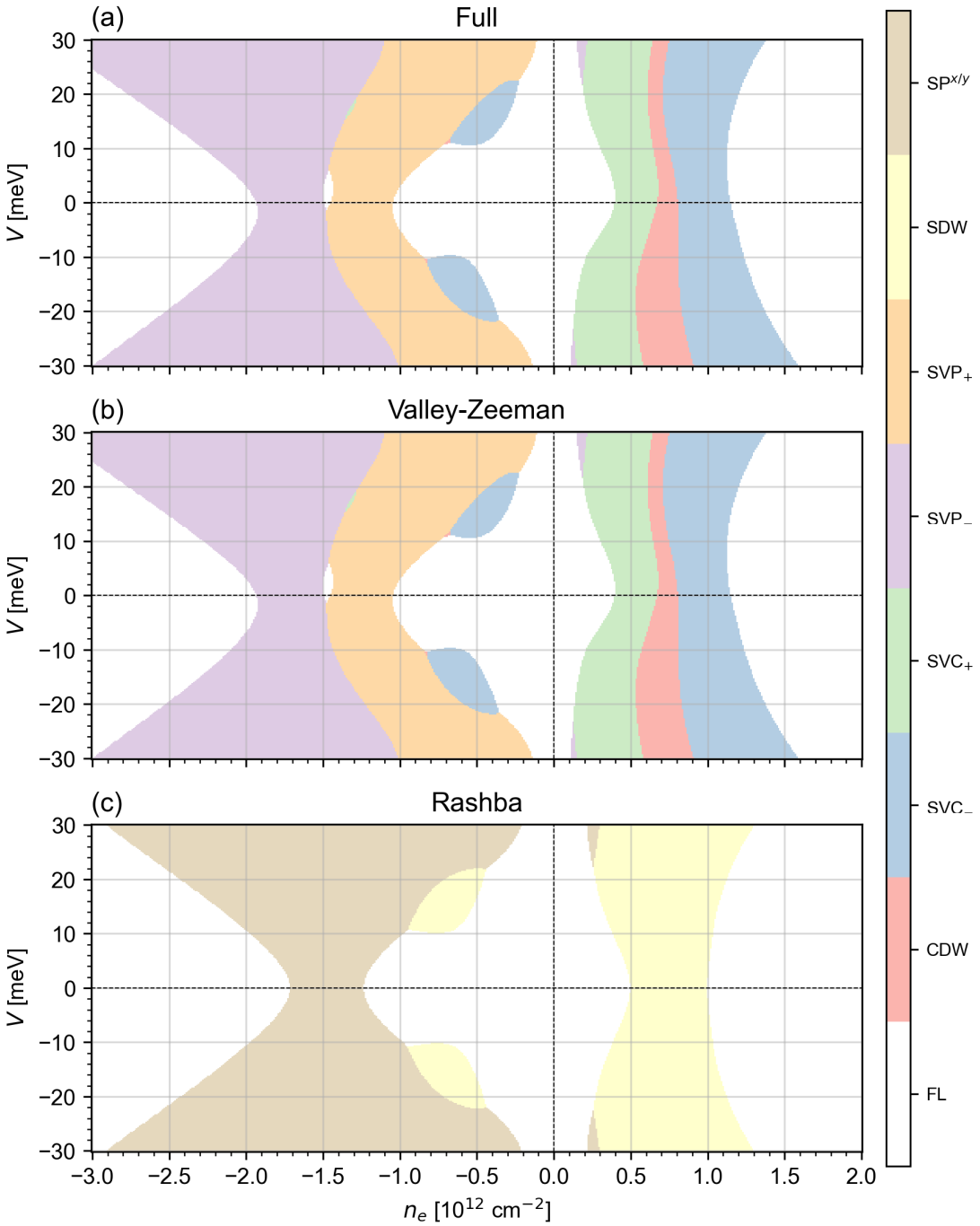

Figure 4.14: Phase diagram of the MoSe2/RTG/WSe2 heterostructure model as a function of the displacement field V and the doping density n_e for three different SO configuration: (a) full proximity-induced SO parametrization, (b) pure Valley-Zeeman SO parametrization, and (c) pure Rashba SO parametrization. Interaction parameters are taken equal to $U_0 = U_1 = 19$ eV. These phases are color-coded to indicate potential instability in the Fermi liquid state (shown in white).

channel instability. Therefore, the order parameter for SDW instability is:

$$\hat{\Sigma}_{\mathrm{SDW}} = \sum_{\bar{a}b} \left[s_z \otimes \tau_{x/y} \right]_{\bar{a}b} \hat{c}^{\dagger}_{\bar{a}} \hat{c}_b \tag{4.56}$$

2. Spin-Polarized (SP), local instability, Stoner derivative with the following order parameter:

$$\hat{\Sigma}_{\mathrm{SP}^{x/y}_{\pm}} = \sum_{\bar{a}b} \left[(\tau_z \pm \tau_0) s_{x/y} \right]_{\bar{a}b} \hat{c}^{\dagger}_{\bar{a}} \hat{c}_b, \tag{4.57}$$

characterized by spin in-plane polarization. $\mathrm{SP}^{x/y}_{\pm}$ correlated phase induces gap opening between spin-valley flavors with an identical product of valley quantum number τ

Therefore, we can conclude that the influence of Rashba SO coupling on the phase diagram of the $MoSe_2$/RTG/WSe_2 heterostructure is minimal, which in turn is a consequence of the mutual suppression of proximity-induced Rashba SO coupling from $MoSe_2$ and WSe_2 substrates, which can be observed from downfolded $k \cdot p$ Hamiltonian for Rashba SO coupling:

$$\hat{h}_R(\mathbf{k}, \tau) = (\lambda^1_R + \lambda^3_R) \frac{(v_F k)^2}{t_1^2} [\cos(2\phi) (\tau \hat{\sigma}_x \hat{s}_y - \hat{\sigma}_y \hat{s}_x) - \sin(2\phi) (\tau \hat{\sigma}_x \hat{s}_x - \hat{\sigma}_y \hat{s}_y)]. \tag{4.58}$$

So, we can introduce new effective Rashba SO coupling amplitude $\tilde{\lambda}_R = \lambda^1_R + \lambda^3_R = 0.233[\mathrm{meV}] - 0.475[\mathrm{meV}\ ] = -0.242[\mathrm{meV}]$. We can observe that the resulting effective Rashba SO coupling, due to different signs of proximity-induced Rashba SO coupling from $MoSe_2$ and WSe_2 substrates, is strongly suppressed and almost equal in amplitude for graphene/$MoSe_2$ case (See Table 4.1).

To summarize, we can state that the effect on $MoSe_2$/RTG/WSe_2 heterostructure phase diagram of Valley-Zeeman SO coupling is more pronounced when compared with Rashba SO coupling. Furthermore, SVP and SVC correlated phases are mainly Valley-Zeeman SO coupling induced.

4.7. Phase diagrams of a ferromagnetic and antiferromagnetic CGT/RTG/CGT heterostructure

4.7.1. Ferromagnetic CGT/RTG/CGT heterostructure: phase diagram

We continue our discussion of the interplay of proximity-induced spin interaction with correlated phenomena by constructing a phase diagram of correlated instabilities for the CGT/RTG/CGT with ferromagnetic (FM) CGT alignments heterostructure. This heterostructure induces strong EX coupling in the RTG, as described in the previous sections. Using RPA in conjunction with the Hartree-Fock method, we repeat the MoSe2/RTG/WSe2 heterostructure analysis for the FM CGT/RTG/CGT heterostructure.

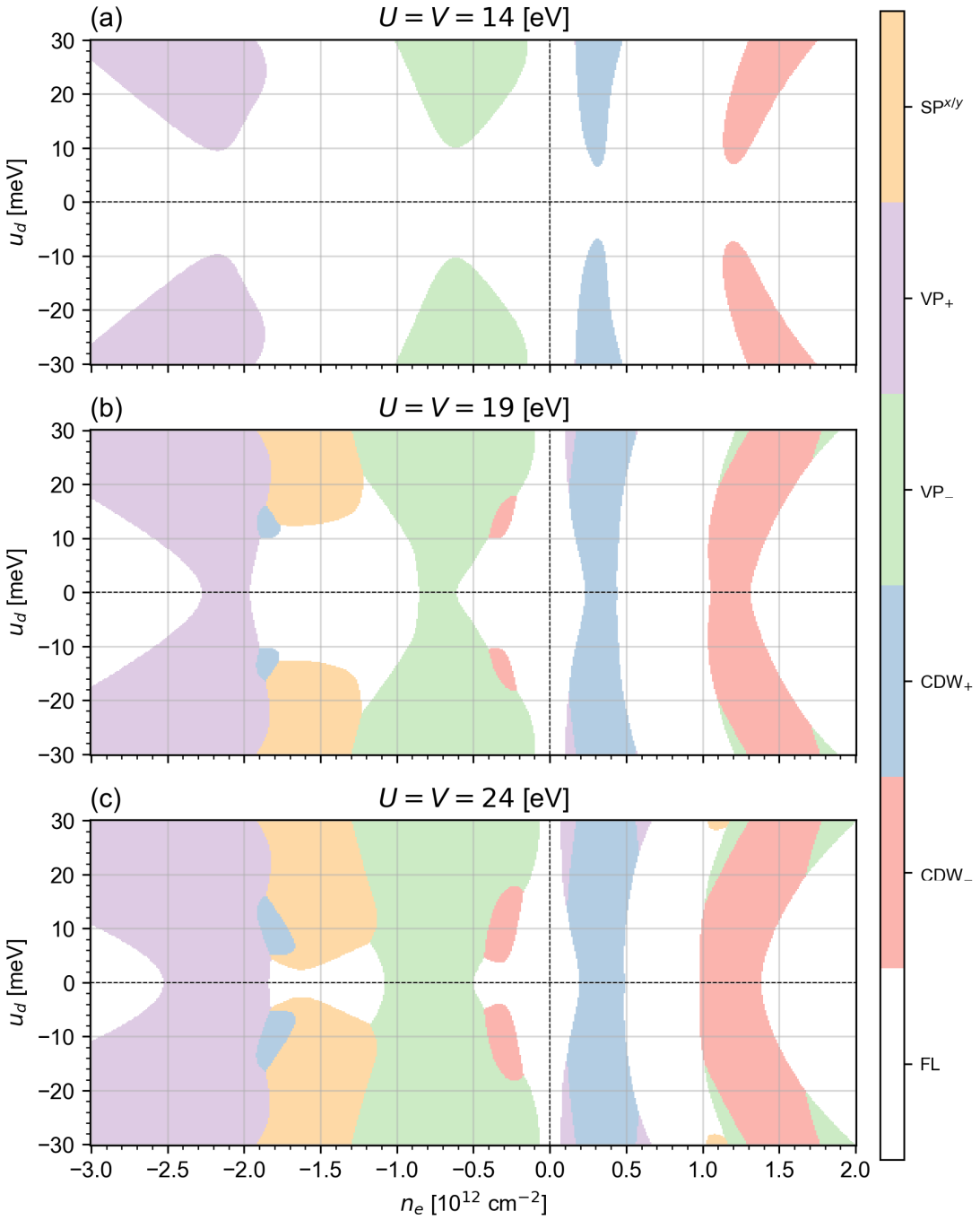

Figure 4.15: Phase diagram of the CGT/RTG/CGT heterostructure with ferromagnetic CGT alignments as a function of the displacement field V and the doping density n_e. The diagram predicts six different phases, with symmetry breaking: CDW± (charge density wave), VP± (valley-polarized state), and $\mathrm{SP}_{\pm}^{x/y}$ (in-plane spin-polarized state). These phases are color-coded to indicate potential instability in the Fermi liquid state (shown in white).

Compared to the MoSe2/RTG/WSe2 heterostructure, with the diagonalization of $\chi^0_{ph}\Gamma^{\mathrm{RPA}}_{ph}$ at zero displacement field $V = 0$ and charge-neutrality point $\mu = 0$, we also identified such instabilities as:

1. Charge-Density-Wave (CDW) instability is characterized by spatial charge modulation with wave vector $\mathbf{q} = \frac{2\pi}{3a}(1, \sqrt{3})$ and is the IVC instability derivative of the charge channel instability. Therefore, the order parameter for CDW instability is:

$$\hat{\Sigma}_{\mathrm{CDW}_\pm} = \sum_{\bar{a}b} \Big[(s_0 \pm s_z) \otimes \tau_{x/y}\Big]_{\bar{a}b} \hat{c}^\dagger_{\bar{a}} \hat{c}_b \tag{4.59}$$

   Such splitting indicates that only two spin-valley flavors can form a correlated CDW phase. From Eq.(4.59), we can state that CDW phases represent spin-conservative inter-valley hopping.

2. Valley-Polarized (VP) instability is local, so is a Stoner instability derivative. $\mathrm{VP}_\pm$ instabilities have order parameters as:

$$\hat{\Sigma}_{\mathrm{VP}_\pm} = \sum_{\bar{a}b} [(s_z \pm s_0)\tau_z]_{\bar{a}b} \hat{c}^\dagger_{\bar{a}} \hat{c}_b, \tag{4.60}$$

   and characterized by charge-valley polarization. So, the $\mathrm{VP}_\pm$ correlated phase induces a gap opening between spin-valley flavors with an identical spin quantum number s_z product.

3. Spin-Polarized (SP) instability is also local, Stoner derivative with the following order parameter:

$$\hat{\Sigma}_{\mathrm{SP}^{x/y}_\pm} = \sum_{\bar{a}b} \Big[(\tau_z \pm \tau_0)s_{x/y}\Big]_{\bar{a}b} \hat{c}^\dagger_{\bar{a}} \hat{c}_b, \tag{4.61}$$

   and it is characterized by spin in-plane polarization. $\mathrm{SP}^{x/y}_\pm$ correlated phase induces a gap opening between spin-valley flavors with an identical product of valley quantum number τ.

Determining possible instabilities, we calculated the phase diagram with ferromagnetic CGT alignments. Figure 4.15 shows the resulting phase diagram. The IVC phase splits into two $\mathrm{CDW}_\pm$ phases, while the Stoner phase splits into four instabilities: two $\mathrm{VP}_\pm$ and two $\mathrm{SP}^{x/y}_\pm$ phases. Similar to the $\mathrm{CDW}_\pm$ phases in the $MoSe_2$/RTG/WSe_2 heterostructure, the $\mathrm{SP}^{x/y}_\pm$ phases in the CGT/RTG/CGT with ferromagnetic CGT alignments have almost degenerate character, and their separation does not strongly depend on model parameters due to the insignificant difference in the critical parameter λ^Σ_c. Due to the almost degenerate character of $\mathrm{SP}^{x/y}_\pm$ phases, we will not examine their band structure using the Hartree-Fock method.

4.7.2. Ferromagnetic CGT/RTG/CGT heterostructure: correlated band structure

As in the case of the MoSe2/RTG/WSe2 heterostructure, we predict Lifshitz transitions near points on the phase diagram for the CGT/RTG/CGT heterostructure with

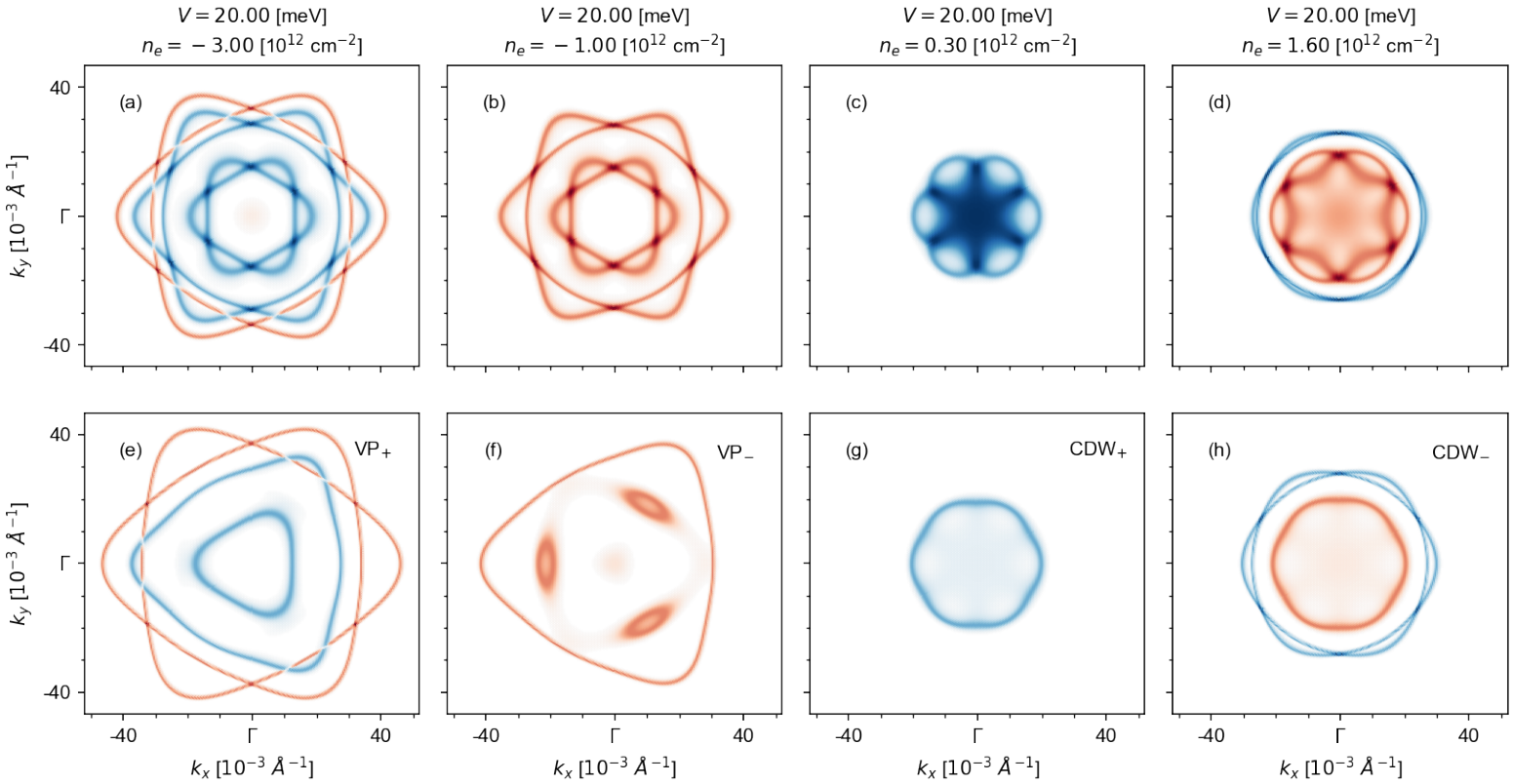

Figure 4.16: Fermi surfaces of the CGT/RTG/CGT heterostructure with ferromagnetic CGT alignments with a zero displacement field. Spin polarization is indicated in red for spin up and blue for spin down. The top row of panels (a),(b),(c), and (d) correspond to the K valley, and the bottom row of the panels (e),(f),(g), and (j) to the K'. The first column (a) and (e) shows the Fermi surface, which leads to VP_+ instability, second (b) and (f) - VP_-, third (c) and (g) - CDW_+, and last (d) and (h) - CDW_-.

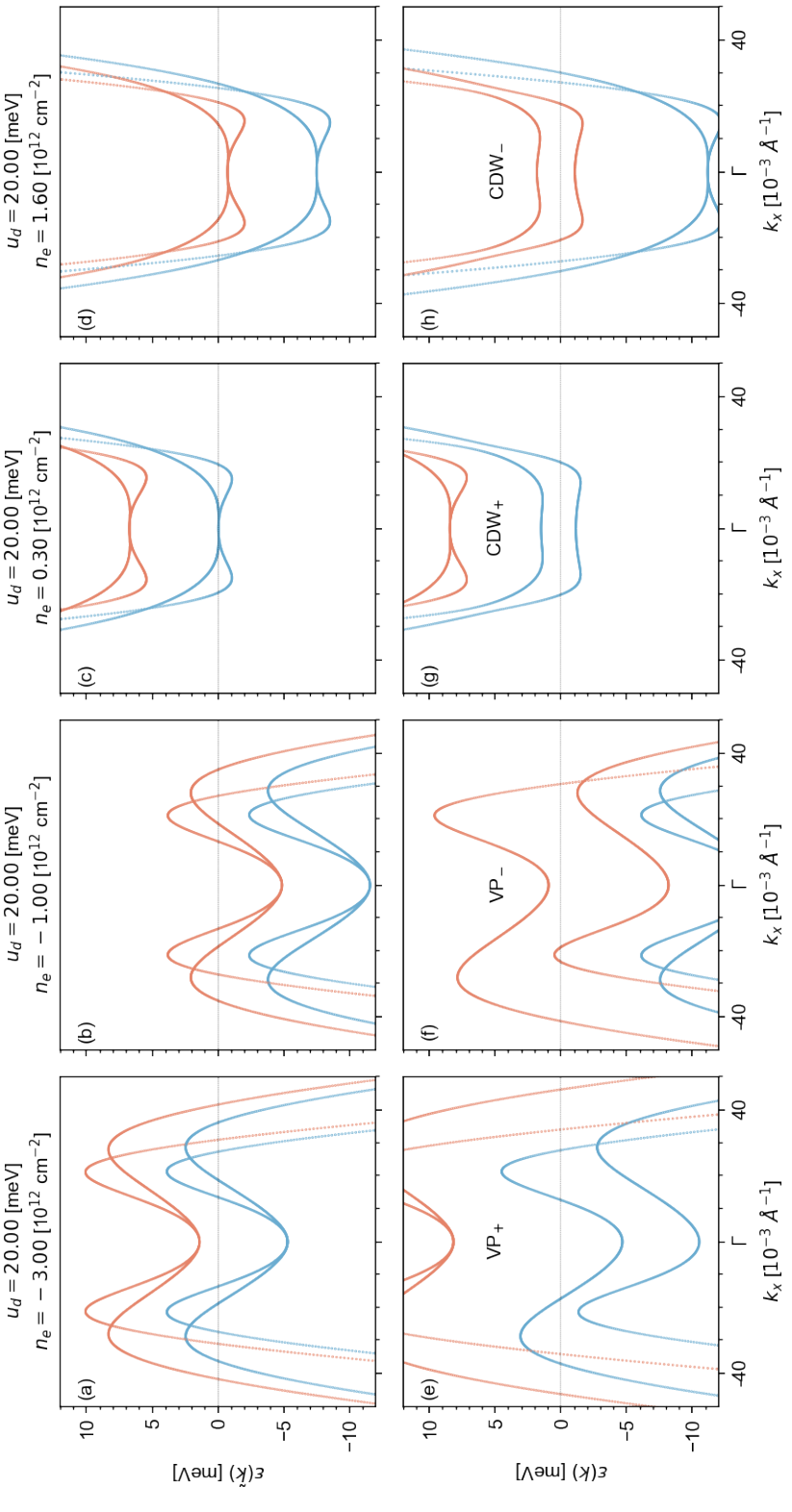

Figure 4.17: Folded to crystallographic Γ point band structure of a CGT/RTG/CGT heterostructure with ferromagnetic CGT alignments at displacement field equal to $V = 20$ meV and finite doping levels, with and without interaction corrections. The top row (a-d) shows Hartree-Fock band structures for VP$_+$, VP$_-$, CDW$_+$, and CDW$_-$ instabilities, respectively. The bottom row (e-j) shows band structures without interaction corrections. Spin polarization is indicated in red (spin up) and blue (spin down).

ferromagnetic CGT alignments, where correlated phases emerge. In Figure 4.16, the calculated Fermi surfaces are shown at zero displacement field level but at a finite doping level corresponding to the predicted points of the phase diagram where the appearance of correlated phases is expected. The first column panels (a) and (e) show the Fermi surface leading to VP_+ instability, the second column panels (b) and (f) show VP_-, the third (c) and (g) show CDW_+, and the last (d) and (h) show CDW_-.

Using the Hartree-Fock method, we calculated the band structure with interaction correction for VP_+, VP_-, CDW_+, and CDW_- correlated phases. We show the resulting band structures in Fig.4.17. As in the case of the MoSe2/RTG/WSe2 heterostructure, we predict the opening of a correlated gap and obtain values of correlated gaps for each correlated phase. For the calculated band structures presented in Fig.4.17, we obtained the following values of the correlated gaps: For panel (b), corresponding to VP_- instability $\gamma_{VP_-} = 1.869$ meV, for panel (c), corresponding to CDW_+ instability $\gamma_{CDW_+} = 0.911$ meV, and for panel (d), corresponding to CDW_- instability $\gamma_{CDW_-} = 0.747$ meV, for panel (a), corresponding to VP_+ instability, we do predict the value correlated gap equal to $\gamma_{VP_-} = 1.823$ meV.

4.7.3. Antiferromagnetic CGT/RTG/CGT heterostructure: phase diagram

The last heterostructure whose phase diagram we will look at is the CGT/RTG/CGT heterostructure with AFM CGT alignment. This structure differs in that at zero displacement field, it has mirror symmetry, which in turn protects the band structure of this system from spin splitting. However, with a finite displacement field, mirror symmetry is violated, and, in combination with proximity-induced EX coupling, a Kane-Mele-model-like spin order appears. Repeating the same procedure applied to the previous heterostructure, CGT/RTG/CGT heterostructure with FM CGT alignment, we obtained the band structure shown in Fig.4.18. As for CGT/RTG/CGT heterostructure with FM CGT alignment, $SP_{\pm}^{x/y}$ phases have almost degenerate behavior.

All correlated phases we observe in the FM CGT/RTG/CGT heterostructure are shown in the phase diagram in Fig.4.18. However, unlike the FM CGT/RTG/CGT heterostructure phase diagram, we observe asymmetry concerning the displacement field. Therefore, we can claim that we are keeping a magneto-correlation effect — strong sensitivity of the correlated phases to the relative magnetization orientations (parallel or antiparallel) of the encapsulating ferromagnetic layers. The phase diagram is sensitive to the magnetic ordering of the CGT layers. Based on this effect, we can propose a magnetic field-controlled correlated valve.

4.7.4. Antiferromagnetic CGT/RTG/CGT heterostructure: correlated band structure

Also, in addition to analyzing the phase diagram, we built Fermi surfaces, but for the finite displacement field $V = 10$ meV for inducing spin splitting to visualize the Lifshitz transition. The resulting Fermi surfaces are shown in Fig.4.19. As for the previous heterostructures, we observe Lifshitz transitions only for one spin-valley pair, which forms

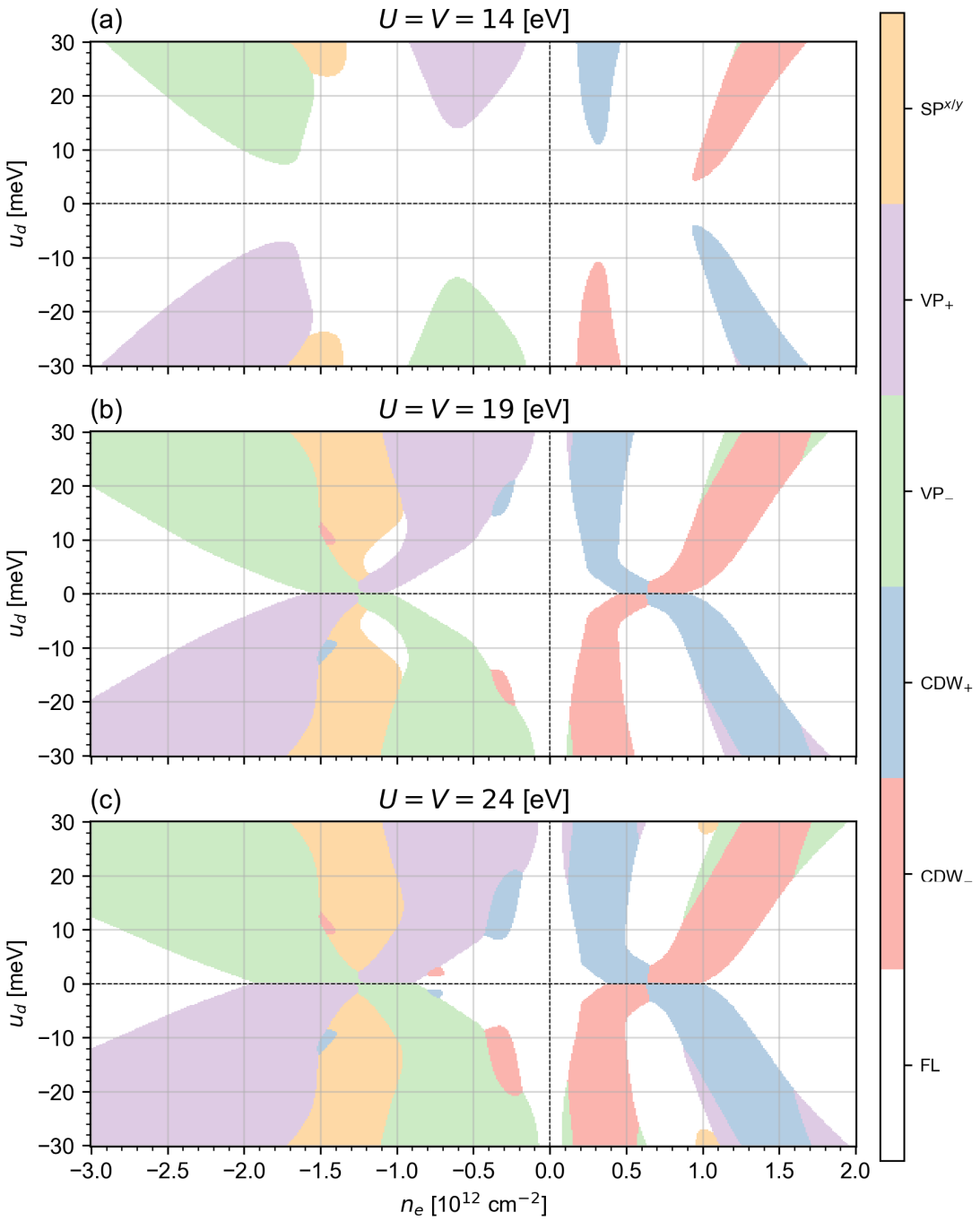

Figure 4.18: Phase diagram of the CGT/RTG/CGT heterostructure with antiferromagnetic CGT alignments as a function of the displacement field V and the doping density n_e. The diagram predicts six different phases, with symmetry breaking: CDW± (charge density wave), VP± (valley-polarized state), and $\mathrm{SP}_{\pm}^{x/y}$ (in-plane spin-polarized state). These phases are color-coded to indicate potential instability in the Fermi liquid state (shown in white).

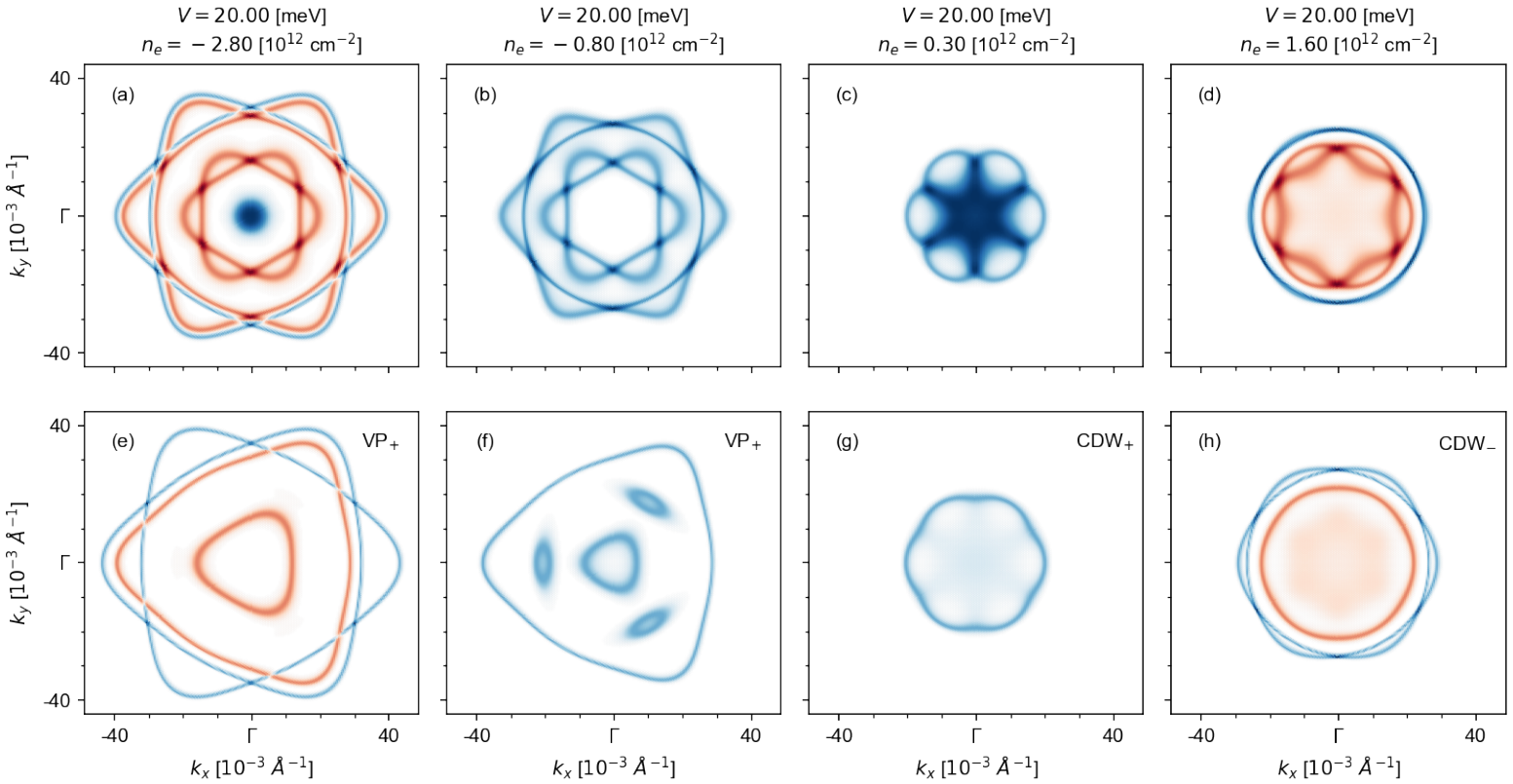

Figure 4.19: Fermi surfaces of the CGT/RTG/CGT heterostructure with antiferromagnetic CGT alignments with a zero displacement field. Spin polarization is indicated in red for spin up and blue for spin down. The top row of panels (a),(b),(c), and (d) correspond to the K valley, and the bottom row of the panels (e),(f),(g), and (j) to the K'. The first column (a) and (e) shows the Fermi surface, which leads to VP_+ instability, second (b) and (f) - VP_-, third (c) and (g) - CDW_+, and last (d) and (h) - CDW_-.

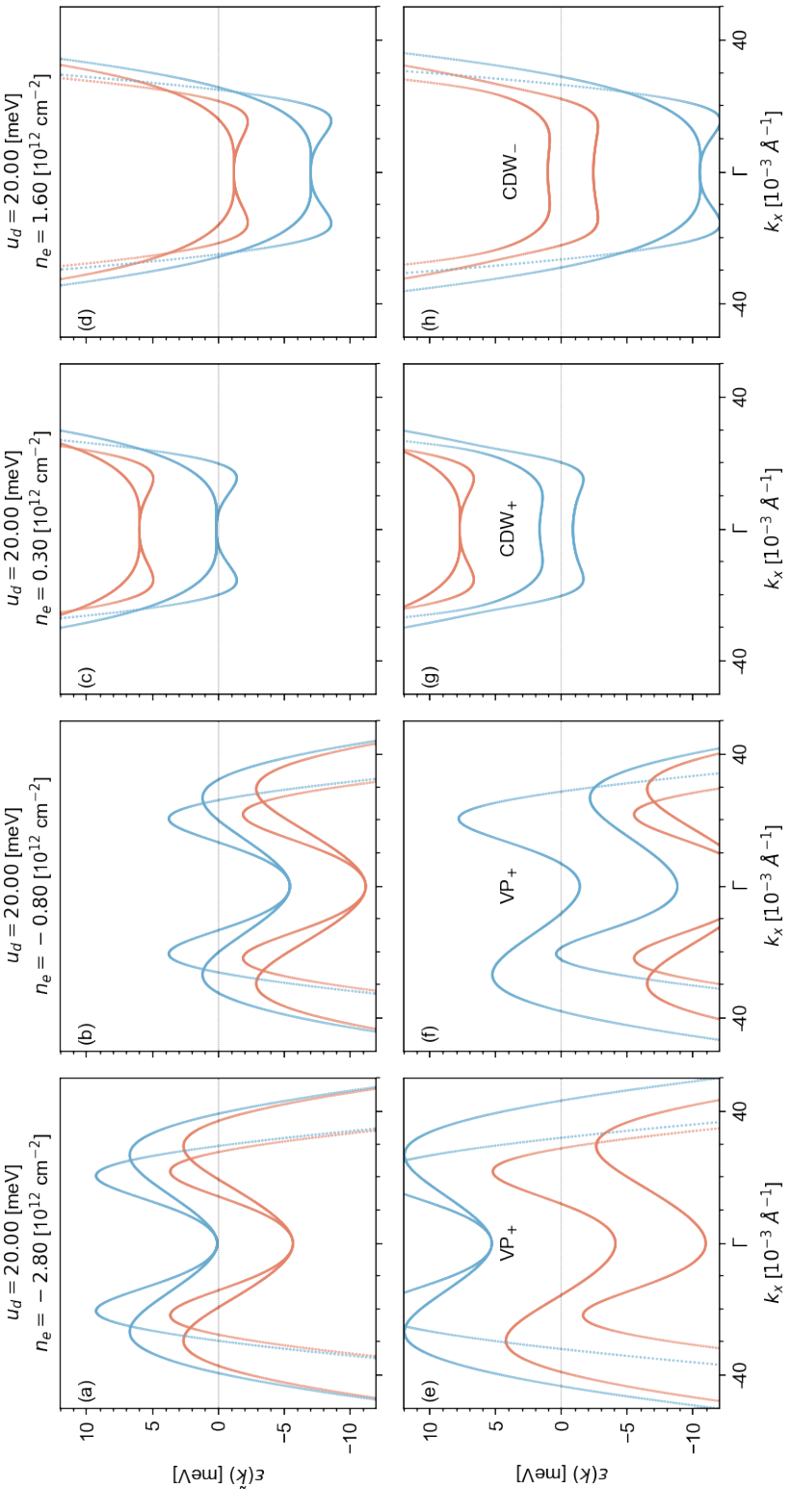

Figure 4.20: Folded to crystallographic Γ point band structure of a CGT/RTG/CGT heterostructure with antiferromagnetic CGT alignments at displacement field equal to $V = 20$ meV and finite doping levels, with and without interaction corrections. The top row (a-d) shows Hartree-Fock band structures for VP$_+$, VP$_-$, CDW$_+$, and CDW$_-$ instabilities, respectively. The bottom row (e-j) shows band structures without interaction corrections. Spin polarization is indicated in red (spin up) and blue (spin down).

a correlated phase.

Calculated examples of correlated band structures for CGT/RTG/CGT heterostructure with AFM CGT alignment are shown in Fig.4.20. We also calculated the correlated gap values: For panel (a), corresponding to VP_+ instability, we do predict the value correlated gap equal to $\gamma_{VP_-} = 2.134$ meV, for panel (b), corresponding to VP_+ instability $\gamma_{VP_+} = 1.787$ meV, for panel (c), corresponding to CDW_+ instability $\gamma_{CDW_+} = 0.890$ meV, and for panel (d), corresponding to CDW_- instability $\gamma_{CDW_-} = 0.958$ meV.

The amplitudes of the non-zero correlated gaps in ferro- and antiferromagnet CGT-/RTG/CGT heterostructures are comparable with the values of EX coupling parameters induced by the proximity effect, which directly indicates the reason for the substantial modification of the CGT/RTG/CGT heterostructure with ferromagnetic CGT alignments phase diagram shown in Fig.4.15, compared to the pristine RTG phase diagram, in Fig.4.10. It is an additional argument that RTG is an excellent platform for studying the interplay of proximity-induced EX coupling with correlated phenomena.

4.8. Conclusions

Our study on RTG delved into the effects of proximity-induced RTG and EX coupling on its correlated phase diagram. Using ab initio-fitted effective models, we discovered a range of spin-valley resolved instabilities brought about by RTG proximity effects. Interestingly, a unique spin-valley-coherent phase emerged due to valley-Zeeman coupling. We also observed that proximity EX removed phase degeneracies, making the correlated phases sensitive to magnetization orientations of the encapsulating magnetic layers. Our research underscores that correlation phenomena are not exclusive to moiré structures, and our findings suggest that RTG, even without moiré patterns, can exhibit strong electronic correlations. By leveraging van der Waals engineering, we could tune electronic band structures, introduce RTG fields and spin polarization to graphene, and model correlated phase diagrams of the resulting system. The presented phase diagrams for various heterostructures further elucidate these effects. Overall, our work offers valuable insights for spintronics, highlighting the potential of Coulomb-induced spin-valley couplings in RTG.

5. Swapping exchange and spin-orbit induced correlated phases in ex-so-tic van der Waals heterostructures

5.1. Introduction

Having considered the RTG system as a platform for studying the interaction of electronic correlations and spin interactions caused by the proximity effect, our next step was to explore a more experimentally widespread graphene system manifesting correlation effects - Bernal Bilayer Graphene (BBG) [228, 229, 230, 231, 232, 233, 234, 235, 267].

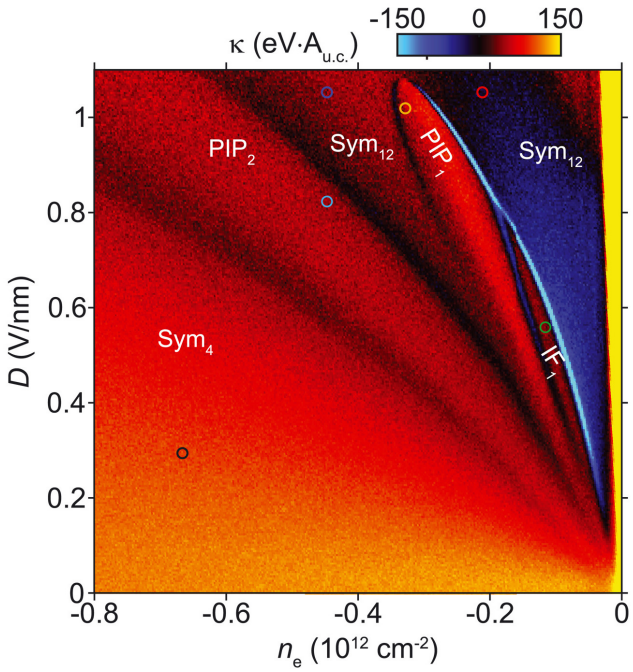

Figure 5.1: Experimentally determined inverse compressibility of pristine BBG at zero magnetic field. Adapted from [228].

In condensed matter physics, twisted graphene structures have been a fertile ground for discovering a plethora of novel electronic correlation effects [173, 174, 175, 176]. However, recent advancements have shown that moiré patterns are not the sole avenue for exploring

correlated physics. Specifically, RTG has exhibited quarter and half-metallic states [222, 223, 224, 225, 226, 227] as well as superconductivity [266, 268, 269, 259, 260, 224, 270, 271]. Furthermore, BBG has been the stage for the observation of isospin magnetism and spin-polarized superconductivity [228, 229, 230, 231, 232, 233, 234, 235, 267]. The experimental results depicted in Figure 5.1, taken from [228], showcase the inverse compressibility $\frac{\partial \mu}{\partial n_e}$ of the Fermi liquid in BBG at zero magnetic field. The diagram displays negative values, indicating the presence of strong electron correlations within this system [240]. However, further data is required to uncover the nature of the correlated phases and measure the local magnetic structure, spin, and charge transport. A common thread linking these phenomena is the presence of van Hove singularities near the charge neutrality point, which amplify electron-electron interactions [177, 178, 239]. Intriguingly, these correlated phases can be tuned by a displacement field, altering the electronic levels of the van Hove singularities [222, 266, 228, 229].

In addition to intrinsic properties, the electronic states of 2D materials in van der Waals heterostructures can be significantly influenced by proximity effects [96]. For instance, materials like graphene, which inherently exhibit weak spin-orbit coupling, can experience enhanced spin interactions due to these effects [64, 272, 66]. Both theoretically predicted [134, 241, 86, 68, 69, 242, 243, 244, 245, 246, 78, 242, 243, 244, 247] and experimentally confirmed [108, 109, 111, 74, 91, 112, 90, 113, 114, 117, 248, 110], proximity-induced spin-orbit (SO) and exchange (EX) interactions have been observed in BBG-based heterostructures. Specifically, various types of SO couplings like valley-Zeeman, Kane-Mele, and Rashba, along with (anti)ferromagnetic EX couplings, have been identified, typically causing spin splittings on the milli-electronvolt (meV) scale [134, 108, 109, 111, 74, 91, 112, 90, 113, 114, 117, 248, 241, 86, 68, 69, 242, 243, 134, 244, 247, 245, 246, 249, 242, 243, 244, 248, 110, 247].

One of the most captivating outcomes of these proximity effects is the ability to interchange the spin couplings, EX and SO, by applying a displacement field. This phenomenon emerges from the interplay between short-range proximity interactions and layer polarization induced by the external field. A particularly relevant material system for experimental study is BBG encapsulated on one side by a robust SO material like WS_2 and on the other by a magnetic semiconductor such as $Cr_2Ge_2Te_6$ (CGT). This unique heterostructure, termed as 'ex-so-tic,' allows for the selective imprinting of either SO or EX coupling onto the Bloch states of BBG [243].

Given the capability of BBG to host various correlated phases, we pose the question: Is it feasible to switch between phases induced by EX and SO couplings? Our study demonstrates that 'ex-so-tronic' devices can provide on-demand correlated phases. It is achieved by altering the effective single-particle excitation Hamiltonians through layer polarization. Although our conclusions have broader implications, we focus on the WS_2/BBG/CGT system, for which an effective orbital and spin-interaction Hamiltonian has been derived using DFT [242, 243]. The recent discovery of the potential for a significant increase in the critical temperature of the superconducting transition in BBG/TMDC systems [229], supported by theoretical predictions [237, 236, 273, 274, 267], highlights the promising direction of studying the interplay of correlation phenomena in multilayer graphene systems with the spin interactions caused by the proximity effect.

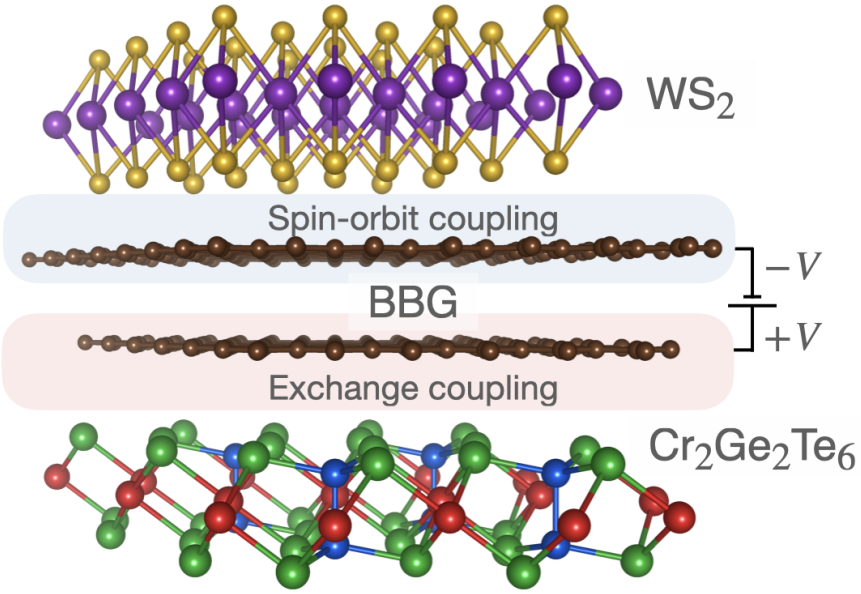

Figure 5.2: Scheme of an ex-so-tic heterostructure comprising BBG encapsulated by WS_2 and CGT, which proximitize the BBG by SO (WS_2) and EX (CGT) interactions.

To scrutinize the stability of these phases, we employ the random-phase approximation (RPA) [161, 162, 163, 255, 256, 257]. Initially, we examine the particle-hole instabilities in pristine BBG, which features correlated phases such as intervalley coherence (IVC) [258] and Stoner instabilities [259, 260]. The spin interactions induced by proximity SO and EX couplings lift the spin and valley degeneracies in IVC and Stoner phases, leading to a rich landscape of emergent spin-valley correlated phases. These phases can be effectively swapped in 'ex-so-tic' heterostructures like WS_2/BBG/CGT. The evidence for the intricate interplay between SO and EX interactions also manifests in the single-particle (Hartree-Fock) excitation spectra, which we calculated in our study.

5.2. Bernal Bilayer Graphene: electronic structure overview

Since its discovery, graphene has been extensively studied due to its remarkable properties. BBG presents intriguing phenomena and potential applications, characterized by a unique electronic band structure resulting from a specific stacking order. In this section, we explore the electronic properties of BBG.

BBG, also known as AB-stacked bilayer graphene, has a unique electronic structure resulting from the specific stacking order of its two layers, as depicted in Fig. 5.3 (c). In monolayer graphene, the electronic band structure exhibits Dirac cones, where the conduction and valence bands meet at the Dirac points, resulting in a zero bandgap semimetal behavior. However, the interlayer coupling in BBG modifies this structure,

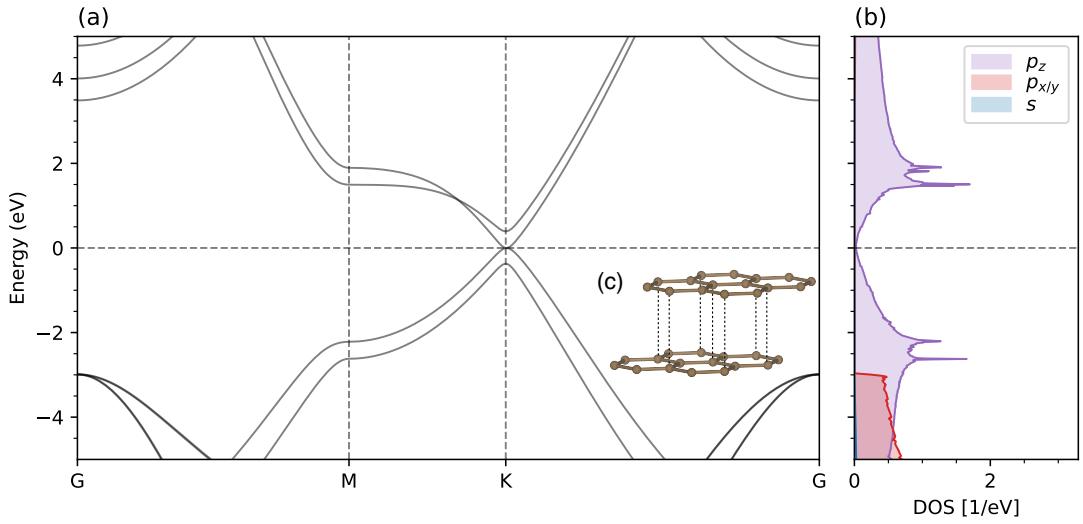

Figure 5.3: BBG's band structure (a) and orbital-resolved density of states (b) are calculated, along with its crystal structure (c).

whereby the Dirac cones from the individual layers hybridize, leading to parabolic bands near the Fermi level, as represented in Fig. 5.3 (a). As in monolayer graphene, in BBG p_z orbitals, extending from the graphene plane, form π-bands near the Fermi energy (See Fig. 5.3 (b)). The robust interlayer coupling in BBG is due to π-orbital overlap between layers, resulting in a modified band structure.

The minimal tight-binding Hamiltonian for BBG captures interlayer interactions by representing them in terms of hopping parameters between different atomic sites:

$$\begin{aligned}\hat{H} = &-\gamma_0 \sum_{s,\langle ij\rangle} \left(\hat{c}^\dagger_{A_l s}(\mathbf{R}_i)\hat{c}_{B_s}(\mathbf{R}_j) + \hat{c}^\dagger_{B_l s}(\mathbf{R}_j)\hat{c}_{A_l s}(\mathbf{R}_i)\right) \\ &-\gamma_1 \sum_{s,i} \left(\hat{c}^\dagger_{A_1 s}(\mathbf{R}_i)\hat{c}_{B_2 s}(\mathbf{R}_i) + \hat{c}^\dagger_{B_2 s}(\mathbf{R}_j)\hat{c}_{A_1 s}(\mathbf{R}_i)\right)\end{aligned} \tag{5.1}$$

where $\hat{c}^\dagger_{(A_l/B_l)s}(\mathbf{R}_i)$ $\left(\hat{c}^\dagger_{(A/B)s}(\mathbf{R}_i)\right)$ is the creation (annihilation) operator for an electron at graphene sublattice A/B, with spin s, at unit cell i and graphene layer l. The most crucial of these parameters are the intra-layer nearest-neighbor hopping term, similar to monolayer graphene, denoted as γ_0, and the inter-layer hopping term between vertically aligned atoms (A1 and B2 sites), represented as γ_1. The interlayer coupling leads to the hybridization of the Dirac cones from the individual layers, resulting in the formation of parabolic bands and the potential for a tunable bandgap. These additional terms can introduce subtle effects and refine the predicted band structure.

If we define

$$\psi_{\mathbf{k}} = (\hat{c}_{A_1\uparrow}(\mathbf{k})\hat{c}_{A_1\downarrow}(\mathbf{k})\hat{c}_{B_1\uparrow}(\mathbf{k})\hat{c}_{B_1\downarrow}(\mathbf{k})\hat{c}_{A_2\uparrow}(\mathbf{k})\hat{c}_{A_2\downarrow}(\mathbf{k})\hat{c}_{B_2\uparrow}(\mathbf{k})\hat{c}_{B_2\downarrow}(\mathbf{k}))^T \tag{5.2}$$

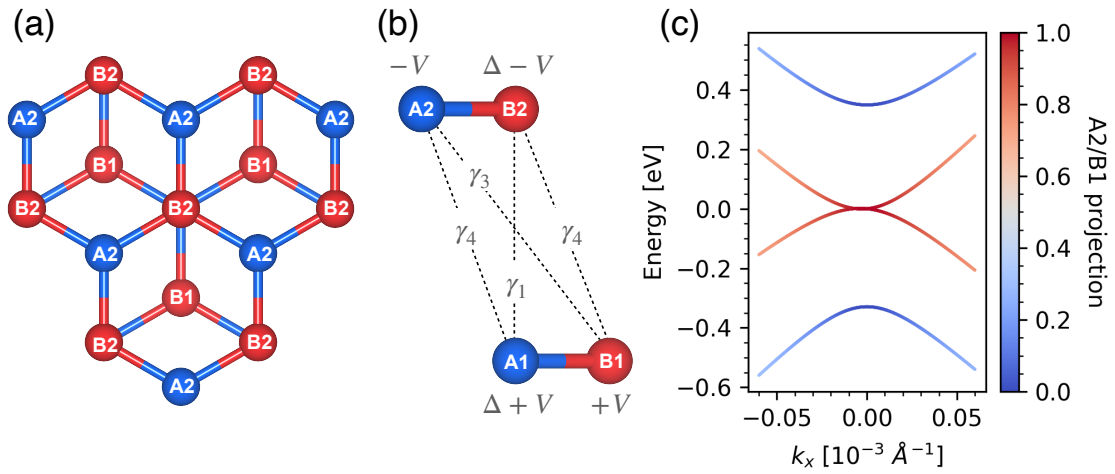

Figure 5.4: (a) The top-down view of the BBG lattice, (b) The BBG unit cell displays interlayer orbital hoppings and calculated single-particle electronic dispersions at K valley (c) without displacement fields for pristine BBG. Panel (c) is color-coded to denote atomic projections on lattice sites A1/B2, as in panel (b). The Fermi level corresponds to a zero energy value.

and perform a Fourier transformation of Eq.(5.1) , we can write

$$\hat{H} = \sum_{\mathbf{k}} \psi^{\dagger}_{\mathbf{k}} h(\mathbf{k}) \psi_{\mathbf{k}} \tag{5.3}$$

where matrix $h(\mathbf{k})$, the Bloch Hamiltonian, takes the form

$$h(\mathbf{k}) = \begin{pmatrix} 0 & \gamma_0 f(\mathbf{k}) & 0 & \gamma_1 \\ \gamma_0 f^*(\mathbf{k}) & 0 & 0 & 0 \\ 0 & 0 & 0 & \gamma_0 f(\mathbf{k}) \\ \gamma_1 & 0 & \gamma_0 f^*(\mathbf{k}) & 0 \end{pmatrix} \otimes s_0, \tag{5.4}$$

with $f(\mathbf{k}) = -\left(\sqrt{3}a/2\right)(\tau k_x - i k_y)$ is the linearized nearest-neighbor structural function with graphene's lattice constant a, and $\tau = \tau_{K/K'} = \pm 1$ is the valley index. While the primary hopping terms γ_0 and γ_1 capture BBG's essential electronic features, a more refined description might consider higher-order hopping terms, such as interlayer hoppings γ_3 between A_2 and B_1 lattice sites and γ_4 between lattice sites pairs such as A_1/A_2 and B_1/B_2. Therefore, taking into account γ_3, γ_4, and structural asymmetry between lattice sites A_1/B_2 and A_2/B_1 via onsite potential Δ we can rewrite Eq. (5.4) as

$$h(\mathbf{k}) = \begin{pmatrix} \Delta & \gamma_0 f(\mathbf{k}) & \gamma_4 f^*(\mathbf{k}) & \gamma_1 \\ \gamma_0 f^*(\mathbf{k}) & 0 & \gamma_3 f(\mathbf{k}) & \gamma_4 f^*(\mathbf{k}) \\ \gamma_4 f(\mathbf{k}) & \gamma_3 f^*(\mathbf{k}) & 0 & \gamma_0 f(\mathbf{k}) \\ \gamma_1 & \gamma_4 f(\mathbf{k}) & \gamma_0 f^*(\mathbf{k}) & \Delta \end{pmatrix} \otimes s_0. \tag{5.5}$$

All above-describe hoppings with onsite potential Δ are depicted in Fig.5.4(b), and the resulting bandstructure from Hamiltonian (5.5) for K valley is represented in Fig.5.4(c).

A fundamental property of BBG is its tunable bandgap. Unlike monolayer graphene, an external electric field can open and adjust a bandgap in BBG. Applying this perpendicular electric field alters the potential difference between the layers, causing a shift in the electronic bands and opening a bandgap by an additional term in the Hamiltonian

$$\hat{H}_V = V \sum_{s,li} (-1)^{l+1} \left(\hat{n}_{A_l s}(\mathbf{R}_i) + \hat{n}_{B_l s}\right) \tag{5.6}$$

Therefore, for the bottom layer, depicted in Fig.5.4(b), we have $+V$ potential, while for the top layer $-V$, which results in a potential difference between the two layers equal to $2V$. Within the tight-binding framework, this is incorporated as an onsite energy term, which subsequently modifies the band structure, enabling the opening and tuning of a bandgap. Including Eq.(5.6) in Eq.(5.5) we obtain

$$h(\mathbf{k}) = \begin{pmatrix} \Delta + V & \gamma_0 f(\mathbf{k}) & \gamma_4 f^*(\mathbf{k}) & \gamma_1 \\ \gamma_0 f^*(\mathbf{k}) & +V & \gamma_3 f(\mathbf{k}) & \gamma_4 f^*(\mathbf{k}) \\ \gamma_4 f(\mathbf{k}) & \gamma_3 f^*(\mathbf{k}) & -V & \gamma_0 f(\mathbf{k}) \\ \gamma_1 & \gamma_4 f(\mathbf{k}) & \gamma_0 f^*(\mathbf{k}) & \Delta - V \end{pmatrix} \otimes s_0. \tag{5.7}$$

This adaptability is significant for electronic and optoelectronic applications, as it facilitates the transition of BBG from a semimetal to a semiconductor, as shown in Fig. 5.5 (a) and (b), where we visualize the electronic bandstructure of BBG at a finite displacement field V near $\pm K$ point in BBG Brillioun zone. As in the case of RTG in Chapter 4, the band structure of BBG becomes flatter, and the density of states near the van Hove singularity increases with increasing V as shown in Fig. 5.5 (c) with consideration of finite temperature broadening ($T = 0.4$ K). In what follows, we point out that all calculations in this Chapter are done at a temperature equal to $T = 1/(k_B\beta) = 0.4$ K.

In Fig. 5.4 (c), we plot the atomic projected band structure on the A2/B1 lattice site to show that the band structure near the Fermi level is mainly localized on the A2 and B1 atoms. Therefore, we can assume that we can downfold four by four BBG Bloch Hamiltonian from Eq. (5.4) into two by two Bloch Hamiltonian, using the technique described in Appendix C, as

$$\tilde{h}(\mathbf{k}) = \frac{(v_F k)^2}{\gamma_1} \left(\cos(2\phi)\sigma_x + \tau \sin(2\phi)\sigma_y\right) \otimes s_0. \tag{5.8}$$

Here, $v_F = (\sqrt{3}a/2)\gamma_0$ is the Fermi velocity of the Dirac electron, Pauli matrices $\hat{\sigma}_i$ are defined based on A_2/B_1 sites and $\tan\phi = k_y/k_x$. The Hamiltonian (5.8) only considers γ_0 and γ_1 hoppings and neglects γ_3 and γ_4 for simplicity. Displacement field V can be represented in basis of A2/B1 lattice sites as

$$\tilde{h}_V(\mathbf{k}) = \left(V\left(\frac{(v_F k)^2}{\gamma_1^2} - 1\right)\sigma_z + \mathcal{O}(V^2)\right) \otimes s_0 \tag{5.9}$$

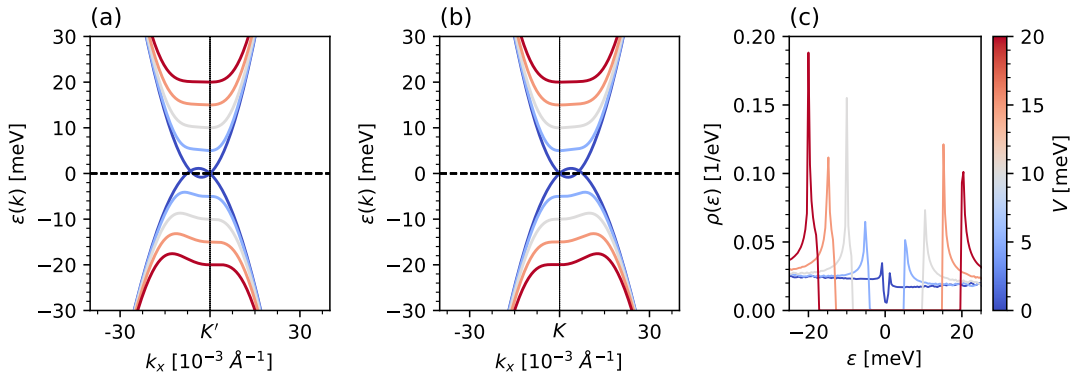

Figure 5.5: Calculated the low-energy electronic dispersions at K' (a) and K (b) using $\hat{h}(\mathbf{k}, \tau)$ and the low-energy density of states (c) with and without displacement fields for pristine RTG. The amplitude of the displacement field is color-coded.

where we can note $\frac{(v_F k)^2}{\gamma_1^2}$ term. This component, in the presence of a finite potential V, modifies the band structure forming the so-called "Mexican hat" [264], shown in Fig. 5.6, when the straight slot moves from the center K or K' valley to a finite moment k. However, in Fig. 5.6, we can observe trigonal warping of BBG bandstructure at finite displacement field V. This effect is mainly due to γ_3 hopping, which can be represented as an additional term to Hamiltonian (5.8)

$$\tilde{h}_{\gamma_3}(\mathbf{k}) = v_3 k \left(\cos(\phi)\sigma_x + \tau \sin(\phi)\sigma_y\right) \otimes s_0 \tag{5.10}$$

where $v_3 = (\sqrt{3}a/2)\gamma_3$. Since Eq.(5.10) $\propto e^{i\phi\tau}$, while Eq.(5.8) $\propto e^{i2\phi\tau}$, we low-energy band structure of BBG has ϕ beating that result in trigonal warping. In turn, γ_4 hopping introduces only a Fermi velocity correction to the Eq. (5.8) component without fundamental modifications to the band structure, just like onsite potential Δ.

To summarize, we have considered all the components of the complete Bloch Hamiltonian (5.7) for BBG. The BBG band structure has two main effects: the presence of a "Mexican hat" with a finite displacement field V and trigonal warping caused by γ_3 hopping. Trigonal warping and "Mexican hat" induce a Lifshitz transition responsible for the appearance of van Hove singularity in the low-energy region. The ability to broadly control the band structure using an external V field, including control of the energy position of van Hove singularity and density of states at van Hove singularity, makes BBG an extremely attractive material for studying strong correlations.

5.3. Proximity-induced spin interaction in ex-so-tic BBG heterostructure

We incorporate two specific couplings, SO and EX, to model the behavior of proximitized BBG within a WS_2/BBG/CGT heterostructure. The SO coupling arises from the

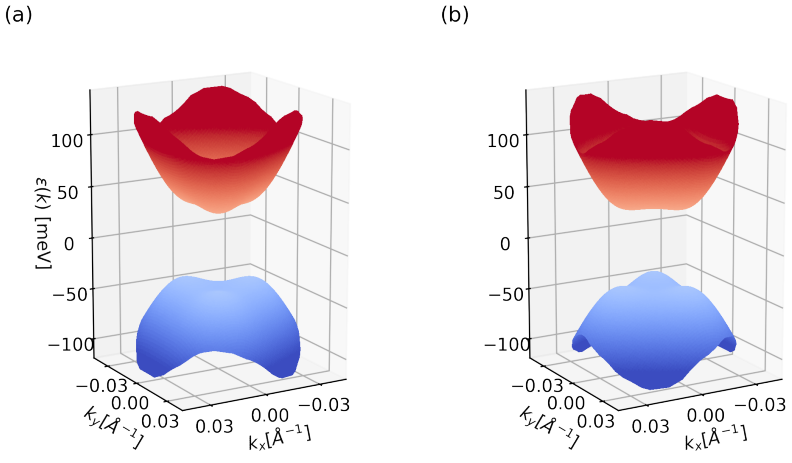

Figure 5.6: Low-energy electronic bandstructure at K' (a) and K (b) calculated from $\hat{h}(\mathbf{k}, \tau)$ Eq.(5.7) with displacement fields $V = 40$ meV for pristine BBG. Color code denotes band energy.

WS_2 layer, while the EX coupling is due to the CGT layer. These couplings have been demonstrated to have significant magnitudes, approximately around 1 meV. It was confirmed through both theoretical *ab initio* DFT calculations and experimental measurements, specifically weak-antilocalization measurements [85].

The interactions induced by EX and SO couplings are described near the K and K' valleys in the Hamiltonian, which are given by:

$$\hat{h}_{\text{prox}}(\tau) = \sum_l \hat{h}^l_{\text{vz}}(\tau) + \hat{h}^l_{\text{ex}}(\tau) \tag{5.11}$$

The terms represent valley-Zeeman (vz) SO and EX (ex) coupling.

The representation of these interactions is as follows:

$$\hat{h}^l_{\text{vz}}(\tau) = \begin{pmatrix} \tau\, \lambda^{A_l}_{\text{vz}}\, s_z & 0 \\ 0 & -\tau\, \lambda^{B_l}_{\text{vz}}\, s_z \end{pmatrix} \tag{5.12}$$

$$\hat{h}^l_{\text{ex}}(\tau) = \begin{pmatrix} -\lambda^{A_l}_{\text{ex}}\, s_z & 0 \\ 0 & -\lambda^{B_l}_{\text{ex}}\, s_z \end{pmatrix} \tag{5.13}$$

These equations are parameterized by specific sublattice and layer-related couplings, denoted as $\lambda^{A_l/B_l}_{\text{vz}}$ and $\lambda^{A_l/B_l}_{\text{ex}}$. The term s_z represents the spin Pauli matrix. Each matrix $\hat{h}^l$ is a 4×4 matrix that operates in a basis that resolves both spin and sublattice: $(A_{l\uparrow}, A_{l\downarrow}, B_{l\uparrow}, B_{l\downarrow})$. Here, the layer l can be either the bottom layer ($l = 1$) or the top layer ($l = 2$).

Notably, SO coupling in graphene induced by TMDCs is of the valley-Zeeman type. As a result, the relationship between the couplings for the two sublattices is given by $\lambda^{A_l}_{\text{vz}} \approx -\lambda^{B_l}_{\text{vz}}$.

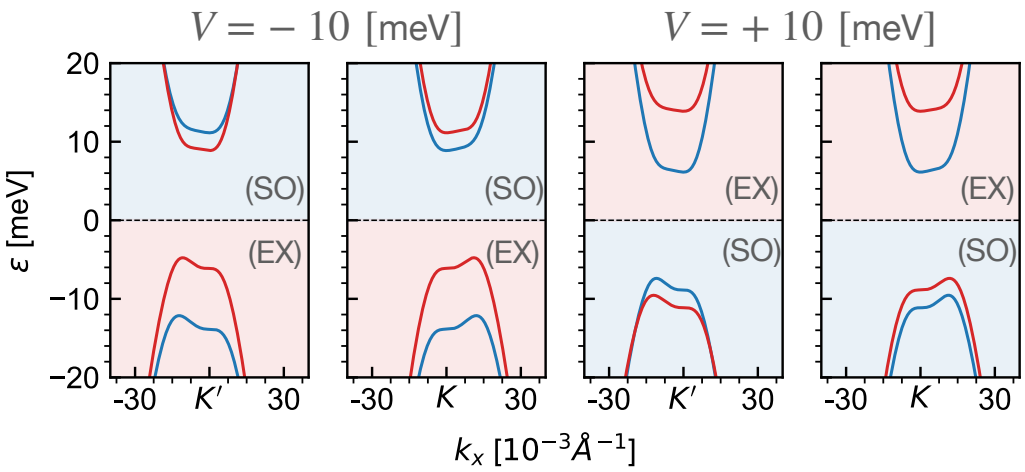

Figure 5.7: Calculated electronic band structure at low energy for the WS_2/BBG/CGT system near the K and K' points. The band structure was obtained with a potential V set to either +10 meV or -10 meV. The color-coded bands show spin polarization, with red representing spin-up electrons and blue representing spin-down electrons. It is worth noting that the spin quantization axis, z, is perpendicular to the layers of the material.

The numerical values for the parameters of the single-particle Hamiltonian, $\hat{h}(\mathbf{k}, \tau) = \hat{h}_0(\mathbf{k}, \tau) + \hat{h}_{\text{prox}}(\tau)$, where $\hat{h}_0$ is pristine BBG Bloch Hamiltonian (5.7), are taken from the *ab initio* results of Ref. [243] and presented in Table.5.1. The calculated low-energy band dispersions for WS_2/BBG/CGT are shown in Fig. 5.7. The signs of V and electron doping n_e determine the dominant proximity spin interaction. If both V and n_e positive or negative, the electrons at the Fermi level experience proximity EX coupling, while if the signs of V and n_e are opposite, the electrons at the Fermi level have strong proximity SO or EX couplings, we use labels (SO) and (EX) in Fig. 5.7, respectively.

We look at the impact of EX and SO couplings in detail. To begin with, we calculate a band structure for different levels of displacement field V, considering only SO coupling with turned-off EX coupling. Figure 5.8 shows the resulting band structure. As we can note, the SO splitting of the valence band and the conduction band depends on the sign of the displacement field V; therefore, the configuration of the WS_2/BBG heterostructure can be a spin-field Datta-Das transistor, based on the assumption that the type of excess carries, such as hole or electron doping, does not depend on the sign of displacement field. As Figure 5.8 shows, the spin-valley splitting of the possible WS_2/BBG heterostructure strictly corresponds to the Valley-Zeeman ordering. Consequently, in this heterostructure, the manifestation of correlated phases corresponding to SO interaction, described in Chapter 4 for the $MoSe_2$/CGT/WSe_2 heterostructure, is possible, which will be confirmed in our further reasoning.

We also calculate the band structure of the WS_2/BBG/CGT heterostructure with

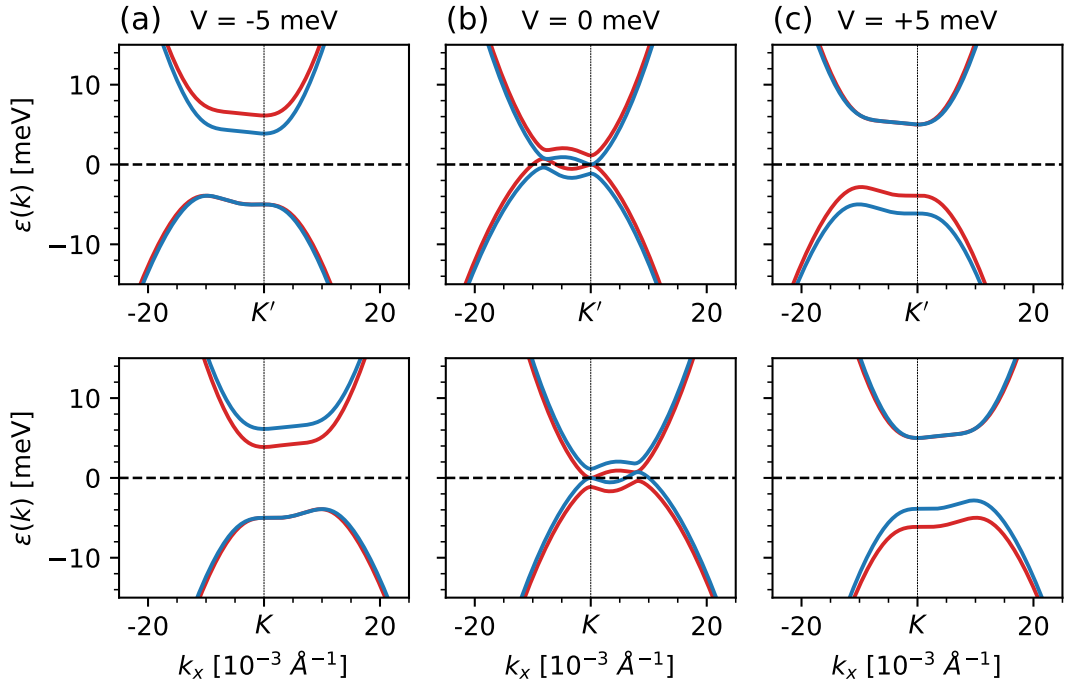

Figure 5.8: Calculated electronic band structure at low energy for the WS_2/BBG/CGT system near the K and K' points with turned off EX coupling. The band structure was obtained with a potential V set to either -5 meV (a), 0 meV (b), and +5meV (c). The color-coded bands show spin polarization, with red representing spin-up electrons and blue representing spin-down electrons.

turned-off SO coupling at finite displacement field V to map the net effect of EX coupling on the electronic structure of this system. Figure 5.9 shows the resulting zone structure as we can see, as with EX coupling disabled in Figure 5.8, EX coupling "flows" from the valence band to the conduction band as the displacement field V increases. The V displacement field sign controls the ferromagnetic splitting: negative values of V will introduce spin splitting of the valence band, while positive values will introduce spin splitting of the conduction band. Thus, by controlling the displacement field V, it is possible to implement an EX spin valve for spin-polarized excess charge carriers.

Summing up, we can state that the ex-so-tic WS_2/BBG/CGT heterostructure has incredible properties at the single-particle level. This heterostructure makes building various spintronic devices, such as spin-field Datta-Das transistors and exchanging spin valves possible. The manifestation of such spin possibilities and possible correlation effects can attract interest from theoretical and experimental studies.

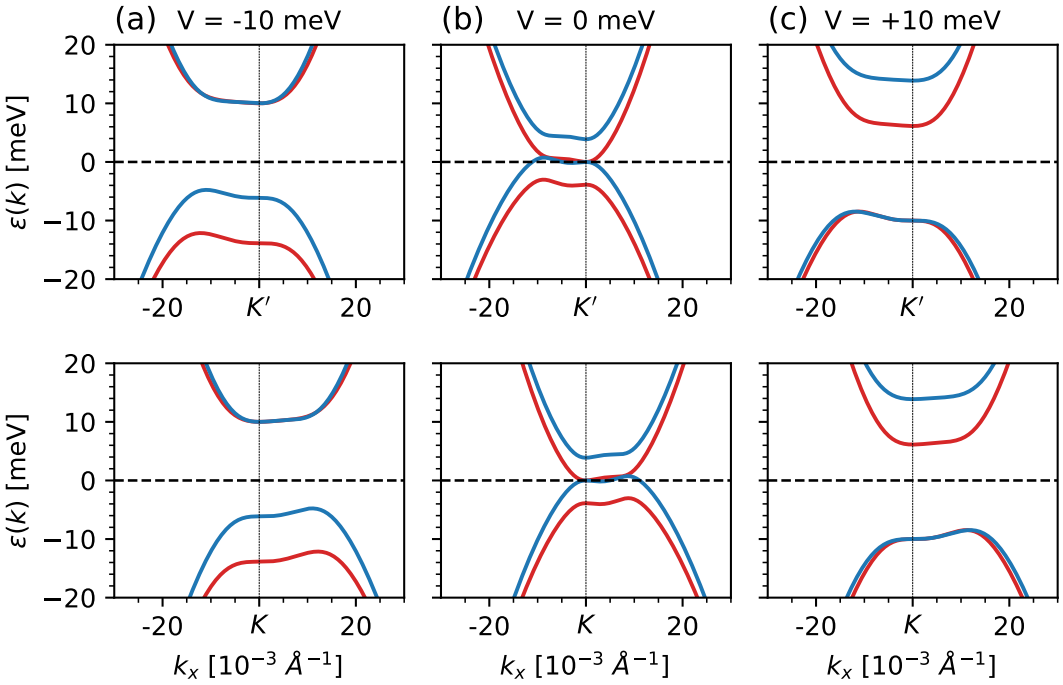

Figure 5.9: Calculated electronic band structure at low energy for the WS_2/BBG/CGT system near the K and K' points with turned off SO coupling. The band structure was obtained with a potential V set to either -10 meV (a), 0 meV (b), and +10 meV (c). The color-coded bands show spin polarization, with red representing spin-up electrons and blue representing spin-down electrons.

5.4. Correlated phenomena in pristine BBG

To describe correlated phenomena in BBG, we used the SU(4)-symmetric interaction Hamiltonian, as in the case of RTG-based systems described in Chapter 4. The full Hamiltonian of the system can be described as:

$$\hat{H} = \hat{H}_{\text{kin}} + \hat{H}_{\text{int}} - \mu\hat{N}, \tag{5.14}$$

where μ is the chemical potential, $\hat{N}$ is the number of electrons operator, the kinetic term $\hat{H}_{\text{kin}}$ and the interaction term $\hat{H}_{\text{int}}$, which in turn have the form

$$\hat{H}_{\text{kin}} = \sum_{\mathbf{k}\tau,si,s'j} \left[\hat{h}(\mathbf{k},\tau)\right]_{si,s'j} \hat{c}^{\dagger}_{s\tau i}(\mathbf{k})\hat{c}_{s'\tau j}(\mathbf{k}), \tag{5.15}$$

$$\hat{H}_{\text{int}} = U_0(n_{\uparrow K}n_{\downarrow K} + n_{\uparrow K'}n_{\downarrow K'}) + U_1 n_K n_{K'}. \tag{5.16}$$

In this equation, the operator $\hat{c}^{(\dagger)}_{s\tau i}(\mathbf{k})/\hat{c}_{s\tau i}(\mathbf{k})$ acts as the creation/annihilation operator for Bloch electrons with a specific spin, denoted as s, which can be either up ($\uparrow$) or

γ_0[eV]	2.432
γ_1[eV]	0.365
γ_3[eV]	-0.273
γ_4[eV]	-0.164
Δ[meV]	8.854
$\lambda_I^{A_2}$[meV]	1.132
$\lambda_I^{B_2}$[meV]	-1.132
$\lambda_X^{A_1}$[meV]	-3.874
$\lambda_X^{B_1}$[meV]	3.874

Table 5.1: The numerical values for the parameters of the single-particle Hamiltonian of WS_2/BBG/CGT heterostructure.

down ($\downarrow$), and are associated with a valley (τ), either K or K', a sublattice (i), and a valley-momentum ($\mathbf{k}$). Our research focuses on a simplified interaction model containing intra- and inter-valley interactions characterized by repulsive couplings. Specifically, U_0 represents intravalley interactions, while U_1 symbolizes intervalley interactions. Both U_0 and U_1 are positive, indicating their repulsive nature. We introduce the spin-valley number operator $n_{s\tau}$, constrained by a momentum cutoff Λ:

$$n_{s\tau} = \sum_{|\mathbf{k}|<\Lambda} \sum_i \hat{c}^\dagger_{s\tau i}(\mathbf{k}) \hat{c}_{s\tau i}(\mathbf{k}), \tag{5.17}$$

which leads to the valley-specific number operator $n_\tau = n_{\uparrow\tau} + n_{\downarrow\tau}$. Based on prior research, we set both U_0 and U_1 to 19 eV and the momentum cutoff Λ to 0.06 Å^{-1}. We assume these interaction parameters to be consistent even when extending our study to more complex systems like ex-so-tic heterostructures based on BBG.

Before starting the study of correlation effects in ex-so-tic heterostructures based on BBG, it is required to clarify these effects in pristine BBG for completeness. For this, as in the case of pristine RTG in Chapter 4, we use RPA, which has proven effective in finding correlated phases.

In pristine BBG, we only found Stoner and IVC instabilities. Since this system has SU(2) symmetry, there is no possibility to induce spin-resolved correlated phases. Therefore, we calculated the critical parameter λ_c^Σ corresponding to the RPA susceptibility divergence criterion for correlated IVC phases and Stoner at a finite doping level of n_e and a displacement field of V as

$$\lambda_c^\Sigma(n_e, u_d) = \frac{1}{\|\Sigma\|^2} \langle \Sigma | \chi^0_{ph}(n_e, u_d) \Gamma^{\mathrm{RPA}}_{ph} | \Sigma \rangle \tag{5.18}$$

for two particular order parameters

$$\hat{\Sigma}_{\mathrm{Stoner}} = \sum_{\bar{a}b} \left[s \otimes \tau_{0/z} \right]_{\bar{a}b} \hat{c}^\dagger_{\bar{a}} \hat{c}_b \tag{5.19}$$

and

$$\hat{\Sigma}_{\mathrm{IVC}} = \sum_{\bar{a}b} \left[s \otimes \tau_{x/y} \right]_{\bar{a}b} \hat{c}^{\dagger}_{\bar{a}} \hat{c}_b \tag{5.20}$$

where s represents any Hermitian operator in spin subspace.

Figure 5.10 presents obtained BBG phase diagram. This diagram categorizes areas where no instabilities appear as the Fermi-liquid. Stoner and IVC instabilities manifest in the chart, occurring in either the hole-doping or electron-doping regions and at different displacement field V amplitude.

As in the case of the pristine RTG described in Chapter 4, for the pristine BBG, due to the vast number of free parameters such as the electron doping level n_e, the displacement field V and the electron interaction parameter $U = U_0 = U_1$, it seems to us impossible to analytically determine the separation boundaries of the IVC and Stoner phases. However, the Stoner phase in the region of hole doping follows the position of the van Hove singularity up to the region of high displacement field V. The particle-hole asymmetry of the pristine BBG phase diagram follows the particle-hole asymmetry of Bloch Hamiltonian (5.7) of pristine BBG. We can also note a significant decrease in the area of correlated phases in the phase diagram of the pristine BBG, in comparison with the phase diagram of the pristine RTG, with similar interaction parameters. This effect is because the band structure of the pristine RTG is much flatter due to the γ_6 hopping connecting the outer layers of the RTG in Eq.(4.1).

5.5. WS_2/BBG/CGT heterostructure phase diagramm

In the subsequent phase of our research, we focused on determining the phase diagram for the complex WS_2/BBG/CGT heterostructure. We aimed to pinpoint all the possible correlated phases within this specific heterostructure. To achieve this, we performed the diagonalization of the susceptibility function χ^0_{ph} multiplied by the Random Phase Approximation (RPA) vertex function $\Gamma^{\mathrm{RPA}}_{ph}$ at zero displacement field $V = 0$, and at the charge-neutrality point $\mu = 0$.

The WS_2/BBG/CGT heterostructure presents unique challenges due to the absence of SU(2) spin symmetry. Additionally, it features both SO and EX coupling. As a result of these complexities, our calculations revealed spin-resolved instabilities inherent to systems with both SO and EX coupling mechanisms.

1. Spin-Valley-Coherent (SVC) IVC Instability Induced SO-Coupling: This type of instability is characterized by a spatial modulation, represented by the wave vector $\mathbf{q} = \frac{2\pi}{3a}(1, \sqrt{3})$. It manifests through a phenomenon known as spin-valley-flip hopping. The representation of the order parameter for this SVC instability is given by:
$$\hat{\Sigma}_{\mathrm{SVC}_{\pm}} = \sum_{\bar{a}b} \left[s_x \tau_x \pm s_y \tau_y \right]_{\bar{a}b} \hat{c}^{\dagger}_{\bar{a}} \hat{c}_b \tag{5.21}$$

2. Spin-Valley-Polarized (SVP) Stoner Instability Induced by SO-Coupling: This instability is localized $\mathbf{q} = 0$. The order parameter for this SVP instability is

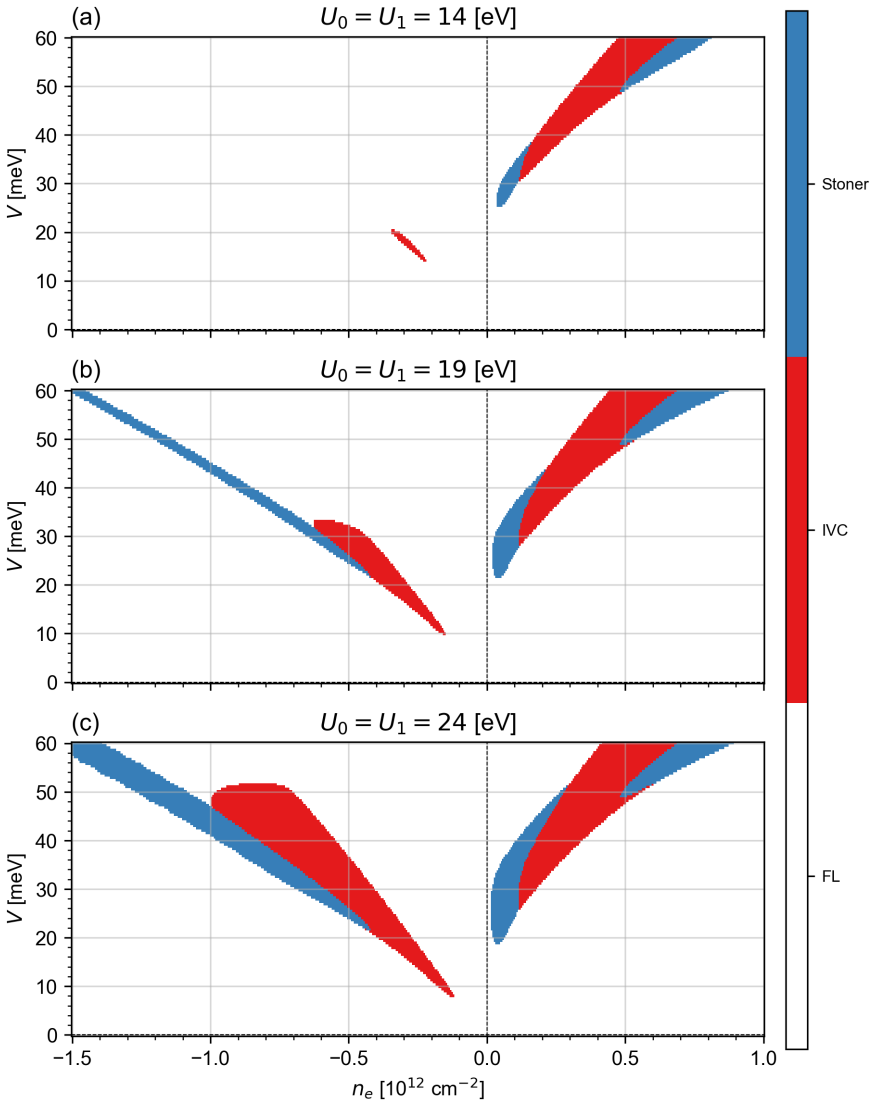

Figure 5.10: Phase diagram of pristine BBG for different electron doping levels n_e and displacement fields V. There are two main phases: intervalley coherent (IVC) and Stoner instability. The white background represents stable Fermi liquid (FL).

defined as:

$$\hat{\Sigma}_{\mathrm{SVP}_\pm} = \sum_{\bar{a}b} [s_z\tau_0 \pm s_0\tau_z]_{\bar{a}b}\, \hat{c}^\dagger_{\bar{a}}\hat{c}_b \tag{5.22}$$

3. Charge-Density-Wave (CDW) IVC Instability Induced by EX-Coupling: This instability is marked by a spatial modulation in charge, with the wave vector $\mathbf{q} = \frac{2\pi}{3a}(1, \sqrt{3})$. The order parameter for the CDW instability is:

$$\hat{\Sigma}_{\mathrm{CDW}_\pm} = \sum_{\bar{a}b} \Big[(s_0 \pm s_z) \otimes \tau_{x/y}\Big]_{\bar{a}b}\, \hat{c}^\dagger_{\bar{a}}\hat{c}_b \tag{5.23}$$

4. Valley-Polarized (VP) Stoner Instability Induced by EX-Coupling: It is another localized instability $\mathbf{q} = 0$. The order parameter for this VP instability is:

$$\hat{\Sigma}_{\mathrm{VP}_\pm} = \sum_{\bar{a}b} [(s_z \pm s_0)\tau_z]_{\bar{a}b}\, \hat{c}^\dagger_{\bar{a}}\hat{c}_b \tag{5.24}$$

All the instabilities described above exhibit correlations that are divided between spin-valley flavor pairs. For instance, the SVP phase is distributed among pairs having different spin-valley quantum numbers $s_z\tau = \pm 1$. On the other hand, the VP phase is solely spread over the valley quantum number τ.

After conducting an in-depth analysis of all possible particle-hole correlated phases in ex-so-tic WS_2/BBG/CGT heterostructure, we have generated a correlated phase diagram, as illustrated in Figure 5.11. This diagram unveils a more intricate set of behaviors compared to the more pristine BBG-only system. In our previous discussions on the band structure of this system, we emphasized the role of the displacement field V and the electron doping level n_e in determining the nature of energy band splitting at the Fermi level. Specifically, when the product of the displacement field and electron doping level (Vn_e) is positive, EX splitting of energy bands occurs at the Fermi level. Conversely, when $Vn_e < 0$, SO splitting takes place. Based on these observations, we have identified four distinct operational regimes in the phase diagram:

1. SO Coupling with Hole Doping: Occurs when $V > 0$ and $n_e < 0$.
2. SO Coupling with Electron Doping: Occurs when $V < 0$ and $n_e > 0$.
3. EX Coupling with Electron Doping: Occurs when $V > 0$ and $n_e > 0$.
4. EX Coupling with Hole Doping: Occurs when $V < 0$ and $n_e < 0$.

Further scrutiny of the phase diagram reveals that when the Fermi level intersects bands with strong proximity to SO coupling, the Stoner phase evolves into two unique $\mathrm{SVP}_\pm$ states. These states display spin-valley polarization along the $\pm z$ axis. In contrast, the IVC phase transitions into spin-valley coherent states, denoted as $\mathrm{SVC}_\pm$. This behavior is primarily influenced by valley-Zeeman SO coupling, as referenced in [68].

Similarly, when the Fermi level intersects bands with strong EX coupling, the Stoner phase transitions into valley-polarized states ($\mathrm{VP}_\pm$), and the IVC phase transitions into

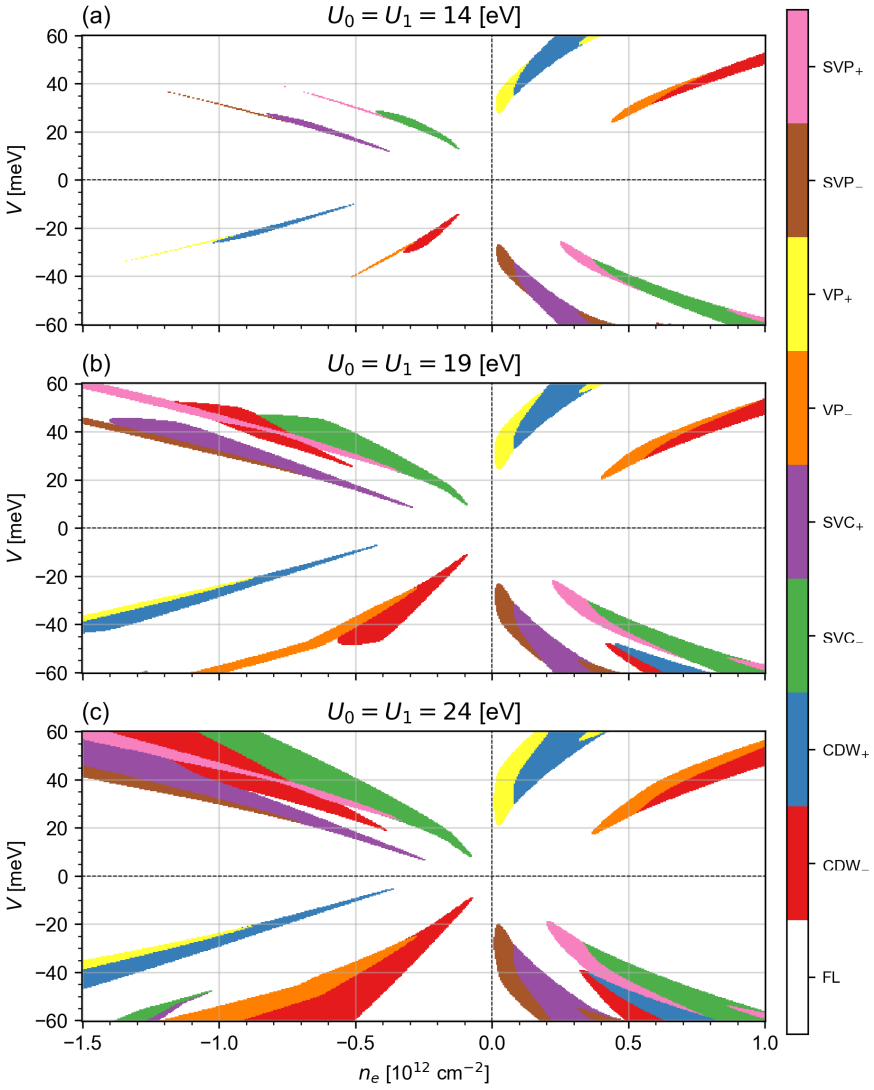

Figure 5.11: Phase diagram of the ex-so-tic WS_2/BBG/CGT heterostructure as a function of the displacement field V and the doping density n_e. The diagram predicts eight different phases, with symmetry breaking: CDW± (charge density wave), SVC± (spin-valley coherence), $VP_\pm$ (valley polarized state), and $SVP_\pm$ (spin-valley polarized state). These phases are color-coded to indicate potential instability in the Fermi liquid state (shown in white).

charge density wave states ($CDW_{\pm}$). A closer look at the van Hove singularities (van Hove singularities) reveals that two $SVC_{\pm}$ phases emerge when influenced by valley-Zeeman SO coupling. These phases involve a combination of both spin and valley matrices—s_x, s_y, τ_x, and τ_y—and can be interpreted as inter-valley spin-flip hopping that conserves the spin-valley quantum number. It results in a correlated SVC phase, facilitated by Coulomb interactions, and reduces kinetic energy.

In contrast, when van Hove singularities are influenced by EX interactions, two spin-polarized $CDW_{\pm}$ phases emerge. Unlike $SVC_{\pm}$, these phases involve only the s_0 and s_z spin matrices but similarly intertwine the valleys via the τ_x matrix. Both $SVC_{\pm}$ and $CDW_{\pm}$ exhibit spatial modulations defined by the wave vector $\mathbf{q} = \frac{2\pi}{3a}(1, \sqrt{3})$. This results in an expansion of the BBG unit cell into a "magnetic" $\sqrt{3} \times \sqrt{3}$-unit cell, thereby reducing the size of the Brillouin zone and causing both valleys to fold into the Γ point. Future discussions will employ the $\mathbf{k}$ vector, measured relative to the center of this reduced Brillouin zone.

5.6. Hartree-Fock correlated band structure

The natural progression of our research involved an in-depth analysis of the band structure in the correlated phases of a unique heterostructure based on BBG. We employed the Hartree-Fock method, which we elaborated on in Chapter 4, to conduct this analysis. Specifically, we focused on four primary correlated phases: SVP_{-} and SVC_{-}, which are influenced by SO proximity-induced coupling, as well as VP_{+} and CDW_{-}, which are affected by EX proximity-induced coupling.

The outcomes of our calculations are visually represented in Figure 5.12, where the band structure is folded to the (Γ) point in the Brillouin zone. Interestingly, our findings align with those related to the RTG heterostructure discussed in the preceding Chapter. While we did not detect a full gap opening indicative of a Mott transition, we did observe the emergence of a correlated gap. This phenomenon is adequately captured at the mean-field level by the order parameters we have previously described.

To quantify these observations, we estimated the amplitude of the correlated gap for each phase. For the SVP_{-} and SVC_{-} phases, the amplitude was calculated to be $\Gamma^{\text{Hund}}_{ph,\text{SVP}_-} = 0.124$ meV and $\Gamma^{\text{Hund}}_{ph,\text{SVC}_-} = 0.121$ meV, respectively. Similarly, for the VP_{+} and CDW_{-} phases, the amplitude was found to be $\Gamma^{\text{Hund}}_{ph,\text{VP}_+} = 0.134$ meV and $\Gamma^{\text{Hund}}_{ph,\text{CDW}_-} = 0.112$ meV, respectively. Notably, these gap values are in close agreement with the amplitude of the proximity-induced couplings. It strongly corroborates the significant impact of proximity-induced couplings on the phase diagram of the WS_2/BBG/CGT heterostructure.

Additionally, we scrutinized changes to the Fermi surface when correlations were introduced. In Figure 5.13, we display the spin-resolved Fermi surfaces folded to the Γ point, both with and without the influence of correlation effects. The observed behavior closely resembles that found in the case of RTG, described in Chapter 4. Specifically, introducing correlations triggers a Lifshitz transition, leading to a variation in the number of Fermi surface pockets. Importantly, it is evident that these correlation effects do not

entirely obliterate the Fermi surface. This observation highlights the differences between the correlated phases found in BBG-based heterostructures and those in a Mott insulator.

5.7. Hund's coupling

In this section, we present preliminary results that indicate the possibility of inducing a superconducting instability by Hund's coupling.

While exploring the correlated phases in multilayer graphene heterostructures, we were intrigued by a particular question. Specifically, we wondered what would happen if we deviated from the conventional SU(4) interaction model, which is highly symmetrical and straightforward. To investigate this, we introduced a relatively uncomplicated additional term to the interaction model, the intervalley Hund's interaction [260, 275]. This interaction can be represented as follows [260, 276, 259]:

$$\hat{H}_{\text{Hund}} = J\left(n_{\uparrow K} - n_{\downarrow K}\right)\left(n_{\uparrow K'} - n_{\downarrow K'}\right), \tag{5.25}$$

In this equation, J signifies the amplitude of Hund's interaction, which, based on general assumptions, should be smaller than SU(4) interaction amplitude $U_0 = U_1$. The sign of J is crucial as it determines the nature of the interaction—either ferromagnetic when negative or antiferromagnetic when positive.

The Hund's interaction necessitates a modification to the existing irreducible RPA vertex, denoted as Γ^{RPA}_{ph}, in the particle-hole channel. Specifically, an extra component, $\Gamma^{\text{Hund}}_{ph}$, must be added to account for the Hund's interaction. This additional component can be expressed as follows:

$$\Gamma^{\text{Hund}}_{ph,0033} = \Gamma^{\text{Hund}}_{ph,0110} = \Gamma^{\text{Hund}}_{ph,1122} = \Gamma^{\text{Hund}}_{ph,2332} = +J, \tag{5.26}$$

$$\Gamma^{\text{Hund}}_{ph,0011} = \Gamma^{\text{Hund}}_{ph,0330} = \Gamma^{\text{Hund}}_{ph,1221} = \Gamma^{\text{Hund}}_{ph,233} = -J. \tag{5.27}$$

It is worth noting that any components of the $\Gamma^{\text{Hund}}_{ph}$ tensor that is not explicitly mentioned can be derived using the relation:

$$\Gamma^{\text{Hund}}_{ph,abcd} = \Gamma^{\text{Hund}}_{ph,dcba}. \tag{5.28}$$

This relation allows for the complete characterization of the $\Gamma^{\text{Hund}}_{ph}$ tensor, thereby providing a comprehensive framework for incorporating Hund's interaction into the particle-hole channel. Thus, Γ^{RPA}_{ph} must include both the component from SU(4) interaction model from Eq. (4.25) and the component from Hund's interaction from Eq. (5.27).

5.7.1. Hund's coupling induces correlated phases

The primary objective of our test was to delve into the different phases that the Hund's interaction might induce. To illustrate this, we refer to figure 5.14, which presents the phase diagrams. These diagrams are mapped as functions of two key parameters: Hund's interaction parameter, denoted as J, and the SU(4) model where $U_0 = U_1$.

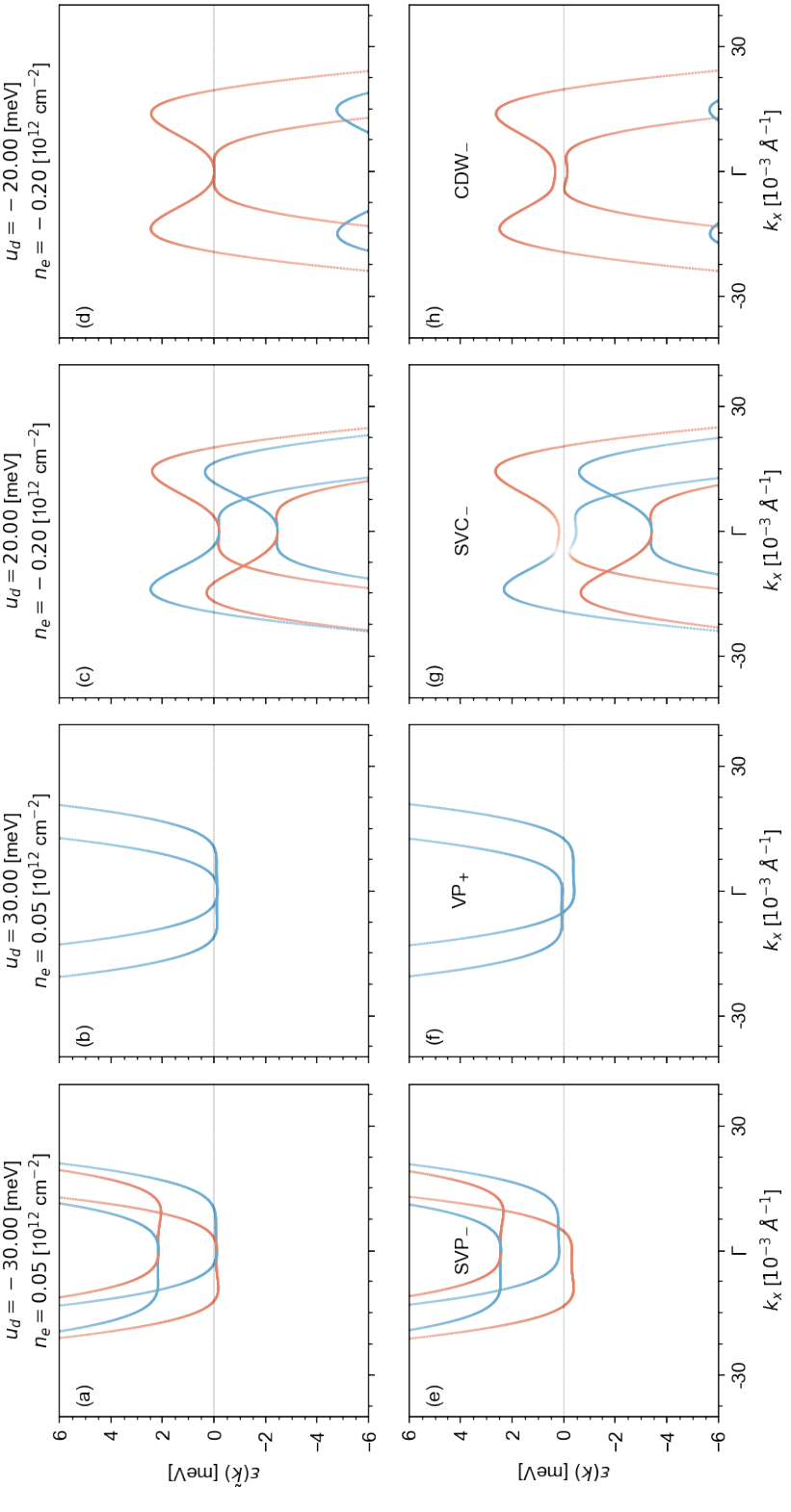

Figure 5.12: Folded to crystallographic Γ point band structure of a WS_2/BBG/CGT heterostructure at the finite displacement field and finite doping levels, with and without interaction corrections. The top row (a-d) shows Hartree-Fock band structures for SVP_+, SVP_-, SVC_-, and SVC_+ instabilities, respectively. The bottom row (e-j) shows band structures without interaction corrections. Spin polarization is indicated in red (spin up) and blue (spin down).

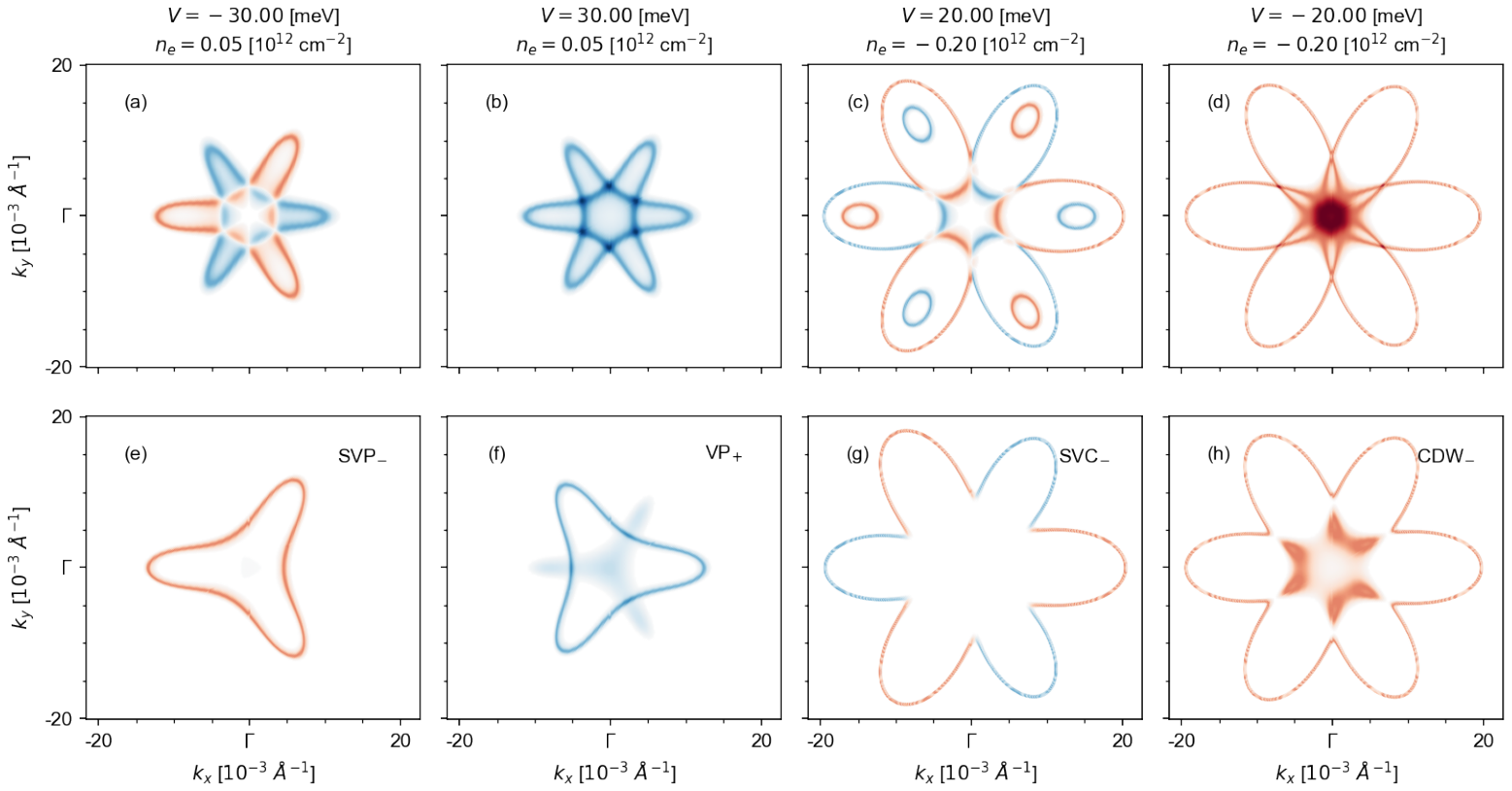

Figure 5.13: Folded to crystallographic Γ point band structure of a WS_2/BBG/CGT heterostructure at the finite displacement field and finite doping levels, with and without interaction corrections. The top row (a-d) shows Hartree-Fock band structures for SVP_+, SVP_-, SVC_-, and SVC_+ instabilities, respectively. The bottom row (e-j) shows band structures without interaction corrections. Spin polarization is indicated in red (spin up) and blue (spin down).

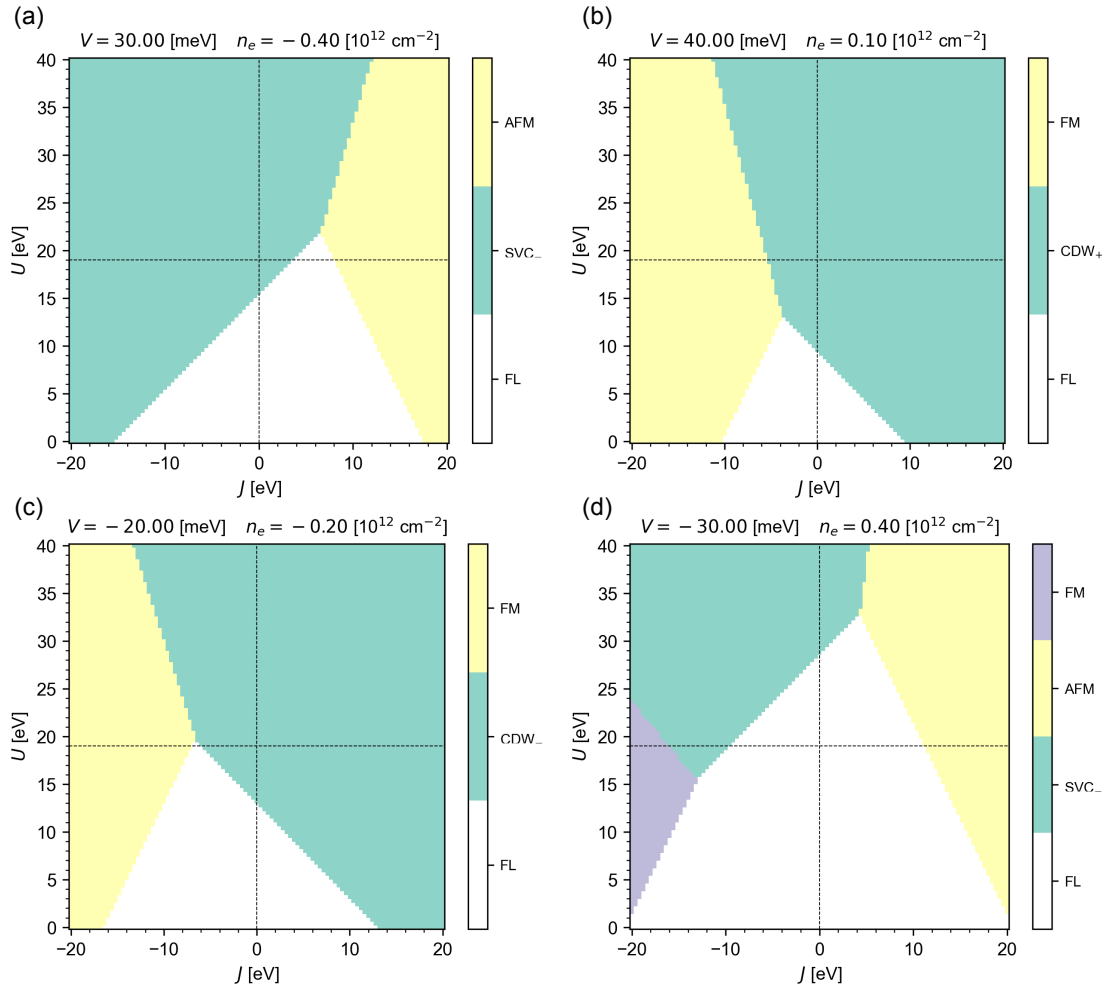

Figure 5.14: Phase diagrams of the ex-so-tic WS_2/BBG/CGT heterostructure as a function of the interaction parameter U of the fully rotation symmetric SU(4) model and the Hund's interaction parameter J for four doping modes and proximity-induced couplings: (a) hole doping with SO coupling, (b) electron doping with EX coupling, (c) hole doping with EX coupling and (d) electron doping with SO coupling.

For clarity, we have examined these interactions under four sets of displacement field and doping parameters. Each of these sets corresponds to a specific mode: SO-coupled hole filling at panel (a), EX-coupled electron filing at panel (b), EX-coupled hole filing at panel (c), and SO-coupled electron filing at panel (d). Each mode provides a unique perspective on the interaction and its implications, offering a comprehensive view of the phenomenon under study.

From our observations, the outcomes align with our expectations. When we look at the Hund's interaction parameter, its negative values indicate ferromagnetic ordering. It leads to a full spin-polarized (SP), ferromagnetic-like ordering. The representation of this order parameter is given by:

$$\hat{\Sigma}_{\mathrm{SP}} = \sum_{\bar{a}b} \left[\tau_0 s_{x/y/z}\right]_{\bar{a}b} \hat{c}^{\dagger}_{\bar{a}} \hat{c}_b, \tag{5.29}$$

On the other hand, when the Hund's interaction parameter, denoted as J, takes on positive values, it signifies antiferromagnetic ordering. This results in a full spin-valley-polarized (SVP) ordering. The expression for this order parameter is:

$$\hat{\Sigma}_{\mathrm{SVP}} = \sum_{\bar{a}b} \left[\tau_z s_{x/y/z}\right]_{\bar{a}b} \hat{c}^{\dagger}_{\bar{a}} \hat{c}_b. \tag{5.30}$$

Selecting a specific value for the Hund's interaction parameter J poses challenges. The theoretical models available for aligning with experimental data come with a plethora of free parameters. Making a definitive choice becomes intricate. Additionally, we find it computationally intensive when considering a first-principles evaluation using the cRPA method [277]. As a result, determining the entire phase diagram becomes a daunting task. Due to these complexities, we have sidesteped the discussion on how the Hund's interaction influences the outcomes.

5.7.2. Hund's coupling induces superconductivity

We faced fascinating predictions in exploring the effects of Hund's interaction on correlation within a unique heterostructure based on BBG. Specifically, we found that the Hund's interaction could induce a superconducting state. To validate and understand this phenomenon, we embarked on a journey to map out the phase diagram that would confirm the presence of a superconducting state. Our methodology was comprehensive; we employed the RPA and a combination of the parquet and linearized Eliashberg equation described in Chapters 3 and 4.

Breaking down our approach, the initial step was to craft an irreducible vertex in the particle-particle channel. It was achieved using the parquet equation. We further determined the fully reducible vertex in the particle-hole channel, leveraging the Random Phase Approximation. The resulting irreducible particle-particle vertex can be represented as:

$$\Gamma_{pp,a\bar{b}c\bar{d}} = \Lambda_{a\bar{b}c\bar{d}} + \Phi_{ph,a\bar{b}c\bar{d}} - \Phi_{ph,a\bar{d}c\bar{b}}, \tag{5.31}$$

The symbol Λ denotes the fully irreducible vertex in the given equation, and Φ_{ph} is the fully reducible vertex when considering the particle-hole channel. It can be elaborated upon and expressed in the following manner:

$$\Phi_{ph,a\bar{b}c\bar{d}} = \sum_{\bar{f}e\bar{g}h} \Gamma^{\mathrm{RPA}}_{ph,a\bar{b}e\bar{f}} \chi^{\mathrm{RPA}}_{ph,\bar{f}e\bar{g}h} \Gamma^{\mathrm{RPA}}_{ph,h\bar{g}c\bar{d}} \tag{5.32}$$

It is crucial to note that in the context of RPA, $\Gamma^{\mathrm{RPA}}_{ph}$ is equivalent to Λ.

In the preceding sections, there has been a discussion on the methodology to compute χ^0_{ph}. Computation is based on the generalized Lindhards' susceptibility formula, which can be referenced from Eq.(4.14):

$$\chi^0_{ph,\bar{a}b\bar{c}d}(\omega,\mathbf{q}) = \frac{1}{N_\mathbf{k}}\sum_{\mathbf{k}}\sum_{ij} u^*_{n\bar{a}}(\mathbf{k})u_{mb}(\mathbf{k}+\mathbf{q})u^*_{m\bar{c}}(\mathbf{k}+\mathbf{q})u_{nd}(\mathbf{k})\frac{f(\varepsilon_n(\mathbf{k})) - f(\varepsilon_m(\mathbf{k}+\mathbf{q}))}{i\omega + \varepsilon_m(\mathbf{k}+\mathbf{q}) - \varepsilon_n(\mathbf{k})} \tag{5.33}$$

In our research, we strategically chose to simplify our calculations and the subsequent interpretation of our results. Specifically, we assumed that Γ_{pp} is entirely local, represented as $\mathbf{q} = 0$, and wholly static, denoted as $\omega = 0$. As a result of this approximation, we constructed Γ_{pp} using $\chi^0_{ph}(\omega = 0, \mathbf{q} = 0)$.

We employed the linear algebra of two-particle Green's functions within a particle-hole channel to delve deeper into the methodology. Hence, using two-particle linear algebra, detailed in Appendix B, we were able to compute the dressed RPA susceptibility, χ^{RPA}_{ph}, using the following equation:

$$\chi^{\mathrm{RPA}}_{ph,\bar{a}b\bar{c}d} = \sum_{f\bar{e}h\bar{g}} \left[1 - \chi^0_{ph,\bar{a}b\bar{e}f}\Gamma^{\mathrm{RPA}}_{ph,f\bar{e}h\bar{g}}\right]^{-1} \chi^0_{ph,\bar{g}h\bar{c}d} \tag{5.34}$$

Having derived the χ^{RPA}_{ph}, we then proceeded to construct Γ_{pp} using the parquet equation, as referenced in equation (5.31). However, a crucial point to note is the role of λ_c from the equations:

$$\lambda_c\Sigma_{\bar{a}b} = \sum_{\bar{e}f\bar{g}h} \chi^0_{ph,\bar{a}b\bar{e}f}\Gamma^{\mathrm{RPA}}_{ph,f\bar{e}h\bar{g}}\Sigma_{\bar{g}h}, \tag{5.35}$$

When the value of λ_c surpasses unity, constructing Γ_{pp} becomes unfeasible due to the divergence observed in χ^{RPA}_{ph}. It implies that the RPA method becomes unsuitable for calculating the Cooper instability via the linearized Eliashberg equation whenever we detect correlated particle-hole instabilities in the phase diagram. Consequently, within this theoretical framework's confines, it is impossible to witness the simultaneous presence of correlated phases in particle-hole and particle-particle channels.

Now, we must determine the last missing ingredient for the linearized Eliashberg equation - bare susceptibility in particle-particle channel χ^0_{pp}. As in the case of bare susceptibility in particle-hole channel χ^0_{ph}, we used the transformed generalized Lindhards' susceptibility formula, but for the particle-particle channel:

$$\begin{aligned}\chi^0_{pp,\bar{a}b\bar{c}d}(\omega,\mathbf{q}) &= -\frac{1}{N_\mathbf{k}\beta}\sum_{\nu\mathbf{k}} G_{d\bar{a}}(\nu,\mathbf{k})G_{b\bar{c}}(\omega-\nu,\mathbf{q}-\mathbf{k}) \\ &= -\frac{1}{N_\mathbf{k}\beta}\sum_{\nu\mathbf{k}} \underbrace{\left(\sum_i \frac{u_{nd}(\mathbf{k})u^*_{n\bar{a}}(\mathbf{k})}{i\nu-\varepsilon_n(\mathbf{k})}\right)}_{G_{d\bar{a}}(\nu,\mathbf{k})} \underbrace{\left(\sum_j \frac{u_{mb}(\mathbf{q}-\mathbf{k})u^*_{m\bar{c}}(\mathbf{q}-\mathbf{k})}{i\omega-i\nu-\varepsilon_m(\mathbf{q}-\mathbf{k})}\right)}_{G_{b\bar{c}}(\omega-\nu,\mathbf{q}-\mathbf{k})} \\ &= -\frac{1}{N_\mathbf{k}}\sum_{\mathbf{k}}\sum_{ij} u^*_{n\bar{a}}(\mathbf{k})u_{mb}(\mathbf{q}-\mathbf{k})u^*_{m\bar{c}}(\mathbf{q}-\mathbf{k})u_{nd}(\mathbf{k}) \\ &\qquad \frac{1-f(\varepsilon_n(\mathbf{k}))-f(\varepsilon_m(\mathbf{q}-\mathbf{k}))}{i\omega-\varepsilon_m(\mathbf{q}-\mathbf{k})-\varepsilon_n(\mathbf{k})}\end{aligned} \tag{5.36}$$

In static $\omega = 0$ and local $\mathbf{q} = 0$ limit, Eq.(5.36) can be rewritten as:

$$\begin{aligned}\chi^0_{pp,\bar{a}b\bar{c}d}(\omega,\mathbf{q}) = \frac{1}{N_\mathbf{k}}\sum_{\mathbf{k}}\sum_{ij} u^*_{n\bar{a}}(\mathbf{k})u_{mb}(\mathbf{q}-\mathbf{k})u^*_{m\bar{c}}(\mathbf{q}-\mathbf{k})u_{nd}(\mathbf{k}) \\ \frac{1-f(\varepsilon_n(\mathbf{k}))-f(\varepsilon_m(-\mathbf{k}))}{\varepsilon_m(-\mathbf{k})+\varepsilon_n(\mathbf{k})}\end{aligned} \tag{5.37}$$

In our analysis, we deliberately chose to exclude the dependence of the generalized susceptibility on the sublattice subindex. This decision stems from the fact that the interaction Hamiltonian of the SU(4) model, as Hund's coupling, does not factor in the sublattice degrees of freedom. As a direct consequence of this omission, it becomes feasible for us to eliminate the sublattice degrees of freedom from the generalized susceptibility, as denoted by equation (4.18). It can be expressed as:

$$\tilde{\chi}^0_{pp,\bar{a}b\bar{c}d} = \sum_{ij}\chi^0_{pp,(\bar{a}i)(bj)(\bar{c}i)(dj)} \tag{5.38}$$

In this equation, the indices $\bar{a}, b, \bar{c}$, and d are symbolic representations that exclusively encode the spin s and the valley τ quantum number combination. On the other hand, the indices i and j are representative of the sublattice indices. As a result, the term $\tilde{\chi}^0_{pp}$ encapsulates information solely on the spin-valley degrees of freedom. For the sake of simplicity and clarity in subsequent discussions, we will adopt the notation χ^0_{pp} to refer to $\tilde{\chi}^0_{pp}$.

To address the problem, we have meticulously gathered all the components required to solve the linearized Eliashberg equation. This equation can be represented as:

$$\lambda_c\Delta_{\bar{a}\bar{b}} = \sum_{ef\bar{g}\bar{h}}\chi^0_{pp,\bar{a}e\bar{b}f}\Gamma_{pp,e\bar{h}f\bar{g}}\Delta_{\bar{g}\bar{h}}, \tag{5.39}$$

where

$$\hat{\Delta} = \sum_{\bar{a}\bar{b}}\Delta_{\bar{a}\bar{b}}\hat{c}^\dagger_{\bar{a}}\hat{c}^\dagger_{\bar{b}} \tag{5.40}$$

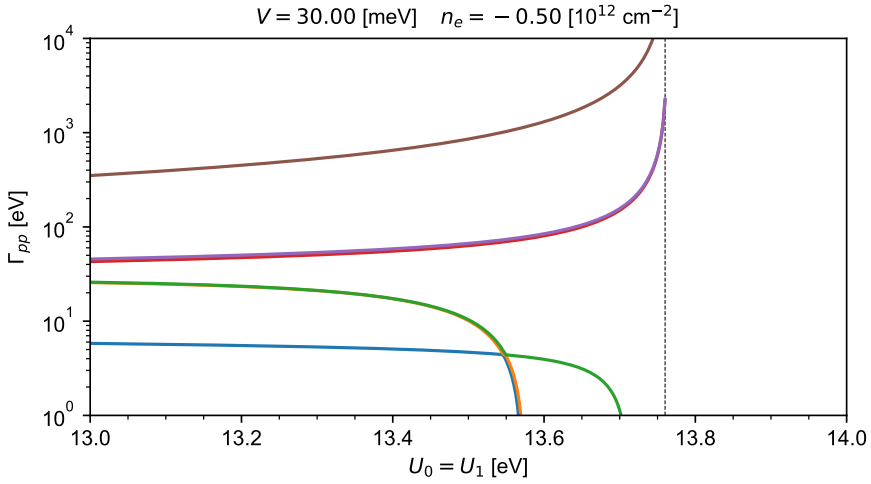

Figure 5.15: Dependence of the channels amplitude of the diagonalized irreducible vertex Γ_{pp} in the particle-particle channel obtained using RPA on the interaction parameter SU(4) model $U_0 = U_1$. The vertical dashed line indicates the critical value of the interaction parameter SU(4) model, corresponding to the divergence χ_{ph}^{RPA}.

The term, denoted by $\hat{\Delta}$, is crucial as it corresponds to the superconducting order parameter associated with Cooper instability.

To initiate our study, we examined the pristine BBG's phase diagram and the unique heterostructure WS_2/BBG/CGT. Our assumptions were based solely on SU(4) type interactions within these systems. Despite our thorough study, we could not identify any specific point in the phase diagram of either the unaltered or the unique BBG-based systems that indicates the presence of a superconducting state. This particular observation can be attributed to the pronounced symmetry of the Hamiltonian interaction. Such a high degree of symmetry means that the degree at which a specific interaction channel, denoted as Γ_{pp}, diminishes to zero, leading to superconducting ordering, is almost identical to the degree at which the same channel intensifies or diverges to infinity. This intensification mirrors the closeness of the divergence χ_{ph}^{RPA}, which subsequently results in the emergence of a particle-hole instability.

It is noteworthy to mention that the regions where the superconducting state remains stable for SU(4) type interactions are incredibly minute within the parametric space defined by the interaction parameter SU(4) $U_0 = U_1$, the displacement field V, and the doping level n_e. Such regions pose a challenge for detection when using numerical calculations. To elucidate further, the figure 5.15 we reference displays the Γ_{pp} channels, which are derived from the diagonalization of Γ_{pp}, in line with the linear algebra detailed in appendix B. There is a critical value for the SU(4) interaction parameter $U_0 = U_1 = 13.76$ eV, at which the divergence χ_{ph}^{RPA} is observed. However, when $U_0 = U_1 = 13.57$ eV, one of the Γ_{pp} channels undergoes softening due to the Kohn-Luttinger mechanism [278, 279, 259, 280, 281], turning it attractive (indicating a negative value).

The stability space that results from the superconducting state is approximately 0.2 eV within the interaction parameter SU(4) parametric space. This further underscores the elusive characteristics of superconductivity when considering the SU(4) interaction model.

In the figure labeled Figure 5.15, it is necessary to distinguish between the different interpretations of the "divergence rates" associated with both Stoner and IVC channels Γ_{pp}. In particular, the term "divergence level" refers to the tendency of specific channels to either lead to infinity or fall into the negative realms. The sign ascribed to these "divergence levels" is not merely coincidental; proximity to the emerging particle-hole instability profoundly affects it. As the system approaches the emerging particle-hole instability for the IVC channel, the "divergence rates" for Γ_{pp} will take on positive values tending to infinity. Conversely, the "divergence rates" for Γ_{pp} associated with the Stoner channel will take a negative sign, which means a descent into negative values.

The title of this section underscores a significant observation: the role of Hund's coupling in the induction of superconductivity. Through our study, we discerned that incorporating Hund's coupling leads to a marked enhancement in the parametric stability of superconducting states. Figure 5.16 showcases two distinct phase diagrams to offer a more straightforward visual representation. These are plotted concerning the SU(4) interaction parameter and the Hund's coupling, represented as J. Specifically, panels (a) and (b) illustrate two scenarios: the first encompasses hole doping in conjunction with SO coupling, while the second pertains to EX coupling. It should be noted that with electron doping, sufficient superconductivity is difficult to 'catch' numerically, even in the presence of the Hund's interaction.

Beyond the previously discussed particle-hole instabilities, our study also revealed a spectrum of particle-particle instabilities, categorized as follows:

1. Singlet Cooper Instability: This form of instability is characterized by its zero final quantum spin and valley numbers. The corresponding order parameter is:

$$\hat{\Delta}_{\text{Singlet}_\pm} = \sum_{\bar{a}\bar{b}} i \left[s_y \tau_x \pm s_x \tau_y \right]_{\bar{a}\bar{b}} \hat{c}^\dagger_{\bar{a}} \hat{c}^\dagger_{\bar{b}} \tag{5.41}$$

2. Triplet Cooper Instability: Distinguished by a non-zero spin quantum number and a zero valley number, its order parameter is:

$$\hat{\Delta}_{\text{Triplet}_\pm} = \sum_{\bar{a}\bar{b}} i\tau_y \left[s_0 \pm s_z \right]_{\bar{a}\bar{b}} \hat{c}^\dagger_{\bar{a}} \hat{c}^\dagger_{\bar{b}} \tag{5.42}$$

3. ex-so-tic Type Cooper Instability - Singlet Pair-Density-Wave (PDW) [282]: Unique for its zero spin quantum number and a non-zero valley number, its order parameter is:

$$\hat{\Delta}_{\text{PDW}_\pm} = \sum_{\bar{a}\bar{b}} i s_y \left[\tau_0 \pm \tau_z \right]_{\bar{a}\bar{b}} \hat{c}^\dagger_{\bar{a}} \hat{c}^\dagger_{\bar{b}} \tag{5.43}$$

   A Pair-Density-Wave (PDW) is a theoretical superconductivity state distinct from the conventional superconducting state. In a conventional superconductor, electron

pairs condense into a state with a uniform phase, leading to zero electrical resistance. In contrast, the superconducting order parameter oscillates in a PDW state in space, leading to a modulated pairing amplitude. In our case, modulation wavevector is equal to intervalley momentum $\mathbf{q} = \frac{2\pi}{3a}(1, \sqrt{3})$. This state has been proposed to exist in certain high-temperature superconductors and is believed to coexist or compete with other electronic orders, such as charge or spin density waves.

It is crucial to note that the existence of the **Triplet Pair-Density-Wave** is deemed unfeasible. This assertion stems from the fact that the order parameters for this Cooper instability type are:

$$\hat{\Delta} = \sum_{\bar{a}\bar{b}} [s_z\tau_0 \pm s_0\tau_z]_{\bar{a}\bar{b}}\, \hat{c}^\dagger_{\bar{a}} \hat{c}^\dagger_{\bar{b}} = 0 \tag{5.44}$$

It culminates in a value of zero, affirming its non-existence.

From the phase diagram depicted in figure 5.16, we can observe a distinct pattern related to superconducting ordering. Specifically, when we focus on Hund's antiferromagnetic interaction regime, a Singlet type of superconducting ordering emerges. This particular ordering is closely situated near the SVP ordering. Intriguingly, this pattern mirrors the behavior seen in the phase diagrams of high-temperature superconductors. In such superconductors, the singlet superconducting $d-wave$ ordering is found to be neighboring the antiferromagnetic ordering.

On the other hand, when we shift our attention to the region characterized by the ferromagnetic Hund's interaction, a different type of superconducting ordering is evident. Here, we notice the presence of triplet superconducting ordering, which is closely associated with SP ordering. This observation is not unique to this system. When we examine systems of heavy fermions, we find a similar trend. In the phase diagrams of these systems, triplet superconducting ordering is found to be adjacent to ferromagnetism. This consistency across different systems underscores the intricate relationship between superconducting orderings and their neighboring interactions.

To validate the above reasoning, we constructed phase diagrams for pristine BBG. In this endeavor, we set the interaction parameters at $U_0 = U_1 = 16$ eV and explored the effects of $J = \pm 4$ eV. These diagrams were plotted against the displacement field V and the electron doping level n_e. The resulting diagrams can be viewed in figure 5.19.

The results show that the nature of the Hund's interaction plays a pivotal role in determining the types of orderings. Specifically:

1. For the antiferromagnetic Hund's interaction, represented by J and showcased in panel (a):
   - The Stoner phase transitions into the SVP phase.
   - The IVC phase evolves into the CDW phase.
   - This interaction also induces a "coat" effect, corresponding to singlet superconducting ordering.
2. On the other hand, for the ferromagnetic Hund's interaction, depicted in panel (b):

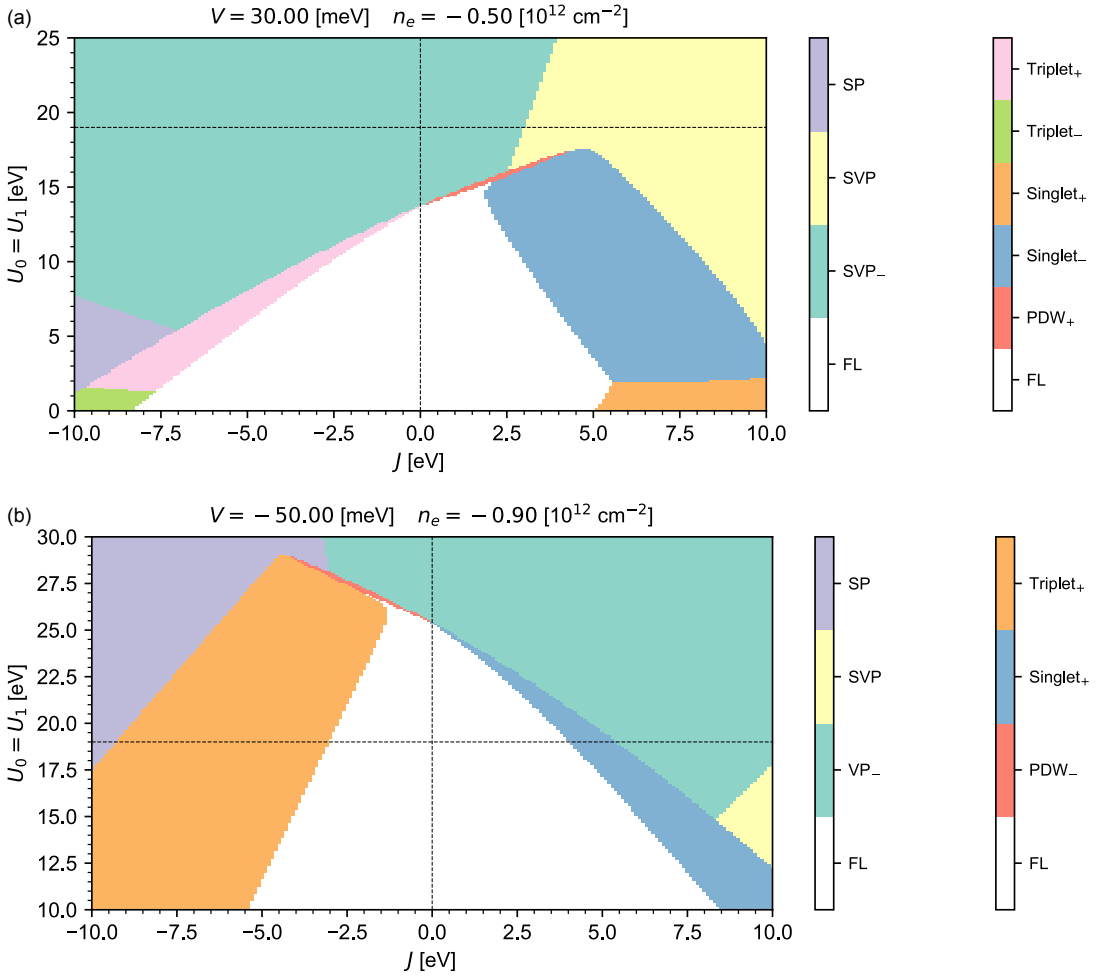

Figure 5.16: Comparative Phase Diagrams for Two Distinct Regimes of WS_2/BBG/CGT system as a function of SU(4) interaction parameter $U_0 = U_1$ and Hund's interaction parameter J: (a) Incorporating hole doping in conjunction with SO coupling, and (b) hole doping paired with EX coupling. Each diagram distinctly forecasts the emergence of various phases. These are further categorized into two channels: the particle-particle interactions (represented by the left color bars) and the particle-hole interactions (depicted by the right color bars). The color gradations within these diagrams serve as indicators, with each hue signifying a specific phase. Notably, the white regions within the diagrams highlight areas with no potential instability within the Fermi liquid state.

- The Stoner phase transforms into the SP phase.
- The IVC phase shifts to the SVC phase.
- This interaction results in a "coat" over particle-hole instability, indicative of triplet superconducting ordering.

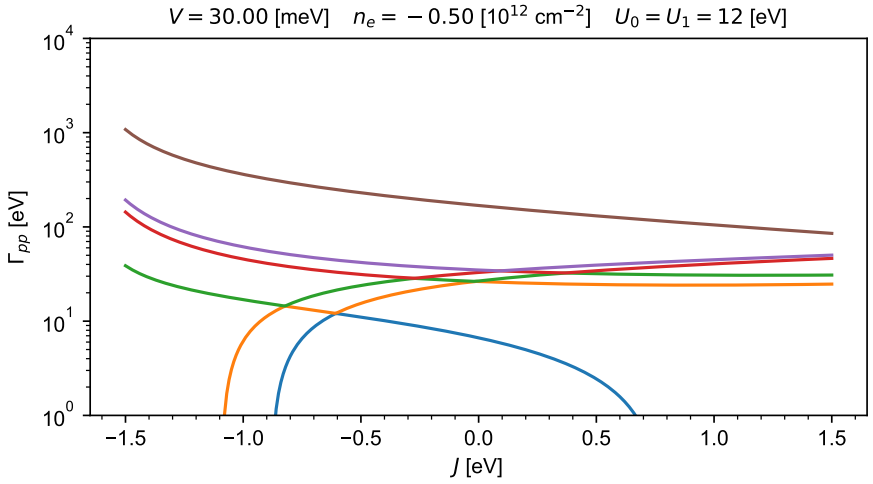

Figure 5.17: Dependence of the channels amplitude of the diagonalized irreducible vertex Γ_{pp} in the particle-particle channel obtained using RPA on the Hund's interaction parameter J.

It is worth noting that there is no evidence of superconducting ordering in the absence of the Hund's interaction.

We also have undertaken a comprehensive calculation of the phase diagram for the WS_2/BBG/CGT heterostructure, mainly focusing on the influence of Hund's coupling. Our analysis is grounded on what we believe to be realistic SU(4) interaction parameters, specifically with $U_0 = U_1 = 16$ eV. The results of this analysis, which incorporate Hund's coupling values of $J = \pm 4$, are illustrated in figure 5.19.

Upon examining the figure, several observations can be made:

1. Panel (a) showcases the antiferromagnetic nature of Hund's coupling with a value of $J = +4$ eV. It is predominantly associated with singlet superconducting ordering. Notably, these orderings are primarily observed in regions corresponding to SO-coupled filings.

2. Conversely, panel (b) highlights the ferromagnetic nature of Hund's coupling, represented by a value of $J = -4$ eV. In this scenario, the dominant feature is the triplet superconducting ordering. These orderings are predominantly found in regions that align with EX-coupled filings.

3. An additional point of interest is the PDW phase. It is worth noting that identifying this phase is particularly challenging when considering the parametric space displacement field, denoted as V, and the electron level of doping, represented by n_e.

In essence, our analysis underscores the pivotal role of Hund's coupling in influencing the superconducting orderings within the WS_2/BBG/CGT heterostructure.

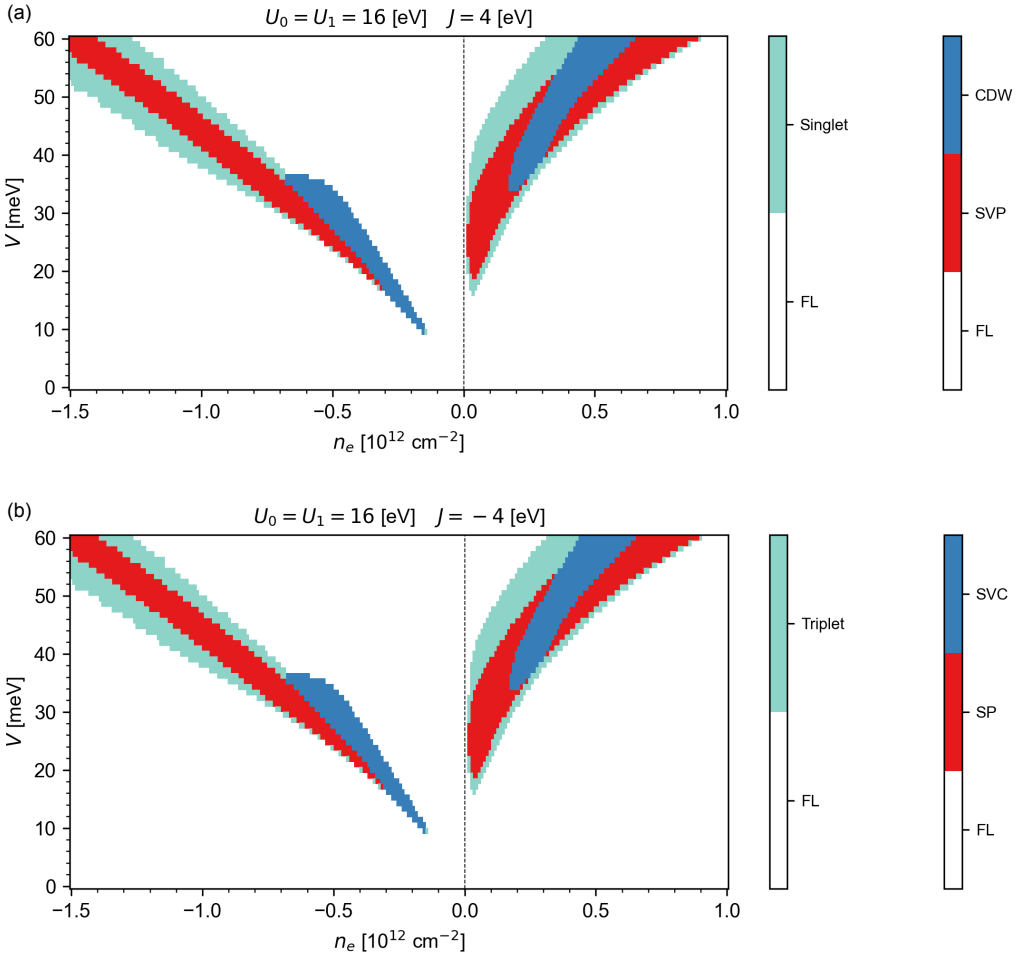

Figure 5.18: Phase Diagrams for Two Distinct Interaction Regimes: $U_0 = U_1 = 16$ eV and $J = 4$ eV at the panel (a) and $J = -4$ eV of pristine BBG system as function displacement field V and electron level of doping n_e. Each diagram distinctly forecasts the emergence of various phases. These are further categorized into two channels: the particle-particle interactions (represented by the left color bars) and the particle-hole interactions (depicted by the right color bars). The color gradations within these diagrams serve as indicators, with each hue signifying a specific phase. Notably, the white regions within the diagrams highlight areas with no potential instability within the Fermi liquid state.

However, the main question remains open: Why does the Hund's interaction stabilize superconductivity? The answer is quite evident from the analysis of superconductivity for the SU(4) interaction model. The Hund's interaction introduces a significant imbalance between Stoner and IVC channels of the fully irreducible vertex in particle-particle channel Γ_{pp}, thereby essentially separating in the parametric space the points of divergence, both

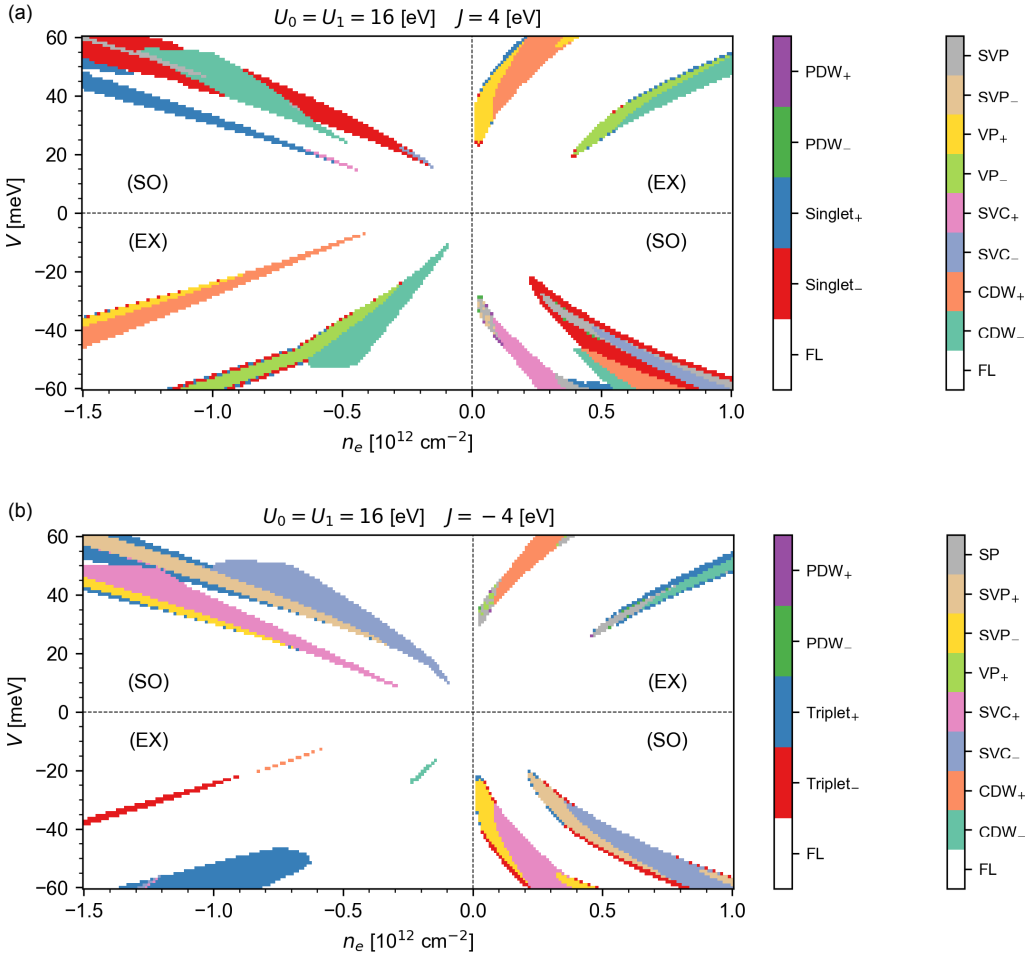

Figure 5.19: Phase Diagrams for Two Distinct Interaction Regimes: $U_0 = U_1 = 16$ eV and $J = 4$ eV at the panel (a) and $J = -4$ eV of WS_2/BBG/CGT system as function displacement field V and electron level of doping n_e. Each diagram distinctly forecasts the emergence of various phases. These are further categorized into two channels: the particle-particle interactions (represented by the left color bars) and the particle-hole interactions (depicted by the right color bars). The color gradations within these diagrams serve as indicators, with each hue signifying a specific phase. Notably, the white regions within the diagrams highlight areas with no potential instability within the Fermi liquid state.

to infinity and to negative values, of different channels Γ_{pp}, as shown in the figure 5.17. The softening of Γ_{pp} channels corresponding to superconducting ordering occurs much faster and far from the χ_{ph}^{RPA} divergences.

Such logic suggests what will happen if, even in the absence of the Hund's interaction, we introduce asymmetry into the SU(4) interaction model through the nonequivalence of the

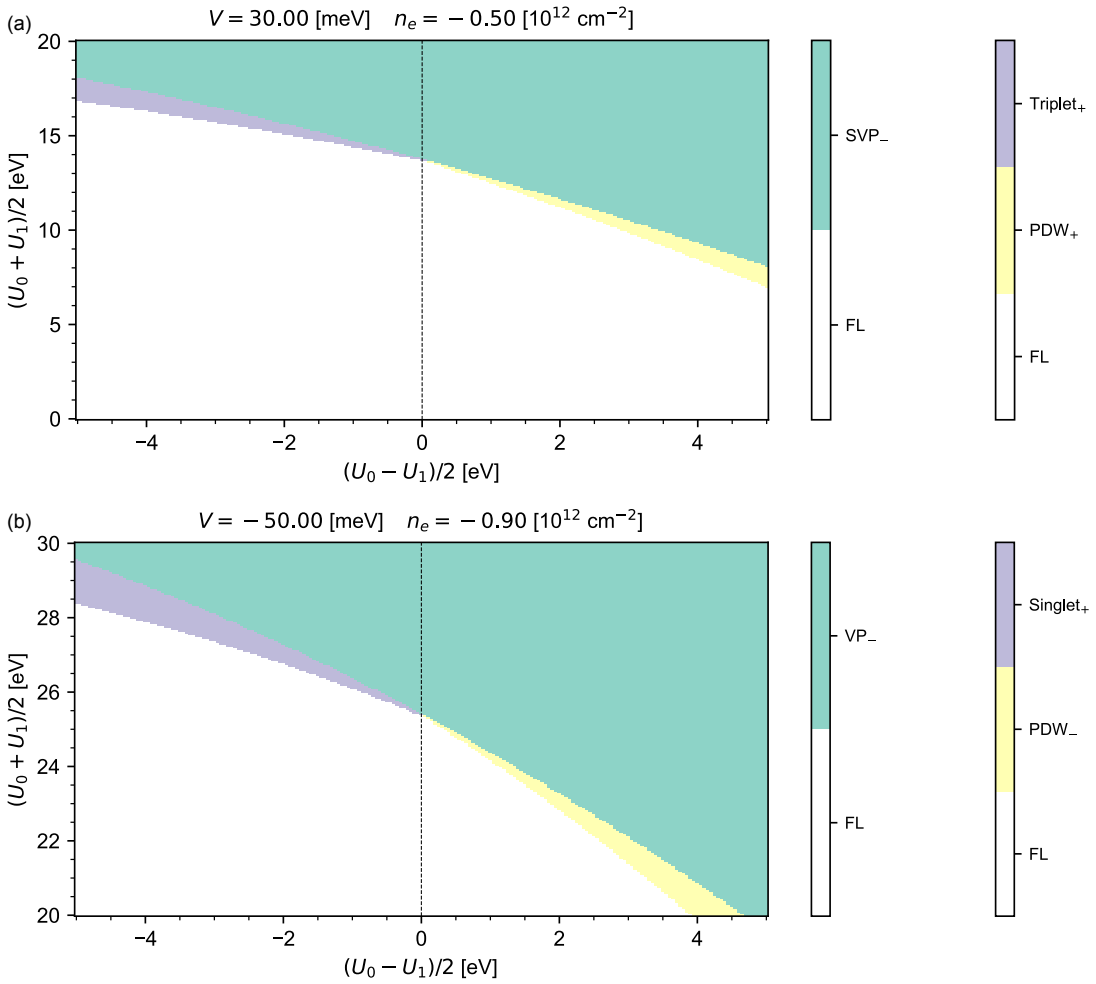

Figure 5.20: Comparative Phase Diagrams for Two Distinct Regimes as a function of SU(4) interaction parameter $(U_0 + U_1)/2$ and SU(4) interaction parameter imbalance $(U_0 - U_1)/2$: (a) Incorporating hole doping in conjunction with SO coupling, and (b) hole doping paired with EX coupling. Each diagram distinctly forecasts the emergence of various phases. These are further categorized into two channels: the particle-particle interactions (represented by the left color bars) and the particle-hole interactions (depicted by the right color bars). The color gradations within these diagrams serve as indicators, with each hue signifying a specific phase. Notably, the white regions within the diagrams highlight areas with no potential instability within the Fermi liquid state.

intervalley and intravalley interaction $U_0 \neq U_1$, we should also obtain superconductivity. To do this, we constructed a phase diagram, again for two modes: hole doping in conjunction with SO coupling and EX coupling, as a function of $(U_0 + U_1)/2$ and $(U_0 - U_1)/2$, represented by the Figure 5.20. As can be seen from the results, we indeed observe superconductivity, but now in a narrower parametric space.

Amazingly, we observe singlet superconducting ordering in the case of EX-coupled hole filling. In contrast, in the case of SO-coupled filling, we observe triplet superconducting ordering, which is consistent with experimental data [266]. The imbalance induces a superconducting state when the intravalley interaction U_0 is less than the intervalley interaction U_1. This behavior has already been observed in theoretical work [283, 259, 260]. However, a significant imbalance towards the intravalley interaction U_1 induces Pair-Density-Wave ordering, Cooper instability with a finite momentum equal to the intervalley momentum.

The relationship between intravalley and intervalley interactions presents a distinct contrast to Hund's interaction, as it does not lead to a broad parametric region where the superconducting state remains stable. When we evaluate the complete phase diagram, taking into account the displacement field V and the electron level of doping n_e, it becomes evident that there are no significant stable regions of any superconducting order parameters. Based on our detailed calculations, we can confidently assert that Hund's interaction is the primary driving force behind the emergence of superconductivity in BBG-based systems.

5.8. Conclusions

We delve into the intricate behavior of ex-so-tic heterostructures, specifically those based on BBG, using RPA and Hartree-Fock methods. Our predictions indicate a fascinating phenomenon: the correlated states of these heterostructures can transition between SO and EX-driven phases. It suggests that a singular device constructed with these heterostructures can manifest a comprehensive range of correlated phases. This spectrum spans from the uniform Stoner valley-polarized phase to more complex states, such as the spatially modulated spin-polarized Charge Density Wave and the intriguing spin-flip-valley-flip spin-valley coherences.

While our research delves explicitly into the DFT parametrization of a particular stacking configuration, namely the WS_2/BBG/CGT, it is essential to note the broader implications of our findings. They transcend this specific configuration and apply to a myriad of twisted structures. These structures exhibit modified proximity spin interactions and can be paired with various encapsulating SO materials. Furthermore, our conclusions are equally relevant for an assortment of magnetic semiconductors and insulators, emphasizing the universality and significance of our research in the broader context of quantum mechanics and material science.

Also, we arrived at a significant conclusion in our most recent studies on systems that utilize ex-so-tic heterostructures with BBG. While it may be the final point we are highlighting, it is of lesser importance, and we found that Hund's interaction could be the primary driving force behind the superconducting ordering observed in experiments. The superconducting order parameter is particularly sensitive to the sign of the Hund's interaction. This sensitivity provides us with a unique opportunity. By analyzing the experimental data on the superconducting order parameter, we can reverse engineer the information to gain deeper insights into the nature and characteristics of Hund's

interaction within a specific system. It could be pivotal in understanding the underlying mechanisms at play.

Summary and Outlook

Interplay of correlated phenomena and proximity-induced spin interactions in multilayer graphene systems

Chapter 4 explores the correlated phases of rhombohedral trilayer graphene (RTG) that are influenced by spin-orbit and exchange coupling induced by proximity. Our study's main goal was to uncover the impact of spin-orbit and exchange proximity effects on the RTG's correlated phase diagram. To achieve this, we employed ab initio-fitted effective models of RTG encapsulated by transition metal dichalcogenides and ferromagnetic $Cr_2Ge_2Te_6$. The Coulomb interactions were integrated within the random-phase approximation, providing insights into potential correlated phases across different displacement fields and doping levels. Our research revealed a range of spin-valley resolved Stoner and intervalley coherence instabilities caused by spin-orbit proximity effects. The main finding is a spin-valley-coherent phase, which emerges due to the valley-Zeeman coupling. Our study also discovered the role of proximity exchange in eliminating phase degeneracies by biasing the spin direction, showing that the correlated phases are highly sensitive to the magnetization orientations of the surrounding ferromagnetic layers.

In addition to RTG, we explored ex-so-tic van der Waals heterostructures in Chapter 5, which use electrically tunable layer polarization to switch proximity-induced exchange or spin-orbit coupling within the electronically active region. Our study focused on Bernal bilayer graphene (BBG), which is encapsulated by a layered magnet ($Cr_2Ge_2Te_6$) on one side and a potent spin-orbit material (WS_2) on the other. As for RTG, we employed ab initio-fitted realistic, effective models for ex-so-tic van der Waals heterostructure WS_2/BBG/$Cr_2Ge_2Te_6$ with the random-phase approximation, which was used to discern the correlated phases. In comparison to the phase diagrams of RTG-based heterostructures discussed in Chapter 4, the phase diagram of the WS_2/BBG/CGT heterostructure is more complex. It predicts numerous symmetry-breaking phases, such as the charge density wave, spin-valley coherence, spin-valley polarized state, and valley polarized state. An exciting discovery was that the displacement field could swap two correlated phases caused by valley-Zeeman SO and EX couplings for a particular doping level. It allows for exploring the complete range of correlated phases in a single device.

In addition to the correlated phases in BBG, at the end of Chapter 5 we presented preliminary results on the influence of the Hund interaction on possible superconductivity in multilayer proximitized graphene systems, using BBG as a particular example and theoretical arguments in favor of the possible induction of superconductivity by the Hund interaction in these systems.

Although extensive research has been conducted on the theoretical study of correlated

systems in multilayer graphene systems with proximity-induced SO and EX couplings, some questions still need to be answered. One such question pertains to calculating correlated states in an external magnetic field. Additionally, several configurations of proximity effect Hamiltonians, such as Kane-Mele SO, still need to be considered. The critical temperatures and magnetic field also need further exploration, which can be done using the theoretical formalism presented in this thesis. The most significant question is the nature of superconductivity in multilayer graphene systems and how proximity-induced SO and EX couplings can affect their properties. The upcoming workload is much larger than what has been completed, highlighting the vastness of the field of the interplay of correlated phenomena with proximity-induced spin interactions in multilayer graphene systems.

In conclusion, our study profoundly explains the interplay between proximity-induced spin-orbit and exchange couplings and their role in sculpting the RTG's and BBG's correlated phases. Future studies should focus on the practical applications of these findings and seek experimental validation of the predicted phases to enrich our understanding of the system.

The emergence of lone pseudohelical pairs and pure spin-current states

In Chapter 2 of this thesis, we explore the behavior of edge states in proximitized graphene ribbons and flakes under the influence of a perpendicular magnetic field. Our focus is on understanding the formation and transformation of these states, particularly in the case of proximity-induced valley-Zeeman and Rashba spin-orbit couplings. Two distinct edge states emerge without a magnetic field: strongly localized pseudohelical and weakly localized intravalley states. However, we revealed that the intravalley states disappear when the magnetic field surpasses a critical magnetic field, leaving only the pseudohelical edge states in zigzag graphene ribbons. In finite graphene flakes, pseudohelical states behave differently. When the magnetic field is more significant than the critical one, pseudohelical states perfectly reflect at armchair edges, causing standing waves at the zigzag edges. Interestingly, these waves don't carry any charge current but transport a pure spin current.

A comprehensive tight-binding Hamiltonian model was employed to simulate the behavior of Dirac electrons in proximitized graphene. The model captured the nuances of spin-orbit interactions induced by proximity effects with transition metal dichalcogenides, particularly WSe2. Additionally, our study explored Landau levels in the bulk system, providing insights into the behavior of edge states under magnetic fields. The magnetic field can shift the bulk band gap, mainly formed between non-zero Landau levels.

These findings have significant implications for spintronics, offering a pathway to design systems with unique magnetic and spin properties by leveraging the behavior of edge states in proximitized graphene. Our research provides a theoretical framework to understand the behavior of edge states in proximitized graphene under magnetic fields, potentially leading to innovative applications in spintronics and quantum computing.

The study of edge states in proximitized multilayer graphene systems and their stability under the influence of a magnetic field is an area that can be further explored. It includes investigating novel correlated instabilities described in Chapters 4 and 5, such as the *spin-valley-coherent* state. This direction is unknown and has significant potential for practical technological applications and deepening our understanding of the physics of correlated states in multilayer graphene systems.

A. Wick theorem

In many practical cases, we need to evaluate the expectation values of higher-order operators, such as the two-particle Green function, with a non-interacting Hamiltonian. Wick's theorem is a useful theoretical tool in such cases [284].

In this appendix, we consider a Hamiltonian

$$\hat{H}_0 = \sum_i \varepsilon_i \hat{c}_i^\dagger \hat{c}_i \tag{A.1}$$

i is an arbitrary set of single-particle quantum numbers, such as orbital, spin, and momentum. We will also use the shorthand notation

$$A_i = \hat{c}_i \quad \text{or} \quad \hat{c}_i^\dagger \tag{A.2}$$

for a simplicity, there $\hat{c}^\dagger$ and $\hat{c}$ fermionic creation and anihhilation operators. It is necessary to discuss the time evolution of creation and annihilation using the equation of motion

$$\partial_\tau \hat{c}_i(\tau) = -\left[\hat{c}_i(\tau), \hat{H}_0\right] = -\varepsilon_i \hat{c}_i(\tau) \tag{A.3}$$

Solving Eq.(A.3) we obtain

$$\hat{c}_i(\tau) = e^{-\tau\varepsilon_i}\hat{c}_i \tag{A.4}$$

Moreover, using Heisenberg's formulation of the evolution of the operator, we can write

$$\hat{c}_i(\tau) = e^{\tau\hat{H}_0}\hat{c}_i e^{-\tau\hat{H}_0} \tag{A.5}$$

Combining Eq.(A.5) and Eq.(A.3), we can define

$$\hat{c}_i e^{-\tau\hat{H}_0} = e^{-\tau\hat{H}_0}\hat{c}_i e^{-\tau\varepsilon_i} \tag{A.6}$$

The analogous equation we can derive for a fermion creation operator

$$\hat{c}_i^\dagger e^{-\tau\hat{H}_0} = e^{-\tau\hat{H}_0}\hat{c}_i^\dagger e^{\tau\varepsilon_i} \tag{A.7}$$

So, we can summarize the following equation

$$A_i e^{-\tau\hat{H}_0} = e^{-\tau\hat{H}_0} A_i e^{s_i\tau\varepsilon_i} \tag{A.8}$$

where

$$s_i = \begin{cases} +1 & A_i = \hat{c}_i^\dagger \\ -1 & A_i = \hat{c}_i \end{cases} \tag{A.9}$$

A.1. Wick theorem of time-independent operators

First of all, we prove the Wick theorem for time-independent operators. We analyze the following expectation value of n creation and n annihilation operators in arbitrary order:

$$\langle A_1 A_2 ... A_{2n} \rangle = \frac{1}{Z} \mathrm{Tr} \left(e^{-\beta \hat{H}_0} A_1 A_2 ... A_{2n} \right) \tag{A.10}$$

For fermionic operators

$$[A_i, A_j] = A_i A_j - A_j A_i \tag{A.11}$$

We can use

$$A_i A_j = [A_i, A_j] + A_j A_i \tag{A.12}$$

to rewrite operator under trace of Eq.(A.10) as

$$A_1 A_2 A_3 ... A_{2n} = [A_1, A_2] \, A_3 ... A_{2n} + A_2 A_1 A_3 ... A_{2n}. \tag{A.13}$$

So, it follows that

$$\begin{aligned} A_1 A_2 ... A_{2n} = & \sum_{i=2}^{2n} (-1)^{i-2} A_2 ... A_{i-1} \, [A_1, A_i] \, A_{i+1} ... A_{2n} \\ & + (-1)^{2n-1} A_2 A_3 ... A_{2n} A_1. \end{aligned} \tag{A.14}$$

Using the cyclic property of the trace, we can write

$$\begin{aligned} \langle A_2 A_3 ... A_{2n} A_1 \rangle = & \frac{1}{Z} \mathrm{Tr} \left(e^{-\beta \hat{H}_0} A_2 A_3 ... A_{2n} A_1 \right) \\ = & \frac{e^{s_1 \beta \varepsilon_1}}{Z} \mathrm{Tr} \left(e^{-\beta \hat{H}_0} A_1 A_2 A_3 ... A_{2n} \right) \\ = & e^{s_1 \beta \varepsilon_1} \langle A_1 A_2 A_3 ... A_{2n} \rangle \end{aligned} \tag{A.15}$$

and combining this property with Eq.(A.10) and (A.14), we can write

$$\langle A_1 A_2 A_3 ... A_{2n} \rangle = \sum_{i=2}^{2n} (-1)^{i-2} \langle A_2 ... A_{i-1} \frac{[A_1, A_i]}{1 + e^{s_1 \beta \varepsilon_1}} A_{i+1} ... A_{2n} \rangle \tag{A.16}$$

continuing the discussion and using relations

$$\langle \hat{c}_i^\dagger \hat{c}_j^\dagger \rangle = 0, \quad \langle \hat{c}_i^\dagger \hat{c}_j \rangle = \frac{\left[\hat{c}_i^\dagger, \hat{c}_j \right]}{1 + e^{s_i \beta \varepsilon_i}}, \quad \langle \hat{c}_i \hat{c}_j^\dagger \rangle = \frac{\left[\hat{c}_i, \hat{c}_j^\dagger \right]}{1 + e^{s_i \beta \varepsilon_i}}, \quad \langle \hat{c}_i \hat{c}_j \rangle = 0 \tag{A.17}$$

we can rewrite (A.16) as

$$\langle A_1 A_2 A_3 ... A_{2n} \rangle = \sum_{i=2}^{2n} (-1)^{i-2} \langle A_1 A_i \rangle \langle A_2 ... A_{i-1} A_{i+1} ... A_{2n} \rangle \tag{A.18}$$

By repeating this procedure for the remaining operators, we can prove Wick's theorem by obtaining the sum over all possible pairwise operator combinations. The two main examples of two-particle Green function are:

$$\langle \hat{c}_1^\dagger \hat{c}_2 \hat{c}_3^\dagger \hat{c}_4 \rangle = \langle \hat{c}_1^\dagger \hat{c}_2 \rangle \langle \hat{c}_3^\dagger \hat{c}_4 \rangle - \langle \hat{c}_1^\dagger \hat{c}_4 \rangle \langle \hat{c}_3^\dagger \hat{c}_2 \rangle \tag{A.19}$$

and

$$\langle \hat{c}_1^\dagger \hat{c}_2^\dagger \hat{c}_3 \hat{c}_4 \rangle = \langle \hat{c}_1^\dagger \hat{c}_4 \rangle \langle \hat{c}_2^\dagger \hat{c}_3 \rangle - \langle \hat{c}_1^\dagger \hat{c}_3 \rangle \langle \hat{c}_2^\dagger \hat{c}_4 \rangle \tag{A.20}$$

A.2. Wick theorem of time-dependent operators

Time-dependent n-particle Green function we can define as

$$G^n(\tau_{i_1}, ..., \tau_{i_n}, \tau_{j_1}, .., \tau_{j_n}) = (-1)^n \langle T \hat{c}_{i_1}(\tau_{i_1}) ... \hat{c}_{i_n}(\tau_{i_n}) \hat{c}_{j_n}^\dagger(\tau_{j_n}) ... \hat{c}_{j_1}^\dagger(\tau_{j_1}) \rangle \tag{A.21}$$

The corresponding Wick theorem is

$$G^n(\tau_{i_1}, ..., \tau_{i_n}, \tau_{j_1}, .., \tau_{j_n}) = \sum_P (-1)^P G^1(\tau_{i_1}, \tau_{j_{P(1)}}) ... G^1(\tau_{i_n}, \tau_{j_{P(n)}}) \tag{A.22}$$

where sum $\sum_P$ runs over all possible permutations $P(1, 2, ..., n) = (j_1, j_2, ..., j_n)$ and P itself is the order of the permutation and

$$G^1(\tau_i, \tau_j) = -\langle T \hat{c}_i(\tau_i) \hat{c}_j^\dagger(\tau_j) \rangle \tag{A.23}$$

is the noninteracting single particle Green function. Therefore, for the time-dependent two-particle Green's function, Wick's theorem is stated as

$$G^2(\tau_{i_1}, \tau_{i_2}, \tau_{j_1} \tau_{j_2}) = \underbrace{G^1(\tau_{i_1}, \tau_{j_1}) G^1(\tau_{i_2}, \tau_{j_2})}_{P=0} - \underbrace{G^1(\tau_{i_1}, \tau_{j_2}) G^1(\tau_{i_2}, \tau_{j_1})}_{P=1} \tag{A.24}$$

B. Two-particle linear algebra

B.1. Particle-Hole channel

The product of susceptibility and vertex in a particle-hole channel is written as follows:

$$P_{\bar{a}b\bar{d}c} = \sum_{\bar{u}v} \chi^0_{ph,\bar{a}b\bar{u}v} \Gamma_{ph,v\bar{u}c\bar{d}} \tag{B.1}$$

Therefore, we can rewrite this equation in matrix form, as a product of matrices:

$$P_{(\bar{a}b),(\bar{d},c)} = \chi^0_{ph,(\bar{a}b),(v\bar{u})} \cdot \Gamma_{ph,(v\bar{u}),(\bar{d}c)} \tag{B.2}$$

Thus, to convert a two-particle function in a particle-hole channel into a matrix form from a tensor one, you need to transpose the last two indices and transform it from tensor form to matrix. In the same way, we can calculate inverse functions for the particle-hole channel in matrix form, for example in the case of calculating susceptibility in the Random Phase Approximation framework.

$$\underbrace{\chi^{\mathrm{RPA}}_{ph,(\bar{a}b),(d\bar{c})}}_{\chi^{\mathrm{RPA}}_{ph,\bar{a}b\bar{c}d}} = \sum_{f\bar{e}h\bar{g}} \left[1 - \underbrace{\chi^0_{ph,(\bar{a}b)(f\bar{e})}}_{\chi^0_{ph,\bar{a}b\bar{e}f}} \underbrace{\Gamma^{\mathrm{RPA}}_{ph,(f\bar{e})(\bar{g}h)}}_{\Gamma^{\mathrm{RPA}}_{ph,f\bar{e}h\bar{g}}} \right]^{-1}_{(\bar{a}b),(\bar{g}h)} \underbrace{\chi^0_{ph,(\bar{g}h)(d\bar{c})}}_{\chi^0_{ph,\bar{g}h\bar{c}d}} \tag{B.3}$$

B.2. Particle-Particle channel

In the case of particle-particle channel, the product of susceptibility and vertex is written as follows:

$$P_{\bar{a}\bar{b}\bar{c}\bar{d}} = \sum_{uv} \chi^0_{pp,\bar{a}u\bar{b}v} \Gamma_{pp,v\bar{c}u\bar{d}} \tag{B.4}$$

So, we can rewrite this equation in matrix form, as a product of matrices:

$$P_{(\bar{b}\bar{a}),(\bar{c}\bar{d})} = \chi^0_{pp,(\bar{b}\bar{a}),(uv)} \cdot \Gamma_{pp,(uv),(\bar{c}\bar{d})} \tag{B.5}$$

To transform a two-particle function in the particle-hole channel into a matrix form from a tensor form, it is necessary to transpose the order of the indices as follows: first to second, second to third and third to first and transform from tensor form to matrix.

We can diagonalize the vertex Γ_{pp} by decomposing it into separate channels as follows:

$$u_{pp}\phi_{pp,(uv)} = \sum_{(\bar{c}\bar{d})} \Gamma_{pp,(uv),(\bar{c}\bar{d})} \phi_{pp,(\bar{c}\bar{d})} \tag{B.6}$$

where $u_p p$ is eigenvalues of Γ_{pp}, which corresponds to the interaction in the channel ϕ_{pp}.

C. Hamiltonian downfolding

Suppose we have a single-particle Hamiltonian H of high dimension, and we need to derive a low-dimensional Hamiltonian in the subspace A, which would effectively reproduce the physics near the energy ε. An effective downfolding procedure is often used for this [285]. To begin, we decompose our Hamiltonian H as follows:

$$H = \begin{pmatrix} H^{AA} & H^{AB} \\ H^{BA} & H^{BB} \end{pmatrix} \tag{C.1}$$

where subspace B denotes the entire space of the Hamiltonian H not included in the subspace A. Thus, H^{AB} and H^{BA}, denote the hybridization between subspaces A and B. To describe the downfolding procedure, we will use Green's function. We can derive the following equation

$$\begin{pmatrix} \omega 1^{AA} - H^{AA} & -H^{AB} \\ -H^{BA} & \omega 1^{BB} - H^{BB} \end{pmatrix} \cdot \begin{pmatrix} G^{AA}(\omega) & G^{AB}(\omega) \\ G^{BA}(\omega) & G^{BB}(\omega) \end{pmatrix} = \begin{pmatrix} 1^{AA} & 0^{BA} \\ 0^{AB} & 1^{BB} \end{pmatrix} \tag{C.2}$$

where ω is real frequencies. Carrying out matrix multiplication, we get the following set of equations

$$-H^{BA}G^{AA}(\omega) + (\omega 1^{BB} - H^{BB})G^{BA}(\omega) = 0^{BA} \tag{C.3}$$

$$-H^{AB}G^{BA}(\omega) + (\omega 1^{AA} - H^{AA})G^{AA}(\omega) = 1^{AA} \tag{C.4}$$

Therefore, we can solve this set of equations and get

$$\left(\omega 1^{AA} - H^{AA} - \Sigma^{AA}(\omega)\right) G^{AA}(\omega) = 1^{AA} \tag{C.5}$$

where

$$\Sigma^{AA}(\omega) = H^{AB}\left[\omega 1^{BB} - H^{BB}\right]^{-1} H^{BA} \tag{C.6}$$

Equation (C.5) gives an exact solution for the Green's function $G^{AA}(\omega)$ describing the physics of the subsystem A. We can assume that there is the following effective Hamiltonian $\tilde{H}^{AA}(\omega)$, which will effectively reproduce the Green's function $G^{AA}(\omega)$ as follows:

$$\left(\omega 1^{AA} - \tilde{H}^{AA}(\omega)\right) G^{AA}(\omega) = 1^{AA} \tag{C.7}$$

Equating equation (C.5) to equation (C.7) and solving we get

$$\tilde{H}^{AA}(\omega) = H^{AA} + H^{AB}\left[\omega 1^{BB} - H^{BB}\right]^{-1} H^{BA} \tag{C.8}$$

Thus, when substituting ε instead of ω into the equation (C.8), we obtain an effective Hamiltonian in the subspace A that effectively reproduces the physics of the system near the energy ε.

Bibliography

[1] M. Born and R. Oppenheimer, "Zur Quantentheorie der Molekeln", Annalen der Physik **389**, 457 (1927).

[2] P. Hohenberg and W. Kohn, "Inhomogeneous Electron Gas", Phys. Rev. **136**, B864 (1964).

[3] W. Kohn, "Nobel Lecture: Electronic structure of matter—wave functions and density functionals", Rev. Mod. Phys. **71**, 1253 (1999).

[4] R. M. Martin, *Electronic Structure: Basic Theory and Practical Methods* (Cambridge University Press, 2004).

[5] M. Levy, "Universal variational functionals of electron densities, first-order density matrices, and natural spin-orbitals and solution of the ν -representability problem", Proceedings of the National Academy of Sciences **76**, 6062 (1979).

[6] K. Held, "Electronic structure calculations using dynamical mean field theory", Advances in Physics **56**, 829 (2007).

[7] S. Posysaev, "Applications of density functional theory for modeling metal-semiconductor contacts, reaction pathways, and calculating oxidation states", (2018).

[8] W. Kohn and L. J. Sham, "Self-Consistent Equations Including Exchange and Correlation Effects", Phys. Rev. **140**, A1133 (1965).

[9] D. M. Ceperley and B. J. Alder, "Ground State of the Electron Gas by a Stochastic Method", Phys. Rev. Lett. **45**, 566 (1980).

[10] M. Gell-Mann and K. A. Brueckner, "Correlation Energy of an Electron Gas at High Density", Phys. Rev. **106**, 364 (1957).

[11] K. Burke, "Perspective on density functional theory", The Journal of Chemical Physics **136** (2012).

[12] R. M. Martin, L. Reining, and D. M. Ceperley, *Interacting Electrons* (Cambridge University Press, 2016).

[13] A. J. Garza and G. E. Scuseria, "Predicting Band Gaps with Hybrid Density Functionals", The Journal of Physical Chemistry Letters **7**, 4165 (2016).

[14] J. P. Perdew, K. Burke, and M. Ernzerhof, "Generalized Gradient Approximation Made Simple", Phys. Rev. Lett. **77**, 3865 (1996).

[15] K. Burke, "Perspective on density functional theory", The Journal of Chemical Physics **136**, 150901 (2012).

[16] A. D. Becke, "Density-functional thermochemistry. III. The role of exact exchange", The Journal of Chemical Physics **98**, 5648 (1993).

[17] A. J. Cohen, P. Mori-Sánchez, and W. Yang, "Challenges for Density Functional Theory", Chemical Reviews **112**, 289 (2012).

[18] U. von Barth and L. Hedin, "A local exchange-correlation potential for the spin polarized case. i", Journal of Physics C: Solid State Physics **5**, 1629 (1972).

[19] C. R. Jacob and M. Reiher, "Spin in density-functional theory", International Journal of Quantum Chemistry **112**, 3661 (2012).

[20] P. Jambrina and J. Aldegunde, "Computational Tools for the Study of Biomolecules", in "Computer Aided Chemical Engineering", pp. 583–648 (Elsevier, 2016).

[21] M. Brooks, M. Richter, and L. Sandratskii, "Density Functional Theory: Magnetism", in "Encyclopedia of Materials: Science and Technology", pp. 2059–2070 (Elsevier, 2001).

[22] I. Turek, "Ab Initio Calculations of Curie Temperatures", in "Encyclopedia of Materials: Science and Technology", pp. 1–6 (Elsevier, 2008).

[23] G. L. Oliver and J. P. Perdew, "Spin-density gradient expansion for the kinetic energy", Phys. Rev. A **20**, 397 (1979).

[24] F. Giustino, *Materials modelling using density functional theory* (Oxford University Press, London, England, 2014).

[25] I. Žutić, J. Fabian, and S. Das Sarma, "Spintronics: Fundamentals and applications", Rev. Mod. Phys. **76**, 323 (2004).

[26] P. Schwerdtfeger, "The Pseudopotential Approximation in Electronic Structure Theory", ChemPhysChem **12**, 3143 (2011).

[27] Wikipedia, "Pseudopotential — Wikipedia, The Free Encyclopedia", `http://en.wikipedia.org/w/index.php?title=Pseudopotential&oldid=1148156981` (2023), [Online; accessed 02-August-2023].

[28] M. L. Cohen and J. R. Chelikowsky, *Electronic structure and optical properties of semiconductors*, Springer Series in Solid-State Sciences (Springer, Berlin, Germany, 2012).

[29] V. W. zhe Yu, J. Moussa, and V. Blum, "Accurate frozen core approximation for all-electron density-functional theory", The Journal of Chemical Physics **154** (2021).

[30] D. R. Hamann, M. Schlüter, and C. Chiang, "Norm-Conserving Pseudopotentials", Phys. Rev. Lett. **43**, 1494 (1979).

[31] D. R. Hamann, "Optimized norm-conserving Vanderbilt pseudopotentials", Phys. Rev. B **88**, 085117 (2013).

[32] L. Kleinman and D. M. Bylander, "Efficacious Form for Model Pseudopotentials", Phys. Rev. Lett. **48**, 1425 (1982).

[33] D. Vanderbilt, "Soft self-consistent pseudopotentials in a generalized eigenvalue formalism", Phys. Rev. B **41**, 7892 (1990).

[34] P. E. Blöchl, "Projector augmented-wave method", Phys. Rev. B **50**, 17953 (1994).

[35] P. Pyykko, "Relativistic effects in structural chemistry", Chemical Reviews **88**, 563 (1988).

[36] A. K. Rajagopal and J. Callaway, "Inhomogeneous Electron Gas", Phys. Rev. B **7**, 1912 (1973).

[37] A. H. MacDonald and S. H. Vosko, "A relativistic density functional formalism", Journal of Physics C: Solid State Physics **12**, 2977 (1979).

[38] T. Frank, "Ab initio studies of extrinsic spin-orbit coupling effects in graphene and quantum Monte Carlo simulations of phosphorene", (2019).

[39] P. A. M. Dirac and R. H. Fowler, "The quantum theory of the electron", Proceedings of the Royal Society of London. Series A, Containing Papers of a Mathematical and Physical Character **117**, 610 (1928).

[40] M. Weissbluth, *Atoms and molecules* (Elsevier, 2012).

[41] G. B. Bachelet and M. Schlüter, "Relativistic norm-conserving pseudopotentials", Phys. Rev. B **25**, 2103 (1982).

[42] G. H. Wannier, "The Structure of Electronic Excitation Levels in Insulating Crystals", Phys. Rev. **52**, 191 (1937).

[43] J. C. Slater and G. F. Koster, "Simplified LCAO Method for the Periodic Potential Problem", Phys. Rev. **94**, 1498 (1954).

[44] W. Kohn, "Analytic Properties of Bloch Waves and Wannier Functions", Phys. Rev. **115**, 809 (1959).

[45] J. D. Cloizeaux, "Orthogonal Orbitals and Generalized Wannier Functions", Phys. Rev. **129**, 554 (1963).

[46] C. W. Groth, M. Wimmer, A. R. Akhmerov, and X. Waintal, "Kwant: a software package for quantum transport", New Journal of Physics **16**, 063065 (2014).

[47] D. Moldovan, Miša Anđelković, and Francois Peeters, "pybinding v0.9.5: a Python package for tight-binding calculations", (2020).

[48] O. Parcollet, M. Ferrero, T. Ayral, H. Hafermann, I. Krivenko, L. Messio, and P. Seth, "TRIQS: A toolbox for research on interacting quantum systems", Computer Physics Communications **196**, 398 (2015).

[49] E. P. Wohlfarth, "The Theoretical and Experimental Status of the Collective Electron Theory of Ferromagnetism", Rev. Mod. Phys. **25**, 211 (1953).

[50] G. H. Wannier, "Dynamics of Band Electrons in Electric and Magnetic Fields", Rev. Mod. Phys. **34**, 645 (1962).

[51] N. Marzari, A. A. Mostofi, J. R. Yates, I. Souza, and D. Vanderbilt, "Maximally localized Wannier functions: Theory and applications", Rev. Mod. Phys. **84**, 1419 (2012).

[52] G. Pizzi, V. Vitale, R. Arita, S. Blügel, F. Freimuth, G. Géranton, M. Gibertini, D. Gresch, C. Johnson, T. Koretsune, J. Ibañez-Azpiroz, H. Lee, J.-M. Lihm, D. Marchand, A. Marrazzo, Y. Mokrousov, J. I. Mustafa, Y. Nohara, Y. Nomura, L. Paulatto, S. Poncé, T. Ponweiser, J. Qiao, F. Thöle, S. S. Tsirkin, M. Wierzbowska, N. Marzari, D. Vanderbilt, I. Souza, A. A. Mostofi, and J. R. Yates, "Wannier90 as a community code: new features and applications", Journal of Physics: Condensed Matter **32**, 165902 (2020).

[53] N. Marzari and D. Vanderbilt, "Maximally localized generalized Wannier functions for composite energy bands", Phys. Rev. B **56**, 12847 (1997).

[54] K. S. Novoselov, A. K. Geim, S. V. Morozov, D. Jiang, Y. Zhang, S. V. Dubonos, I. V. Grigorieva, and A. A. Firsov, "Electric Field Effect in Atomically Thin Carbon Films", Science **306**, 666 (2004).

[55] A. H. Castro Neto, F. Guinea, N. M. R. Peres, K. S. Novoselov, and A. K. Geim, "The electronic properties of graphene", Rev. Mod. Phys. **81**, 109 (2009).

[56] W. Han, R. K. Kawakami, M. Gmitra, and J. Fabian, "Graphene spintronics", Nature Nanotechnology **9**, 794 (2014).

[57] L. Banszerus, M. Schmitz, S. Engels, J. Dauber, M. Oellers, F. Haupt, K. Watanabe, T. Taniguchi, B. Beschoten, and C. Stampfer, "Ultrahigh-mobility graphene devices from chemical vapor deposition on reusable copper", Science Advances **1** (2015).

[58] N. Petrone, C. R. Dean, I. Meric, A. M. van der Zande, P. Y. Huang, L. Wang, D. Muller, K. L. Shepard, and J. Hone, "Chemical Vapor Deposition-Derived Graphene with Electrical Performance of Exfoliated Graphene", Nano Letters **12**, 2751 (2012).

[59] V. E. Calado, S.-E. Zhu, S. Goswami, Q. Xu, K. Watanabe, T. Taniguchi, G. C. A. M. Janssen, and L. M. K. Vandersypen, "Ballistic transport in graphene grown by chemical vapor deposition", Applied Physics Letters **104** (2014).

[60] C. Soldano, A. Mahmood, and E. Dujardin, "Production, properties and potential of graphene", Carbon **48**, 2127 (2010).

[61] P. Giannozzi, S. Baroni, N. Bonini, M. Calandra, R. Car, C. Cavazzoni, D. Ceresoli, G. L. Chiarotti, M. Cococcioni, I. Dabo, A. D. Corso, S. de Gironcoli, S. Fabris, G. Fratesi, R. Gebauer, U. Gerstmann, C. Gougoussis, A. Kokalj, M. Lazzeri, L. Martin-Samos, N. Marzari, F. Mauri, R. Mazzarello, S. Paolini, A. Pasquarello, L. Paulatto, C. Sbraccia, S. Scandolo, G. Sclauzero, A. P. Seitsonen, A. Smogunov, P. Umari, and R. M. Wentzcovitch, "QUANTUM ESPRESSO: a modular and open-source software project for quantum simulations of materials", Journal of Physics: Condensed Matter **21**, 395502 (2009).

[62] P. Giannozzi, O. Andreussi, T. Brumme, O. Bunau, M. B. Nardelli, M. Calandra, R. Car, C. Cavazzoni, D. Ceresoli, M. Cococcioni, N. Colonna, I. Carnimeo, A. D. Corso, S. de Gironcoli, P. Delugas, R. A. DiStasio, A. Ferretti, A. Floris, G. Fratesi, G. Fugallo, R. Gebauer, U. Gerstmann, F. Giustino, T. Gorni, J. Jia, M. Kawamura, H.-Y. Ko, A. Kokalj, E. Küçükbenli, M. Lazzeri, M. Marsili, N. Marzari, F. Mauri, N. L. Nguyen, H.-V. Nguyen, A. O. de-la Roza, L. Paulatto, S. Poncé, D. Rocca, R. Sabatini, B. Santra, M. Schlipf, A. P. Seitsonen, A. Smogunov, I. Timrov, T. Thonhauser, P. Umari, N. Vast, X. Wu, and S. Baroni, "Advanced capabilities for materials modelling with Quantum ESPRESSO", Journal of Physics: Condensed Matter **29**, 465901 (2017).

[63] A. A. Mostofi, J. R. Yates, G. Pizzi, Y.-S. Lee, I. Souza, D. Vanderbilt, and N. Marzari, "An updated version of wannier90: A tool for obtaining maximally-localised Wannier functions", Computer Physics Communications **185**, 2309 (2014).

[64] M. Gmitra, S. Konschuh, C. Ertler, C. Ambrosch-Draxl, and J. Fabian, "Band-structure topologies of graphene: Spin-orbit coupling effects from first principles", Phys. Rev. B **80**, 235431 (2009).

[65] J. C. Boettger and S. B. Trickey, "First-principles calculation of the spin-orbit splitting in graphene", Phys. Rev. B **75**, 121402 (2007).

[66] S. Konschuh, M. Gmitra, and J. Fabian, "Tight-binding theory of the spin-orbit coupling in graphene", Phys. Rev. B **82**, 245412 (2010).

[67] J. Sichau, M. Prada, T. Anlauf, T. J. Lyon, B. Bosnjak, L. Tiemann, and R. H. Blick, "Resonance Microwave Measurements of an Intrinsic Spin-Orbit Coupling Gap in Graphene: A Possible Indication of a Topological State", Phys. Rev. Lett. **122**, 046403 (2019).

[68] M. Gmitra and J. Fabian, "Graphene on transition-metal dichalcogenides: A platform for proximity spin-orbit physics and optospintronics", Phys. Rev. B **92**, 155403 (2015).

[69] M. Gmitra, D. Kochan, P. Högl, and J. Fabian, "Trivial and inverted Dirac bands and the emergence of quantum spin Hall states in graphene on transition-metal dichalcogenides", Phys. Rev. B **93**, 155104 (2016).

[70] K. Zollner, M. Gmitra, T. Frank, and J. Fabian, "Theory of proximity-induced exchange coupling in graphene on hBN/(Co, Ni)", Phys. Rev. B **94**, 155441 (2016).

[71] V. T. Phong, N. R. Walet, and F. Guinea, "Effective interactions in a graphene layer induced by the proximity to a ferromagnet", 2D Materials **5**, 014004 (2017).

[72] Z. Qiao, W. Ren, H. Chen, L. Bellaiche, Z. Zhang, A. H. MacDonald, and Q. Niu, "Quantum Anomalous Hall Effect in Graphene Proximity Coupled to an Antiferromagnetic Insulator", Phys. Rev. Lett. **112**, 116404 (2014).

[73] J. Zhang, B. Zhao, T. Zhou, Y. Xue, C. Ma, and Z. Yang, "Strong magnetization and Chern insulators in compressed graphene/CrI_3 van der Waals heterostructures", Phys. Rev. B **97**, 085401 (2018).

[74] T. S. Ghiasi, J. Ingla-Aynés, A. A. Kaverzin, and B. J. van Wees, "Large Proximity-Induced Spin Lifetime Anisotropy in Transition-Metal Dichalcogenide/Graphene Heterostructures", Nano Letters **17**, 7528 (2017).

[75] S. Zihlmann, A. W. Cummings, J. H. Garcia, M. Kedves, K. Watanabe, T. Taniguchi, C. Schönenberger, and P. Makk, "Large spin relaxation anisotropy and valley-Zeeman spin-orbit coupling in WSe_2/graphene/h-BN heterostructures", Phys. Rev. B **97**, 075434 (2018).

[76] M. V. Kamalakar, A. Dankert, J. Bergsten, T. Ive, and S. P. Dash, "Spintronics with graphene-hexagonal boron nitride van der Waals heterostructures", Applied Physics Letters **105** (2014).

[77] S. Omar and B. J. van Wees, "Spin transport in high-mobility graphene on WS_2 substrate with electric-field tunable proximity spin-orbit interaction", Phys. Rev. B **97**, 045414 (2018).

[78] D. Kochan, S. Irmer, and J. Fabian, "Model spin-orbit coupling Hamiltonians for graphene systems", Phys. Rev. B **95**, 165415 (2017).

[79] S. Irmer, "Theoretical investigations of orbital and spin-orbital effects in functionalized graphene", (2018).

[80] T. Frank, M. Gmitra, and J. Fabian, "Theory of electronic and spin-orbit proximity effects in graphene on Cu(111)", Phys. Rev. B **93**, 155142 (2016).

[81] K. Zollner, M. Gmitra, and J. Fabian, "Heterostructures of graphene and hBN: Electronic, spin-orbit, and spin relaxation properties from first principles", Phys. Rev. B **99**, 125151 (2019).

[82] D. Di Sante, P. Eck, M. Bauernfeind, M. Will, R. Thomale, J. Schäfer, R. Claessen, and G. Sangiovanni, "Towards topological quasifreestanding stanene via substrate engineering", Phys. Rev. B **99**, 035145 (2019).

[83] C. L. Kane and E. J. Mele, "Z_2 Topological Order and the Quantum Spin Hall Effect", Phys. Rev. Lett. **95**, 146802 (2005).

[84] S. Konschuh, "Spin-orbit coupling effects: from graphene to graphite", (2011).

[85] J. Amann, T. Völkl, T. Rockinger, D. Kochan, K. Watanabe, T. Taniguchi, J. Fabian, D. Weiss, and J. Eroms, "Counterintuitive gate dependence of weak antilocalization in bilayer graphene/WSe_2 heterostructures", Phys. Rev. B **105**, 115425 (2022).

[86] T. Naimer, K. Zollner, M. Gmitra, and J. Fabian, "Twist-angle dependent proximity induced spin-orbit coupling in graphene/transition metal dichalcogenide heterostructures", Phys. Rev. B **104**, 195156 (2021).

[87] C. L. Kane and E. J. Mele, "Quantum Spin Hall Effect in Graphene", Phys. Rev. Lett. **95**, 226801 (2005).

[88] L. Sun, L. Rademaker, D. Mauro, A. Scarfato, Á. Pásztor, I. Gutiérrez-Lezama, Z. Wang, J. Martinez-Castro, A. F. Morpurgo, and C. Renner, "Determining spin-orbit coupling in graphene by quasiparticle interference imaging", Nature Communications **14** (2023).

[89] H. Min, J. E. Hill, N. A. Sinitsyn, B. R. Sahu, L. Kleinman, and A. H. MacDonald, "Intrinsic and Rashba spin-orbit interactions in graphene sheets", Phys. Rev. B **74**, 165310 (2006).

[90] F. Herling, C. K. Safeer, J. Ingla-Aynés, N. Ontoso, L. E. Hueso, and F. Casanova, "Gate tunability of highly efficient spin-to-charge conversion by spin Hall effect in graphene proximitized with WSe_2", APL Materials **8**, 071103 (2020).

[91] T. S. Ghiasi, A. A. Kaverzin, P. J. Blah, and B. J. Van Wees, "Charge-to-Spin Conversion by the Rashba-Edelstein Effect in Two-Dimensional van der Waals Heterostructures up to Room Temperature", Nano Lett. **19**, 5959 (2019).

[92] A. M. Hoque, D. Khokhriakov, B. Karpiak, and S. P. Dash, "All-electrical creation and control of giant spin-galvanic effect in 1T-MoTe2/graphene heterostructures at room temperature", (2019), 1908.09367.

[93] J. Zhang, B. Zhao, Y. Yao, and Z. Yang, "Robust quantum anomalous Hall effect in graphene-based van der Waals heterostructures", Phys. Rev. B **92**, 165418 (2015).

[94] J. B. S. Mendes, O. Alves Santos, L. M. Meireles, R. G. Lacerda, L. H. Vilela-Leão, F. L. A. Machado, R. L. Rodríguez-Suárez, A. Azevedo, and S. M. Rezende, "Spin-Current to Charge-Current Conversion and Magnetoresistance in a Hybrid Structure of Graphene and Yttrium Iron Garnet", Phys. Rev. Lett. **115**, 226601 (2015).

[95] M. U. Farooq and J. Hong, "Switchable valley splitting by external electric field effect in graphene/CrI3 heterostructures", npj 2D Materials and Applications **3** (2019).

[96] J. F. Sierra, J. Fabian, R. K. Kawakami, S. Roche, and S. O. Valenzuela, "Van der Waals heterostructures for spintronics and opto-spintronics", Nature Nanotechnology **16**, 856 (2021).

[97] A. Avsar, H. Ochoa, F. Guinea, B. Özyilmaz, B. J. van Wees, and I. J. Vera-Marun, "Colloquium: Spintronics in graphene and other two-dimensional materials", Rev. Mod. Phys. **92**, 021003 (2020).

[98] Z. Wang, D.-K. Ki, H. Chen, H. Berger, A. H. MacDonald, and A. F. Morpurgo, "Strong interface-induced spin–orbit interaction in graphene on WS2", Nat. Commun. **6**, 8339 (2015).

[99] Y. S. Gani, E. J. Walter, and E. Rossi, "Proximity-induced spin-orbit splitting in graphene nanoribbons on transition-metal dichalcogenides", Phys. Rev. B **101**, 195416 (2020).

[100] Y. Li and M. Koshino, "Twist-angle dependence of the proximity spin-orbit coupling in graphene on transition-metal dichalcogenides", Phys. Rev. B **99**, 075438 (2019).

[101] A. David, P. Rakyta, A. Kormányos, and G. Burkard, "Induced spin-orbit coupling in twisted graphene–transition metal dichalcogenide heterobilayers: Twistronics meets spintronics", Phys. Rev. B **100**, 085412 (2019).

[102] T. Naimer, K. Zollner, M. Gmitra, and J. Fabian, "Twist-angle dependent proximity induced spin-orbit coupling in graphene/transition-metal dichalcogenide heterostructures", (2021), `2108.06126`.

[103] A. Pezo, Z. Zanolli, N. Wittemeier, P. Ordejon, A. Fazzio, S. Roche, and J. H. Garcia, "Manipulation of Spin Transport in Graphene/Transition Metal Dichalcogenide Heterobilayers upon Twisting", (2021), `2011.06714`.

[104] A. M. Alsharari, M. M. Asmar, and S. E. Ulloa, "Mass inversion in graphene by proximity to dichalcogenide monolayer", Phys. Rev. B **94**, 241106 (2016).

[105] K. Song, D. Soriano, A. W. Cummings, R. Robles, P. Ordejón, and S. Roche, "Spin Proximity Effects in Graphene/Topological Insulator Heterostructures", Nano Letters **18**, 2033 (2018).

[106] K. Zollner and J. Fabian, "Single and bilayer graphene on the topological insulator Bi_2Se_3: Electronic and spin-orbit properties from first principles", Phys. Rev. B **100**, 165141 (2019).

[107] L. Rademaker and M. Gibertini, "Gate-tunable imbalanced Kane-Mele model in encapsulated bilayer jacutingaite", Physical Review Materials **5**, 044201 (2021).

[108] J. H. Garcia, M. Vila, A. W. Cummings, and S. Roche, "Spin transport in graphene/transition metal dichalcogenide heterostructures", Chem. Soc. Rev. **47**, 3359 (2018).

[109] J. O. Island, X. Cui, C. Lewandowski, J. Y. Khoo, E. M. Spanton, H. Zhou, D. Rhodes, J. C. Hone, T. Taniguchi, K. Watanabe, L. S. Levitov, M. P. Zaletel, and A. F. Young, "Spin–orbit-driven band inversion in bilayer graphene by the van der Waals proximity effect", Nature **571**, 85 (2019).

[110] B. Karpiak, A. W. Cummings, K. Zollner, M. Vila, D. Khokhriakov, A. M. Hoque, A. Dankert, P. Svedlindh, J. Fabian, S. Roche, and S. P. Dash, "Magnetic proximity in a van der Waals heterostructure of magnetic insulator and graphene", 2D Materials **7**, 015026 (2019).

[111] A. M. Hoque, D. Khokhriakov, K. Zollner, B. Zhao, B. Karpiak, J. Fabian, and S. P. Dash, "All-electrical creation and control of spin-galvanic signal in graphene and molybdenum ditelluride heterostructures at room temperature", Communications Physics **4**, 124 (2021).

[112] C. K. Safeer, J. Ingla-Aynés, F. Herling, J. H. Garcia, M. Vila, N. Ontoso, M. R. Calvo, S. Roche, L. E. Hueso, and F. Casanova, "Room-Temperature Spin Hall Effect in Graphene/MoS2 van der Waals Heterostructures", Nano Letters **19**, 1074 (2019).

[113] T. Wakamura, F. Reale, P. Palczynski, M. Q. Zhao, A. T. C. Johnson, S. Guéron, C. Mattevi, A. Ouerghi, and H. Bouchiat, "Spin-orbit interaction induced in graphene by transition metal dichalcogenides", Phys. Rev. B **99**, 245402 (2019).

[114] T. Wakamura, N. J. Wu, A. D. Chepelianskii, S. Guéron, M. Och, M. Ferrier, T. Taniguchi, K. Watanabe, C. Mattevi, and H. Bouchiat, "Spin-Orbit-Enhanced Robustness of Supercurrent in Graphene/WS_2 Josephson Junctions", Phys. Rev. Lett. **125**, 266801 (2020).

[115] J. Amann, T. Völkl, D. Kochan, K. Watanabe, T. Taniguchi, J. Fabian, D. Weiss, and J. Eroms, "Gate-tunable Spin-Orbit-Coupling in Bilayer Graphene-WSe_2-heterostructures", (2021), 2012.05718.

[116] B. Fülöp, A. Márffy, S. Zihlmann, M. Gmitra, E. Tóvári, B. Szentpéteri, M. Kedves, K. Watanabe, T. Taniguchi, J. Fabian, C. Schönenberger, P. Makk, and S. Csonka, "Boosting proximity spin orbit coupling in graphene/WSe_2 heterostructures via hydrostatic pressure", (2021), 2103.13325.

[117] J. Ingla-Aynés, F. Herling, J. Fabian, L. E. Hueso, and F. Casanova, "Electrical Control of Valley-Zeeman Spin-Orbit-Coupling–Induced Spin Precession at Room Temperature", Phys. Rev. Lett. **127**, 047202 (2021).

[118] T. Frank, P. Högl, M. Gmitra, D. Kochan, and J. Fabian, "Protected Pseudohelical Edge States in <math display="inline"> <msub> <mi mathvariant="double-struck">Z</mi> <mn>2</mn> </msub> </math> -Trivial Proximitized Graphene", Phys. Rev. Lett. **120**, 156402 (2018).

[119] T. Frank, P. Högl, M. Gmitra, D. Kochan, and J. Fabian, "Protected Pseudohelical Edge States in <math display="inline"> <msub> <mi mathvariant="double-struck">Z</mi> <mn>2</mn> </msub> </math> -Trivial Proximitized Graphene", Phys. Rev. Lett. **120**, 156402 (2018).

[120] H. Jiang, H. Liu, J. Feng, Q. Sun, and X. C. Xie, "Transport Discovery of Emerging Robust Helical Surface States in $Z_2 = 0$ Systems", Phys. Rev. Lett. **112**, 176601 (2014).

[121] P. Högl, T. Frank, K. Zollner, D. Kochan, M. Gmitra, and J. Fabian, "Quantum Anomalous Hall Effects in Graphene from Proximity-Induced Uniform and Staggered Spin-Orbit and Exchange Coupling", Phys. Rev. Lett. **124**, 136403 (2020).

[122] P. Högl, T. Frank, D. Kochan, M. Gmitra, and J. Fabian, "Chiral Majorana fermions in graphene from proximity-induced superconductivity", Phys. Rev. B **101**, 245441 (2020).

[123] M. Luo, "Topological edge states of a graphene zigzag nanoribbon with spontaneous edge magnetism", Phys. Rev. B **102**, 075421 (2020).

[124] T. Frank and J. Fabian, "Landau levels in spin-orbit coupling proximitized graphene: Bulk states", Phys. Rev. B **102**, 165416 (2020).

[125] B. Yang, M.-F. Tu, J. Kim, Y. Wu, H. Wang, J. Alicea, R. Wu, M. Bockrath, and J. Shi, "Tunable spin–orbit coupling and symmetry-protected edge states in graphene/WS 2", 2D Mater. **3**, 031012 (2016).

[126] C. Li, F. Ye, X. Chen, Y. V. Kartashov, L. Torner, and V. V. Konotop, "Topological edge states in Rashba-Dresselhaus spin-orbit-coupled atoms in a Zeeman lattice", Phys. Rev. A **98**, 061601 (2018).

[127] A. De Martino, A. Hütten, and R. Egger, "Landau levels, edge states, and strained magnetic waveguides in graphene monolayers with enhanced spin-orbit interaction", Phys. Rev. B **84**, 155420 (2011).

[128] J. Lado, N. García-Martínez, and J. Fernández-Rossier, "Edge states in graphene-like systems", Synthetic Metals **210**, 56 (2015).

[129] P. Delplace and G. Montambaux, "WKB analysis of edge states in graphene in a strong magnetic field", Phys. Rev. B **82**, 205412 (2010).

[130] O. Shevtsov, P. Carmier, C. Petitjean, C. Groth, D. Carpentier, and X. Waintal, "Graphene-Based Heterojunction between Two Topological Insulators", Phys. Rev. X **2**, 031004 (2012).

[131] N. Goldman, W. Beugeling, and C. Morais Smith, "Topological phase transitions between chiral and helical spin textures in a lattice with spin-orbit coupling and a magnetic field", Eur. Lett. **97**, 23003 (2012).

[132] B. Scharf, A. Matos-Abiague, I. Žutić, and J. Fabian, "Probing topological transitions in HgTe/CdTe quantum wells by magneto-optical measurements", Phys. Rev. B **91**, 235433 (2015).

[133] J. Böttcher, C. Tutschku, L. W. Molenkamp, and E. M. Hankiewicz, "Survival of the Quantum Anomalous Hall Effect in Orbital Magnetic Fields as a Consequence of the Parity Anomaly", Phys. Rev. Lett. **123**, 226602 (2019).

[134] M. Gmitra, D. Kochan, and J. Fabian, "Spin-Orbit Coupling in Hydrogenated Graphene", Phys. Rev. Lett. **110**, 246602 (2013).

[135] E. I. Rashba, "Graphene with structure-induced spin-orbit coupling: Spin-polarized states, spin zero modes, and quantum Hall effect", Phys. Rev. B **79**, 161409(R) (2009).

[136] V. Y. Tsaran and S. G. Sharapov, "Landau levels and magnetic oscillations in gapped Dirac materials with intrinsic Rashba interaction", Phys. Rev. B **90**, 205417 (2014).

[137] R. Peierls, "Zur Theorie des Diamagnetismus von Leitungselektronen", Zeitschrift für Physik **80**, 763 (1933).

[138] W. Kohn, "Theory of Bloch Electrons in a Magnetic Field: The Effective Hamiltonian", Phys. Rev. **115**, 1460 (1959).

[139] M.-H. Liu, P. Rickhaus, P. Makk, E. Tóvári, R. Maurand, F. Tkatschenko, M. Weiss, C. Schönenberger, and K. Richter, "Scalable Tight-Binding Model for Graphene", Phys. Rev. Lett. **114**, 036601 (2015).

[140] Y.-M. Lin, V. Perebeinos, Z. Chen, and P. Avouris, "Electrical observation of subband formation in graphene nanoribbons", Phys. Rev. B **78**, 161409(R) (2008).

[141] T. P. Cysne, J. H. Garcia, A. R. Rocha, and T. G. Rappoport, "Quantum Hall effect in graphene with interface-induced spin-orbit coupling", Phys. Rev. B **97**, 085413 (2018).

[142] A. L. Fetter and J. D. Walecka, *Quantum Theory of Many-Particle Systems* (McGraw-Hill, Boston, 1971).

[143] A. A. Abrikosov, I. Dzyaloshinskii, L. P. Gorkov, and R. A. Silverman, *Methods of quantum field theory in statistical physics* (Dover, New York, NY, 1975).

[144] J. W. Negele and H. Orland, *Quantum Many-Particle Systems* (CRC Press, 2018).

[145] G. D. Mahan, *Many-particle physics*, Physics of Solids and Liquids (Springer, New York, NY, 2013), 3 edition.

[146] E. Pavarini and E. Koch, *Simulating correlations with computers: Lecture notes of the autumn school on correlated electrons 2021* (2021).

[147] T. Matsubara, "A New Approach to Quantum-Statistical Mechanics", Progress of Theoretical Physics **14**, 351 (1955).

[148] G. Baym and N. D. Mermin, "Determination of Thermodynamic Green's Functions", Journal of Mathematical Physics **2**, 232 (1961).

[149] H. Fehske, R. Schneider, and A. Weisse (eds.), *Computational many-particle physics*, Lecture notes in physics (Springer, Berlin, Germany, 2007), 2008 edition.

[150] R. P. Feynman, "The Theory of Positrons", Phys. Rev. **76**, 749 (1949).

[151] G. A. Baker, *Essentials of padé approximants* (Academic Press, San Diego, CA, 1975).

[152] G. J. Kraberger, R. Triebl, M. Zingl, and M. Aichhorn, "Maximum entropy formalism for the analytic continuation of matrix-valued Green's functions", Phys. Rev. B **96**, 155128 (2017).

[153] J. C. Slater, "The Theory of Complex Spectra", Phys. Rev. **34**, 1293 (1929).

[154] R. D. Mattuck, *A guide to Feynman diagrams in the many-body problem*, Dover Books on Physics (Dover Publications, Mineola, NY, 1992).

[155] G. Rohringer, *New routes towards a theoretical treatment of nonlocal electronic correlations*, Ph.D. thesis (2013).

[156] G. Rohringer, A. Valli, and A. Toschi, "Local electronic correlation at the two-particle level", Phys. Rev. B **86**, 125114 (2012).

[157] G. Rohringer, H. Hafermann, A. Toschi, A. A. Katanin, A. E. Antipov, M. I. Katsnelson, A. I. Lichtenstein, A. N. Rubtsov, and K. Held, "Diagrammatic routes to nonlocal correlations beyond dynamical mean field theory", Rev. Mod. Phys. **90**, 025003 (2018).

[158] R. Kubo, "Statistical-Mechanical Theory of Irreversible Processes. I. General Theory and Simple Applications to Magnetic and Conduction Problems", Journal of the Physical Society of Japan **12**, 570 (1957).

[159] P. C. Martin and J. Schwinger, "Theory of Many-Particle Systems. I", Phys. Rev. **115**, 1342 (1959).

[160] E. E. Salpeter and H. A. Bethe, "A Relativistic Equation for Bound-State Problems", Phys. Rev. **84**, 1232 (1951).

[161] D. Bohm and D. Pines, "A Collective Description of Electron Interactions. I. Magnetic Interactions", Phys. Rev. **82**, 625 (1951).

[162] D. Pines and D. Bohm, "A Collective Description of Electron Interactions: II. Collective vs Individual Particle Aspects of the Interactions", Phys. Rev. **85**, 338 (1952).

[163] D. Bohm and D. Pines, "A Collective Description of Electron Interactions: III. Coulomb Interactions in a Degenerate Electron Gas", Phys. Rev. **92**, 609 (1953).

[164] D. Senechal, A.-M. Tremblay, and C. Bourbonnais (eds.), *Theoretical methods for strongly correlated electrons*, CRM Series in Mathematical Physics (Springer, New York, NY, 2003).

[165] G. Esirgen and N. E. Bickers, "Fluctuation exchange analysis of superconductivity in the standard three-band CuO_2 model", Phys. Rev. B **57**, 5376 (1998).

[166] C.-H. Pao and N. E. Bickers, "Superconductivity in the two-dimensional Hubbard model: One-particle correlation functions", Phys. Rev. B **51**, 16310 (1995).

[167] N. E. Bickers, D. J. Scalapino, and S. R. White, "Conserving Approximations for Strongly Correlated Electron Systems: Bethe-Salpeter Equation and Dynamics for the Two-Dimensional Hubbard Model", Phys. Rev. Lett. **62**, 961 (1989).

[168] D. J. Scalapino, "A common thread: The pairing interaction for unconventional superconductors", Rev. Mod. Phys. **84**, 1383 (2012).

[169] T. Takimoto, T. Hotta, and K. Ueda, "Strong-coupling theory of superconductivity in a degenerate Hubbard model", Phys. Rev. B **69**, 104504 (2004).

[170] A. Kobayashi, S. Katayama, K. Noguchi, and Y. Suzumura, "Superconductivity in Charge Ordered Organic Conductor –α-$(ET)_2I_3$ Salt–", Journal of the Physical Society of Japan **73**, 3135 (2004).

[171] R. Nourafkan, G. Kotliar, and A.-M. S. Tremblay, "Correlation-Enhanced Odd-Parity Interorbital Singlet Pairing in the Iron-Pnictide Superconductor LiFeAs", Phys. Rev. Lett. **117**, 137001 (2016).

[172] J. Bardeen, L. N. Cooper, and J. R. Schrieffer, "Theory of Superconductivity", Phys. Rev. **108**, 1175 (1957).

[173] C. R. Dean, L. Wang, P. Maher, C. Forsythe, F. Ghahari, Y. Gao, J. Katoch, M. Ishigami, P. Moon, M. Koshino, T. Taniguchi, K. Watanabe, K. L. Shepard, J. Hone, and P. Kim, "Hofstadter's butterfly and the fractal quantum Hall effect in moiré superlattices", Nature **497**, 598 (2013).

[174] Y. Kim, P. Herlinger, P. Moon, M. Koshino, T. Taniguchi, K. Watanabe, and J. H. Smet, "Charge Inversion and Topological Phase Transition at a Twist Angle Induced van Hove Singularity of Bilayer Graphene", Nano Letters **16**, 5053 (2016).

[175] Y. Cao, V. Fatemi, S. Fang, K. Watanabe, T. Taniguchi, E. Kaxiras, and P. Jarillo-Herrero, "Unconventional superconductivity in magic-angle graphene superlattices", Nature **556**, 43 (2018).

[176] Y. Cao, V. Fatemi, A. Demir, S. Fang, S. L. Tomarken, J. Y. Luo, J. D. Sanchez-Yamagishi, K. Watanabe, T. Taniguchi, E. Kaxiras, R. C. Ashoori, and P. Jarillo-Herrero, "Correlated insulator behaviour at half-filling in magic-angle graphene superlattices", Nature **556**, 80 (2018).

[177] G. Li, A. Luican, J. M. B. L. dos Santos, A. H. C. Neto, A. Reina, J. Kong, and E. Y. Andrei, "Observation of Van Hove singularities in twisted graphene layers", Nature Physics **6**, 109 (2009).

[178] R. Bistritzer and A. H. MacDonald, "Moiré bands in twisted double-layer graphene", Proceedings of the National Academy of Sciences **108**, 12233 (2011).

[179] I. Brihuega, P. Mallet, H. González-Herrero, G. Trambly de Laissardière, M. M. Ugeda, L. Magaud, J. M. Gómez-Rodríguez, F. Ynduráin, and J.-Y. Veuillen, "Unraveling the Intrinsic and Robust Nature of van Hove Singularities in Twisted Bilayer Graphene by Scanning Tunneling Microscopy and Theoretical Analysis", Phys. Rev. Lett. **109**, 196802 (2012).

[180] L. A. Ponomarenko, R. V. Gorbachev, G. L. Yu, D. C. Elias, R. Jalil, A. A. Patel, A. Mishchenko, A. S. Mayorov, C. R. Woods, J. R. Wallbank, M. Mucha-Kruczynski, B. A. Piot, M. Potemski, I. V. Grigorieva, K. S. Novoselov, F. Guinea, V. I. Fal'ko, and A. K. Geim, "Cloning of Dirac fermions in graphene superlattices", Nature **497**, 594 (2013).

[181] E. Suárez Morell, J. D. Correa, P. Vargas, M. Pacheco, and Z. Barticevic, "Flat bands in slightly twisted bilayer graphene: Tight-binding calculations", Phys. Rev. B **82**, 121407 (2010).

[182] G. T. de Laissardière, D. Mayou, and L. Magaud, "Localization of Dirac Electrons in Rotated Graphene Bilayers", Nano Letters **10**, 804 (2010).

[183] S. Shallcross, S. Sharma, E. Kandelaki, and O. A. Pankratov, "Electronic structure of turbostratic graphene", Phys. Rev. B **81**, 165105 (2010).

[184] A. Luican, G. Li, A. Reina, J. Kong, R. R. Nair, K. S. Novoselov, A. K. Geim, and E. Y. Andrei, "Single-Layer Behavior and Its Breakdown in Twisted Graphene Layers", Phys. Rev. Lett. **106**, 126802 (2011).

[185] P. Moon and M. Koshino, "Energy spectrum and quantum Hall effect in twisted bilayer graphene", Phys. Rev. B **85**, 195458 (2012).

[186] J. M. B. Lopes dos Santos, N. M. R. Peres, and A. H. Castro Neto, "Continuum model of the twisted graphene bilayer", Phys. Rev. B **86**, 155449 (2012).

[187] J. M. B. Lopes dos Santos, N. M. R. Peres, and A. H. Castro Neto, "Graphene Bilayer with a Twist: Electronic Structure", Phys. Rev. Lett. **99**, 256802 (2007).

[188] G. Chaudhary, A. H. MacDonald, and M. R. Norman, "Quantum Hall superconductivity from moiré Landau levels", Phys. Rev. Res. **3**, 033260 (2021).

[189] N. F. Q. Yuan and L. Fu, "Model for the metal-insulator transition in graphene superlattices and beyond", Phys. Rev. B **98**, 045103 (2018).

[190] L. Rademaker, I. V. Protopopov, and D. A. Abanin, "Topological flat bands and correlated states in twisted monolayer-bilayer graphene", Phys. Rev. Res. **2**, 033150 (2020).

[191] S. Javvaji, J.-H. Sun, and J. Jung, "Topological flat bands without magic angles in massive twisted bilayer graphenes", Phys. Rev. B **101**, 125411 (2020).

[192] H. C. Po, L. Zou, A. Vishwanath, and T. Senthil, "Origin of Mott Insulating Behavior and Superconductivity in Twisted Bilayer Graphene", Phys. Rev. X **8**, 031089 (2018).

[193] M. Xie and A. H. MacDonald, "Nature of the Correlated Insulator States in Twisted Bilayer Graphene", Phys. Rev. Lett. **124**, 097601 (2020).

[194] S. Carr, D. Massatt, S. Fang, P. Cazeaux, M. Luskin, and E. Kaxiras, "Twistronics: Manipulating the electronic properties of two-dimensional layered structures through their twist angle", Phys. Rev. B **95**, 075420 (2017).

[195] P. Potasz, M. Xie, and A. H. MacDonald, "Exact Diagonalization for Magic-Angle Twisted Bilayer Graphene", Phys. Rev. Lett. **127**, 147203 (2021).

[196] D. M. Kennes, J. Lischner, and C. Karrasch, "Strong correlations and $d + id$ superconductivity in twisted bilayer graphene", Phys. Rev. B **98**, 241407 (2018).

[197] J. W. F. Venderbos and R. M. Fernandes, "Correlations and electronic order in a two-orbital honeycomb lattice model for twisted bilayer graphene", Phys. Rev. B **98**, 245103 (2018).

[198] F. Wu, E. Hwang, and S. Das Sarma, "Phonon-induced giant linear-in-T resistivity in magic angle twisted bilayer graphene: Ordinary strangeness and exotic superconductivity", Phys. Rev. B **99**, 165112 (2019).

[199] M. Yankowitz, S. Chen, H. Polshyn, Y. Zhang, K. Watanabe, T. Taniguchi, D. Graf, A. F. Young, and C. R. Dean, "Tuning superconductivity in twisted bilayer graphene", Science **363**, 1059 (2019).

[200] X. Lu, P. Stepanov, W. Yang, M. Xie, M. A. Aamir, I. Das, C. Urgell, K. Watanabe, T. Taniguchi, G. Zhang, A. Bachtold, A. H. MacDonald, and D. K. Efetov, "Superconductors, orbital magnets and correlated states in magic-angle bilayer graphene", Nature **574**, 653 (2019).

[201] Y. Xie, A. T. Pierce, J. M. Park, D. E. Parker, E. Khalaf, P. Ledwith, Y. Cao, S. H. Lee, S. Chen, P. R. Forrester, K. Watanabe, T. Taniguchi, A. Vishwanath, P. Jarillo-Herrero, and A. Yacoby, "Fractional Chern insulators in magic-angle twisted bilayer graphene", Nature **600**, 439 (2021).

[202] G. W. Burg, J. Zhu, T. Taniguchi, K. Watanabe, A. H. MacDonald, and E. Tutuc, "Correlated Insulating States in Twisted Double Bilayer Graphene", Phys. Rev. Lett. **123**, 197702 (2019).

[203] P. Rickhaus, F. K. de Vries, J. Zhu, E. Portoles, G. Zheng, M. Masseroni, A. Kurzmann, T. Taniguchi, K. Watanabe, A. H. MacDonald, T. Ihn, and K. Ensslin, "Correlated electron-hole state in twisted double-bilayer graphene", Science **373**, 1257 (2021).

[204] Y. Choi, J. Kemmer, Y. Peng, A. Thomson, H. Arora, R. Polski, Y. Zhang, H. Ren, J. Alicea, G. Refael, F. von Oppen, K. Watanabe, T. Taniguchi, and S. Nadj-Perge, "Electronic correlations in twisted bilayer graphene near the magic angle", Nature Physics **15**, 1174 (2019).

[205] X. Liu, Z. Hao, E. Khalaf, J. Y. Lee, Y. Ronen, H. Yoo, D. H. Najafabadi, K. Watanabe, T. Taniguchi, A. Vishwanath, and P. Kim, "Tunable spin-polarized correlated states in twisted double bilayer graphene", Nature **583**, 221 (2020).

[206] D. Wong, K. P. Nuckolls, M. Oh, B. Lian, Y. Xie, S. Jeon, K. Watanabe, T. Taniguchi, B. A. Bernevig, and A. Yazdani, "Cascade of electronic transitions in magic-angle twisted bilayer graphene", Nature **582**, 198 (2020).

[207] U. Zondiner, A. Rozen, D. Rodan-Legrain, Y. Cao, R. Queiroz, T. Taniguchi, K. Watanabe, Y. Oreg, F. von Oppen, A. Stern, E. Berg, P. Jarillo-Herrero, and S. Ilani, "Cascade of phase transitions and Dirac revivals in magic-angle graphene", Nature **582**, 203 (2020).

[208] A. Kerelsky, L. J. McGilly, D. M. Kennes, L. Xian, M. Yankowitz, S. Chen, K. Watanabe, T. Taniguchi, J. Hone, C. Dean, A. Rubio, and A. N. Pasupathy, "Maximized electron interactions at the magic angle in twisted bilayer graphene", Nature **572**, 95 (2019).

[209] Y. Jiang, X. Lai, K. Watanabe, T. Taniguchi, K. Haule, J. Mao, and E. Y. Andrei, "Charge order and broken rotational symmetry in magic-angle twisted bilayer graphene", Nature **573**, 91 (2019).

[210] H. Polshyn, M. Yankowitz, S. Chen, Y. Zhang, K. Watanabe, T. Taniguchi, C. R. Dean, and A. F. Young, "Large linear-in-temperature resistivity in twisted bilayer graphene", Nature Physics **15**, 1011 (2019).

[211] I. Das, C. Shen, A. Jaoui, J. Herzog-Arbeitman, A. Chew, C.-W. Cho, K. Watanabe, T. Taniguchi, B. A. Piot, B. A. Bernevig, and D. K. Efetov, "Observation of Reentrant Correlated Insulators and Interaction-Driven Fermi-Surface Reconstructions at One Magnetic Flux Quantum per Moiré Unit Cell in Magic-Angle Twisted Bilayer Graphene", Phys. Rev. Lett. **128**, 217701 (2022).

[212] E. Codecido, Q. Wang, R. Koester, S. Che, H. Tian, R. Lv, S. Tran, K. Watanabe, T. Taniguchi, F. Zhang, M. Bockrath, and C. N. Lau, "Correlated insulating and superconducting states in twisted bilayer graphene below the magic angle", Science Advances **5**, eaaw9770 (2019).

[213] L. Balents, C. R. Dean, D. K. Efetov, and A. F. Young, "Superconductivity and strong correlations in moiré flat bands", Nature Physics **16**, 725 (2020).

[214] T. E. Beechem, T. Ohta, B. Diaconescu, and J. T. Robinson, "Rotational Disorder in Twisted Bilayer Graphene", ACS Nano **8**, 1655 (2014).

[215] A. Uri, S. Grover, Y. Cao, J. A. Crosse, K. Bagani, D. Rodan-Legrain, Y. Myasoedov, K. Watanabe, T. Taniguchi, P. Moon, M. Koshino, P. Jarillo-Herrero, and E. Zeldov, "Mapping the twist-angle disorder and Landau levels in magic-angle graphene", Nature **581**, 47 (2020).

[216] A. C. Gadelha, D. A. A. Ohlberg, F. C. Santana, G. S. N. Eliel, J. S. Lemos, V. Ornelas, D. Miranda, R. B. Nadas, K. Watanabe, T. Taniguchi, C. Rabelo, P. P. de Mello Venezuela, G. Medeiros-Ribeiro, A. Jorio, L. G. Cançado, and L. C. Campos, "Twisted Bilayer Graphene: A Versatile Fabrication Method and the Detection of Variable Nanometric Strain Caused by Twist-Angle Disorder", ACS Applied Nano Materials **4**, 1858 (2021).

[217] J. H. Wilson, Y. Fu, S. Das Sarma, and J. H. Pixley, "Disorder in twisted bilayer graphene", Phys. Rev. Res. **2**, 023325 (2020).

[218] N. P. Kazmierczak, M. V. Winkle, C. Ophus, K. C. Bustillo, S. Carr, H. G. Brown, J. Ciston, T. Taniguchi, K. Watanabe, and D. K. Bediako, "Strain fields in twisted bilayer graphene", Nature Materials **20**, 956 (2021).

[219] N. Nakatsuji and M. Koshino, "Moiré disorder effect in twisted bilayer graphene", Phys. Rev. B **105**, 245408 (2022).

[220] R. Samajdar and M. S. Scheurer, "Microscopic pairing mechanism, order parameter, and disorder sensitivity in moiré superlattices: Applications to twisted double-bilayer graphene", Phys. Rev. B **102**, 064501 (2020).

[221] G. Shavit, K. Kolář, C. Mora, F. von Oppen, and Y. Oreg, "Strain disorder and gapless intervalley coherent phase in twisted bilayer graphene", Phys. Rev. B **107**, L081403 (2023).

[222] H. Zhou, T. Xie, A. Ghazaryan, T. Holder, J. R. Ehrets, E. M. Spanton, T. Taniguchi, K. Watanabe, E. Berg, M. Serbyn, and A. F. Young, "Half- and quarter-metals in rhombohedral trilayer graphene", Nature **598**, 429 (2021).

[223] A. L. Szabó and B. Roy, "Metals, fractional metals, and superconductivity in rhombohedral trilayer graphene", Phys. Rev. B **105**, L081407 (2022).

[224] D.-C. Lu, T. Wang, S. Chatterjee, and Y.-Z. You, "Correlated metals and unconventional superconductivity in rhombohedral trilayer graphene: A renormalization group analysis", Phys. Rev. B **106**, 155115 (2022).

[225] C. Huang, T. M. R. Wolf, W. Qin, N. Wei, I. V. Blinov, and A. H. MacDonald, "Spin and orbital metallic magnetism in rhombohedral trilayer graphene", Phys. Rev. B **107**, L121405 (2023).

[226] F. Winterer, F. R. Geisenhof, N. Fernandez, A. M. Seiler, F. Zhang, and R. T. Weitz, "Ferroelectric and anomalous quantum Hall states in bare rhombohedral trilayer graphene", (2023), 2305.04950.

[227] F. R. Geisenhof, F. Winterer, A. M. Seiler, J. Lenz, T. Xu, F. Zhang, and R. T. Weitz, "Quantum anomalous Hall octet driven by orbital magnetism in bilayer graphene", Nature **598**, 53 (2021).

[228] H. Zhou, L. Holleis, Y. Saito, L. Cohen, W. Huynh, C. L. Patterson, F. Yang, T. Taniguchi, K. Watanabe, and A. F. Young, "Isospin magnetism and spin-polarized superconductivity in Bernal bilayer graphene", Science **375**, 774 (2022).

[229] Y. Zhang, R. Polski, A. Thomson, É. Lantagne-Hurtubise, C. Lewandowski, H. Zhou, K. Watanabe, T. Taniguchi, J. Alicea, and S. Nadj-Perge, "Enhanced superconductivity in spin–orbit proximitized bilayer graphene", Nature **613**, 268 (2023).

[230] A. M. Seiler, F. R. Geisenhof, F. Winterer, K. Watanabe, T. Taniguchi, T. Xu, F. Zhang, and R. T. Weitz, "Quantum cascade of correlated phases in trigonally warped bilayer graphene", Nature **608**, 298 (2022).

[231] Y.-Z. Chou, F. Wu, J. D. Sau, and S. Das Sarma, "Acoustic-phonon-mediated superconductivity in Bernal bilayer graphene", Phys. Rev. B **105**, L100503 (2022).

[232] S. C. de la Barrera, S. Aronson, Z. Zheng, K. Watanabe, T. Taniguchi, Q. Ma, P. Jarillo-Herrero, and R. Ashoori, "Cascade of isospin phase transitions in Bernal-stacked bilayer graphene at zero magnetic field", Nature Physics **18**, 771 (2022).

[233] L. Holleis, C. L. Patterson, Y. Zhang, H. M. Yoo, H. Zhou, T. Taniguchi, K. Watanabe, S. Nadj-Perge, and A. F. Young, "Ising Superconductivity and Nematicity in Bernal Bilayer Graphene with Strong Spin Orbit Coupling", (2023), 2303.00742.

[234] A. L. Szabó and B. Roy, "Competing orders and cascade of degeneracy lifting in doped Bernal bilayer graphene", Phys. Rev. B **105**, L201107 (2022).

[235] Y.-Z. Chou, F. Wu, and S. Das Sarma, "Enhanced superconductivity through virtual tunneling in Bernal bilayer graphene coupled to WSe_2", Phys. Rev. B **106**, L180502 (2022).

[236] A. Jimeno-Pozo, H. Sainz-Cruz, T. Cea, P. A. Pantaleón, and F. Guinea, "Superconductivity from electronic interactions and spin-orbit enhancement in bilayer and trilayer graphene", Phys. Rev. B **107**, L161106 (2023).

[237] P. A. Pantaleón, A. Jimeno-Pozo, H. Sainz-Cruz, V. T. Phong, T. Cea, and F. Guinea, "Superconductivity and correlated phases in non-twisted bilayer and trilayer graphene", Nature Reviews Physics **5**, 304 (2023).

[238] Z. Li, X. Kuang, A. Jimeno-Pozo, H. Sainz-Cruz, Z. Zhan, S. Yuan, and F. Guinea, "Charge fluctuations, phonons and superconductivity in multilayer graphene", (2023), 2303.17286.

[239] F. Zhang, B. Sahu, H. Min, and A. H. MacDonald, "Band structure of *ABC*-stacked graphene trilayers", Phys. Rev. B **82**, 035409 (2010).

[240] J. P. Eisenstein, L. N. Pfeiffer, and K. W. West, "Negative compressibility of interacting two-dimensional electron and quasiparticle gases", Phys. Rev. Lett. **68**, 674 (1992).

[241] A. López, L. Colmenárez, M. Peralta, F. Mireles, and E. Medina, "Proximity-induced spin-orbit effects in graphene on Au", Phys. Rev. B **99**, 085411 (2019).

[242] K. Zollner and J. Fabian, "Bilayer graphene encapsulated within monolayers of WS_2 or $Cr_2Ge_2Te_6$: Tunable proximity spin-orbit or exchange coupling", Phys. Rev. B **104**, 075126 (2021).

[243] K. Zollner, M. Gmitra, and J. Fabian, "Swapping Exchange and Spin-Orbit Coupling in 2D van der Waals Heterostructures", Phys. Rev. Lett. **125**, 196402 (2020).

[244] K. Zollner, M. Gmitra, and J. Fabian, "Proximity spin-orbit and exchange coupling in ABA and ABC trilayer graphene van der Waals heterostructures", Phys. Rev. B **105**, 115126 (2022).

[245] K. Zollner, M. Gmitra, T. Frank, and J. Fabian, "Theory of proximity-induced exchange coupling in graphene on hBN/(Co, Ni)", Phys. Rev. B **94**, 155441 (2016).

[246] H. Haugen, D. Huertas-Hernando, and A. Brataas, "Spin transport in proximity-induced ferromagnetic graphene", Phys. Rev. B **77**, 115406 (2008).

[247] K. Zollner and J. Fabian, "Engineering Proximity Exchange by Twisting: Reversal of Ferromagnetic and Emergence of Antiferromagnetic Dirac Bands in Graphene/$Cr_2Ge_2Te_6$", Phys. Rev. Lett. **128**, 106401 (2022).

[248] A. A. Kaverzin, T. S. Ghiasi, A. H. Dismukes, X. Roy, and B. J. van Wees, "Spin injection by spin–charge coupling in proximity induced magnetic graphene", 2D Materials **9**, 045003 (2022).

[249] M. Peralta, E. Medina, and F. Mireles, "Proximity-induced exchange and spin-orbit effects in graphene on Ni and Co", Phys. Rev. B **99**, 195452 (2019).

[250] I. A. Verzhbitskiy, H. Kurebayashi, H. Cheng, J. Zhou, S. Khan, Y. P. Feng, and G. Eda, "Controlling the magnetic anisotropy in Cr2Ge2Te6 by electrostatic gating", Nature Electronics **3**, 460 (2020).

[251] W. Xing, Y. Chen, P. M. Odenthal, X. Zhang, W. Yuan, T. Su, Q. Song, T. Wang, J. Zhong, S. Jia, X. C. Xie, Y. Li, and W. Han, "Electric field effect in multilayer $Cr_2Ge_2Te_6$: a ferromagnetic 2D material", 2D Materials **4**, 024009 (2017).

[252] V. Carteaux, D. Brunet, G. Ouvrard, and G. Andre, "Crystallographic, magnetic and electronic structures of a new layered ferromagnetic compound $Cr_2Ge_2Te_6$", Journal of Physics: Condensed Matter **7**, 69 (1995).

[253] W. Zhuo, B. Lei, S. Wu, F. Yu, C. Zhu, J. Cui, Z. Sun, D. Ma, M. Shi, H. Wang, W. Wang, T. Wu, J. Ying, S. Wu, Z. Wang, and X. Chen, "Manipulating Ferromagnetism in Few-Layered $Cr_2Ge_2Te_6$", Advanced Materials **33** (2021).

[254] M.-G. Han, J. A. Garlow, Y. Liu, H. Zhang, J. Li, D. DiMarzio, M. W. Knight, C. Petrovic, D. Jariwala, and Y. Zhu, "Topological Magnetic-Spin Textures in Two-Dimensional van der Waals $Cr_2Ge_2Te_6$", Nano Letters **19**, 7859 (2019).

[255] K. Kuroki, S. Onari, R. Arita, H. Usui, Y. Tanaka, H. Kontani, and H. Aoki, "Unconventional Pairing Originating from the Disconnected Fermi Surfaces of Superconducting $LaFeAsO_{1-x}F_x$", Phys. Rev. Lett. **101**, 087004 (2008).

[256] S. Graser, T. A. Maier, P. J. Hirschfeld, and D. J. Scalapino, "Near-degeneracy of several pairing channels in multiorbital models for the Fe pnictides", New Journal of Physics **11**, 025016 (2009).

[257] T. A. Maier, S. Graser, P. J. Hirschfeld, and D. J. Scalapino, "d-wave pairing from spin fluctuations in the $K_xFe_{2-y}Se_2$ superconductors", Phys. Rev. B **83**, 100515 (2011).

[258] K. Nomura, S. Ryu, and D.-H. Lee, "Field-Induced Kosterlitz-Thouless Transition in the $N = 0$ Landau Level of Graphene", Phys. Rev. Lett. **103**, 216801 (2009).

[259] Y.-Z. You and A. Vishwanath, "Kohn-Luttinger superconductivity and intervalley coherence in rhombohedral trilayer graphene", Phys. Rev. B **105**, 134524 (2022).

[260] S. Chatterjee, T. Wang, E. Berg, and M. P. Zaletel, "Inter-valley coherent order and isospin fluctuation mediated superconductivity in rhombohedral trilayer graphene", Nature Communications **13**, 6013 (2022).

[261] S. Konschuh, "Spin-orbit coupling effects: from graphene to graphite", (2011).

[262] M. Koshino and E. McCann, "Trigonal warping and Berry's phase $N\pi$ in ABC-stacked multilayer graphene", Phys. Rev. B **80**, 165409 (2009).

[263] A. Kormányos and G. Burkard, "Intrinsic and substrate induced spin-orbit interaction in chirally stacked trilayer graphene", Phys. Rev. B **87**, 045419 (2013).

[264] D. Marchenko, D. V. Evtushinsky, E. Golias, A. Varykhalov, T. Seyller, and O. Rader, "Extremely flat band in bilayer graphene", Science Advances **4** (2018).

[265] Y.-Z. You and A. Vishwanath, "Superconductivity from valley fluctuations and approximate SO(4) symmetry in a weak coupling theory of twisted bilayer graphene", npj Quantum Materials **4**, 16 (2019).

[266] H. Zhou, T. Xie, T. Taniguchi, K. Watanabe, and A. F. Young, "Superconductivity in rhombohedral trilayer graphene", Nature **598**, 434 (2021).

[267] M. Xie and S. Das Sarma, "Flavor symmetry breaking in spin-orbit coupled bilayer graphene", Phys. Rev. B **107**, L201119 (2023).

[268] Y.-Z. Chou, F. Wu, J. D. Sau, and S. Das Sarma, "Acoustic-Phonon-Mediated Superconductivity in Rhombohedral Trilayer Graphene", Phys. Rev. Lett. **127**, 187001 (2021).

[269] A. Ghazaryan, T. Holder, M. Serbyn, and E. Berg, "Unconventional Superconductivity in Systems with Annular Fermi Surfaces: Application to Rhombohedral Trilayer Graphene", Phys. Rev. Lett. **127**, 247001 (2021).

[270] T. Cea, P. A. Pantaleón, V. T. Phong, and F. Guinea, "Superconductivity from repulsive interactions in rhombohedral trilayer graphene: A Kohn-Luttinger-like mechanism", Phys. Rev. B **105**, 075432 (2022).

[271] W. Qin, C. Huang, T. Wolf, N. Wei, I. Blinov, and A. H. MacDonald, "Functional Renormalization Group Study of Superconductivity in Rhombohedral Trilayer Graphene", Phys. Rev. Lett. **130**, 146001 (2023).

[272] S. Konschuh, M. Gmitra, D. Kochan, and J. Fabian, "Theory of spin-orbit coupling in bilayer graphene", Phys. Rev. B **85**, 115423 (2012).

[273] J. B. Curtis, N. R. Poniatowski, Y. Xie, A. Yacoby, E. Demler, and P. Narang, "Stabilizing Fluctuating Spin-Triplet Superconductivity in Graphene via Induced Spin-Orbit Coupling", Phys. Rev. Lett. **130**, 196001 (2023).

[274] Z. Dong, A. V. Chubukov, and L. Levitov, "Transformer spin-triplet superconductivity at the onset of isospin order in bilayer graphene", Phys. Rev. B **107**, 174512 (2023).

[275] A. Georges, L. d. Medici, and J. Mravlje, "Strong Correlations from Hund's Coupling", Annual Review of Condensed Matter Physics **4**, 137 (2013).

[276] Y.-Z. Chou and S. Das Sarma, "Scaling theory of intrinsic Kondo and Hund's rule interactions in magic-angle twisted bilayer graphene", Phys. Rev. B **108**, 125106 (2023).

[277] F. Aryasetiawan, M. Imada, A. Georges, G. Kotliar, S. Biermann, and A. I. Lichtenstein, "Frequency-dependent local interactions and low-energy effective models from electronic structure calculations", Phys. Rev. B **70**, 195104 (2004).

[278] W. Kohn and J. M. Luttinger, "New Mechanism for Superconductivity", Phys. Rev. Lett. **15**, 524 (1965).

[279] Y. Cao, Y. Zhang, Y.-B. Liu, C.-C. Liu, W.-Q. Chen, and F. Yang, "Kohn-Luttinger Mechanism Driven Exotic Topological Superconductivity on the Penrose Lattice", Phys. Rev. Lett. **125**, 017002 (2020).

[280] J. González and T. Stauber, "Kohn-Luttinger Superconductivity in Twisted Bilayer Graphene", Phys. Rev. Lett. **122**, 026801 (2019).

[281] Y.-P. Lin and R. M. Nandkishore, "Kohn-Luttinger superconductivity on two orbital honeycomb lattice", Phys. Rev. B **98**, 214521 (2018).

[282] D. F. Agterberg, J. S. Davis, S. D. Edkins, E. Fradkin, D. J. V. Harlingen, S. A. Kivelson, P. A. Lee, L. Radzihovsky, J. M. Tranquada, and Y. Wang, "The Physics of Pair-Density Waves: Cuprate Superconductors and Beyond", Annual Review of Condensed Matter Physics **11**, 231 (2020).

[283] S. Hörhold, J. Graf, M. Marganska, and M. Grifoni, "Two-bands Ising superconductivity from Coulomb interactions in monolayer $NbSe_2$", 2D Materials **10**, 025008 (2023).

[284] G. C. Wick, "The Evaluation of the Collision Matrix", Phys. Rev. **80**, 268 (1950).

[285] P.-O. Löwdin, "Studies in Perturbation Theory. IV. Solution of Eigenvalue Problem by Projection Operator Formalism", Journal of Mathematical Physics **3**, 969 (1962).

List of publications:
(Relevant to the current thesis)

- Y. Zhumagulov, D. Kochan, and J. Fabian, Swapping exchange and spin-orbit induced correlated phases in ex-so-tic van der Waals heterostructures, arXiv preprint arXiv:2307.16025 (2023)
- Y. Zhumagulov, D. Kochan, and J. Fabian, Emergent correlated phases in rhombohedral trilayer graphene induced by proximity spin-orbit and exchange coupling, arXiv preprint arXiv:2305.14277 (2023)
- Y. Zhumagulov, T. Frank, and J. Fabian, Edge states in proximitized graphene ribbons and flakes in a perpendicular magnetic field: Emergence of lone pseudohelical pairs and pure spin-current states, Physical Review B **105**, 205134 (2022)

(Other publications)

- S. Meier, Y. Zhumagulov, M. Dietl, P. Parzefall, M. Kempf, J. Holler, P. Nagler, P. E. Faria Junior, J. Fabian, T. Korn, and C. Schüller, Emergent trion-phonon coupling in atomically reconstructed MoSe2–WSe2 heterobilayers, Physical Review Research **5**, L032036 (2023)
- A. Kudlis, M. Kazemi, Y. Zhumagulov, H. Schrautzer, A. I. Chernov, P. F. Bessarab, I. V. Iorsh, and I. A. Shelykh, All-optical magnetization control in CrI3 monolayers: A microscopic theory, Physical Review B **108**, 094421 (2023)
- D. Kochan, A. Costa, I. Zhumagulov, and I. Žutić, Phenomenological Theory of the Supercurrent Diode Effect: The Lifshitz Invariant, arXiv preprint arXiv:2303.11975 (2023)
- Z. An, P. Soubelet, Y. Zhumagulov, M. Zopf, A. Delhomme, C. Qian, P. E. Faria Junior, J. Fabian, X. Cao, J. Yang, A. V. Stier, F. Ding, and J. J. Finley, Strain control of exciton and trion spin-valley dynamics in monolayer transition metal dichalcogenides, Physical Review B **108**, L041404 (2023)
- D. Gulevich, Y. V. Zhumagulov, V. Kozin, and I. Tokatly, Excitonic effects in time-dependent density functional theory from zeros of the density response, Physical Review B **107**, 165118 (2023)
- Y. V. Zhumagulov, A. Vagov, D. R. Gulevich, and V. Perebeinos, Electrostatic and Environmental Control of the Trion Fine Structure in Transition Metal Dichalcogenide Monolayers, Nanomaterials **12**, 3728 (2022)

- M. Kazemi, V. Shahnazaryan, Y. Zhumagulov, P. F. Bessarab, and I. Shelykh, Interaction of excitons with magnetic topological defects in 2D magnetic monolayers: localization and anomalous Hall effect, 2D Materials **10**, 015003 (2022)

- Y. V. Zhumagulov, V. D. Neverov, A. E. Lukyanov, D. R. Gulevich, A. V. Krasavin, A. Vagov, and V. Perebeinos, Nonlinear spectroscopy of excitonic states in transition metal dichalcogenides, Physical Review B **105**, 115436 (2022)

- F. S. Covre, P. Faria, V. O. Gordo, C. S. de Brito, Y. V. Zhumagulov, M. D. Teodoro, O. Couto, L. Misoguti, S. Pratavieira, M. B. d. Andrade, et al., Revealing the impact of strain in the optical properties of bubbles in monolayer $MoSe_2$, Nanoscale **14**, 5758 (2022)

- A. E. Lukyanov, I. A. Kovalev, V. D. Neverov, Y. V. Zhumagulov, A. V. Krasavin, and D. Kochan, Strength of the Hubbard potential and its modification by breathing distortion in $BaBiO_3$, Physical Review B **105**, 045131 (2022)

- Y. V. Zhumagulov, S. Chiavazzo, D. R. Gulevich, V. Perebeinos, I. A. Shelykh, and O. Kyriienko, Microscopic theory of exciton and trion polaritons in doped monolayers of transition metal dichalcogenides, npj Computational Materials **8**, 92 (2022)

- V. D. Neverov, A. E. Lukyanov, Y. V. Zhumagulov, A. V. Krasavin, and V. Perebeinos, Polaronic signatures in pristine phosphorene, Physical Review Materials **5**, 054008 (2021)

- A. E. Lukyanov, V. D. Neverov, Y. V. Zhumagulov, A. P. Menushenkov, A. V. Krasavin, and A. Vagov, Laser-induced ultrafast insulator-metal transition in $BaBiO_3$, Physical Review Research **2**, 043207 (2020)

- Y. V. Zhumagulov, A. Vagov, D. R. Gulevich, P. E. Faria Junior, and V. Perebeinos, Trion induced photoluminescence of a doped MoS2 monolayer, The Journal of Chemical Physics **153** (2020)

- Y. V. Zhumagulov, A. Vagov, N. Y. Senkevich, D. R. Gulevich, and V. Perebeinos, Three-particle states and brightening of intervalley excitons in a doped MoS 2 monolayer, Physical Review B **101**, 245433 (2020)

- D. R. Gulevich, Y. V. Zhumagulov, A. Vagov, and V. Perebeinos, Nonadiabatic electron dynamics in time-dependent density functional theory at the cost of adiabatic local density approximation, Physical Review B **100**, 241109 (2019)

- Y. V. Zhumagulov, A. V. Krasavin, A. Lukyanov, V. D. Neverov, A. Yaroslavtsev, and A. P. Menushenkov, Effect of Optical Excitation on the Band Structure and X-Ray Absorption Spectra of BaBiO 3-Based High-Temperature Superconductors: Ab Initio Calculation, JETP Letters **110**, 31 (2019)

- Y. V. Zhumagulov, V. A. Kashurnikov, A. V. Krasavin, A. Lukyanov, and V. D. Neverov, Phase Diagram of the Two-Orbital Model for Iron-Based HTSC: Variational Cluster Approximation, JETP Letters **109**, 45 (2019)
- A. V. Krasavin, P. V. Borisyuk, O. S. Vasiliev, Y. V. Zhumagulov, V. A. Kashurnikov, U. N. Kurelchuk, and Y. Y. Lebedinskii, Calculation of density of states of transition metals: From bulk sample to nanocluster, Review of scientific instruments **89** (2018)
- V. A. Kashurnikov, A. V. Krasavin, and Y. V. Zhumagulov, Momentum distribution and non-Fermi-liquid behavior in low-doped two-orbital model: Finite-size cluster quantum Monte Carlo approach, Physical Review B **94**, 235145 (2016)
- V. A. Kashurnikov, A. V. Krasavin, and Y. V. Zhumagulov, Electron density of states of Fe-based superconductors: Quantum trajectory Monte Carlo method, JETP letters **103**, 334 (2016)

Acknowledgments

I am writing to express my gratitude to Professor Jaroslav Fabian for allowing me to join his scientific group. His scientific and personal mentorship has been invaluable, and I appreciate his willingness to answer my questions and engage in discussions. I am genuinely thankful for this opportunity.

I am thankful for the help and mentoring my colleagues, especially Denis Kochan, Paulo Faria Junior, and Michael Barth, provided. Their guidance and wealth of experience were exceptional. They supported me throughout my studies, providing scientific and personal advice.

I want to express my sincere gratitude to my grandfather, Vyacheslav Nikolaevich Muravyov, for his unshakable faith in me and genuine understanding of my experiences.

Last but not least, I want to express my gratitude towards my wife, Sofia Berdysheva, for her unwavering support and understanding. Without her, I would not have achieved my success.

Finally, I am grateful to the Deutsche Forschungsgemeinschaft (DFG, German Research Foundation) SPP 2244 (Project ID 443416183) for financial support.